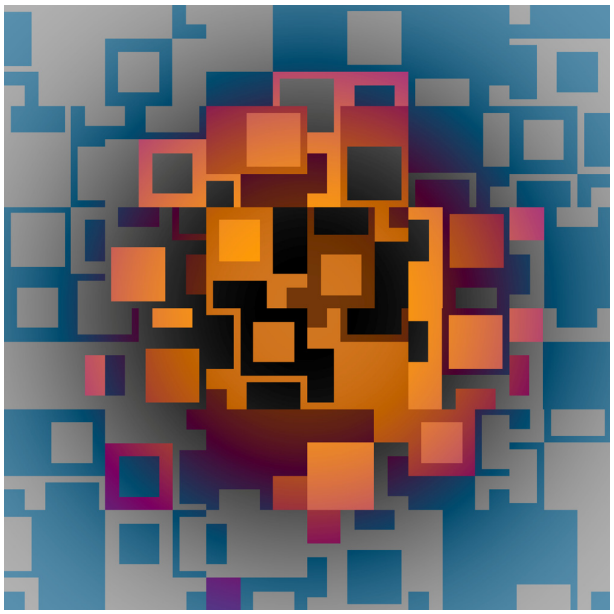

MATHMOD 2018 Extended Abstract Volume

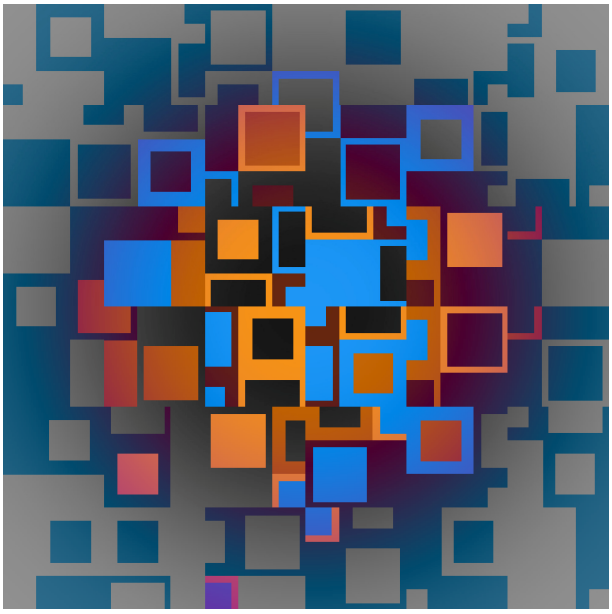

Extended Abstracts of 9th Vienna Conference on Mathematical Modelling

Vienna, Austria, February 21 - 23, 2018

Edited by Felix Breitenecker, Wolfgang Kemmetmüller, Andreas Körner, Andreas Kugi, and Inge Troch
TU Wien

ARGESIM Publisher, Vienna, www.argesim.org
ARGESIM Report no. 55, ISBN: 978-3-901608-91-9 (ebook)
DOI: 10.11128/arep.55

MATHMOD 2018

Extended Abstract Volume

Extended Abstracts of
9th Vienna Conference on Mathematical Modelling

Vienna, Austria, February 21 – 23, 2018

Edited by
Felix Breitenecker, Wolfgang Kemmetmüller,
Andreas Körner, Andreas Kugi, and Inge Troch
TU Wien

ARGESIM Publisher, Vienna, www.argesim.org
ARGESIM Report no. 55, ISBN: 978-3-901608-91-9 (ebook)
DOI: 10.11128/arep.55

Bibliographic Data:

Publisher: ARGESIM Publisher, Vienna
Title: MATHMOD 2018 Extended Abstract Volume
Subtitle: Extended Abstracts of 9th Vienna Conference on Mathematical Modelling, Vienna, Austria, February 21 – 23, 2018
Author(s):
Editor(s): Felix Breitenecker, Wolfgang Kemmetmüller, Andreas Körner, Andreas Kugi, Inge Troch
Series: ARGESIM Reports
Series Editors: Felix Breitenecker, Thorsten Pawletta, Sigrid Wenzel, ASIM
Volume: ARGESIM Report no. 55
ISBN: 978-3-901608-91-9 (ebook)
DOI: 10.11128/arep.55
Generic URL: → www.argesim.org/publications/arep.55
Publication Date: March 1, 2018
Number of Pages: 128 + x pages

Copyright Information / Regulations ARGESIM

ARGESIM is a non-profit scientific society generally aiming for dissemination of information on system simulation - from research via development to applications of system simulation. ARGESIM's primary publication is the journal SNE – Simulation Notes Europe with open access to all contributions; generally, the authors retain the copyright of their SNE contributions. This copyright regulation holds also for other ARGESIM publications, as conference volumes of ASIM conferences, MATHMOD conferences, and special EUROSIM conferences, in consideration of copyright regulations for related conference publications.

About ARGESIM

ARGESIM is a non-profit society generally aiming for dissemination of information on system simulation from research via development to applications of system simulation.
ARGESIM is closely co-operating with EUROSIM, the Federation of European Simulation Societies, and with ASIM, the German Simulation Society. ARGESIM is an 'outsourced' activity from the Mathematical Modelling and Simulation Group of TU Wien, there is also close co-operation with TU Wien (organisationally and personally). Publishing activities are organized by ARGESIM Publisher, with ISBN root 978-3-901608-xx-y and DOI root 10.11128/xx…x. ARGESIM's activities are:

- Publication of the scientific journal SNE - Simulation Notes Europe (Membership Journal of EUROSIM, the Federation of European Simulation Societies) → *www.sne-journal.org*
- Organisation and Publication of the ARGESIM Benchmarks for Modelling Approaches and Simulation Implementations → *www.argesim.org/benchmarks/*
- Publication of the series ARGESIM Reports (for monographs in system simulation, and proceedings of simulation conferences and workshops) → *www.argesim.org/publications/*
- Publication of the special series FBS Simulation - Advances in Simulation / Fortschrittsberichte Simulation (monographs in co-operation with ASIM, the German Simulation Society
- Organisation of the Conference Series MATHMOD Vienna (triennial, in co-operation with EUROSIM, ASIM, and TU Wien) → *www.mathmod.at*
- Organisation of Summerschools and Seminars on Mod&Sim
- Administration and support of ASIM (German Simulation Society → *www.asim-gi.org*) and of EUROSIM (Federation of European Simulation Societies → *www.eurosim.info*)
- Support of ERASMUS and CEEPUS activities in system simulation for TU Wien

ARGESIM – Arbeitsgemeinschaft Simulation News – Working Committee Simulation News – SNE Publication
Mommsengasse 19/8, 1040 Vienna, Austria; Tel +43-1-58801-10111, -10115; Fax +43-1-58801-910111
Email: office@argesim.org, office@sne-journal.org; WWW: www.argesim.org, www.sne-journal.org
Incorporated Austrian Society ZVR No 213056164 – EU VAT ID No ATU 72054279
Bank Account: ARGESIM, IBAN AT07 2011 1828 9115 0800, BIC GIBAATWWXXX, ERSTE BANK VIENNA

FOREWORD

Since 1994, the **MATHMOD Conference Series** invites scientists, engineers, and experts to present their ideas, methods, applications, and results in the field of mathematical modelling and share their experiences in different application domains.

Like a mathematical model, **MATHMOD** has constants, parameters, and variables. Constants are the frequency – triennial – and the date – February; aim and scope are parameters to be tuned with respect to the recent developments in mathematical modelling. Parameters reflect the organisation: the first **MATHMODs** were organised under the flag of *IMACS* (International Association for Mathematics and Computers in Simulation), recent **MATHMOD**s are *IFAC* (International Federation of Automatic Control) co-sponsored conferences with all advantages of *IFAC* online publications for the **MATHMOD** proceedings. The local organisation team at *TU Wien* has been extended: the *Institute of Analysis and Scientific Computing* (*ASC*) has won the *Automation and Control Institute* (*ACIN*) as partner in the organisation of the conference. In addition, *ARGESIM*, a scientific society 'outsourced' from the institutes, developed from local supporter to international publication partner *ARGESIM Publisher* for the **MATHMOD** abstract volumes. New constants are other co-sponsorships, as for instance **MATHMOD** is also a *EUROSIM (Federation of European Simulation Societies) Conference.*

MATHMOD variables are the participants and the contributions. Successful models have output variables, and these are the contributions to the **MATHMOD** conferences. A classification of the contributions in model attribute parameters *Full Contributions*, *Discussion Contributions*, and *Student Contributions* has proven most appropriate. The success variables are the **MATHMOD** participants, spread over twenty-five countries, some concentrated in specific submodels, the very successful **MATHMOD Minisymposia**, some providing contributions to the classic submodels **MATHMOD Thematic Sessions** and **MATHMOD Poster Session**, and crowned by the **MATHMOD Plenary Lectures**.

MATHMOD also developed its conference publications along with the conference series from classical print publications via CD publication to structured electronic publications, resulting in a threefold publication model parameter. The **MATHMOD Proceedings** in the *IFAC-PapersOnLine* proceedings series (www.journals.elsevier.com/ifac-papersonline/) hosted at the *ScienceDirect* web service and the **MATHMOD Extended Abstract Volume** in the online *ARGESIM Reports* (www.argesim.org/mathmod-vienna/) allow for **MATHMOD**'s open access strategy for conference publications. The **MATHMOD Preprint Volume** contains all accepted **MATHMOD** contributions on the **MATHMOD** USB memory stick and serves for the convenience of the participants.

MATHMOD 2018, the *9th Vienna International Conference on Mathematical Modelling*, implemented all these developments in a successful conference with about 280 participants and about 220 contributions in snowy Vienna from February 21 to February 23, 2018 – with a tutorial pre-programme on February 20, 2018.

This **MATHMOD 2018 Extended Abstract Volume** publishes the extended abstracts (two-page abstracts) of all accepted *Discussion Contributions* and *Student Contributions* in the online *ARGESIM Report* 55, ISBN 978-3-901608-91-9, available with open access at the website *www.argesim.org/mathmod-vienna/.*
Seventy-four authors submitted a *Discussion Contribution* and we received eighteen *Student Contributions*. A review by an associate editor and by an IPC reviewer resulted in 49 accepted *Discussion Contributions* and 15 accepted *Student Contributions*. A final presentation check at MATHMOD 2018 and a layout quality check allow us to release 64 *Discussion Contributions* and *Student Contributions* for publication in this **Extended Abstract Volume**.

ARGESIM Publisher already took care on publication of abstracts for previous **MATHMOD** conferences, but this time for **MATHMOD 2018** each contribution is assigned an individual DOI number for quick web access and reliable documentation. Thus, along with the publication of the abstract volume, metadata of the contributions are stored in publication databases for cross-referencing. *ARGESIM Publisher*'s DOI numbers for the **MATHMOD 2018 Extended Abstract Volume** is within the range DOI 10.11128/arep.55.a55nnn, where nnn is the submission number of the contribution.

The **MATHMOD 2018 Proceedings** publish all accepted *Full Contributions* in *Volume* 51 *no*.2 of the *IFAC-PapersOnLine* proceedings series (ISSN 2405-8963) at the ScienceDirect web service *www.journals.elsevier.com/ifac-papersonline/* (open access, individual contribution DOI).

Last but not least, **MATHMOD 2018** also wants to draw attention to the possibilities of **MATHMOD Postconference Publications**. Following the *IFAC* copyright regulations with possible publication of **MATHMOD 2018** contributions in *IFAC* journals, suitably adapted versions of **MATHMOD 2018** contributions which contain sufficiently new material may also be submitted to *MCMDS*, the journal *Mathematical and Computer Modelling of Dynamical* Systems, published by *Taylor and Francis.* Extended contributions with emphasis on simulation may also be submitted to *SNE Simulation Notes Europe*, the scientific journal of *EUROSIM* published by *ARGESIM Publisher*, Vienna.

But **MATHMOD** puts emphasis also on two other very important constants – the socialising constant, and the traditional constant. **MATHMOD**s are providing a – hopefully attractive – **MATHMOD Social Programme**, and **MATHMOD**s continue the tradition with connection to fine arts. Consequently, **MATHMOD 2018** started with a talk on *Hidden Treasures of Vienna*, given by Inge Troch, the founder of MATHMOD. **MATHMOD 2018** presented a *Social Lecture* on modelling and simulation for dancing Viennese waltz, combining mathematical modelling and fine arts. **MATHMOD 2018** continued the co-operation with Vlatko Ceric, professor for stochastics and modelling at University Zagreb, who creates graphics in style of *Algorithmic Art* for **MATHMOD** design – the title page of these proceedings show design from algorithmic art series Birth, *www.veric.net.* And finally yet importantly, **MATHMOD** 2018 celebrates the Viennese Café tradition with the **MATHMOD Café Simulation**, a Viennese-type Café, especially established for **MATHMOD** near the conference office.

As organizers we want to express our sincere thanks to all of you for your help in making the **MATHMOD 2018** conference a success – first to the **MATHMOD 2018** participants, authors, and plenary lecturers. In particular, we appreciate the support of our sponsors and co-sponsors. Special thanks go to the members of the *International Program Committee* (**MATHMOD 2018** with 45 members/associate editors), who did a great job in organizing the review process – in total 541 reviews. A big thank goes to the organizers of the **MATHMOD Minisymposia** – 14 minisymposia and their 25 organizers played a key role for the success of **MATHMOD 2018**.

Moreover, we are proud of the excellent work of all staff members – a big applause to our 28 helping hands for **MATHMOD 2018**. Finally, we thank the *IFAC* publication team for the excellent cooperation, and the ARGESIM Publisher's people for support.

MATHMOD Conference Series – a mathematical model with constants, parameters, and variables: the frequency constant would be glad to meet many variables at **10th MATHMOD 2021**, February 17 – 19, 2021.

Felix Breitenecker, Wolfgang Kemmetmüller, Andreas Körner, Andreas Kugi, Inge Troch
Vienna, February 2018

MATHMOD 2018 – 9th Vienna International Conference on Mathematical Modelling

Sponsored by

TU Wien
Inst. f. Analysis and Scientific Computing and Automation and Control Institute

Co-Sponsored by

- **IFAC** International Federation of Automatic Control →
  - TC 4.2 Mechatronic Systems
  - TC 2.2 Linear Control Systems
- **ARGESIM** Vienna – Arbeitsgemeinschaft Simulation News, Wien → *www.argesim.org*
- EUROSIM – Federation of European Simulation Societies → *www.eurosim.info*
- ASIM – German Simulation Society (Arbeitsgemeinschaft Simulation) → *www.asim-gi.org*

Mutual Co-Sponsors

VDI / VDE – GMA – Society for Measurement and Automatic Control
GAMM Society for Applied Mathematics and Mechanics
OCG Austrian Computer Society
OVE - Österreichischer Verband für Elektrotechnik
OEMG Austrian Mathematical Society
GMAR - Österreichische Gesellschaft für Mess-, Automatisierung- und Robotertechnik
COCOS – Computational Complex Systems - Interfacultary Center TU Wien

Financial Co-Sponsors

The Mathworks, Europe → *www.mathworks.de*
Maplesoft Europe GmbH → *www.maplesoft.com*
LTX Simulation GmbH, Germany → *www.ltx.de*

International Programme Committee

Andreas Kugi (Chair) Austria
Felix Breitenecker (Co-Chair) Austria
Inge Troch (Editor) Austria
Frank Allgöwer Germany
Konstantinos Ampountolas UK
Arnold Baca Austria
Francesco Basile Italy
Carlo Bianca France
Philippe Bogaerts Belgium
Peter Buchholz Germany
Felix L. Chernousko Russia
Erik Dahlquist Sweden
Denis Dochain Belgium
Roman Dyczij-Edlinger Germany
Horst Ecker Austria
Sebastian Engell Germany
Tulga Ersal USA
Gianni Ferretti Italy
Walter Fetter Lages Brasil
Alexia Fürnkranz-Prskawetz Austria
Peter Fritzson Sweden
Jun Fu China
Michael Günther Germany
Knut Graichen Germany
Robert Grino Spain
Biao Huang Canada
Thomas Jones South Africa
Kaj Juslin Finland
Fotis Kopsaftopoulos USA
Bernt Lie Norway
Boris Lohmann Germany
Jan Lunze Germany
Bernhard Manhartsgruber Austria
Wolfgang Mathis Germany
Thomas Meurer Germany
Tony B. Morton Australia
Gasper Music Slovenia
Peter C. Müller Germany
Christian Ott Germany
Carla Pinto Portugal
Julia Puaschunder USA
Joachim Rudolph Germany
Oliver Sawodny Germany
Georg Schitter Austria
Kurt Schlacher Austria
Tatjana Stykel Germany
Mahdi Tavakoli Canada
Alfonso Urquia Spain
Jan Van Impe Belgium
Jun Zhao China

National Organizing Committee

Andreas Körner (Chair)
Wolfgang Kemmetmüller (Co-Chair)
Martin Bicher, Franziska Gorgas, Ruth Leskovar, Johannes Tanzler, Stefanie Winkler

MATHMOD 2018 Invited Lectures

- The Day After Optimal: Mathematical Modelling for Modern Logistics
  Stefan Nickel, Karlsruhe Institute of Technology, Germany
- Big Network Data
  Sofia Olhede, University College London, United Kingdom
- Needle-Tissue Interaction Modeling in Needle-Based Medical Interventions
  Mahdi Tavakoli, University of Alberta, Canada
- Framing, Identification and Simulation of 'Messy' Hydrological Systems
  Günther Blöschl, TU Wien, Austria
- Modelling and Simulation of Viennese Particle Movement (Social Lecture)
  Martin Bicher, Stefanie Winkler, Andreas Körner, TU Wien, Austria

MATHMOD 2018 Minisymposia

- Optimization and Modeling in Biomathematics and Engineering
  Organizers: K. Chudej, Univ. Bayreuth and S.J. Kimmerle, Univ. der Bundeswehr München
- Model Based Design of Experiments: Where to go?
  Organizers: R. Schenkendorf, TU Braunschweig and R.J. Flassig, Max Planck Inst. for Dynamics of Complex Technical Systems, Magdeburg
- Dynamic Models in Management and Economics
  Organizers: S. Leitner and F. Wall, Alpen-Adria Universität Klagenfurt
- Model Reduction
  Organizers: B. Lohmann, TU München, B. Haasdonk, University of Stuttgart, and C. Himpe, Max Planck Institute for Dynamics of Complex Technical Systems
- Mathematical Modelling and Control of Bio-Chemical Processes
  Organizers: J. Van Impe, Katholieke Universiteit Leuven and P. Bogaerts, Universite Libre de Bruxelles
- Mathematical Modelling for Locomotion Mechanics and Mobile Robotics
  Organizers: F.L. Chernousko and N.N. Bolotnik, Institute for Problems in Mechanics of the Russian Academy of Sciences
- Control-oriented Modelling, Control Design and Optimization of Dynamic Systems with Distributed Parameters
  Organizers: H. Aschemann, University of Rostock, and G. Kostin, Institute for Problems in Mechanics of the Russian Academy of Sciences
- Modelling, Simulation and Control for Hydropower Systems
  Organizer: B. Lie, University College of Southeast Norway
- Modelling and Simulation in Solar Thermal Power Plants
  Organizers: E. Juuso, Univ. of Oulu, Finland, and L. J. Yebra, CIEMAT, Plataforma Solar de Almería, Spain
- Object-Oriented Modelling
  Organizers: G. Ferretti and F. Casella, Politecnico di Milano, Italy
- Mathematical Modeling of Strongly Nonlinear Mechanical Dissipative Systems
  Organizers: A.A. Kireenkov, Moscow Institute of Physics and Technology (State University), Russia, and I.I. Kosenko, Moscow Aviation Institute, Russia
- Modelling in Hereditary Continuum Mechanics
  Organizers: A.S. Shamaev, Institute for Problems in Mechanics RAS, Moscow State University, Russia
- Modelling for Control and Optimization of Manufacturing Systems
  Organizers: G. Music, University of Ljubljana, Slovenia
- Modeling and Control of Smart Material Systems
  Organizers: G. Rizzello and J. Rudolph, Saarland University, Germany

MATHMOD 2018 Thematic Sessions

- Model-Based Control
- Biology and Physiology
- Modelling in Education
- Mechanical Systems
- Estimation and Learning
- Industrial Production Systems
- Electrical Systems
- Methods and Tools for Modelling
- Discrete Event Systems and Petri Nets

Contents

Modelling, simulation and parameters estimation for gas networks

T. Rodríguez-Blanco*, D. Sarabia,**
C. de Prada*

** Dpt of Systems Engineering and Automatic Control, University of Valladolid , Doctor Mergelina s/n, 47011, Valladolid, Spain (tania.rodriguez@autom.uva.es, prada@autom.uva.es).*
*** Dpt of Electromechanical Engineering, University of Burgos, Avda. Cantabria s/n, 09006, Burgos, Spain (dsarabia@ubu.es)*

Keywords: Process simulators, estimation parameters, optimization problems, dynamic modelling, natural gas networks.

1. INTRODUCTION

This paper presents a library for the simulation of natural gas networks which contains dynamic components developed in the simulation environment EcosimPro. It comprises the main components of a natural gas network that have been modelled based on mass, energy and momentum balances and additional equations for describing the dynamic behaviour of real gases. The complete model that describes the natural gas transport has been adjusted to real data taken from a 127-km long gas pipeline located in Mexico that is managed by the company Fermaca with a 16-inch pipe nominal diameter, one input, 4 outputs and an altitude difference of 397 m. The results obtained show that the developed models can be used to accurately simulate real natural gas networks. A picture of the appearance of this library is shown in Fig.1:

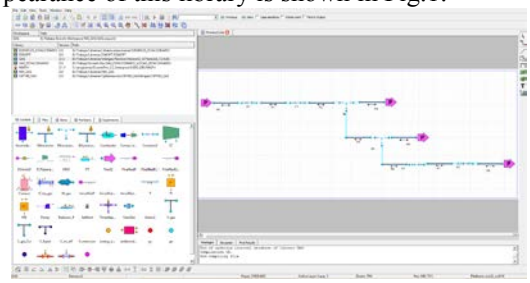

Fig.1. Dynamic library of natural gas networks in EcosimPro.

2. THE FERMACA NETWORK

Fermaca network is a 127-km long gas pipeline with a 16-inch pipe nominal diameter and a total altitude difference of 397 m. The receiver station is located in Palmillas and there are four supply points located in Atlacomulco, Pastejé, San Cayetano and Toluca. The topology is represented by Fig.2 where the existing pressure (PT), temperature (TT), flow (FT) and composition (AT) sensors are represented.

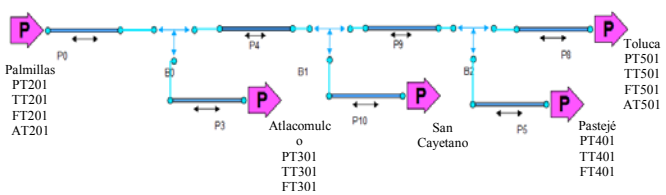

Fig. 2. Fermaca network topology.

The dimensions of the gas pipelines are defined in Table 1.

Table 1. Dimensions of the gas pipelines

Pipe	Length (km)	Altitude difference (m)	Inlet pressure (bar)	Outlet pressure (bar)
P0	64	308	51.55	-
P3	1	0	-	47.90
P4	12	4.5	-	-
P5	1	0	-	47.06
P8	39	80	-	45.53
P9	12	4.5	-	-
P10	1	0	-	Estimated

The complete model comprises 3891 variables with 91 boundary conditions that evolve the inlet gas composition, one inlet and four outlet pressures, the inlet gas temperature and the environment temperature for each pipeline. The total number of equations is 3891 (2523 explicit and 1368 differential equations).

3. PARAMETERS ESTIMATION

Measurements from the inlet and outlet volumetric flow, temperature, concentration and pressure are available. These data have been adjusted by changing the pipeline efficiencies and the environment temperature. These measurements show that, for the chosen period of time, all the variables are in steady-state except the outlet temperatures in P3 and P5. This transient behaviour is because the outlet pipelines are not buried so the effect of the environment temperature on the gas temperature is bigger. The available measurements are graphically represented in Fig. 3, 4 and 5 that show the pressure profile, the temperature profile and the measured volumetric flow respectively.

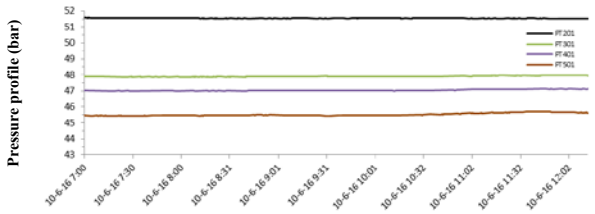

Fig. 3. Pressure profile.

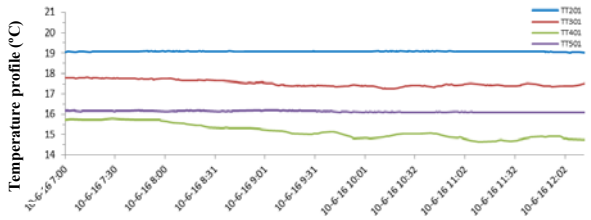

Fig. 4. Temperature profile.

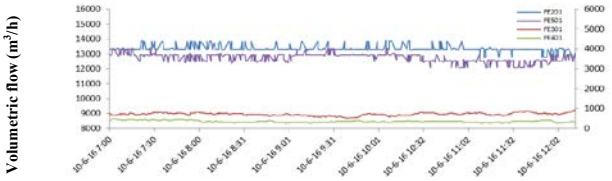

Fig. 5. Measured volumetric flow.

The data reconciliation problem to be solved is described by (1) where it can be observed that the cost function J contains a stationary part to evaluate the differences between the real (y_{real}) and the modelled variables (y_{mod}) at the steady-state, and a dynamic component to evaluate the differences between the reality (y_{d_real}) and the model (y_{d_mod}) for the transient variables. For the dynamic reconciliation an environment temperature profile has been adjusted for P3 and P5 assuming that this profile follows a linear behaviour given by (2) where t is the time expressed in hours:

$$\begin{aligned} &\min_{u} \quad J = (y_{real} - y_{mod})^2 + (y_{d\_real}(t) - y_{d\_mod}(t))^2 \\ &u = [e_{P0} \quad e_{P3} \quad e_{P4} \quad e_{P5} \quad e_{P8} \quad e_{P9} \quad e_{P10} \\ &P_{out\,P10} \quad a_{P3} \quad b_{P3} \quad a_{P5} \quad b_{P5} \quad T_{envP8}] \\ &y_{real} = [Q_{inP0} \quad Q_{inP3} \quad Q_{inP5} \quad Q_{inP3} \quad T_{outP8}] \\ &y_{d\_real} = [T_{outP3} \quad T_{outP5}] \end{aligned} \tag{1}$$

$$T_{env} = a \cdot t + b \tag{2}$$

The NLP optimization problems have been solved using a sequential approach with a sequential quadratic programming (SQP) algorithm implemented in SNOPT library (Gill et al., 2008) and executed in EcosimPro software (EA Int, 2013).

The results obtained are shown in Table 3 which presents the value of the adjusted parameters and Table 4 where the stationary error is presented:

Table 3. Data reconciliation results

Adjusted parameter (u)	Description	Value
e_{P0} (#)	Efficiency of pipeline 0	1.106
e_{P3} (#)	Efficiency of pipeline 3	0.122
e_{P4} (#)	Efficiency of pipeline 4	1.131
e_{P5} (#)	Efficiency of pipeline 5	0.101
e_{P8} (#)	Efficiency of pipeline 8	1.069
e_{P9} (#)	Efficiency of pipeline 9	1.11
e_{P10} (#)	Efficiency of pipeline 10	0.108
P_{outP10} (bar)	Outlet pressure pipeline 10	47.418
a_{P3} (ºC/h)	Slope of T_{envP3}	- 0.749
b_{P3} (ºC)	Intercept of T_{envP3}	23.577
a_{P5} (ºC/h)	Slope of T_{envP5}	- 0.658
b_{P5} (ºC)	Intercept of T_{envP5}	11.62
T_{envP8} (ºC)	Environment temperature P8	16.00

Table 4. Steady-state data reconciliation results

Variable	y_{real}	y_{mod}	Quadratic error
Q_{inP0} (m^3/s)	3.713	3.715	$4 \cdot 10^{-6}$
Q_{outP3} (m^3/s)	0.200	0.199	$1 \cdot 10^{-6}$
Q_{outP5} (m^3/s)	0.097	0.097	0
Q_{outP8} (m^3/s)	3.510	3.494	$2.5 \cdot 10^{-4}$
T_{outP8} (ºC)	16.17	16.178	$6.4 \cdot 10^{-5}$

The obtained results from the dynamic reconciliation are graphically shown in Fig. 6 where the measurements (T_{outP3}, T_{outP5}) and the modelled (T_{modP3}, T_{modP5}) data are compared.

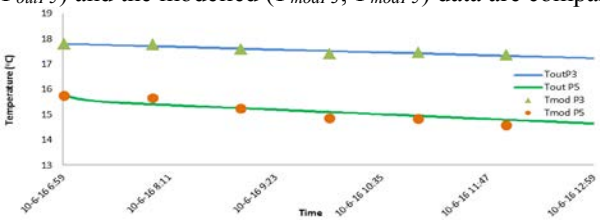

Fig. 6. Dynamic reconciliation result (y_{d_real} and y_{d_mod}), T_{outP3} and T_{outP5}.

6. CONCLUSIONS

In this paper, a library for the simulation of natural gas networks has been presented. In addition, it has been demonstrate that this library can be used to simulate real networks after a previous step of data reconciliation.

Measurements taken from a real network has been used to adjust the model parameters such as: pipe efficiency or environment temperature. To make this, a data reconciliation problem is solved whose cost function combines a stationary part with a dynamic one. The results show that the model is adjusted perfectly to real data which allows using it for real simulations.

ACKNOWLEDGMENTS

The authors wish to express their gratitude to project DPI2015-70975-P of the Spanish MINECO/FEDER for the financial support for this study under FPI grant BES-2013-062737. We would also like to thank Aplein Ingenieros and Intergeo Tecnología for their fruitful cooperation.

REFERENCES

Baliga, B. R., & Patankar, S. V. (1983). *A control volume finite-element method for two-dimensional fluid flow and heat transfer*. Numerical Heat Transfer, 6(3), 245-261.

EA Int, (2013). EcosimPro 5.2. User Manual (http://www.ecosimpro.com).

Gill, P. E., Murray, W., Saunders, M. A. (2008). User's Guide for SNOPT Version 7: Software for Large-Scale Nonlinear Programming.

Rodríguez, T., Sarabia, D. de Prada, C., Valbuena, M., Morales, J.L. (2013). *Modelling and monitoring of natural gas networks*. European Gas Technology Conference (EGATEC 2013).

Schroeder, D. W. (2001). *A tutorial on pipe flow equations*.

Woldeyohannes, A. D., & Majid, M. A. A. (2011). *Simulation model for natural gas transmission pipeline network system*. Simulation Modelling Practice and Theory, 19(1), 196-212.

Analysis of a non-integer order model for the coinfection of HIV and HSV-2

Carla M.A. Pinto * **Ana R.M. Carvalho** **

* *School of Engineering, Polytechnic of Porto, Rua Dr António Bernardino de Almeida, 431, 4200-072 Porto, Portugal (e-mail: cap@isep.ipp.pt).*
** *Faculty of Sciences, University of Porto, Rua do Campo Alegre s/n, 4440-452 Porto, Portugal (email: up200802541@fc.up.pt).*

Abstract: We propose a non-integer order model for the dynamics of the coinfection of HIV and HSV-2. We calculate the reproduction number of the model and study the local stability of the disease-free equilibrium. Simulations of the model for the variation of epidemiologically relevant parameters and the order of the non-integer order derivative, α, reveal interesting dynamics. These results are discussed from an epidemiologically point of view.

Keywords: non-integer order mathematical model, HIV, HSV-2, coinfection

1. INTRODUCTION

HSV-2 and HIV fuel each other. HSV-2 infection increases the risk of acquiring a new HIV infection by approximately three times. In addition, people coinfected with HIV and HSV-2 are more likely to spread HIV to others. HSV-2 is one of the most common infections in people infected with HIV, occurring in 60-90% of the cases. HSV-2 in co-infected persons presents greater severity and more frequent recurrences. Moreover, in the more advanced stage of HIV, HSV-2 can lead to more serious but rare complications such as meningoencephalitis, esophagitis, hepatitis, pneumonitis, retinal necrosis, or disseminated infection, cf. WHO (2017). Several mathematical models have been derived with the purpose of understanding the dynamics of HIV and HSV-2 coinfection. In 2015, cf. Basak et al. (2015) develop a model for the co-infection of HIV and HSV-2. Numerical simulations suggest that the HSV-2 infected individuals are at higher risk of acquiring HIV infection when compared to HSV-2 non infected individuals. It suggests that reducing the effective contact rate of HSV-2 may reduce the disease burden of the co-infection. On the other hand, controlling the transfer rate from HIV class to AIDS class and the control of the transfer rate of the HSV-2 exposed class to the class infected with HSV-2 are also feasible.

Some Concepts of Fractional Calculus

Fractional calculus (FC) is a generalization to an arbitrary (non-integer) order of ordinary differentiation and integration. Leibniz and Lagrange were the first mathematicians to discover and unravel the power of FC. Fractional models have been used in the literature to understand the behaviour of epidemiological models, where the integer-order models fail to give a complete explanation, cf. Arafa et al. (2013); Pinto and Carvalho (2017).

Driven by the aforementioned research, we analyse the dynamics of the HIV and HSV-2 coinfection in a non-integer order mathematical model. In Section 2, we introduce the model. Numerical simulations of the model for distinct values of the order of the fractional derivative and relevant parameters, are presented and discussed in Section 3. Finally, in Section 4, we conclude our work.

2. THE MODEL

In this section, we describe the proposed non-integer order model. The population of the model is divided in ten classes. Susceptible individuals, S, are recruited at rate Π^α. They are infected with HSV-2 at rate $\lambda_1 = \frac{\beta_1^\alpha (I+\theta(Q+Q_H)+\eta I_H)}{N}$, where β_1^α is the transmission rate of HSV-2, and θ and η are modification parameters. Parameter θ, $(0 < \theta < 1)$ models the fact that infectious individuals in the quiescent stage are less infectious. On the contrary, parameter $\eta > 1$ accounts for the increased infectiousness of the coinfected individuals (I_H). Similarly, individuals S are infected with HIV at rate $\lambda_2 = \frac{\beta_2^\alpha (H+E_H+\eta I_H+\theta Q_H)}{N}$, where β_2^α is the HIV transmission rate. All individuals die by natural causes at rate μ^α. Individuals in the latent stage of HSV-2, E, are infected with HIV at rate λ_2 and progress in HSV-2 infection, for the acute phase, at rate σ_1^α. Individuals in the acute phase of HSV-2, I, are infected with HIV at rate λ_2 and move to the quiescent state, at rate q^α. Individuals in the quiescent stage of the HSV-2, Q, return to the acute phase of infection, at rate r^α and are infected with HIV at rate λ_2. Individuals infected with HSV-2, in the acute or quiescent stage, die at rate τ_1^α. Individuals infected with HIV, H, are infected with HSV-2 at rate λ_1 and develop AIDS at rate ρ_1^α. The AIDS induced mortality rate is τ_2^α. Individuals in the latent stage of HSV-2 and infected with HIV, E_H, progress to the acute phase of HSV infection, at rate σ_2^α, and develop AIDS at rate σ_3^α.

Individuals coinfected with HSV-2 and HIV, I_H, move to the quiescent state of the HSV-2 infection, at rate q_H^α and progress in HIV infection at rate σ_4^α. The individuals in the quiescent stage of HSV-2 and infected with HIV, Q_H, return to the acute phase of HSV-2 infection, at rate r_H^α and develop AIDS, at rate σ_5^α. The non-linear system of fractional order ordinary differential equations describing the dynamics of the model is:

$$\begin{aligned}
\frac{d^\alpha S}{dt^\alpha} &= \Pi^\alpha - \lambda_1 S - \lambda_2 S - \mu^\alpha S \\
\frac{d^\alpha E}{dt^\alpha} &= \lambda_1 S - (\lambda_2 + \sigma_1^\alpha + \mu^\alpha) E \\
\frac{d^\alpha I}{dt^\alpha} &= \sigma_1^\alpha E + r^\alpha Q - (\lambda_2 + q^\alpha + \mu^\alpha + \tau_1^\alpha) I \\
\frac{d^\alpha Q}{dt^\alpha} &= q^\alpha I - (\lambda_2 + r^\alpha + \mu^\alpha + \tau_1^\alpha) Q \\
\frac{d^\alpha H}{dt^\alpha} &= \lambda_2 S - (\lambda_1 + \rho_1^\alpha + \mu^\alpha) H \\
\frac{d^\alpha A}{dt^\alpha} &= \rho_1^\alpha H - (\mu^\alpha + \tau_2^\alpha) A \\
\frac{d^\alpha E_H}{dt^\alpha} &= \lambda_1 H + \lambda_2 E - (\sigma_2^\alpha + \sigma_3^\alpha + \mu^\alpha) E_H \\
\frac{d^\alpha I_H}{dt^\alpha} &= \sigma_2^\alpha E_H + \lambda_2 I + r_H^\alpha Q_H - (\sigma_4^\alpha + q_H^\alpha + \mu^\alpha + \tau_1^\alpha) I_H \\
\frac{d^\alpha Q_H}{dt^\alpha} &= q_H^\alpha I_H + \lambda_2 Q - (r_H^\alpha + \sigma_5^\alpha + \mu^\alpha + \tau_1^\alpha) Q_H \\
\frac{d^\alpha A_H}{dt^\alpha} &= \sigma_3^\alpha E_H + \sigma_4^\alpha I_H + \sigma_5^\alpha Q_H - (\mu^\alpha + \tau_2^\alpha) A_H
\end{aligned} \tag{1}$$

The reproduction numbers of the HSV-2 and HIV sub-models are given by:

$$R_1 = \rho(F_1 V_1^{-1}) = \frac{\beta_1^\alpha \sigma_1^\alpha (\theta q^\alpha + \mu^\alpha + r^\alpha + \tau_1^\alpha)}{(\sigma_1^\alpha + \mu^\alpha)(\mu^\alpha + \tau_1^\alpha)(q^\alpha + r^\alpha + \mu^\alpha + \tau_1^\alpha)} \text{ and}$$

$$R_2 = \rho(F_2 V_2^{-1}) = \frac{\beta_2^\alpha}{\rho_1^\alpha + \mu^\alpha} \tag{2}$$

respectively. Thus, R_0, the reproduction number of the full model is:

$$R_0 = \rho(FV^{-1}) = \max\{R_1, R_2\} \tag{3}$$

Lemma 1. The disease-free equilibrium of the system (1) is unstable if $R_0 > 1$.

3. NUMERICAL SIMULATIONS

We simulate the model (1) for different values of the order of the fractional derivative, α, and for relevant parameters. Parameters used in the simulations are: $\beta_1 = 0.06$, $\theta = 0.4$, $\eta = 1.1$, $\beta_2 = 0.055$, $\Pi = \frac{60000}{1000\times 365}$, $\mu = 0.0027$, $\sigma_1 = 0.04$, $r = 0.4$, $q = 0.2$, $\tau_1 = 0.04$, $\rho_1 = 0.4$, $\tau_2 = 0.09$, $\sigma_2 = 0.4$, $\sigma_3 = 0.6$, $r_H = 0.03$, $q_H = 0.03$, $\sigma_4 = 0.4$, $\sigma_5 = 0.3$, and the inicial conditions are: $S(0) = 5000$, $E(0) = 1000$, $I(0) = 500$, $Q(0) = 100$, $H(0) = 1000$, $A(0) = 200$, $E_H(0) = 1000$, $I_H(0) = 500$, $Q_H(0) = 250$ and $A_H(0) = 100$ Basak et al. (2015). We study how the basic reproduction number R_0 varies with r, the backward transmission between the HSV-2 infected individuals, I, and the individuals in the quiescent stage of HSV-2, Q, and with q, the forward transmission between the HSV-2 infected individuals, I, and the individuals in the quiescent stage of HSV-2, Q. Figures 1-2 show that increasing values of r and decreasing values of q boost higher values of R_0. This suggests that controlling transfer rates between I individuals and Q individuals reduces the burden of the disease. This behaviour is repeated for all values of α.

4. CONCLUSION

We propose a non-integer order model for HIV and HSV-2 co-infection. Numerical results of the model suggest that the backward and forward transmission rates between the HSV-2 infected individuals, I, and the individuals in the quiescent stage of HSV-2, Q, can explain the effect of HSV-2 infection on the values of HIV prevalence. Thus, reducing these rates would possibly control the infection. The order of the fractional derivative, α, may be used to distinguish patients when doing fitting data from real patients. Specificities of patients, namely, age, immune system profile, etc, can be well addressed by α, without changing the structure of the model.

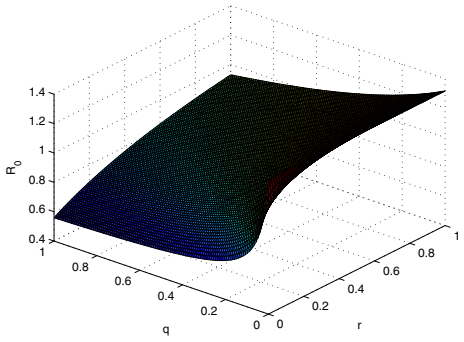

Fig. 1. Effect of r and q, on R_0, for $\alpha = 1$. Parameter values and initial conditions in the text.

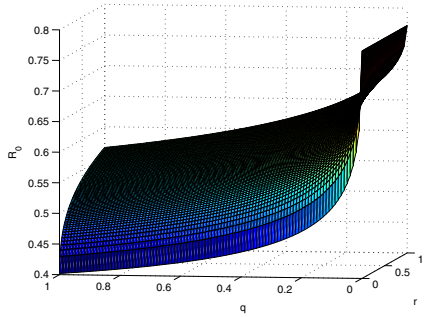

Fig. 2. Effect of r and q, on R_0, for $\alpha = 0.5$. Parameter values and initial conditions in the text.

ACKNOWLEDGEMENTS

Authors were partially funded by the European Regional Development Fund through the program COMPETE and by the Portuguese Government through the FCT under the project PEst-C/MAT/UI0144/2013. AC was partially supported by a FCT grant with reference SFRH/BD/96816/2013.

REFERENCES

Arafa, A., Rida, R., and Khalil, M. (2013). The effect of anti-viral drug treatment of human immunodeficiency virus type 1 (hiv-1) described by a fractional order model. *Appl. Math. Model.*, 37, 2189–2196.

Basak, U., Nayeem, J., and Podder, C. (2015). Mathematical study of hiv and hsv-2 co-infection. *American Journal of Mathematics and Statistics*, 5(1), 15–23.

Pinto, C. and Carvalho, A. (2017). The role of synaptic transmission in a hiv model with memory. *Applied Mathematics and Computation*, 292, 76–95.

WHO (2017). `http://www.who.int/`.

Modelling a Smart-Grid for a Solar Powered Electric Vehicle ⋆

F.J. Gómez * **Luis J. Yebra** ** **Antonio Giménez** *

* *CIESOL, Joint Centre of the University of Almería-CIEMAT. 04120, Almería, Spain (e-mail:fgn891@inlumine.ual.es, agimfer@ual.es).*
** *CIEMAT Research Centre. Plataforma Solar de Almería, 04200 Tabernas, Almería, Spain (e-mail: luis.yebra@psa.es).*

Keywords: Object oriented modelling, electric vehicles, dynamic modelling, automatic control.

1. INTRODUCTION

Mathematical approximations for dynamic modelling of a Smart-Grid used in a electric solar powered small vehicle are developed for model based control purposes. The objective of this paper is to present the first principles and mathematical approximations behind the systems from which the Smart-Grid is composed of, that are mainly: photovoltaic (PV) panel, other renewable sources, battery, DC/DC converter, accessories, motor and regenerative brake. For this objective, the Modelica modelling language offers a complete set of capabilities well known so far and spread in the literature, and the main ideas behind it and, its evolution and description are detailed in (Cellier (1991); Åström et al. (1998); Fritzson P. (2004)). The Modelica Standard Library (MSL) provides an important quantity of proven models to be reused, some of which have been applied in the models presented in this work. For the simulations, the Modelica tool Dymola© (Elmqvist (2012)) has been used. This work is inspired in Dizqah et al. (2012).

Fig. 1 shows the experimental electrical vehicle eCARM used for model validation, developed in the University of Almería for research in Automatic Control.

Fig. 1. eCARM: electrical vehicle used as test rig.

⋆ The authors thanks to the Spanish Ministry of Economy, Industry and Competitiveness and ERDF funds for partially funding this work.

2. DESCRIPTION OF THE SMART-GRID

This section presents the Smart-Grid composition for the solar powered small vehicle. The main components are shown in Fig. 2, where the electric power flows are represented by arrows.

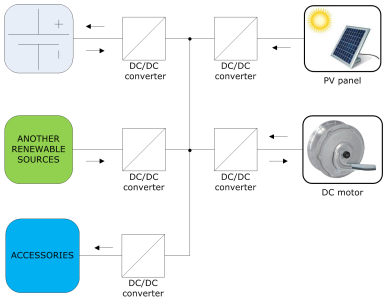

Fig. 2. Schematic diagram of the Smart-Grid modelled.

The bus *receives* power from battery, PV module and DC motor (when working as regenerative brake); and *sends* power to DC motor (when working as motor) and other unidirectional accesories. Please, note that the exchange of power between the battery and the bus is bidirectional. The interface to all devices from the bus is implemented by a DC/DC converter working in unidirectional or bidirectional configurations, so special care has been taken in the selection of this component, and its model features are discussed in the context of the whole Smart-Grid model. All these model devices have been modelled and parameters from commercial solutions have been used in the presented simulations.

3. DYNAMIC MODELLING AND SIMULATION OF THE SMART-GRID

This section presents the main model developed that is composed of the different submodels forming the Smart-Grid. All the models are implemented in the Modelica modelling language. Some of them are formulated in steady state conditions by the use of algebraic equations, p.e.: PV model. Others are formulated by differential and algebraic equations (DAE): the battery, the motor, the load and the DC-DC converter. The models of the components are not presented due to space availability in this document.

Fig. 3 shows the schematic diagram representing the modelled Smart-Grid that is formed by the DC motor, DC/DC converter and a battery. The whole three components works in a bidirectional power flow capability: the DC motor (acting as a load or as a generator), the DC/DC converter (controlling the power flow in one or another direction), and the battery (discharging or charging). The motor electrical interface is connected to a battery through a bidirectional DC/DC converter. In the mechanical interface the motor is connected to a inertia representing the equivalent external load, that itself is connected to and quadratic friction representing the equivalent friction of the vehicle to the environment.

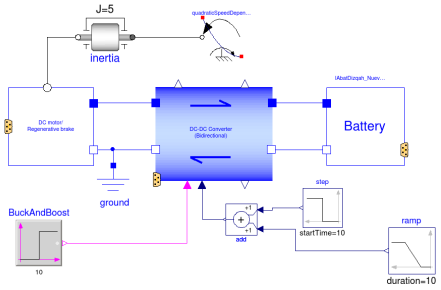

Fig. 3. Schematic diagram of DC motor working as a motor and a regenerative brake.

Simulation results of two experiments in this configuration are presented in Figs. 4 (1st experiment) and 5 (2nd experiment), in which power flow directions inversions are present. In both experiments, during the first 10s the battery is discharging against the DC motor through the DC/DC converter. In this time interval, due to the DC motor electrical power flow a mechanical torque is applied on the inertial load that is accelerated to a maximum angular velocity. After 10s the DC converter power flow is switched back to battery, and the motor begins to work as a generator releasing power from the mechanical subsystem to the electrical one, that is, acting as a generator. This is the basic principle of the regenerative brake, although a more complex arrangement is usually required to implement a complete fully functional regenerative brake. From 10s onwards, while the motor behaves as a regenerative brake, the inertial load is decelerating. Power flow in the DC/DC converter is inverted and now directed from brake (DC motor) to battery. The power flow can be deduced from the sign of the electrical intensity in variables DC_Converter_CurrentToBattery (current from DC converter to battery) and DC_Converter_CurrentToDCMotor (current from DC converter to DC motor) represented both in in Fig. 4. This figure additionally represents the angular velocity of the motor (omega). Fig. 5 represents additional electrical variables of the Smart-Grid in a second experiment: voltages at both sides of DC/DC converter (battery and DC motor), battery charge (BatteryCharge) and duty cycle (DutyCycle) of the DC/DC converter.

4. CONCLUSION

A work in progress of a dynamic model for control design purposes of a Smart-Grid is presented. The model is composed of different components submodels, to be used in the hybrid solar powered experimental vehicle eCARM from

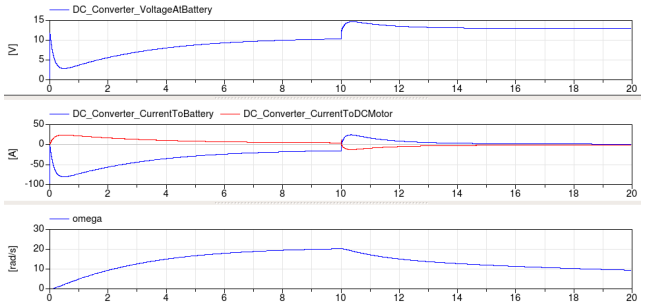

Fig. 4. Simulation of DC motor working in two modes: motor and regenerative brake. 1st experiment.

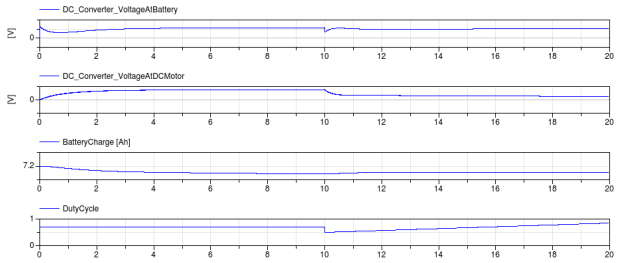

Fig. 5. Simulation of DC motor working in two modes: motor and regenerative brake. 2nd experiment.

University of Almería. The objective of the model is to be used in soft real time simulations and control applications in which the model will be used in complex controllers to be executed in real time. The main model representing the Smart-Grid has been presented and their modelling hypothesis outlined. All the information presented in this work comes from the bibliography sources referenced.

Future works are the calibration and validation of the models with experimental data from eCARM experimental electric vehicle.

ACKNOWLEDGEMENTS

This work has been funded by the National R+D+i Plan Project DPI2014-56364-C2-1/2-R of the Spanish Ministry of Economy, Industry and Competitiveness and ERDF funds.

REFERENCES

Cellier, F.E. (1991). *Continuous System Modeling.* Springer-Verlag New York, Inc., Secaucus, NJ, USA.

Dizqah, A.M., Busawon, K., and Fritzson, P. (2012). Acausal modeling and simulation of the standalone solar power systems as hybrid DAEs. In *The 53rd International Conference of the Scandinavian Simulation Society (SIMS)*, 1–7.

Elmqvist, H. (2012). Dymola User Manual.

Fritzson P. (2004). *Principles of Object-Oriented Modeling and Simulation with Modelica 2.1.* Wiley-IEEE Press.

Åström, K.J., Elmqvist, H., and Mattsson, S.E. (1998). Evolution of Continuous-Time Modeling and Simulation. In R. Zobel and D. Moeller (eds.), *Proceedings of the 12th European Simulation Multiconference, ESM'98*, 9–18. Society for Computer Simulation International, Manchester, UK.

Modeling of Heat Transfer in Controlled Processes for Cylindrical Bodies

Dmitri Knyazkov * **Harald Aschemann** ** **Julia Kersten** **
Georgy Kostin * **Andreas Rauh** ** **Alexander Gavrikov** *

* *A.Ishlinsky Institute for Problems in Mechanics of the Russian Academy of Sciences, Moscow, Russia (e-mail: {knyaz,kostin}@ipmnet.ru)*
** *Chair of Mechatronics, University of Rostock, Rostock, Germany (e-mail: {Harald.Aschemann,Julia.Kersten, Andreas.Rauh}@uni-rostock.de)*

Keywords: Control-oriented modeling, control design and optimization of dynamic systems with distributed parameters; parameter identification, natural convection

1. INTRODUCTION

Reliable modeling is needed when different control strategies are applied to distributed parameter systems, see Butkovsky (1969); Chernousko et al. (1996). Problems of heat transfer control for different simple bodies like cylinders, rods, and bars were recently considered in a large number of papers, e.g., in Kersten et al. (2014); Rauh et al. (2015a,b). In Kostin et al. (2017), an optimal control of the heating of a metal bar was presented. The current paper considers modeling the active heating of a cylindrical body. The cylinder may be aligned either vertically or horizontally. Two Peltier elements provide heat fluxes on both ends of this body. A corresponding experimental setup is available at the Chair of Mechatronics, University of Rostock, Germany. Experimental results obtained from this test rig are used for the identification of the system parameters. Simulations with the identified parameters match the measurements with high accuracy.

2. DESCRIPTION OF THE MODEL

Let us consider the model of a cylinder insulated thermally on both end faces. The cylinder is given by the domain $\Omega = [0, l] \times [0, r_0] \times [0, 2\pi]$, where l is its length and r_0 is its radius. It has free contact with the ambient air over its lateral surface. The cylinder is heated up or cooled down from both end faces by two Peltier elements, which produce two independent heat fluxes F_1 and F_2. The corresponding system of equations is given by

$$\begin{cases} \rho c_\mathrm{p} \dfrac{\partial \vartheta}{\partial \tau} = \lambda \left(\dfrac{\partial^2 \vartheta}{\partial z^2} + \dfrac{1}{r} \dfrac{\partial}{\partial r} \left(r \dfrac{\partial \vartheta}{\partial r} \right) + \dfrac{1}{r^2} \dfrac{\partial^2 \vartheta}{\partial \varphi^2} \right) \quad \text{in } \Omega, \\ \left. \dfrac{\partial \vartheta}{\partial n} \right|_{r=r_0} = \alpha(z, \varphi)(\vartheta(z, r_0, \varphi, \tau) - \vartheta_\mathrm{a}(\tau)), \\ \left. \dfrac{\partial \vartheta}{\partial n} \right|_{z=l} = F_1(u_1(\tau)), \\ \left. \dfrac{\partial \vartheta}{\partial n} \right|_{z=0} = F_2(u_2(\tau)), \\ \vartheta|_{\tau=0} = \vartheta_\mathrm{b}^0. \end{cases} \tag{1}$$

The voltages applied to the elements, $u_1(\tau)$ and $u_2(\tau)$, are adjusted during the active heating, where the functions $u_1(\tau)$, $u_2(\tau)$ are defined for the time interval $\tau \in [0, T]$. The temperature $\vartheta(z, r, \phi, \tau)$ of the cylinder is equal to ϑ_b^0 at the time instant $\tau = 0$. Temperature measurements are available at several distinct locations on the cylinder's circumferential surface. The model has been derived on the basis of the partial differential equation for heat transfer.

When specifying boundary conditions on the circumferential surface of the cylinder, we address the heat exchange with the ambiant air and model the Peltier elements. The latter were studied in Rauh et al. (2015a). The results from Rauh et al. (2015a) are employed to construct the Peltier element operation model, i.e., to define flux functions $F_1(\cdot)$, $F_2(\cdot)$. A series of experiments was performed for this purpose.

The process of heat transfer for a cylindrical body was investigated in Knyazkov et al. (2017). The corresponding analytical results are used in the current paper for estimating the heat exchange with the ambient air. The heat transfer coefficient in the model is estimated both theoretically and experimentally, where the analytical and experimental estimates are in a good agreement (see Fig. 1).

3. RESULTS AND OUTLOOK

The active heating for the aluminum cylinder is modeled by the finite element method and then compared to measurements. Experimental data are only available for the vertically aligned aluminum cylinder. All other results for the different alignments and materials presented in the current paper are outcomes of pure simulations.

An example of a simulation performed for a glass cylinder is described below. The influence of the variability of the heat transfer coefficient along the body surface is investigated. The results of modeling of the controlled heat transfer for the horizontally aligned glass cylinder are shown in Fig. 2. Solid lines show the temperatures at the points $L_i = (\frac{l}{2}, r_0, \frac{\pi}{4}(i-1))$, $i = 1, \ldots, 5$, for the constant heat transfer coefficient $\overline{\alpha}$, while the dashed lines stand for

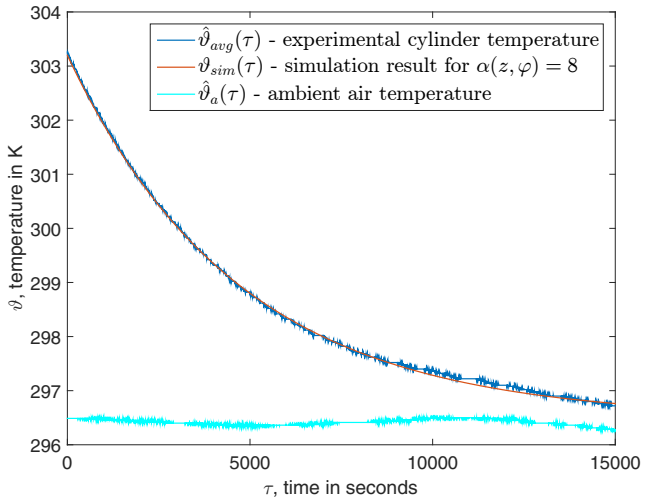

Fig. 1. Simulated average temperature $\vartheta_{\mathrm{sim}}(\tau_k)$ fits the experimental averaged temperature $\hat{\vartheta}_{\mathrm{avg}}(\tau)$ for the constant heat transfer coefficient $\alpha(z,\varphi) = 8$. Here, $\hat{\vartheta}_{\mathrm{avg}}(\tau)$ is the average of experimentally measured temperatures for the aluminum cylinder. The experimental ambient air temperature $\hat{\vartheta}_{\mathrm{a}}(\tau)$ is shown by the cyan curve

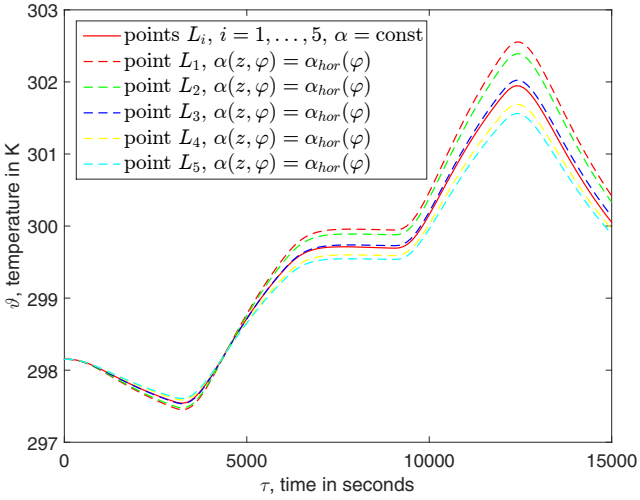

Fig. 2. Heating simulation for the horizontally aligned glass cylinder for two cases: $\alpha(z,\varphi) = \overline{\alpha}$ and $\alpha(z,\varphi) = \alpha_{\mathrm{hor}}(\varphi)$

the specified dependency $\alpha_{\mathrm{hor}}(\varphi)$ of the convective heat transfer coefficient on the azimuth angle. The difference in temperature is significant when the dependency of the convective heat transfer coefficient on the azimuth angle is taken into account as compared with the case when a constant averaged value of this coefficient is utilized.

The results show that the obtained temperature can differ by several K when the body is heated by 10–15 K. This demonstrates that the variability of the heat transfer coefficient along the surface of the body should be taken into account when considering a problem of heat transfer in materials that have a small conductivity.

One of the future goals on the topic is to consider the case of heating with Peltier elements that have passively or actively cooled units from the side that is not in direct contact with the cylinder. An experiment with a glass cylinder should be performed that can justify the influence of the heat transfer coefficient's variability on the temperature distribution inside the body. It will be very useful in this case to register not only the temperature in a fixed number of surface points, but also the distribution of the surface temperature during the heating process. This can be done by optical measurement techniques.

The designed model and the developed computational approach can be used when modeling the heat transfer for more sophisticated control laws. An example of optimal control for the described system can be found in Gavrikov and Kostin (2017). However that model did not take into account the position dependency of the heat transfer coefficient. The simplified analytical expressions for the heat transfer coefficient from Knyazkov et al. (2017) can be applied for an analytical Fourier analysis or for control design when the dependency of the coefficient on the position on the lateral surface of the cylinder is taken into account.

REFERENCES

Butkovsky, A.G. (1969). *Theory of Optimal Control of Distributed Parameter Systems.* Elsevier, New York, USA.

Chernousko, F.L., Ananievski, I.M., and Reshmin, S.A. (1996). *Control of Nonlinear Dynamical Systems: Methods and Applications.* Springer-Verlag, Berlin-Heidelberg.

Gavrikov, A. and Kostin, G. (2017). Boundary control of heat transfer processes in a cylindrical body. *Proceedings of the 22nd International Conference on Methods and Models in Automation and Robotics (MMAR), Miedzyzdroje, 2017*, 192–196.

Kersten, J., Rauh, A., and Aschemann, H. (2014). Finite element modeling for heat transfer processes using the method of integro-differential relations with applications in control engineering. *Proc. of the 19th International Conference on Methods and Models in Automation and Robotics (MMAR), Miedzyzdroje, 2014*, 606–611.

Knyazkov, D., Kostin, G., and Saurin, V. (2017). Influence of free convection on heat transfer in control problems for a cylindrical body. *Proceedings of the 22nd International Conference on Methods and Models in Automation and Robotics (MMAR), Miedzyzdroje, Poland, 2017*, 58–63.

Kostin, G., Rauh, A., Aschemann, H., and Saurin, V. (2017). Optimal multivariable flux control of heat transfer in a metal bar. *Proceedings of the 22nd International Conference on Methods and Models in Automation and Robotics (MMAR), Miedzyzdroje, 2017*, 186–191.

Rauh, A., Kersten, J., and Aschemann, H. (2015a). Experimental validation of LMI approaches for robust control design of a spatially three-dimensional heat transfer process. *Proceedings of the 20th International Conference on Methods and Models in Automation and Robotics (MMAR), Miedzyzdroje, 2015*, 11–16.

Rauh, A., Kersten, J., and Aschemann, H. (2015b). Robust control for a spatially three-dimensional heat transfer process. *Proc. of the 8th IFAC Symposium on Robust Control Design (ROCOND), Bratislava, Slovakia, 2015. IFAC-PapersOnLine*, 48(14), 101–106.

Dynamical Modelling and Parameters Identification of Real Power Plant Synchronous Generator and Excitation System

Abolfazl Khodadadi* Behrooz Zaker* Ramtin Khalili* Seyed Mehdi Hosseini* Shahab Karrari* Mehdi Karrari*

**Electrical Engineering Department, Amirkabir University of Technology, Tehran, Iran*
(*Emails: {a.khodadadi, zaker.behrooz, ramtin.khalili, sm-hosseini, shkarrari, karrari}@aut.ac.ir*)

Abstract: This paper presents a mathematical modelling and parameter identification for the excitation system with detailed model of comprising cards and synchronous generator. Then, the parameters of overall model are identified using an optimization algorithm. Data for identification process is obtained from online measurements of a 154MW gas power plant which is acquired from a data acquisition system. The validation process is carried out in Power Factory DIgSILENT software and the proper matching between simulation results and measurements data demonstrates the accuracy of the proposed model.

Keywords: electric power systems, parameter identification, close-loop identification, excitation systems, synchronous generator.

1. INTRODUCTION

Due to the inaccessibility to all of the power plant documents, having the mismatch between the existent documents and real system and altering the dynamic and static parameters with the passage of time, the dynamic parameters identification is essential for predicting the behavior of overall power network in the transient analyses. Even if the manufacturer proposed the as-built parameters, the validity of these parameters should be verified via field tests after five years. In the synchronous generator section, there are two identification methods: 1) offline identification and 2) online identification. In the offline methods, the synchronous generator is out of service and various techniques like frequency response, least squares, and dc excitation ones will be employed. In online methods a small exogenous signal is injected to the in-service machine in order to have no dominant effect on the normal operation of the system.

Generally, the direct method of excitation system identification necessitates the availability of excitation current and voltage which is not accessible in brushless excitation systems. However, the comprehensive identification of synchronous generator parameters makes the direct method possible in the brushless excitation systems.(Zaker *et al.*, (2016))

In this paper, a mathematical modeling and parameter identification of synchronous generator and excitation system for a real gas power plant are presented. In this model, the effective parameters are identified using imperialistic competitive algorithm (ICA). The identified parameters are put in a general single synchronous generator and excitation system framework in the Power Factory DIgSILENT Software and the simulation results are compared with experimental results measured from a real 154MW gas power plant.

2. GENERATOR MODELLING

In this section, the seventh-order model of synchronous generator is considered. The advantage of this model is to consider the impacts of stator and damper windings comparing to the low-order linear structure such as Heffron-Philips. As a general role for synchronous generator modeling in a single machine system, flux linkages are chosen as the state variables. As it was stated before, this excitation system is a brushless type in which there is no way to measure the synchronous generator excitation current and voltage. Therefore, indirect method should be employed for the identification process.

3. EXCITATION MODELLING

This section consists of various parts each of which plays an important role in the overall performance of the system. The understudy excitation system is an alternator-supplied rectifier which employs ac alternator to produce dc current for the main generator field winding. In this section, the model of each card within the excitation system with a short description on each one is presented.

3.1 Main Regulator Section (RS Card)

This is the main section of automatic excitation system in which by implementing two types of controller, PI and PID, the regulation and stability functions are addressed.

3.2 Under-Excitation Detection (LSES Card)

This device prevents the de-magnetization of the generator when absorbing reactive power, and maintains the generator within its operating limits.

3.3 Over-Flux Section (LUF2 Card)

This card provides the U/f image of a three-phase system which is related to the excitation system flux, and the difference between this voltage image and an adjustable reference voltage (ΔU/f).

3.4 Power System Stabilizer (SP1 Card)

This card provides the RS regulation card with a stabilizing signal as a function of the generator active power deviations. In fact, the oscillatory nature of the active power signal contains dynamical modes which their inclusion in the AVR section can enhance the power system dynamic performance.

3.5 Pulse Generation Section (GITS Card)

This section elaborates the control pulses for the thyristor bridge. The output of this bridge is connected to the exciter field windings. The result is a rectified voltage proportional to the control voltage of the AVR.

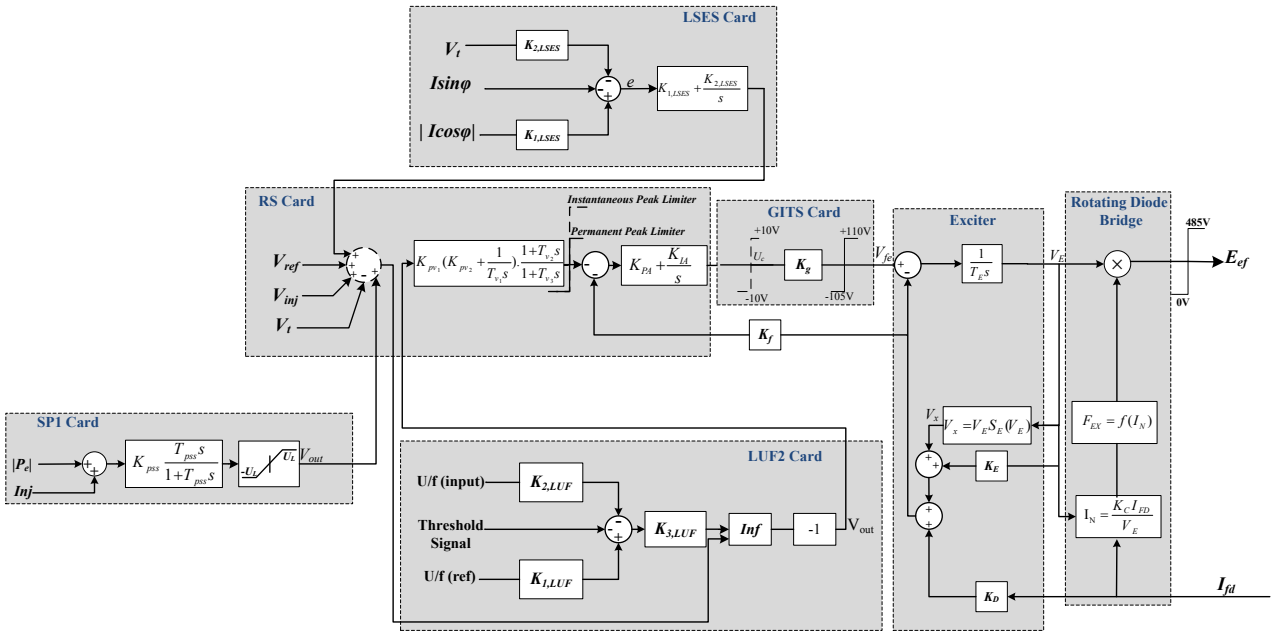

Fig. 1. The overall block diagram for modelling the excitation system

3.6 Exciter

In this excitation systems, the responsibility of exciter is to provide the ac voltage as the input to the rotating diode on the main shaft of synchronous machine.

3.7 Rotating Diode Bridge

The three-phase diode bridge rectifier is commonly employed to rectify the output voltage of ac exciter. The inductive effect of ac source which is modeled with inductive reactance and referred to as the commutating reactance makes a delay in the process of commutation.

3.8 Overall Model

Concatenating the aforementioned sections to a single, comprehensive model, the overall block diagram for modelling the ac excitation system in this unit will be obtained. This model is depicted in Fig. 1. The comprising parameters are identified through an optimization algorithm considering the terminal voltage as the objective function.

4. EXPERIMENTAL VERIFICATION

In order to verify the validity of proposed dynamical modelling and parameter estimation results, various experiments have been carried out on the 154 MW gas power plant.

4.1 High Active Power and Positive Reactive Power

In this test, a ±100mV voltage signal is injected to the AVR reference and the resulting outputs are recorded. (Fig. 2.)

4.2 High Active Power and Negative Reactive Power

Likewise, in this test, a ±100mV voltage signal is injected to the AVR reference with different reactive power and the resulting outputs are recorded (Fig. 3.).

5. CONCLUSIONS

This paper presents a comprehensive modelling and identification procedure for the excitation system and synchronous generator parameters. In order to identify the dynamical parameters, a metaheuristic algorithm is employed and the terminal voltage of synchronous generator is used as the objective function. The accuracy of the proposed modelling is justified through experimental results on a real gas power plant.

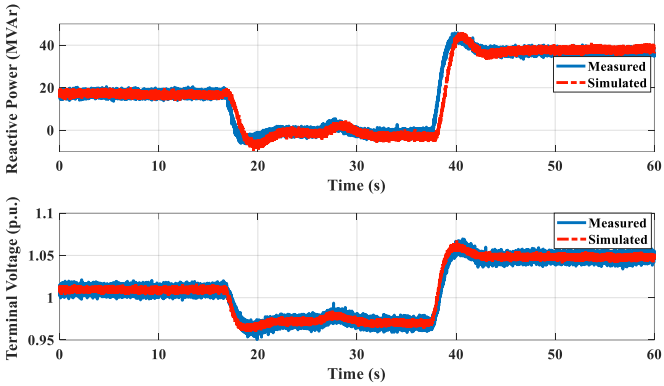

Fig. 2. The waveforms of measured and simulated signal for reactive power and terminal voltage at P=100MW and Q=17 MVAr.

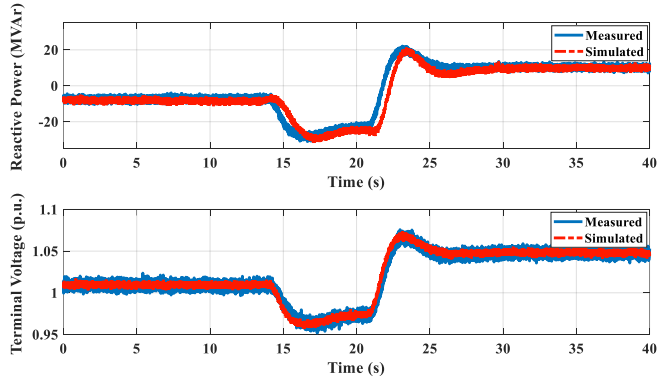

Fig. 3. The waveforms of measured and simulated signal for reactive power and terminal voltage at P=100MW and Q=-7.48MVAr.

6. REFERENCES

Zaker, B. *et al.* (2016) 'Simultaneous Parameter Identification of Synchronous Generator and Excitation System Using Online Measurements', *IEEE Transactions on Smart Grid*, 7(3), pp. 1230–1238. doi: 10.1109/TSG.2015.2478971.

A simple dynamic model for mitochondrial metabolism

G. Sváb * **G. Szederkényi** ** **G. Horvath** * **L. Tretter** *

* *Department of Medical Biochemistry, Semmelweis University, Budapest, Hungary, (e-mail: gergely@svab.hu)*
** *Faculty of Information Technology and Bionics, Pázmány Péter Catholic University, Budapest, Hungary (e-mail: szederkenyi@itk.ppke.hu)*

Abstract: A simple dynamical model is proposed in this paper to describe the main time-varying quantities in mitochondrial metabolism. The model is given in the form of kinetic ordinary differential equations containing 11 state equations. The parameters of the model were determined from the literature or from the authors' own laboratory measurements. The obtained simulation result is in good agreement with actual observation for simulating an ischemic process.

Keywords: biomedical systems, dynamical modeling, simulation, differential equations

1. INTRODUCTION

In the Neurobiochemistry working group (Institute of Medical Biochemistry, Semmelweis University), we have taken enzyme kinetic measurements of several mitochondrial enzymes, and we have determined and analyzed interactions between enzymes and substrates. Therefore, a suitable quantitative (mathematical) model is constructed which describes the temporal changes in the quantities of citric acid cycle's (CAC) molecules. The modeling goal in this research phase is to describe qualitatively the increased/decreased operation of the catalyzing enzymes as well as the modified operation of the intermediate molecules.

In previous studies similar models were constructed, it belongs to our goals is to promote further development compared to the known models and to expand them in other aspects. In Wu et al. (2007) the model can predict the individual factors effects (NADH, ATP, metabolic fluxes) in the regulation of CAC function and projects the effect of pH and membrane potential changes on ATP synthesis. In Korla and Mitra (2014) examination of the process of the CAC, electron transport chain and ATP synthesis is described. Reactions of the CAC are described with eight differential equations with Michaelis-Menten reaction kinetic. Korla et al. (2015) extends the earlier model with two transporter systems.

2. BIOLOGICAL BACKGROUND

2.1 Process description

Mitochondria are cell organelles with prokaryotic origin that established endosymbiosis with ancient eukaryotic cells during evolution. CAC is a complex enzyme system in mitochondria, and a key step of metabolism. Mitochondria produce energy during the catabolic degradation of carbohydrates, fats, proteins and nucleic acids. Additionally, molecules of the CAC take part as precursors in the construction of the anabolic procedures (Nelson and Cox (2012)).

2.2 The modeled reactions

In this work we modeled the reactions of CAC, and 3 mitochondrial transporters. The following list contains the reactions and their catalyzing enzymes/transporters involved in our model (Number of reaction, name of enzyme, Enzyme Commission (EC) number of enzyme).

R1: Citrate synthase (CS, 4.1.3.7):
$Acetyl\text{-}CoA + oxaloacetate \rightarrow citrate$
R2: Aconitase (ACON, 4.2.1.3):
$Citrate \rightleftharpoons isocitrate$
R3: Isocitrate dehydrogenase (IDH, 1.1.1.41):
$Isocitrate + NAD^+ \rightarrow oxoglutarate + CO_2 + NADH$
R4: Oxoglutarate dehydrogenase (OGDH, 1.2.4.2):
$Oxoglutarate + CoA\text{-}SH + NAD^+ \rightarrow succinyl\text{-}CoA + CO_2 + NADH$
R5: Succinyl-Coenzyme A ligase (SUCLA, 6.2.1.4):
$Succinyl\text{-}CoA + GDP + P \rightarrow succinate + CoA\text{-}SH + GTP$
R6: Succinate dehydrogenase (SDH, 1.3.5.1):
$Succinate + FAD \rightarrow fumarate + FADH_2$
R7: Fumarase (FH, 4.2.1.2):
$Fumarate + H_2O \rightleftharpoons malate$
R8: Malate dehydrogenase (MDH, 1.1.1.37):
$Malate + NAD^+ \rightleftharpoons oxaloacetate + NADH$
R9: Citrate transporter (CTP):
$Citrate + H^+ \rightleftarrows malate$
R10: Dicarboxylate carrier (DIC):
$HPO_4^{2-} \rightleftarrows malate$
R11: Oxoglutarate carrier (OGC):
$Oxoglutarate \rightleftarrows malate$

⋆ The project has been partially supported by the European Union, co-financed by the European Social Fund through the grants EFOP-3.6.3-VEKOP-16-2017-00002 and EFOP-3.6.3-VEKOP-16-2017-00009

3. KINETIC MODEL OF CITRIC-ACID CYCLE

3.1 Modeling goals

The modeling goals are the following:

(1) To determine the concentrations of substrates which participate in these reactions between physiological conditions.
(2) To predict the new equilibrium status after we modified initial conditions.
(3) To model the changed dynamic of the system in case of specific diseases via using pathological parameters of enzymes and/or pathological initial conditions.

3.2 Parameters

Table 1 contains the kinetic parameters. Source of parameters is the literature and some of them were measured in Institute of Medical Biochemistry, Semmelweis University, namely the values corresponding to OGDH, SDH and MDH.

E or T	substrate	V_{max} (μmol/min)	K_M (μM)
CS	oxaloacetate	1.88	4
ACON	citrate	3.4	470
	isocitrate		120
IDH	isocitrate	0.1	140
OGDH	oxoglutarate	0.0086	71
SUCLA	succinil-CoA	0.39	40
SDH	succinate	0.299	251
FH	fumarate	0.721	13
	malate		140
MDH	malate	1.616	580
	oxaloacetate		52
CTP (T)	citrate	10.5	32/27
	malate	11.5	250/60
DIC (T)	malate	6	490/920
	HPO_4^{2-}	6	1410/930
OGC (T)	oxoglutarate	9.5	310/170
	malate	10	1360/710

Table 1. Parameters and values of enzymes and transporters

3.3 The applied kinetics

Differential equations were described by parameters of enzymes and transporters using the Michaelis-Menten kinetic model. The general form of the reaction rates is

$$V([S]) = \frac{V_{max} \cdot [S]}{K_M + [S]}$$

Rates of reversible reactions and transports are described with two opposite reactions. We assume constant cell concentrations, because the volume of cell is much larger than that of the mitochondrium.

4. COMPUTATIONAL RESULTS FOR SIMULATING REGENERATION AFTER ISCHEMY

The simulations were implemented in MATLAB. We examine a pathological metabolic status after acute ischemy. In this state there is a significant change in substrate concentrations. Based on literature data, the altered initial conditions were the following: citrate decreases to 370 μM, oxoglutarate to 26 μM, fumarate to 180 μM, malate to 795 μM, and succinate to 1355 μM.

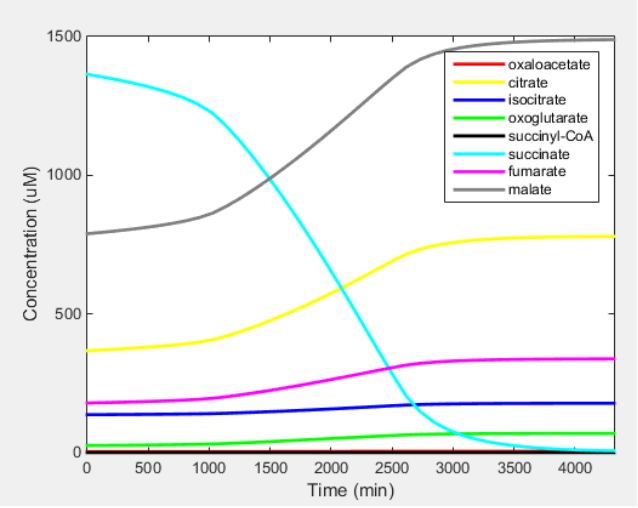

Fig. 1. Changes of concentrations after acute ischemia

The simulation shows that after ischemic status concentrations of substrates are going to physiological concentrations, as the system tries to recover physiological status (Figure 1). Moreover, we can observe that approximately three days are needed to restore normal concentrations of mitochondrial intermediates. These results show us that this model gives good results qualitatively, but further improvements are needed by parameter calibration and by the extension with other transporters.

5. CONCLUSION

A simple dynamic model for describing the dynamics of key quantities in mitochondrial metabolism was proposed in this paper. The model is written in the form of 12 nonlinear ODEs using Michaelis-Menten kinetics. The model was used successfully to simulate recovery from ischemy.

REFERENCES

Korla, K. and Mitra, C. (2014). Modelling the krebs cycle and oxidative phosphorylation. *Journal of Biomolecular Structure and Dynamics*, 32, 242–256.

Korla, K., Vadlakonda, L., and Mitra, C. (2015). Kinetic simulation of malate-aspartate and citrate-pyruvate shuttles in association with krebs cycle. *Journal of Biomolecular Structure and Dynamics*, 33(11), 2390–403.

Nelson, D.L. and Cox, M.M. (2012). *Lehninger Principles of Biochemistry*. WH Freeman, 6 edition.

Wu, F., Yang, F., Vinnakota, K., and Beard, D. (2007). Computer modeling of mitochondrial tricarboxylic acid cycle, oxidative phosphorylation, metabolite transport, and electrophysiology. *The Journal of Biological Chemistry*, 282(34), 24525–37.

On the Periodic Motion of a Two-Body System Upward Along an Inclined Straight Line with Dry Friction ⋆

Tatiana Yu. Figurina *

* *Ishlinsky Institute for Problems in Mechanics RAS, 101-1 Vernadsky Ave, Moscow 119526 Russia, e-mail:t_figurina@mail.ru*

Abstract: The possibility of a two-body system to move upward along an inclined line is investigated. The system is controlled by the force of interaction of the bodies so that the distance between the bodies and their velocities are periodic functions of time. The friction between the bodies and the line is Coulomb's dry friction. Necessary and sufficient conditions for the possibility of periodic upward motion of the system are proved. The motion is possible if and only if the smaller body can start moving upward the line from a state of rest while the bigger body is at rest. An algorithm of the upward motion is presented.

Keywords: limbless locomotion, Coulomb's friction, periodic motion

1. STATEMENT OF THE PROBLEM

Consider a system of two interacting bodies of masses M and m on an inclined plane. Coulomb's dry friction forces act between the bodies and the plane. The force of interaction of the bodies changes the velocities of the bodies, which changes the friction forces that are external forces for the system. Thus, the control of the force of interaction leads to the control of the system's center of mass. The bodies are assumed to move along a fixed line l on an inclined plane. Denote by $\alpha \in [0, \pi/2)$ the angle between line l and the horizontal plane. The bodies are modeled by point masses. Let x and y be the coordinates along line l, and v and V the velocities of bodies m and M, respectively. Without loss of generality we assume $M > m$. Let k be the coefficient of friction against the plane for bodies m and M and g the acceleration due to gravity.

The motion of the system along the line is governed by the equations

$$\begin{array}{l} \dot{x} = v, \qquad \dot{y} = V, \\ m\dot{v} = -mg\sin\alpha + F + F_m, \\ M\dot{V} = -Mg\sin\alpha - F + F_M \end{array} \tag{1}$$

where F denotes the force applied to body m by body M, and F_m and F_M denote Coulomb's friction forces applied to the bodies by the plane. The friction forces are defined by the relations

$$\begin{array}{c} F_m = -kmg\cos\alpha\,\mathrm{sgn}\,v, \quad v \neq 0, \\ |F_m| \le kmg\cos\alpha, \quad v = 0, \\ F_M = -kMg\cos\alpha\,\mathrm{sgn}\,V, \quad V \neq 0, \\ |F_M| \le kMg\cos\alpha, \quad V = 0 \end{array} \tag{2}$$

We consider the motions of the system in which the distance between the bodies and the velocities of both bodies are expressed by time-periodic functions, $y(t+T) - x(t+T) \equiv y(t) - x(t)$, $v(t+T) \equiv v(t)$, $V(t+T) \equiv V(t)$. Here, T is the time period which may be chosen arbitrarily.

⋆ This study was supported by the Russian Foundation for Basic Research (projects 17-01-00652, 17-51-12025).

In other words, we consider the motions with constant shifts of each body for the period, the shift being the same for both bodies: $y(t+T) - y(t) \equiv x(t+T) - x(t) \equiv \text{const}$. We call such motions periodic motions. When considering the motions of the system during a period, the periodicity conditions are equivalent to the boundary conditions

$$y(T) - y(0) = x(T) - x(0),\ v(T) = v(0),\ V(T) = V(0) \tag{3}$$

The question is whether the periodic motion of the system upward along the line is possible.

We assume that if there is no interaction between the bodies and both bodies are at rest at some time instant, they will remain at rest on the inclined line. This assumption implies

$$\mathrm{tg}\,\alpha \le k \tag{4}$$

Additionally, we require that the force governing the uniform upward motion of the smaller body m be not equal in its absolute value to the force governing the uniform downward motion of the larger body M, $kmg\cos\alpha + mg\sin\alpha \neq kMg\cos\alpha - Mg\sin\alpha$. This condition can be written as

$$\mathrm{tg}\,\alpha \neq k\frac{M-m}{M+m} \tag{5}$$

This is necessary for determining uniquely which of the bodies will start moving first from the state of rest of the entire system when an appropriate interaction force begins to act.

Problem. Find the condition allowing the periodic motion for the two-body system upward along the inclined line, provided that relations (1) -(5) and the inequality

$$x(T) > x(0) \tag{6}$$

hold.

2. CRITERIA OF POSSIBILITY OF THE PERIODIC UPWARD MOTION

Proposition. The periodic motion of the two-body system upward along an inclined line is possible if and only if

$$\operatorname{tg}\alpha < k\frac{M-m}{M+m} \tag{7}$$

Proof. Let us prove first the sufficiency of the condition (7). To do so, we will construct explicitly a periodic motion of the system that shifts it upward along line l, provided that inequality (7) holds. Let the system be at rest at the beginning of the motion, $v(0) = V(0) = 0$. At the first stage of the motion, body m moves downward, while body M moves upward. Choose some time interval $[0,\, t_0]$ and a constant interaction force F so that body M begins to move upward, namely, let $F \equiv -(Mg\sin\alpha + kMg\cos\alpha + A)$, $A > 0$. Then body M will move with an acceleration upward and body m will move with an acceleration downward,

$$\begin{aligned} &M\dot V = A,\\ &m\dot v = -(M+m)g\sin\alpha - (M-m)kg\cos\alpha - A \end{aligned} \tag{8}$$

After that we stop controlling the system and set $F \equiv 0$ for an interval $[t_0, t_1]$, with the duration of this interval being large enough for both bodies to have time to come to a stop due to friction, so that $V(t_1) = v(t_1) = 0$. Denote $x(t_1) = x_1$, $y(t_1) = y_1$, $y_1 > 0$, $x_1 < 0$.

Let at the second stage of the motion body m overtake body M, while body M is at rest. Define the control force F as follows:

$$\begin{aligned} &F(t) = mg\sin\alpha + kmg\cos\alpha + B, \quad t\in[t_1, t_1+\delta],\\ &F(t) = mg\sin\alpha + kmg\cos\alpha - B,\ t\in[t_1+\delta, t_1+2\delta] \end{aligned} \tag{9}$$

If the value of B is small enough, body M stays at rest. Indeed, the inequality (7) implies that there exists a positive value B such that the inequality

$$mg\sin\alpha + kmg\cos\alpha + B + Mg\sin\alpha < kMg\cos\alpha \tag{10}$$

holds. This inequality means that the value of the sliding friction force for body M is greater than the modulus of the sum of all other forces applied to this body; hence body M is at rest. The motion of body m is governed by the equations

$$\begin{aligned} &m\dot v = B, \quad t\in[t_1, t_1+\delta], \qquad v(t_1) = 0\\ &m\dot v = -B, \quad t\in[t_1+\delta, t_1+2\delta] \end{aligned} \tag{11}$$

At the time instant $t_1 + 2\delta$, body m comes to a stop, $v(t_1+2\delta) = 0$. By equating the distance travelled by body m for time 2δ to the value $y_1 - x_1$, one can find the duration $2\delta = 2\sqrt{\frac{m}{B}(y_1 - x_1)}$ required for body m to overtake body M and to come to a stop. By letting $T = t_1 + 2\delta$ we complete the construction of the control subject to which the system is at rest at the beginning and at the end of the period and both bodies travel the distance $y_1 > 0$ upward along line l. This completes the proof of sufficiency of the condition (7).

Now we will prove the necessity of (7). Let us suppose that the periodic motion of the system upward along the line is possible. Denote by u the velocity of the center of masses of the system

$$u = (m+M)^{-1}(mv + MV) \tag{12}$$

Equations (1) involve the equation of motion for the center of mass:

$$(m+M)\dot u = -(m+M)g\sin\alpha + F_M + F_m \tag{13}$$

If the upward motion of the system is possible, then a time interval exists such that the center of mass velocity is positive on this interval. Hence, one can take a time instant t_* from the left neighborhood of the point of maximum of the function $u(t)$, so that the velocity is positive and its derivative is nonnegative at this point,

$$u(t_*) > 0, \qquad \dot u(t_*) \ge 0. \tag{14}$$

The first inequality (14) means that $v(t_*) > 0$ or $V(t_*) > 0$. If $V(t_*) > 0$, then $F_M = -kMg\cos\alpha$ and the second inequality (14) cannot hold by virtue of equation (13) and the inequalities $|F_m| \le kmg\cos\alpha$ and $m < M$. The center of mass necessarily decelerates if the larger body moves forward. Let now $v(t_*) > 0$. Then $F_m = -kmg\cos\alpha$, and the second inequality (14), with (13) being taken into account, can be represented as follows:

$$F_M \ge (m+M)g\sin\alpha + kmg\cos\alpha \tag{15}$$

Hence, taking into account the relation $|F_M| \le kMg\cos\alpha$ we obtain $k(M-m)g\cos\alpha \ge (M+m)g\sin\alpha$. This inequality combined with condition (5) lead to (7), which completes the proof of the necessity of the inequality (7).

Remark 1. This proposition can be reformulated as follows. The periodic motion of a two-body system upward along an inclined line is possible if and only if body m can move upward with nonnegative acceleration while body M is at rest. The equivalence of the reformulation to the proposition is proved by the facts that the inequality (7) is equivalent to inequality (10) with B from the right-hand neighborhood of zero and inequality (10) provides the motion of body m upward with nonnegative acceleration with body M at rest.

Remark 2. Let the system of n interacting bodies with masses

$$m_1 \le m_2 \le \cdots \le m_n, \quad M_* = \sum_{i=1,..n} m_i \tag{16}$$

on an inclined line with dry friction be considered. The periodic motion of this system upward along an inclined line is possible if and only if the body with minimal mass m_1 can move upward with a nonnegative acceleration, with all other bodies being at rest. This condition implies

$$\operatorname{tg}\alpha < k\frac{M_* - 2m_1}{M_*} \tag{17}$$

The proof of the necessity of this condition is similar to that for a two-body system. The sufficiency is proved by presenting the motion similar to that presented above, for which at the first stage bodies m_i, $i = 2, \dots n$ move as a single whole (as the larger body for the two-body case), and at the second stage all these bodies are at rest.

Remark 3. Let now two bodies of the system have different coefficients of friction and let the friction be anisotropic. Denote by k_m^+, k_m^- and k_M^+, k_M^- the coefficients of friction for upward and backward motions of bodies m and M, respectively. We assume that at least one of the inequalities $k_M^- M > k_m^+ m$, $k_m^- m > k_M^+ M$ holds and that the system can stay at rest, which implies

$$\operatorname{tg}\alpha < (k_M^- M + k_m^- m)(M+m)^{-1} \tag{18}$$

The periodic motion of the system upward along an inclined line is possible if and only if

$$\operatorname{tg}\alpha < \frac{\max\{k_M^- M - k_m^+ m,\ k_m^- m - k_M^+ M\}}{M+m} \tag{19}$$

or, which is the same, one body can move upward with nonnegative acceleration while the other body is at rest. The proof of this remark is similar to that of Proposition.

Avoiding Ill-Conditioning on Object-Oriented Models of Hydraulic Actuation Systems

Andrea Giorgio Bartolini * **Francesco Casella** **
Alberto Leva **

* *Dynamica s.r.l. 26100 Cremona, Italy (e-mail: andrea.bartolini@dynamica-it.com).*
** *Politecnico di Milano, Dipartimento di Elettronica, Informazione e Bioingegneria, 20133 Milano, Italy (e-mail: francesco.casella,alberto.leva@polimi.it)*

Keywords: Hydraulic systems, equation-based modelling, object-oriented modelling.

1. INTRODUCTION

The object-oriented modelling paradigm (see, e.g., Mattsson et al. (1998), Tiller (2001)) allows to build system models by connecting component or sub-system models in an arbitrary fashion through connectors, as long as the connection makes sense from a physical point of view, without worrying about the internal structure or implementation of the components.

Object-oriented languages and modelling tools have been used for a long time for the modelling of hydraulic systems, where pressurized oil is used to power mechanical equipment, see, e.g., the HyLib library (Beater, 2000), which later became the commercial HydraulicsLibrary, or other modelling libraries described by Harman (2006) and Paredis (2008). Several papers describe applications of these libraries to specific modelling needs, see, e.g., Harman (2006), or Chandrasekar and Tummescheit (2014).

In all these models, hydraulic dynamics is strongly coupled with mechanical dynamics. In principle, based on the time scale or frequency range of phenomena one is interested into for a specific simulation study, it would be possible to leave out the compressibility effects of the fluid and/or the inertia of some mechanical elements in some component models. In their recent experience, the authors have found out that allowing complete freedom in taking into account these phenomena can lead to severe numerical issues when system models are built out of them. To the author's knowledge, this aspect has never been explicitly discussed in the literature.

The goal of this paper is to explain these issues by means of a simple paradigmatic system model, and to provide guidelines for library developers to allow the arbitrary connection of component models, according to the object-oriented modelling principles.

2. THE PARADIGMATIC SYSTEM MODEL

The paradigmatic system is shown in Fig. 1. A rigid cylindrical chamber of section A containing a compressible fluid (usually oil) at pressure p, with nominal density ρ_0

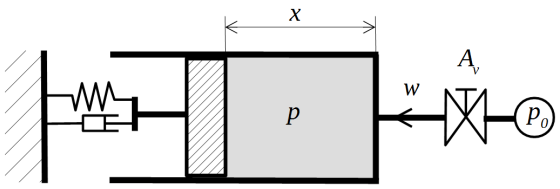

Fig. 1. Sketch of the paradigmatic system

at pressure p_0 and compressibility k_p, is delimited by a piston of mass m on the left side and by a valve with mass flow rate w and flow coefficient A_v on the right side. The piston is connected to a mechanical load with elastic coefficient k_x and friction coefficient k_v, which applies a force F on the piston that is the result of the elastic and friction effects plus an extra prescribed force F_0. The valve outlet is connected to a reservoir with fixed pressure p_0.

The system model is declaratively defined by the following set of differential-algebraic equations (DAEs).

$$A[\rho_0 + k_p(p - p_0)]\dot{x} + Axk_p\dot{p} - w = 0 \quad (1)$$
$$\dot{x} - v = 0 \quad (2)$$
$$m\dot{v} - Ap - F = 0 \quad (3)$$
$$F - F_0 + k_x x + k_v v = 0 \quad (4)$$
$$w - A_v\sqrt{\rho_0|p_0 - p|}sign(p_0 - p) = 0 \quad (5)$$

where Eq. (1) is the mass balance in the chamber, Eqs. (2)-(3) describe the piston motion, Eq. (4) describes the mechanical load, and Eq. (5) the valve flow. F_0 and A_v are known system inputs, functions of time.

3. STRUCTURAL ANALYSIS

The system (1)-(5) is a DAE in the form $F(y, \dot{y}, v, t) = 0$; this DAE has index one if the Jacobian matrix $\frac{\partial F}{\partial z}$ (where z collects all terms in $\dot{y}$ and v) has a non-zero determinant, which means that the system can be locally solved for z given y and t.

If both fluid compressibility and mechanical inertia are taken into account, then $m > 0$ and $k_p > 0$. In this case, it turns out that

$$\left|\frac{\partial F}{\partial z}\right| = k_p m A x. \tag{6}$$

As the cross section A is obviously positive, the system has index 1 provided that $x > 0$, i.e., the chamber is not completely empty of oil, which is a reasonable assumption for the validity of such a model.

When the load is much less stiff than the fluid, one may want to neglect the fluid compressibility, i.e., set $k_p = 0$, to get rid of one fast state in the model. In this case

$$\left|\frac{\partial F}{\partial z}\right| = \frac{A_v m}{2\sqrt{p_0 - p}} sign(p_0 - p) \tag{7}$$

The determinant is undefined when $p = p_0$, but this is due to the slightly naive formulation of the valve equation (5), whose derivative with respect to p approaches infinity as $p \to p_0$. This problem can be solved by using a more appropriate formulation of that law that does not become singular at that point, e.g., by substituting the function $\sqrt{h} sign(h)$ with the function

$$\frac{h}{\sqrt[4]{h^2 + \epsilon^2}} \tag{8}$$

which is close to the original function when $|h| \gg \epsilon$ but has a finite derivative in the neighbourhood of zero (Casella, 1999). Then

$$\left|\frac{\partial F}{\partial z}\right| = \frac{A_v m}{\sqrt{\epsilon}} \tag{9}$$

In this case the index of the system is normally 1, but becomes 2 when the valve is closed ($A_v = 0$), which is a completely normal condition in hydraulic system models.

Alternatively, when the piston has a small mass (e.g., it is a membrane), one may want to neglect it, setting $m = 0$, but still accountinf for the fluid compressibility $k_p > 0$. In this case

$$\left|\frac{\partial F}{\partial z}\right| = k_p k_v x A \tag{10}$$

Now, by assumption $k_p > 0$, $A > 0$, and $x > 0$ if the chamber is not empty. In principle, the model is index 1 if the viscous friction term k_v is non-zero. This is in general a critical assumption: for example, if one is modelling an accumulator with a membrane, it is very hard to identify a viscous friction term, as the reaction force of the membrane is inherently only depending on its deformation. If more sophisticated friction models were used, the condition equivalent to $k_v \neq 0$ would be that is is always possible to invert the force-velocity relationship, computing the force given the velocity, which for example not possible when modelling stiction.

In the extreme case, one may want to avoid the stiff dynamics entirely and neglect both fluid compressibility and inertia, thus setting $k_p = 0$ and $m = 0$. In this case

$$\left|\frac{\partial F}{\partial z}\right| = \rho_0 A^2 + \frac{A_v k_v}{\sqrt{\epsilon}} \tag{11}$$

Since $A_v \geq 0$, and assuming $k_v \geq 0$, that is, if a viscous friction term is present, it is dissipative, then the system is always index 1. If more sophisticated friction models including stiction are used, it is impossible to say based on this analysis that the system will always be index 1, as they may entail $k_v < 0$ during transients. Further analysis would be necessary, taking into account such friction models explicitly, but this goes beyond the scope of this paper.

4. DISCUSSION AND CONCLUSION

The analysis carried out in the previous section shows that in the two intermediate cases, and possibly in the last one, the system can change the index during simulation, which will cause a run-time error in existing equation-based, object-oriented modelling tools (EOOLTs), that cannot handle this case. This results gives a concise and clear explanation of the numerical problems that were experienced with real-life models taking the same modelling assumptions.

The results of the analysis suggest that the best option to guarantee the safe and robust simulation of equation-based, object-oriented hydraulic systems coupling fluid dynamics and mechanical dynamics is to always take into account both fluid compressibility and mechanical inertia of pistons and membranes, even though this may end up in modelling very stiff dynamics. Neglecting both fluid compressibility and mechanical inertia can be an option to reduce the number of fast modes in the system's dynamics, but only if simple enough (e.g. linear) models are used to represent friction phenomena. In the author's opinion, these findings are particularly useful for developers of reusable component libraries for hydraulic power and actuation systems.

REFERENCES

Beater, P. (2000). Modelling and digital simulation of hydraulic systems in design and engineering education using Modelica and HyLib. In *Proceedings of the Modelica Workshop 2000*, 1–8. Modelica Association, Lund, Sweden.

Casella, F. (1999). *Modelling, Simulation, and Control of a Geothermal Power Plant*. Ph.D. thesis, Politecnico di Milano.

Chandrasekar, S. and Tummescheit, H. (2014). Physical design of hydraulic valves in Modelica. In *Proceedings of the 10th International Modelica Conference*, 627–636. Lund, Sweden.

Harman, P. (2006). Modelling automotive hydraulic systems using the Modelica ActuationHydraulics library. In *Proceedings of the 5th International Modelica Conference*, 399–403. Vienna, Austria.

Mattsson, S.E., Elmqvist, H., and Otter, M. (1998). Physical system modeling with Modelica. *Control Engineering Practice*, 6(4), 501–510.

Paredis, C. (2008). An open-source Modelica library of fluid power models. In *Bath/ASME Symposium on Fluid Power and Motion Control*, 1–14. Bath, UK.

Tiller, M. (2001). *Introduction to physical modelling with Modelica*. Kluwer.

Stability Analysis of Nonlinear Singular Systems via Polytopic Models of the Characteristic Equation ⋆

Marcelino Sánchez * **Juan Carlos Arceo** * **Victor Estrada-Manzo** *
Miguel Bernal *

* *Dept. of Electrical and Electronics Engineering, Sonora Institute of Technology, 5 de Febrero 818 Sur, C.P. 85000, Cd. Obregon, Sonora, Mexico, miguel.bernal@itson.edu.mx*

Abstract: This report explores asymptotic stability of nonlinear singular systems, i.e., differential algebraic equations with a descriptor state-space representation, by means of a polytopic rewriting of the "generalised characteristic polynomial" (determinant of the corresponding nonlinear pencil). It is shown that, via linearisation arguments, the Edge Theorem can be adapted for analysis purposes by taking into account that singularity of systems translates into degree dropping of some vertex polynomials.

Keywords: Nonlinear Singular Systems, Linear Matrix Inequalities, Characteristic Polynomial.

1. INTRODUCTION

State-space forms of singular nonlinear systems are *descriptors* (Dai, 1989):

$$E(x)\dot{x}(t) = A(x)x(t), \tag{1}$$

where $x(t) \in \mathbb{R}^n$ is the state, $A(x)$, $E(x) \in \mathbb{R}^{n\times n}$ are smooth matrix nonlinear functions, and, importantly, $E(x)$ has not full rank. Simulation of these systems requires proper initialisation to hold the algebraic restrictions along the time (Brenan et al., 1995); moreover, sudden loss of rank in $E(x)$ may lead to instantaneous novel algebraic restrictions which might be consistent/inconsistent, persistent/evitable. Simulation of DAEs is largely based on the Pantelides algorithm in Pantelides (1988) which, under certain conditions, transforms it into an ordinary differential equation (ODE). Since we are interested in stability of equilibrium points, in the sequel, it will be assumed that $x = 0$ is an equilibrium point of (1). Lyapunov-based analysis of such systems is still on course, based on generalised Lyapunov functions, descriptor redundancy forms, and/or the Finsler's Lemma (Ishihara and Terra, 2002); only particular cases are available in the nonlinear case: when explicit algebraic restrictions are provided (Ebenbauer and Allgöwer, 2007), the rank of $E(x)$ is fixed (quasi-linear) (Riaza and Zufiria, 2001), or $E(x)$ is constant (Yang et al., 2013).

This paper adopts a different perspective: it considers matrix $sE(x) - A(x)$ as a *generalised pencil* and $\det(sE(x) - A(x))$ as the *generalised characteristic polynomial* associated to (1); based on them, stability is established by mimicking eigenvalue tests from linear systems theory. Since (1) is not a linear-parameter- nor a time-varying system, guaranteeing that the roots of $\det(sE(x) - A(x))$ are always in the left half of the complex plane $\mathbb{C}^-$ is enough to ensure asymptotic stability of the origin by linearisation arguments. To check the eigenvalue condition for a given a compact subset of the state space $\Omega \subset \mathbb{R}^n$, our proposal rewrites $\det(sE(x) - A(x))$ as a polytope of vertex polynomials; then, a variety of tests derived from the Edge Theorem (Bartlett et al., 1988) come at hand to provide sufficient conditions for the polytope to be stable; these tests are expressed in the form of linear matrix inequalities (LMIs) (Boyd et al., 1994). Importantly, the singular nature of the systems is mirrored by degree dropping of some vertex polynomials, which obliges to recur to further refinements of the Edge Theorem (Białas and Góra, 2012).

⋆ The authors would like to thank the support provided by the CONACYT scholarships 423601 and 415714, the postdoctoral fellowship for CVU 366627, the ITSON PROFAPI Project CA-18 2017-0088, and the PFCE 2016-17.

2. POLYTOPES OF POLYNOMIALS

A bounded expression can always be written as a convex sum of its bounds; indeed, given $z \in \left[z^0, z^1\right]$, it can be algebraically checked that $z = w_0(z)z^0 + w_1(z)z^1$ with $w_0(z) = \left(z^1 - z\right)/\left(z^1 - z^0\right)$ and $w_1(z) = 1 - w_0(z)$; therefore, assuming all non-constant terms $z_j(x) \in \left[z_j^0, z_j^1\right]$, $j \in \{1, 2, \ldots, r\}$ in the coefficients of $\det(sE(x) - A(x))$ are bounded in Ω, where $z_j^0 = \min_{x\in\Omega} z(x)$ and $z_j^1 = \max_{x\in\Omega} z(x)$, they can be written as

$$z_j(x) = \underbrace{\left(\frac{z_j^1 - z_j(x)}{z_j^1 - z_j^0}\right)}_{w_0^j(x)} z_j^0 + \underbrace{\left(\frac{z_j(x) - z_j^0}{z_j^1 - z_j^0}\right)}_{w_1^j(x)} z_j^1, \tag{2}$$

where $w_0^j(x) + w_1^j(x) = 1$, $0 \le w_i^j(x) \le 1$, $i \in \{0, 1\}$ for any $x \in \Omega$ (convex sum property).

Once this is made, $\det(sE(x) - A(x))$ can be rewritten as a polytope of polynomials in s; each of these vertexes has constant coefficients which correspond to a particular combination of minima and maxima of the r non-constant terms in $\det(sE(x) - A(x))$. Let $\mathbf{i} = (i_1, i_2, \ldots, i_r)$, $\forall j : i_j \in \{0, 1\}$, $\mathbf{w_i}(z) = w_{i_1}^1(z)w_{i_2}^2(z)\cdots w_{i_r}^r(z)$; then:

$$\det(sE(x) - A(x)) = \sum_{\mathbf{i}} \mathbf{w_i}(z)p_{\mathbf{i}}(s), \tag{3}$$

where $\sum_{\mathbf{i}} \mathbf{w_i}(z) = \sum_{i_1=0}^{1}\sum_{i_2=0}^{1}\cdots\sum_{i_r=0}^{1} w_{i_1}^1(z)w_{i_2}^2(z)\cdots w_{i_r}^r(z) = 1$, $0 \le \mathbf{w_i}(z) \le 1$, $p_{\mathbf{i}} = \det(sE(x) - A(x))|_{\mathbf{w_i}=1}$. Since $\operatorname{rank}(E(x)) < n$ certain vertex polynomials $p_{\mathbf{i}}(s)$ will present *degree dropping*.

Example 1. Consider the nonlinear singular system

$$\begin{bmatrix}(x_1-x_2)^2 & 0\\ 0 & 1\end{bmatrix}\begin{bmatrix}\dot{x}_1\\ \dot{x}_2\end{bmatrix}=\begin{bmatrix}1 & -1\\ -1-x_1^2 & -2\end{bmatrix}\begin{bmatrix}x_1\\ x_2\end{bmatrix}, \tag{4}$$

whose generalised characteristic polynomial is

$$(x_1-x_2)^2\,s^2+\left(2(x_1-x_2)^2-1\right)s-x_1^2-3. \tag{5}$$

As expected, sudden loss of rank in the left-hand side of (4) and degree dropping of (5) occur when $x_1 - x_2 = 0$. An exact polytopic rewriting of (5) for the compact set Ω where $z_1(x) = (x_1 - x_2)^2 \in [0, \alpha]$ and $z_2(x) = x_1^2 \in [0, \beta]$ with $\alpha, \beta > 0$, can be done by writing (3) with $p_{00}(s) = -s - 3$, $p_{01}(s) = -s - \beta - 3$, $p_{10}(s) = \alpha s^2 + (2\alpha - 1)s - 3$, and $p_{11}(s) = \alpha s^2 + (2\alpha - 1)s - \beta - 3$ as vertex polynomials, and $w_0^1(z) = \left(\alpha - (x_1 - x_2)^2\right)/\alpha$, $w_0^2(z) = \left(\beta - x_1^2\right)/\beta$, $w_1^1 = 1 - w_0^1$, and $w_1^2 = 1 - w_0^2$ as convex interpolating functions. Again, degree dropping occurs in vertex polynomials $p_{00}(s)$ and $p_{01}(s)$ as a result of the system singularities.

3. POLYNOMIAL-BASED STABILITY

Let $H(\cdot) \in \mathbb{R}^{n\times n}$ denote the Hurwitz matrix of a polynomial $p(s) = a_n s^n + a_{n-1}s^{n-1} + \cdots + a_1 s + a_0$. Since the seminal paper of Białas (1985), sufficient and necessary conditions for the stability of convex combinations of two n-th degree stable polynomials have been established by constructing an "edge-like" test which examines whether the real eigenvalues of the composite matrix $H_{12} = -H(p_1(s))H^{-1}(p_2(s))$ are strictly negative, where $p_1(s) = s^n + a_{n-1}s^{n-1} + \ldots + a_1 s + a_0$ and $p_2(s) = s^n + b_{n-1}s^{n-1} + \ldots + b_1 s + b_0$ are the stable polynomials in the convex combination $\lambda p_1(s) + (1 - \lambda)p_2(s)$, $\lambda \in [0, 1]$. This criterium has been put into an LMI form for polytopes of stable polynomials (Sánchez and Bernal, 2017). When degree dropping of some vertex polynomials occur, refinements exist that are based on further considerations on the geometry of the complementary regions (Białas and Góra, 2012).

Theorem 1. Assume the origin $x = 0$ of the nonlinear singular system (1) is an equilibrium point. Assume also that the system has a generalised characteristic polynomial with exact convex representation (3) in the compact set Ω. Then, the origin $x = 0$ is asymptotically stable in the sense of singular systems if there exists matrices $M_{\mathbf{ij}}$ of adequate dimension, such that LMIs

$$M_{\mathbf{ij}} + M_{\mathbf{ij}}^T > 0,\; H(p_{\mathbf{i}})M_{\mathbf{ij}}H^T(p_{\mathbf{j}}) + H(p_{\mathbf{j}})M_{\mathbf{ij}}^T H^T(p_{\mathbf{i}}) \geq 0, \tag{6}$$

are feasible for all $\mathbf{i}, \mathbf{j} \in \{0, 1\}^r$ such that $\deg(p_{\mathbf{j}}) \geq \deg(p_{\mathbf{i}})$, $\mathbf{i} \neq \mathbf{j}$, provided each vertex polynomial $p_{\mathbf{i}}$ is stable.

Proof. If conditions (6) hold, then $M_{\mathbf{ij}} + M_{\mathbf{ij}}^T > 0$ and $H^{-1}(p_{\mathbf{j}})H(p_{\mathbf{i}})M_{\mathbf{ij}} + M_{\mathbf{ij}}^T H^T(p_{\mathbf{i}})H^{-T}(p_{\mathbf{j}}) \geq 0$ hold, which implies that the real eigenvalues of each $H^{-1}(p_{\mathbf{j}})H(p_{\mathbf{i}})$ are all non-negative (Ebihara and Onishi, 2009). This, in turn, implies that the convex sum (3) is a polytope of stable polynomials with possibly degree dropping in some of its vertexes (Białas and Góra, 2012). Recall that the convex sum (3) is algebraically equivalent to $p(s, x) = \det(sE(x) - A(x))$ for all $x \in \Omega$, which therefore implies that there is a $P \in \mathbb{R}^{n\times n}$ such that $E^T(0)P = P^T E(0) \geq 0$ and $PA(0) + A^T(0)P \leq 0$. Thus, a linearisation argument allows using $V(x) = x^T E^T(0)Px$ as a Lyapunov function for all the trajectories in a sufficiently small vicinity within a subset $\mathcal{X} \subset \mathbb{R}^n$ with $\dim(\mathcal{X}) \leq \operatorname{rank}(E(0))$, to which the dynamics of the system are restricted, i.e., asymptotic stability of the origin $x = 0$ in the sense of singular systems is granted.

Example 1 (continued): *Consider again the nonlinear singular system* (4) *in example 1, whose characteristic polynomial is given in* (5)*. Modelling as shown thereby with* $\alpha = 100$ *and* $\beta = 25$ *leads to four polynomials* $p_{00}(s) = -s-3$, $p_{01}(s) = -s-28$, $p_{10}(s) = 100s^2 + 199s - 3$, *and* $p_{11}(s) = 100s^2 + 199s - 28$, *where the last two are unstable. This implies the test is unable to establish stability in this region, which is consistent with the fact that it includes unstable trajectories. Notwithstanding, since* $E(x)$ *loses rank in* $x_1 - x_2 = 0$ *leading to a persistent algebraic restriction which includes the origin, the generalised characteristic polynomial can be reduced to* $p(s, x) = -s - 3 + x_1^2$ *which, taking* $z_2(x)$ *can be modelled as the convex sum of* $p_0(s) = -s - 3$ *and* $p_1(s) = -s - 28$ *whose associated Hurwitz matrices yield feasible LMI conditions in Theorem 1 with*

$$H(p_0)=\begin{bmatrix}-1 & 0\\ 0 & -3\end{bmatrix},\; H(p_1)=\begin{bmatrix}-1 & 0\\ 0 & -28\end{bmatrix},\; M_{12}=\begin{bmatrix}0.5053 & 0\\ 0 & 0.0061\end{bmatrix}.$$

This result confirms that stable trajectories are indeed those in the algebraic restriction $x_1 - x_2 = 0$ *where* $E(x)$ *loses rank.*

REFERENCES

Bartlett, A.C., Hollot, C.V., and Lin, H. (1988). Root locations of an entire polytope of polynomials: It suffices to check the edges. *Mathematics of Control, Signals and Systems*, 1(1), 61–71.

Białas, S. (1985). A necessary and sufficient condition for the stability of convex combinations of stable polynomials or matrices. *Bulletin of the Polish Academy of Sciences*, 33(9-10), 473–480.

Białas, S. and Góra, M. (2012). A few results concerning the hurwitz stability of polytopes of complex polynomials. *Linear Algebra and its Applications*, 436(5), 1177–1188.

Boyd, S., Ghaoui, L.E., Feron, E., and Belakrishnan, V. (1994). *Linear Matrix Inequalities in System and Control Theory*, volume 15. SIAM: Studies In Applied Mathematics, Philadelphia, USA.

Brenan, K.E., Campbell, S.L., and Petzold, L.R. (1995). *Numerical solution of initial-value problems in differential-algebraic equations*. SIAM.

Dai, L. (1989). *Singular Control Systems*. Springer-Verlag.

Ebenbauer, C. and Allgöwer, F. (2007). Stability analysis of constrained control systems: An alternative approach. *Systems & Control Letters*, 56(2), 93–98.

Ebihara, Y. and Onishi, Y.and Hagiwara, T. (2009). Robust performance analysis of uncertain LTI systems: Dual LMI approach and verifications for exactness. *IEEE Transactions on Automatic Control*, 54(5), 938–951.

Ishihara, J.Y. and Terra, M. (2002). On the Lyapunov theorem for singular systems. *IEEE Transactions on Automatic Control*, 47(11), 1926–1931.

Pantelides, C.C. (1988). The consistent initialization of differential-algebraic systems. *SIAM Journal on Scientific and Statistical Computing*, 9(2), 213–231.

Riaza, R. and Zufiria, P.J. (2001). Stability of singular equilibria in quasilinear implicit differential equations. *Journal of Differential Equations*, 171(1), 24–53.

Sánchez, M. and Bernal, M. (2017). A convex approach for reducing conservativeness of kharitonovs-based robustness analysis. *IFAC-PapersOnLine*, 50(1), 832–837.

Yang, C., Sun, J., and Zhang, Q.and Ma, X. (2013). Lyapunov stability and strong passivity analysis for nonlinear descriptor systems. *IEEE Transactions on Circuits and Systems I: Regular Papers*, 60(4), 1003–1012.

Model-Based Design of Experiments: Where to go?

Robert J. Flassig [*] **René Schenkendorf** [**,***]

[*] *Max Planck Institute for Dynamics of Complex Technical Systems, Process Systems Engineering, Sandtorstraße 1, 39106 Magdeburg, Germany (e-mail: flassig@mpi-magdeburg.mpg.de)*
[**] *Braunschweig University of Technology, Institute of Energy and Process Systems Engineering, Franz-Liszt-Straße 35, 38106 Braunschweig, Germany (e-mail: r.schenkendorf@tu-braunschweig.de)*
[***] *Braunschweig University of Technology, Center of Pharmaceutical Engineering (PVZ), Franz-Liszt-Straße 35a, 38106 Braunschweig, Germany*

1. INTRODUCTION

Design of experiments (DoE) is a set of well-established and over 100 years evolved rational methodologies for validating and discovering relationships between controls and responses of an input-output system in a data efficient way. The philosophy behind DoE is that controls or factors affect the system's response. The response of a system to a specific control may be observed and thus by an appropriate set of applied controls (=DoE), one may gather information of the system's mechanism to disentangle the relationship between controls and responses. Responses may comprise system states but also observables or performance measures derived from the system states.

The use of mathematical models for analysing complex processes is a powerful tool to gain a deep system understanding. However, this approach requires realistic, predictive mathematical models. During the model development phase, scientists have to cope with numerous challenges, e.g., limited knowledge about the underlying mechanisms, lack or exorbitance of dynamic or static experimental data, large experimental and process variability. Given a specific model class, a plethora of many different methodologies to optimally identify a specific model class structure have been developed since the mid of 20th century. This includes on the one hand methods for discrimination of competing structures but also methods for parameter estimation. We would like to discuss, whether further methodologies in the direction of model-based design are still needed, and if yes, to what extent. Further, given the trend of gathering massive data of a system of interest we highlight the analogy of DoE for systems identification and big data analysis. Within the age of digitalization, analysis and modelling of big data have become an active field of DoE application. Big data typically comprise massive volume, heterogeneous and unexplored data collected in areas across science (e.g. structural biology, particle physics), health (e.g. genomics, predictive healthcare), economics (e.g. market analysis), ecology, business (e.g. process monitoring), Web 2.0 sources (e.g. social media, internet of things) and robotics (e.g. sensoring data) (Fan et al., 2014). To extract information, modelling big data with empirical (statistical) or mechanistic models with classical approaches is often note feasible and thus, several approaches from design of experiments have emerged to facilitate big data modelling. Specifically, model-based DoE supplies a rational for targeted sampling in divide-and-conquer algorithms or for sequential learning, which in classical DoE is known as sequential or multi-stage DoE (Box and Draper, 1986). The classic DoE based on statistical performance measures, e.g., A-, D-, E-, I-, T-optimality, have been complemented by probabilistic model-based performance measures. These measures include global sensitivities, information-based criteria and Bayesian inference based on the posterior calculation, which have been massively studied and applied in systems biology (Schenkendorf and Mangold, 2013; Flassig and Sundmacher, 2012).

2. DOE FOR BIG DATA ANALYSIS

Over the last decade, many research and engineering disciplines have become more and more data intense. Big data have arisen from innovative experiments, measurement and monitoring devices generating high-dimensional, massive sample sizes. Big data are therefore often difficult to analyse, and the extraction of information is notoriously laborious. In a sense, a big dataset can be understood as a complex system that is yet to be identified. Thus, the goal of modelling and analysing big data is similar to what is desired in complex systems identification: (i) understanding of the interdependencies of factors and responses that shape the dataset and (ii) accurate predictions of future outcomes. As in classical systems identification, the maxim of data efficiency is given. At first sight, this requirement seems awkward. It is the high-dimensional, massive sample property that generates several interesting emergent phenomena: scalability, storage bottleneck, noise accumulation, spurious correlation, incidental endogeneity and measurement errors (Fan et al., 2014).

During the initial rise of big data, statistics and related disciplines of data analysis have failed to adequately address big data properties and related challenges (Wang et al., 2016). The situation has changed recently when big data challenges in many different application areas have naturally driven the development of new big data method-

ologies. Even though it is easy to see that model-based DoE methodologies for complex systems identification can be tailored to cope with the emerging phenomena in big data, studies and methodologies to DoE-based big data approaches have only recently been developed (Drovandi et al., 2017).

Initially, big data methods have considered the entire dataset, and thus scalability has been the focus. Scalability has been addressed by methods including 'divide-and-conquer' approaches (Guha et al., 2012), Bayesian inference based on a consensus Monte Carlo algorithm (Huang and Gelman, 2005; Scott et al., 2016), principle component analysis (Kettaneh et al., 2005), clustering approaches (Bouveyron and Brunet-Saumard, 2014), least angle regression (Efron et al., 2004), and sparsity assumptions (Hastie et al., 2015). In contrast to using the complete dataset, DoE-based methods have been recently developed following the paradigm that a well-chosen subset of the big dataset can deliver equivalent answers compared to the full dataset at considerably less effort (Drovandi et al., 2017). As in classical DoE for systems identification or in Bayesian optimization, exploration and exploitation are the pillars of optimally analysing big data. An advantage of the DoE-based approach to big data is the avoidance of pitfalls resulting from big data effects and classical, well-established statistics can be applied. However, the DoE itself needs to be well chosen.

3. OUTLOOK: WHERE TO GO?

Uncertainty quantification, meta-modelling and big data modelling are active fields of application of DoE. Whereas uncertainty quantification has advanced its methods to efficient non-linear transformations of random variables, we still need improvements when it comes to optimizing stochastic, distributed complex systems. The optimization of systems with stochastic spatio-temporal fluctuations in combination with distributed properties is a challenging task, either from the modelling but also from the optimization point of view. The current popularity of Bayesian optimization and machine learning algorithms should be used to foster cross-disciplinary research including classic DoE; sequential design, Bayesian optimization and adaptive learning are three sides of the same coin. A coalition between researchers from classical DoE, Bayesian optimization and machine learning community in combination with applications in the areas of big data applications (e.g. process monitoring, earth science, genomics, internet of things, robotics, social media), biotechnology, pharmaceutics and systems medicine will have a bride future in terms of scientific and socio-economic impact.

DoE-based big data analysis is in the need of further research in the direction of noise accumulation and spurious patterns in high dimensional data, improvement of computational and algorithmic efficiency and stability and mastering heterogeneity, experimental variations and statistical bias associated with combining data from different sources (Fan et al., 2014).

Finally, even though model-based DoE approaches have been very much advanced over the last decades, the hard work still needs to be done: given a specific problem, scientists and engineers still have to think critically about the problem. This also includes a keen awareness of strengths and weaknesses of their chosen tools. This statement may seem trivial, however, in the time of open source libraries, out of the box solutions, nearly limitless computing power and time pressure, superficial understanding of modelling and simulation methods can be disastrous. This implicates that we as the community have to provide access and support to well-documented open source implementations, tutorials and workshops. The recent MATHMOD Minisymposium *Model-Based Design of Experiments: Where to go?* is heading in this direction bringing experts from different fields together and taking up the viewpoints of the modelling and the big data community.

REFERENCES

Bouveyron, C. and Brunet-Saumard, C. (2014). Model-based clustering of high-dimensional data: A review. *Computational Statistics & Data Analysis*, 71, 52–78.

Box, G.E.P. and Draper, N.R. (1986). *Empirical Model-building and Response Surface*. John Wiley & Sons, Inc., New York, NY, USA.

Drovandi, C.C., Holmes, C., McGree, J.M., Mengersen, K., Richardson, S., and Ryan, E.G. (2017). Principles of experimental design for big data analysis. *Statistical science : a review journal of the Institute of Mathematical Statistics*, 32(3), 385–404.

Efron, B., Hastie, T., Johnstone, I., Tibshirani, R., Ishwaran, H., Knight, K., Loubes, J.M., Massart, P., Madigan, D., Ridgeway, G., Rosset, S., Zhu, J., Stine, R., Turlach, B., Weisberg, S., Johnstone, I., and Tibshirani, R. (2004). Least angle regression. *Annals of Statistics*, 32(2), 407–499. Cited By 3701.

Fan, J., Han, F., and Liu, H. (2014). Challenges of big data analysis. *National science review*, 1(2), 293–314.

Flassig, R.J. and Sundmacher, K. (2012). Optimal design of stimulus experiments for robust discrimination of biochemical reaction networks. *Bioinformatics*, 28(23), 3089–3096.

Guha, S., Hafen, R., Rounds, J., Xia, J., Li, J., Xi, B., and Cleveland, W.S. (2012). Large complex data: divide and recombine (d&r) with rhipe. *Stat*, 1(1), 53–67.

Hastie, T., Tibshirani, R., and Wainwright, M. (2015). *Statistical learning with sparsity: the lasso and generalizations*. CRC press.

Huang, Z. and Gelman, A. (2005). Sampling for bayesian computation with large datasets.

Kettaneh, N., Berglund, A., and Wold, S. (2005). Pca and pls with very large data sets. *Computational Statistics & Data Analysis*, 48(1), 69–85.

Schenkendorf, R. and Mangold, M. (2013). Online model selection approach based on Unscented Kalman Filtering. *Journal of Process Control*, 23(1), 44–57. doi: 10.1016/j.jprocont.2012.10.009.

Scott, S.L., Blocker, A.W., Bonassi, F.V., Chipman, H.A., George, E.I., and McCulloch, R.E. (2016). Bayes and big data: The consensus monte carlo algorithm. *International Journal of Management Science and Engineering Management*, 11(2), 78–88.

Wang, C., Chen, M.H., Schifano, E., Wu, J., and Yan, J. (2016). Statistical methods and computing for big data. *Statistics and its interface*, 9(4), 399.

Nonlinear rock and roll - Modeling and control of parametric resonances in wave energy devices

Josh Davidson * **Tamas Kalmar-Nagy** ** **Giuseppe Giorgi** *
John V. Ringwood *

* *Centre for Ocean Energy Research, Maynooth University, Ireland (e-mail: josh.davidson@mu.ie).*
** *Dept Fluid Dynamics, Budapest University of Technology and Economics, Hungary (e-mail: kalmarnagy@ara.bme.hu)*

Keywords: Five to ten keywords, preferably chosen from the IFAC keyword list.

1. INTRODUCTION

The concept of resonance is well known in the study of wave energy converters (WECs), with the natural frequency of WECs typically designed to resonate with the external excitation provided by the input wave field. Parametric resonance, on the other hand, has received very little attention, likely due to the complexity of the models required to capture this nonlinear phenomenom, compared to the traditional linear/frequency domain models favoured in WEC research and analysis. This presentation examines the modeling methods available for simulating, analysing and controlling parametric resonances in wave energy devices. The traditional linear hydrodynamic models are discussed and contrasted against nonlinear hydrodynamic modelling approaches, in terms of model fidelity and computational requirements. The effect of the mooring system dynamics on the parametric excitation of the WEC system is discussed and modelling methods reviewed. Finally, the effect of the WEC's power take-off (PTO) system on extracting energy from the WEC and controlling the occurance of parametric resonance is detailed.

2. PARAMETRIC RESONANCE IN WECS

Parametric resonance is a phemonenon caused by the time-varying changes in the parameters of a system (Fossen and Nijmeijer (2011)). While resonance causes the oscillations of a system to grow linearly with time (until damping limits further growth), parametric resonance causes an exponential increase in oscillation amplitude, and can often be unexpected since it is a nonlinear phenomenom not predicted by linear analyses. Parametric resonance has been observed and studied in floating bodies, dating back to the work of Froude (1861) who described that large roll motions occur when a ship's roll natural period is twice the heave/pitch natural period. This parametric coupling between modes of motion has been investigated in offshore engineering fields, where parametric resonance is considered an unwanted problem (with container ships losing cargo due to large parametric roll motions for example), and research focussing on suppression and stabilisation of parametric pitch/roll.

Likewise, parametric resonance has been observed to induce large amplitude pitch/roll motions for WECs, however very little investigation has been undertaken. Babarit et al. (2009) assessed the potential of an advanced numerical model in capturing the nonlinear hydrodynamics of a pitching type WEC, as compared against physical wave tank experiments. Of interest, for wave frequencies close to half the WEC roll natural frequency, parametric roll was observed in the experiments, which was only predicted by advanced nonlinear hydrodynamic models, but not the traditional linear ones. Tarrant and Meskell (2016) investigated the parametric resonance in a 2-body self-reacting WEC, due to the varying centre of mass as the bodies translate relative to each other. Gomes et al. (2017) investigated experimentally how additional damping may surpress the parametric resonance in a spar-bouy type oscillating water column (OWC) WEC. In these studies, the effect of parametric resonance was detrimental to the WEC performance, reducing the power capture as energy was parametrically transferred from the primary mode of motion into other modes.

However, unlike most other offshore applications, the large amplitude motions caused by parametric resonance could also be considered as beneficial for certain types of WECs designed to extract energy from these modes. Olvera et al. (2001) first proposes utilising parametric resonance, for the case of an OWC, whereby the parametric excitation caused by varying the volume of the OWC chamber is investigated (Olvera et al. (2007)). Orazov (2011) and Diamond et al. (2015) propose a class of WEC that utilises parametric resonance by a mass-modulation scheme, whereby the mass of a WEC element is varied in time through control that either varied the added mass or takes on water. In addition to stabilisation, Galeazzi and Pettersen (2012) outlines using control to induce parametric resonance in floating bodies, citing wave energy as one area where this application may be desirable. This topic was also recently debated at the *2017 Maynooth Wave Energy Workshop*, during an open forum discussion session (Clement (2017)).

⋆ This paper is based upon work supported by Science Foundation Ireland under Grant No. 13/IA/1886.

Parametric resonance may therefore be considered either detrimental or beneficial for different types of WECs, and control systems may need to be designed to either mitigate or induce this effect.

3. WEC FORCES AND CONTROL

The forces on the WEC comprise: the force from the fluid, the force from the mooring system and the force from the PTO (in addition to gravity). The modelling of each of these forces and their role in the parametric resonance of a WEC is discussed in this presentation.

3.1 Fluid force

A range of methods have been developed to model the fluid-structure interaction, details of which can be found in Folley (2016). This presentation discusses the traditional linear hydrodynamic modelling techniques, classically used due to computational restrictions in solving the full nonlinear Navier-Stokes set of equations, but which are unable to capture the nonlinear phemonena of parametric resonance. Modifyig these linear modeling techniques to be cast into the form of the classic Mathieu-Hill equation for studying parametric resonance is then discussed. Next, nonlinear potential flow methods are discussed and example results from Giorgi and Ringwood (2018) presented. The role of viscous damping is then discussed, along with methods to model this effect. Finally, the high-fidelity / computationally expensive approaches offered by CFD are explored.

3.2 Mooring force

The role in which the mooring system can serve in either inducing or mitigating parametric resonance, and methods to model these mooring effects, is discussed in this presentation. For example, mooring forces can introduce cross-coupling between the heave and pitch/roll modes of motion, depending on where the mooring line(s) is attached to the WEC. Also, drag forces on the mooring lines can present a large source of energy dissipation from the WEC. These and other effects are discussed in detail, drawing upon the indepth review of the mathematical modelling of mooring systems for WECs given in Davidson and Ringwood (2017).

3.3 PTO force

The PTO system converts the mechanical energy in the WEC into other forms of energy (electric, hydraulic, etc.) via the PTO force. The PTO force can act in a chosen degree of freedom with a specified amplitude and is therefore a useful control input. The role in which the PTO can be used to control parametric resonance in a WEC is explored in this presentation, considering traditional energy maximising control methods for WECs Ringwood et al. (2014), as well as other methods such as nonlinear energy sinks Vakakis et al. (2008).

4. CONCLUSION

A range of mathematical models, spanning the 'model fidelity-computational requirement' plane, are available for the analysis and control of parametric resonance in WECs. Low fidelity models are useful for quick analyses of the stability properties, where as higher fidelity, more computationally heavy, models are useful for evaluation purposes or system identification of lower fidelity models.

REFERENCES

Babarit, A., Mouslim, H., Clément, A., and Laporte-Weywada, P. (2009). On the numerical modelling of the nonlinear behaviour of a wave energy converter. In *Proceedings of the 28th International Conference on Offshore Mechanics & Arctic Engineering*.

Clement, A. (2017). Instabilities of wecs: Good news? bad news? Available at: www.eeng.nuim.ie/coer/past-events/2017-maynooth-wave-energy-workshop/.

Davidson, J. and Ringwood, J.V. (2017). Mathematical modelling of mooring systems for wave energy converters a review. *Energies*, 10(5), 666.

Diamond, C.A., Judge, C.Q., Orazov, B., Savaş, Ö., et al. (2015). Mass-modulation schemes for a class of wave energy converters: Experiments, models, and efficacy. *Ocean Engineering*, 104, 452–468.

Folley, M. (2016). *Numerical Modelling of Wave Energy Converters: State-of-the-Art Techniques for Single Devices and Arrays*. Academic Press.

Fossen, T. and Nijmeijer, H. (2011). *Parametric resonance in dynamical systems*. Springer.

Froude, W. (1861). *On the rolling of ships*. Institution of Naval Architects.

Galeazzi, R. and Pettersen, K.Y. (2012). *Parametric resonance in dynamical systems*, chapter Controlling Parametric Resonance: Induction and Stabilization of Unstable Motions, 305–327. Springer.

Giorgi, G. and Ringwood, J.V. (2018). Analytical formulation of nonlinear froude-krylov forces for pitching point absorbers. In *Submitted to the 37th International Conference on Ocean, Offshore and Arctic Engineering*.

Gomes, R., Malvar Ferreira, J., Ribeiro e Silva, S., Henriques, J., and Gato, L. (2017). An experimental study on the reduction of the dynamic instability in the oscillating water column spar buoy. In *Proceedings of the 12th European Wave and Tidal Energy Conference*.

Olvera, A., Prado, E., and Czitrom, S. (2001). Performance improvement of owc systems by parametric resonance. In *Proceedings of the 4th European Wave Energy Conference*.

Olvera, A., Prado, E., and Czitrom, S. (2007). Parametric resonance in an oscillating water column. *Journal of Engineering Mathematics*, 57(1), 1–21.

Orazov, B. (2011). *A novel excitation scheme for an ocean wave energy converter*. Ph.D. thesis.

Ringwood, J.V., Bacelli, G., and Fusco, F. (2014). Energy-maximizing control of wave-energy converters: The development of control system technology to optimize their operation. *IEEE Control Systems*, 34(5), 30–55.

Tarrant, K. and Meskell, C. (2016). Investigation on parametrically excited motions of point absorbers in regular waves. *Ocean Engineering*, 111, 67–81.

Vakakis, A.F., Gendelman, O.V., Bergman, L.A., McFarland, D.M., Kerschen, G., and Lee, Y.S. (2008). *Nonlinear Targeted Energy Transfer in Mechanical and Structural Systems: I and II*. Springer-Verlag, Berlin and New York.

A dynamic model of a sodium/salt PCM energy storage system

Zebedee Kee, Joe Coventry and John Pye*

Research School of Engineering, Australian National University, Canberra, Australia.
**Tel: +61 2 6125 8778; email: john.pye@anu.edu.au.*

1. BACKGROUND

Thermal energy storage (TES) implemented in Concentrated Solar Power (CSP) addresses the issue of time mismatch between energy demand and supply. With TES, CSP plants can be operated flexibly to ensure power supply matches demand, maximising revenue.

Direct two-tank TES with a molten eutectic mixture of $NaNO_3$ and KNO_3 is the currently dominant commercial choice in CSP. However, chemical stability issues limit operating temperatures which in turn limit the thermal conversion efficiency of the CSP plant's power cycle. It is therefore desirable to explore alternative storage/transport media such as liquid sodium which are suitable for high temperature applications (Coventry et. al. 2015).

In this work, we present a novel TES system involving a sodium heat pipe in direct contact with NaCl PCM. This combination is appealing due to high storage temperatures, low receiver losses and the potentially minimised cost of the storage subsystem.

2. INTRODUCTION

NaCl has a low cost and high melting point of around 1073K, which is also similar to the saturation temperature of sodium heat transfer fluid (HTF) at slightly sub-atmospheric pressures.

A dynamic system model of the HTF-PCM storage within a CSP system was implemented in OpenModelica evaluate key dynamic aspects of the system such as the temperature response of the PCM whilst heat is added/removed from the storage vessel, and movement of liquid sodium between the receiver and storage trays. Several design parameters which include PCM container dimensions, quantities of PCM and HTF material, and charging/discharging rates could then be optimised for maximum exergetic efficiency, and in future, minimum levelised cost of electricity (LCOE).

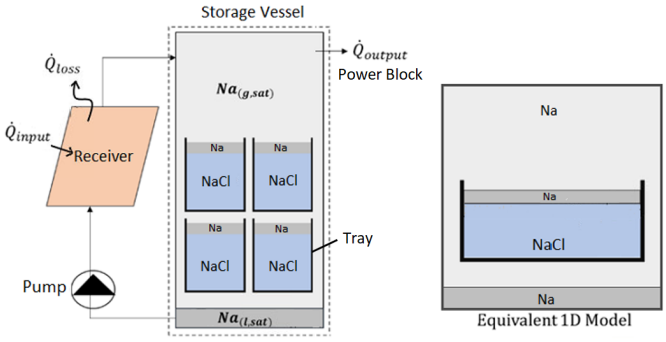

Figure 1: Left: Conceptual design of the TES subsystem. Right: Equivalent model used in simulation.

3. DESIGN CONCEPT

A simplified model of the HTF-PCM configuration includes a storage vessel containing saturated Na liquid-vapour at a temperature T_{Na} in contact with the top surface of the NaCl contained in trays (Figure 1). Heat is delivered to the isochoric vessel via a sodium boiler receiver at T_{Na}, which operates for 6 hours a day and is shut down for the remaining 18 hours. In the 18 hours, heat is discharged from the storage vessel into a Carnot power cycle at T_{Na}.

During the charging process, Na vapour condenses on top of a pool of Na liquid. Excess condensing sodium overflows from the sides of the tray walls to the bottom of the vessel, where it can be pumped back for re-boiling in the receiver. During discharging, liquid sodium is boiled off the top of the PCM surface and must be replenished by pumping from the bottom of the vessel.

4. MODEL ASSUMPTIONS

The sodium HTF was modelled as a single component, two-phase mixture at temperature T_{Na}. T_{Na} is calculated at each time step using specific enthalpy and specific volume constraints and equations provided by Fink and Leibowitz (1995).

The sodium receiver was modelled as an isothermal blackbody cavity receiver with fixed concentration ratio (CR) direct normal irradiance (DNI) for 6 hours each day. During the remaining 18 hours, the system the discharges at a rate $\dot{Q}_{\text{output}}$ which is set to 1/3 of $\dot{Q}_{\text{input}}$ or until the total energy stored by the vessel returned to zero.

During charging, the heat transfer process between HTF and PCM was assumed to be conduction-dominated due to the low Prandtl number of liquid metals, and thus modelled via an extra thermal resistance term. During discharging, the effective thermal resistance of the liquid Na layer was assumed to be zero due to the large heat transfer coefficient associated with pool boiling. The temperature gradient within the liquid Na pool is assumed to be small enough such that the effect on the two-phase Na HTF model is negligible.

Heat transfer within the PCM was modelled using a numerical scheme involving 1D finite-difference, enthalpy formulation with mushy node idealisation (Sharma et. al. 2009; Dutil et. al. 2011). This numerical scheme was described to have relatively simple implementation, with a single governing equation for both solid and liquid phases. All PCM trays were assumed to experience identical heat transfer, and as such, were represented using a single equivalent tray (Figure 1).

The numerical scheme was validated against an exact Neumann solution to the Stefan Problem (Alexiades & Solomon, 1993). The output of the numerical scheme with constant properties was observed to converge to the exact solution as the mesh resolution was increased.

To simulate a real-world TES configuration, the temperature distribution within the PCM was determined at each time-step using a enthalpy-temperature relationship; which was then used to determine temperature-dependent properties such as density ρ (kg/m^3) and thermal conductivity k (W/m·K). Due to the high operating temperature of the system and the semi-transparent characteristic of liquid NaCl, the k values of effective radiative-conductive heat transfer (RCT) were used.

5. EXERGY CALCULATIONS

To obtain a measure of round trip exergy efficiency, the rate of exergy into and out of the HTF-PCM control volume was calculated at each timestep with $T_0 = 300$ K as the reference temperature. The exergy destruction within the PCM (between the nodes) via conduction was also calculated to determine if exergy is destroyed mainly during charging or discharging.

6. MODELICA IMPLEMENTATION

The set of ordinary differential equations with respect to time were solved using OpenModelica with the *dassl* solver with a tolerance of 1×10^{-6}.

Table 1. System design parameters

Parameter	Value
Concentration Ratio	1000
Receiver Area	5×10^{-3} m²
Direct Normal Irradiance, DNI	1000 W/m²
Initial volume of NaCl @ 300K	0.1 m³
Total vessel volume	10.1 m³
Mass of Na	30.0 kg
Initial Temperature of all components	1050 K
Wall	$1.5 \times L_{NaCl}$

The NaCl PCM was assumed to have a uniform cross-sectional area, A_{NaCl} and a depth L_{NaCl}. A parametric study on the effect of L_{NaCl} given constant initial volume was performed to investigate the effect of PCM dimensions on the exergetic performance of the overall storage subsystem.

7. RESULTS

An exergy efficiency X_{out}/X_{in} of 91.9% was achieved using PCM of depth 0.02 m; this decreases to 86.4% at 0.10 m.

At higher PCM depths, a larger temperature difference is required to sustain the heat flux from the HTF to the PCM due to increasing thermal resistance between the HTF and the PCM's melting front. This causes the temperature of the HTF to increase rapidly as heat is added to the system during the charging phase. This leads to increased radiative losses at the receiver and large temperature gradients within the PCM. The large temperature gradients lead to high exergy destruction rates within the PCM.

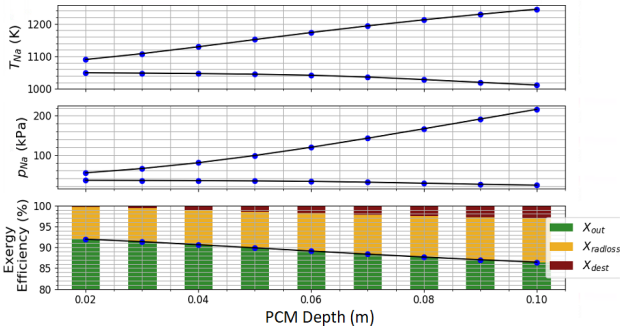

Figure 2: Daily variation in temperatures and pressures and charge-discharge exergy efficiency with respect to PCM tray depth.

A direct consequence of temperature variation in the two-phase equilibrium sodium is the variation in pressure within the storage vessel. Minimising the maximum pressure and pressure variation of the HTF would be advantageous in reducing material costs of the storage vessel and avoiding material fatigue of its components.

8. CONCLUSION AND FURTHER WORK

The depth of the PCM has a significant effect on the daily temperature and pressure variations of the HTF, which in turn affect exergy efficiency of the CSP system. This is consistent with the fact that heat transfer between the HTF and PCM is limited by the heat conduction within the PCM.

The benefit of using thin trays of PCM would be counteracted by the increased material costs needed to fabricate the trays. As such, a cost vs. performance optimisation would allow the best design to be determined.

Further work would involve an annual performance simulation of a complete CSP plant which utilizes the sodium/salt PCM storage concept. Parameters such as PCM depth, ratio of HTF to PCM and different control strategies would be optimized for minimum LCOE.

REFERENCES

Alexiades V, Solomon AD (1993). Mathematical Modelling of Melting and Freezing Processes, Hemisphere Publishing. Corporation, Washington DC.

Coventry J, Andraka C, Pye J, Blanco M, Fisher J (2015). A review of sodium receiver technologies for central receiver solar power plants, *Solar Energy* **122**, pp. 749-762.

Dutil Y, Rousse DR, Salah NB, Lassue S, Zalewsk L (2011), A review on phase-change materials: Mathematical modelling and simulations, *Renewable and Sustainable Energy Reviews* **15**, pp. 112-130.

Fink JK, Leibowitz L (1995). Thermodynamic and Transport properties of Sodium Liquid and Vapor, Argonne National Laboratory, Report no. ANL/RE-95/2.

Sharma A, Tyagi VV, Chen CR, Buddhi D (2009). Review on thermal energy storage with phase change materials and applications, *Renewable and Sustainable Energy Reviews* **13**, pp. 318-345.

Reduction of Metabolic Networks keeping Core Dynamics ⋆

C. López Zazueta, * **O. Bernard,** * **J.L. Gouzé.** *

* *Université Côte d'Azur, Inria, INRA, CNRS, UPMC Univ. Paris 06, BIOCORE team, France (e-mail: claudia.lopez-zazueta@inria.fr, olivier.bernard@inria.fr, jean-luc.gouze@inria.fr).*

Keywords: Metabolic engineering, Model reduction, Quasi Steady State Approximation, Tikhonov Theorem, Biological systems, Microalgae.

1. INTRODUCTION

Metabolic modeling has proved to be a very powerful tool to get a better insight into the metabolism of an organism. This approach has gained accuracy in the last decades, and turns out to be particularly efficient to improve production of target molecules, by understanding biological processes that influence metabolism. In particular, it allows to assess the main fluxes throughout a metabolic network (Baroukh et al., 2014; Nazaret and Mazat, 2008). But resulting models are of high dimension and difficult to use for control purpose.

For example, metabolic modeling has clarified production of triacylglycerols from microalgae and carbohydrates from cyanobacteria (Baroukh et al., 2015). Both compounds can then be turned into biofuel (biodiesel and bioethanol, respectively) with expected reduced environmental impacts (Lardon et al., 2009).

Metabolisms of microalgae and cyanobacteria are driven by the solar flux which supports fixation of CO_2. Periodic fluctuation of light induces instationarity of their metabolisms, with accumulation of metabolites (especially lipids and carbohydrates). Therefore, such metabolisms are never at steady state.

However, most of the approaches dedicated to metabolism analysis assume balanced growth, i.e. Steady State Assumption (SSA), which leads to rough approximations. For instance, Flux Balance Analysis (FBA) (Orth et al., 2010) or Macroscopic Bioreaction Models (MBM) (Provost et al., 2006) are based on linear algebra to solve the equation $M \cdot V = 0$, where M is the stoichiometric matrix and V is the vector of intracellular reaction rates.

Some approaches have attempted to introduce dynamics, for example, assuming that cell optimizes at each time instant an objective criterion using Dynamical Flux Balance Analysis (DFBA) (Mahadevan et al., 2002) or considering external conditions that might change continuously in a hybrid system, as proposed in Kaplan et al. (2009). But all of them address specific processes and a general mathematical framework has never been established.

⋆ Claudia López Zazueta was supported by the National Council of Science and Technology of Mexico through the program CONACYT-SECRETARÍA DE ENERGÍA-SUSTENTABILIDAD ENERGÉTICA 2015.

Furthermore, metabolic models are of high dimension, which makes their mathematical analysis and parameter identification complex. Identifying conditions to maximize productivity by a rigorous mathematical analysis is generally not possible.

Here we propose a method to reduce the dimension of a dynamical metabolic system, which is appropriate to derive model based control strategies. Contrary to nearly all existing works, the idea is to keep some dynamical components of the model, that are necessary especially when dealing with microalgae and cyanobacteria.

A first attempt in this direction was carried out with the DRUM method (Baroukh et al., 2014). This modeling approach considers subnetworks in Quasi Steady State (QSS), which are interconnected by metabolites that can accumulate. Then, Elementary Flux Modes (EFM) are computed in each subnetwork to reduce them using Quasi Steady State Assumption (QSSA). As result, the dynamics of accumulative metabolites form a reduced system of Ordinary Differential Equations (ODE).

DRUM approach has proven to provide sound results, with very efficient representation of accumulation of lipids and carbohydrates in microalgae submitted to light/dark cycles. However, as almost all methods developed for metabolic analysis, it relies on a series of assumptions whose mathematical bases have not been rigorously established. Beyond QSSA, which assumes "fast" and "slow" parts on the metabolism without delimiting them, these approaches also neglect intracellular dilution due to growth.

2. RESULTS AND DISCUSSION

The main objective of our work is to provide mathematical foundations for the reduction of metabolic networks to low dimensional dynamical models. In a first stage, we simplify the problem assuming linear kinetics in a metabolic network. For reducing the system accurately, we propose a dynamical approach that relies on time scale separation and the QSSA.

The reduction of a linear kinetic model, with a continuous input and a constant factor of dilution caused by growth, is analyzed through this method. The system is composed of subnetworks of fast reactions, which are connected by

The proof is omitted due to the limited space. However, it can easily be checked that the sum of the local volume constraint upper bounds equals the global volume constraint upper bound, i.e. $\sum_{l\in\mathcal{L}} V_l = V$.

4. GAME THEORY APPROACH

To determine the failure distribution p_l, we consider the particular case wherein some opponents try to identify the weakest point of the structure. In such worst case scenarios, game theory can be employed to determine the failure distribution while guaranteeing robustness (Holmberg et al., 2017).

The situation can be compared to a penalty shoot-out in a soccer game. There are two players, a kicker and a keeper. The kicker aims at the areas of the goal where it is difficult for the keeper to reach, i.e. the extreme left or right. However, the keeper tries to predict the best action of the kicker and he concludes that the kicker will aim at the goal extremities, which is not convenient for the kicker as his strategy is leaked. As a result, the options of both players converge towards some compromising points.

Similarly, design problems considering unexpected failure can be interpreted as a game between a "failure" player and a "structure" player. The failure player tries to choose the subdomain l that maximizes the structural damage while the structure player tries to limit the amount of material within the targeted areas. In game theory, this is a standard two player zero-sum game. The utility of the failure player is the compliance of the structure after failure and the utility of the structure player is the opposite. The resulting failure distribution p_l can be computed as a mixed Nash equilibrium of the game. The mixed Nash equilibra of two player games can be computed using the Lemke-Hawson algorithm (Papadimitriou, 2007).

5. EXAMPLE AND CONCLUSION

The design problem described in Fig. 1 is solved to exemplify the proposed method. The available amount of material is set to 50% of the design domain which is divided into $L = 8 * 16 = 128$ subdomains. It is assumed that the subdomain loses all its material if a failure occurs.

The failure distribution p_l is first computed from the game theory problem. To reduce computation time, the number of subdomains is reduced to eight. The players have six options since the two subdomains where the load is applied need material to withstand the load. The mixed Nash equilibrium computed by Lemke-Hawson algorithm is not uniform as illustrated in Fig. 2, which means that specific subdomains are targeted by the failure player. The local volume constraint V_l is then computed based on (4). The optimized solution is illustrated in Fig. 3.

This first example illustrates the validity of the proposed approach. Comparing to a standard optimization, the compliance is higher, meaning that the structure is less stiff but it is however more robust against unexpected failure.

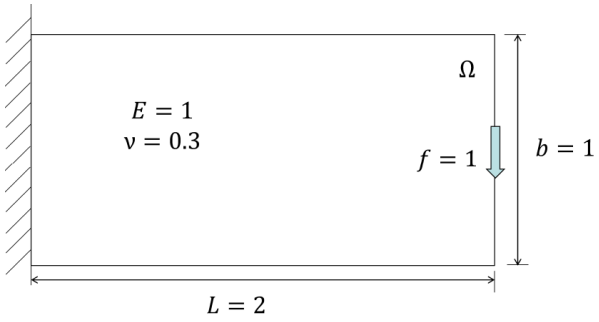

Fig. 1. Design problem description

0	0.5
0	
0	
0	0.5

Fig. 2. Failure probability distribution result

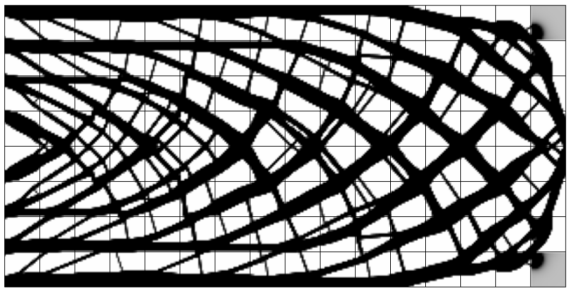

Fig. 3. Optimal robust structure in game situation

REFERENCES

Bendsøe, M. (1989). Optimal shape design as a material distribution problem. *Structural optimization*, 1, 193–202. doi:10.1007/s004190050248.

Holmberg, E., Thore, C.J., and Klarbring, A. (2017). Game theory approach to robust topology optimization with uncertain loading. *Structural and Multidisciplinary Optimization*, 55(4), 1383–1397.

Kawamoto, A., Matsumori, T., Yamasaki, S., Nomura, T., Kondoh, T., and Nishiwaki, S. (2011). Heaviside projection based topology optimization by a pde-filtered scalar function. *Structural and Multidisciplinary Optimization*, 44(1), 19–24. doi:10.1007/s00158-010-0562-2.

Papadimitriou, C.H. (2007). The complexity of finding nash equilibria. In N. Nisan, T. Roughgarden, E. Tardos, and V.V. Vazirani (eds.), *Algorithmic Game Theory*, 29–51. Cambridge University Press, New York, USA.

Rozvany, G., Zhou, M., and Birker, T. (1992). Generalized shape optimization without homogenization. *Structural optimization*, 4(3), 250–252. doi:10.1007/BF01742754.

Tromme, E., Kawamoto, A., and Guest, J.K. (2017). Multiscale topology optimization based on reduction methods for additive manufacturing. *Structural and Multidisciplinary Optimization*, To be submitted.

Wu, J., Aage, N., Westermann, R., and Sigmund, O. (2017). Infill optimization for additive manufacturing – approaching bone-like porous structures. *IEEE Transactions on Visualization and Computer Graphics*, PP(99), 1–1. doi:10.1109/TVCG.2017.2655523.

Design of Robust Structures Against Unexpected Failures

Tatsuya Iwase * **Emmanuel Tromme** * **Atsushi Kawamoto** *

* *Multiphysics Analysis & Design Program, Toyota Central R&D Labs, Aichi, Japan (e-mail: {tiwase;etromme;atskwmt}@mosk.tytlabs.co.jp).*

Keywords: Topology optimization, robustness, local volume constraint, failure, game theory.

1. INTRODUCTION

Enforcing local volume constraints in the design problem turns out to be an efficient approach to increase structural robustness against uncertainties (Wu et al., 2017). By constraining locally the available amount of material, the optimized design exhibits infill patterns which reflects a more uniform and periodic distribution of the material. This method can notably produce results exhibiting bone-like structures which are known to be robust against load uncertainty. Compared to a deterministic approach, the robustness is often achieved at the cost of reducing the component stiffness (Tromme et al., 2017). However, the justification of using local volume constraints has not been well discussed in the context of robust topology optimization. Moreover, no standard methodology exists to determine the local volume constraint upper bound.

This study aims to explain the relationship between robustness and local volume constraints and to propose a method defining the upper bound of local volume constraints for a given failure distribution. To compute the failure probability distribution, a game theory approach is adopted. A standard design problem is solved to illustrate the developed method.

2. ROBUST TOPOLOGY OPTIMIZATION

Standard topology optimization problem is usually formulated as a compliance minimization problem (stiffness maximization) subject to a global volume constraint. Mathematically, the formulation reads

$$\begin{aligned} \underset{\boldsymbol{\phi}}{\text{minimize}} \quad & f_0 = \mathbf{f}^T \mathbf{d} \\ \text{subject to} \quad & \mathbf{K}(\boldsymbol{\phi})\,\mathbf{d} = \mathbf{f}, \\ & \sum_{e\in\Omega} \rho_e(\boldsymbol{\phi})\, v_e \le V, \\ & -1 \le \phi_i \le 1, \quad \forall i \in \Omega, \end{aligned} \tag{1}$$

where Ω is the design domain, $\mathbf{K}$ the stiffness matrix, $\mathbf{d}$ the displacement vector and $\mathbf{f}$ the force vector. The element density and the element volume are represented respectively by ρ_e and v_e. The vector $\boldsymbol{\phi}$ gathers the design variables.

Topology optimization problems are known to be ill-posed and prone to checkerboard issues and mesh dependency. In this paper, the Helmholtz PDE based filter is adopted and introduces the relationship between the design variable $\boldsymbol{\phi}$ and the element density $\boldsymbol{\rho}$ (Kawamoto et al., 2011). To mathematically enforce a 0-1 material distribution, the SIMP interpolation scheme is considered (Bendsøe, 1989; Rozvany et al., 1992).

Ensuring robustness via local volume constraints is straightforward as it simply adds a set of constraints to the design problem (1). Those local constraints are expressed as

$$\sum_{k\in\Omega_l} \rho_k v_k \le V_l, \quad \text{for } l \in \mathcal{L} = \{1 \dots L\}, \tag{2}$$

where L is the number of design domain subdivisions and V_l the upper bound of the subdomain l. The subdivision verifies

$$\bigcup_{l\in\mathcal{L}} \Omega_l = \Omega \quad \text{and} \quad \Omega_i \cap \Omega_j = 0, \text{ for } i \ne j. \tag{3}$$

3. UNEXPECTED FAILURE

The present study focuses on design problems considering unexpected failures. It is assumed that failure arises from an unexpected load other than $\mathbf{f}$ and that the probability distribution of the failure does not depend on the structure nor on the load vector. This situation can occur due to defects in production, accidental impacts during transportation or aged deterioration for instance.

The failure distribution is represented by p_l ($l \in \mathcal{L}$) with $\sum_{l\in\mathcal{L}} p_l = 1$. If the structure undergoes a failure in the subdomain l, the stiffness drops in that region. Therefore, if an algorithm could predict that the subdomain l will have a failure, it would be advantageous to remove material in l and to redistribute it in other subdomains. Hence, the larger failure probability p_l is expected, the smaller amount of material, i.e. the smaller upper bound V_l, should be applied.

The problem is to compute the upper bound V_l based on the given probability distribution p_l. For this purpose, we assume a design process that reallocates uniformly materials in other subdomains. The following lemma summarizes the main achievement of this research as it gives a relationship between the upper bound of the local volume constraints and the probability distribution.

Lemma 1. If the failure distribution p_l is given, the upper bound of the local volume constraint V_l can be computed as

$$V_l = \frac{1-p_l}{L-1} V, \quad \text{for } l \in \mathcal{L}. \tag{4}$$

The proof is omitted due to the limited space. However, it can easily be checked that the sum of the local volume constraint upper bounds equals the global volume constraint upper bound, i.e. $\sum_{l\in\mathcal{L}} V_l = V$.

4. GAME THEORY APPROACH

To determine the failure distribution p_l, we consider the particular case wherein some opponents try to identify the weakest point of the structure. In such worst case scenarios, game theory can be employed to determine the failure distribution while guaranteeing robustness (Holmberg et al., 2017).

The situation can be compared to a penalty shoot-out in a soccer game. There are two players, a kicker and a keeper. The kicker aims at the areas of the goal where it is difficult for the keeper to reach, i.e. the extreme left or right. However, the keeper tries to predict the best action of the kicker and he concludes that the kicker will aim at the goal extremities, which is not convenient for the kicker as his strategy is leaked. As a result, the options of both players converge towards some compromising points.

Similarly, design problems considering unexpected failure can be interpreted as a game between a "failure" player and a "structure" player. The failure player tries to choose the subdomain l that maximizes the structural damage while the structure player tries to limit the amount of material within the targeted areas. In game theory, this is a standard two player zero-sum game. The utility of the failure player is the compliance of the structure after failure and the utility of the structure player is the opposite. The resulting failure distribution p_l can be computed as a mixed Nash equilibrium of the game. The mixed Nash equilibra of two player games can be computed using the Lemke-Hawson algorithm (Papadimitriou, 2007).

5. EXAMPLE AND CONCLUSION

The design problem described in Fig. 1 is solved to exemplify the proposed method. The available amount of material is set to 50% of the design domain which is divided into $L = 8 * 16 = 128$ subdomains. It is assumed that the subdomain loses all its material if a failure occurs.

The failure distribution p_l is first computed from the game theory problem. To reduce computation time, the number of subdomains is reduced to eight. The players have six options since the two subdomains where the load is applied need material to withstand the load. The mixed Nash equilibrium computed by Lemke-Hawson algorithm is not uniform as illustrated in Fig. 2, which means that specific subdomains are targeted by the failure player. The local volume constraint V_l is then computed based on (4). The optimized solution is illustrated in Fig. 3.

This first example illustrates the validity of the proposed approach. Comparing to a standard optimization, the compliance is higher, meaning that the structure is less stiff but it is however more robust against unexpected failure.

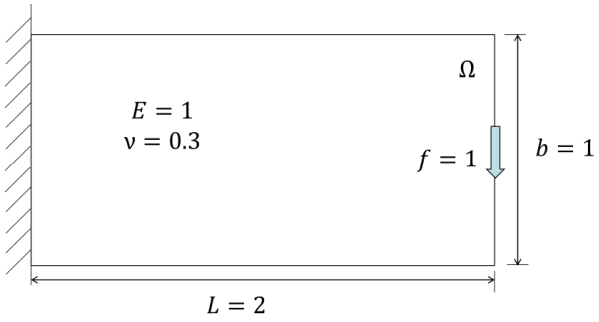

Fig. 1. Design problem description

0	0.5
0	
0	
0	0.5

Fig. 2. Failure probability distribution result

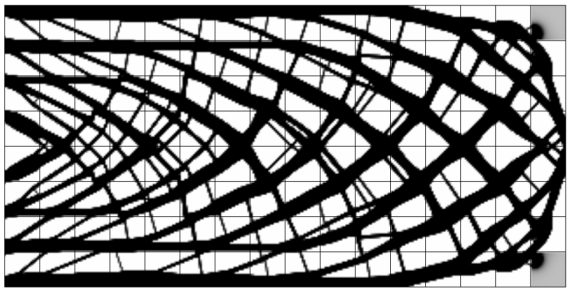

Fig. 3. Optimal robust structure in game situation

REFERENCES

Bendsøe, M. (1989). Optimal shape design as a material distribution problem. *Structural optimization*, 1, 193–202. doi:10.1007/s004190050248.

Holmberg, E., Thore, C.J., and Klarbring, A. (2017). Game theory approach to robust topology optimization with uncertain loading. *Structural and Multidisciplinary Optimization*, 55(4), 1383–1397.

Kawamoto, A., Matsumori, T., Yamasaki, S., Nomura, T., Kondoh, T., and Nishiwaki, S. (2011). Heaviside projection based topology optimization by a pde-filtered scalar function. *Structural and Multidisciplinary Optimization*, 44(1), 19–24. doi:10.1007/s00158-010-0562-2.

Papadimitriou, C.H. (2007). The complexity of finding nash equilibria. In N. Nisan, T. Roughgarden, E. Tardos, and V.V. Vazirani (eds.), *Algorithmic Game Theory*, 29–51. Cambridge University Press, New York, USA.

Rozvany, G., Zhou, M., and Birker, T. (1992). Generalized shape optimization without homogenization. *Structural optimization*, 4(3), 250–252. doi:10.1007/BF01742754.

Tromme, E., Kawamoto, A., and Guest, J.K. (2017). Multiscale topology optimization based on reduction methods for additive manufacturing. *Structural and Multidisciplinary Optimization*, To be submitted.

Wu, J., Aage, N., Westermann, R., and Sigmund, O. (2017). Infill optimization for additive manufacturing – approaching bone-like porous structures. *IEEE Transactions on Visualization and Computer Graphics*, PP(99), 1–1. doi:10.1109/TVCG.2017.2655523.

Parametric Reduction for Simplified Posture Classification Model

Peter Dabnichki*. Arnold Baca, Martin Groeber***, Maria Del Pilar Garcia Souto******

**School of Engineering, RMIT University, Melbourne, 3001, Australia*
(Tel: +61399257278; e-mail: peter.dabnichki@rmit.edu.au)
*** Dept of Biomechanics and Computer Science in Sport, University of Vienna*
A-1150 Vienna, Austria (arnold.baca@univie.ac.at)
**** Dept of Biomechanics and Computer Science in Sport, University of Vienna*
A-1150 Vienna, Austria (martin.groeber@univie.ac.at)
*****Dept of Medical Physics and Biomedical Engineering, University College London*
London, WC1E 6BT, UK, (e-mail: p.garciasouto@ucl.ac.uk)

1. INTRODUCTION

The continuous increase in sedentary work over the last decades has resulted in a higher risk of hypertension, overweight, obesity, diabetes and musculoskeletal problems. Furthermore prolonged seating affects the thermal comfort requirements commonly leading to unhealthy workplace temperatures and conditions (Garcia Souto et al, 2013; Michael et al, 2017).

Traditionally sitting related research has been an area of interest for patients with impaired mobility (Dabnichki & Taktak, 1998). More recently a variety of interventions have been proposed and developed ranging from activity programs aiming to reduce sedentary time to posture recognition tools prompting the user to avoid ergonomically inappropriate postures (Schwartz et al. 2013). To date most posture recognition models have predominantly relied on video based approaches that are controversial for implementation during work and travel..

These models play an essential role in bridging the gap between movement/posture data and static and dynamic analysis of forces occurring. However, all these models require different number of inputs and are not easily applied in practical situations (Dabnichki et al, 1998).

In this work we demonstrate how through model sensitivity analysis we reduce the required inputs, the sampling frequency and inherent complexity of the anthropometric model to develop a simple method of posture recognition. We do not discuss the developed classification that is compliant with ergonomic practice as it is outside the scope of this work.

2. MODEL BUILDING AND COMPLEXITY REDUCTION

The model was built through the use of biomechanical analysis to observe and classify postures using an imaged based system with integrated GRF data collection. The purpose of this process was to reduce the complexity of the model and ultimately eliminate the use of image data. We describe the steps in this process below.

2.1 Combined image and force data collection and analysis

In order to gain better insight into the kinetic trace of the postures considered we mounted an office chair of a force plate and conducted integrated data collection with on-line force analysis.

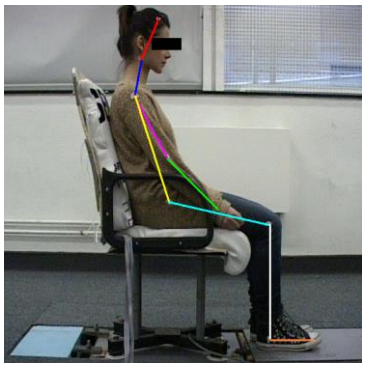

Fig.1. Data collection set-up for automated posture analysis.

which in the simplified model form is

$$\overrightarrow{GRF} \times \overrightarrow{COP} = \overrightarrow{w_1} \times \overrightarrow{COM_1} + \overrightarrow{w_2} \times \overrightarrow{COM_2} + \overrightarrow{w_3} \times \overrightarrow{COM_3} + \overrightarrow{f} \times \overrightarrow{d_f} = 0$$

where we use the standard notation for the ground reaction force, centre of mass and centre of pressure. The w_i indicates the respective weights of the 3 modified segments and f is the generalkised friction force and d_f is the distance of its point of application from the origin of the reference system

2.2 Detailed force analysis

In the second stage of the process we looked into the influence of the position and movement of different parts on the body on the balace of forces and moments (sensitivity analysis) produced some surprising outcomes for us and luckily they were very pleasing.

2.3 Analysis of body balance

Having achieved model reduction we needed to find out whther a posture described this way complies with the two fundamental mechanical principles. i.e. the balance of forces and the balance of moments. Hence it was essential to establish where the imaginary centre of mass should be pllaced. Here we need to point out that the analysis of this assumes 3D coordinates as the medial-lateral movement is considred as adaptive parameter.

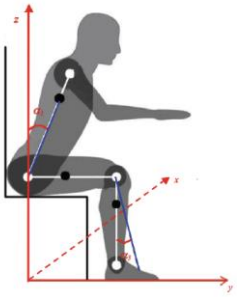

Fig.2. Simplified anthropometric model.

of the centre of mass of the Upper Body Segment (with a small perturbation parameter). Similarly the location of the centre of mass of the Lower Body was assumed to coincide with the location of the centre of mass of the Calves as their mass is an order higher than that of the feet, although there is a slight adjustment made in the sagittal plane.

This reduction means that to build a model for an individual, one needs just height and weight. Accuracy would improve if gender is indicated but it is not a firm requirement. Furthermore depending on the implementation there is a built-in procedure for weight verification so strictly speaking weight input is also optional.

3. MODEL OVERVIEW AND IMPLEMENTATION

The model described in the previous was tested in an on-line automated system in several stages. The first stage was to test it on random samples of the pre-collected data and compare to visual classification already tagged. Again using the existing data an "inverse" simulation was then run to obtain the CoP position based on the visual input from the modified body segments. The reliability criterion was the position of the centre of pressure and whether it is identifiable with the assumed posture.

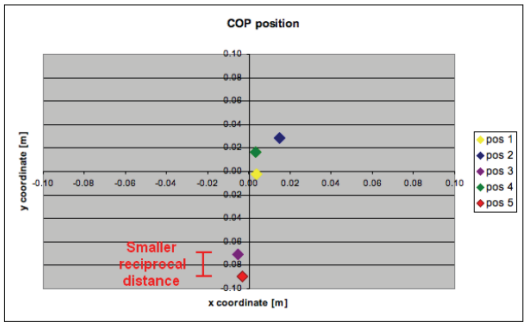

Fig. 3. Position of the centre of pressure on the force plate.

The results yielded for the posture classification proved to be clear and allow unambiguous classification in about 85% of the cases. As already discussed the dominant effect is in the sagittal plane and it is used as the fastest indicator. The

4. SYSTEM CONSTRAINTS AND FURTHER DEVELOPMENT

The results that the current work produced are pleasing as with a small degree of personalisation the accuracy exceeds 90%. However, the algorithm heavily relies on the accuracy of the force data measurement of all 12 force components (and this number cannot be reduced without compromising the COP estimate which in turn will drastically reduce the success rate in posture recognition. From the very beginning we have been well aware that the use of a force plate in everyday environment is neither practical nor likely.

The reduced reliability is likely to prompt us to use more elaborate artificial intelligence based methods combined with system self-calibration. The system is likely to only use the model in the initial assessment and then use a learning algorithm to adapt to the individual behaviour. Still the relatively low frequency of action provides good analytical opportunities to reduce the guessing element in the process of classification. We are also looked into possibility of a chair mounted force plate equivalent to measure the total force.

On the theoretical front we are looking into the topological characterisation of the areas of uncertainty for the key points allocation to reduce the grey areas of uncertain classification. This is particularly important when a new subject is introduced.

REFERENCES

Dabnichki, P. and Taktak D. (1998) Pressure variation under the ischial tuberosity during a push cycle, *Medical Enineering & Physics*, 20(4), 242-56.

Dabnichki, P., Lauder, M., Aritan, S., 1997 Accuracy evaluation of an on-line kinematic system via dynamic tests, *Journal of Medical Engineering & Technology*, 21(2), 53-66,

Garcia-Souto, M. and Dabnichki, P., 2016, Core and local skin temperature: 3-24 months old toddlers and comparison to adults. *Building and Environment*, 104, 286-295

Garcia-Souto M. and Dabnichki P. (2013) Skin temperature distribution and thermoregulatory response during prolonged seating. *Building and Environment*, 69, 14–21

Michael K, Garcia-Souto MDP and Dabnichki, P. (2017) An investigation of the suitability of Artificial Neural Networks for the prediction of core and local skin temperatures when trained with a large and gender-balanced database. Appl Soft Comp, 50, 327-343

Schwartz, B. (2015) Cognitive and biomechanical effects of postural changes in office environments. *Proceeding of the 61th Spring-Congress on the Society for Ergonomics and Work Science*, Karlsruhe, Germany

Design of Optimal RF Pulses for NMR as a Discrete-Valued Control Problem ⋆

Christian Clason * **Carla Tameling** ** **Benedikt Wirth** ***

* *Faculty of Mathematics, Universität Duisburg-Essen, 45117 Essen, Germany (e-mail: christian.clason@uni-due.de)*
** *Institute for Mathematical Stochastics, Universität Göttingen, Goldschmidtstr. 7, 37077 Göttingen, Germany (e-mail: carla.tameling@mathematik.uni-goettingen.de)*
*** *Applied Mathematics, Universität Münster, Einsteinstr. 62, 48149 Münster, Germany (e-mail: benedikt.wirth@uni-muenster.de)*

Keywords: multibang control, convex relaxation, semismooth Newton, Bloch equation, NMR

1. INTRODUCTION

Designing optimal radiofrequency (RF) pulses for nuclear magnetic resonance (NMR) imaging consists of driving a collection of spin systems using external electromagnetic fields of minimal energy to a desired spin state. However, in some cases the hardware only allows a discrete set of pulse phases and amplitudes. In contrast to methods based on quantization (Dridi et al., 2015), we aim to compute such pulses by solving a suitable optimal control problem.

A standard model for NMR is given by the Bloch equation in a rotating reference frame without relaxation, i.e.,

$$\frac{\mathrm{d}}{\mathrm{d}t}\mathbf{M}^{(\omega)}(t) = \mathbf{M}^{(\omega)}(t) \times \mathbf{B}^{(\omega)}(t)\,, \quad \mathbf{M}^{(\omega)}(0) = \mathbf{M}_0,$$

which describes the temporally evolving magnetization $\mathbf{M}^{(\omega)} \in \mathbb{R}^3$ of an ensemble of spins rotating at the same resonance offset frequency ω (called *isochromat*), starting from a given equilibrium magnetization $\mathbf{M}_0 \in \mathbb{R}^3$ (e.g., aligned to a strong external field). The time-varying effective magnetic field $\mathbf{B}^{(\omega)}(t)$ is of the form

$$\mathbf{B}^{(\omega)}(t) = (\omega_x(t), \omega_y(t), \omega)^T,$$

where $u(t) := (\omega_x(t), \omega_y(t)) \in \mathbb{R}^2$ can be controlled. The aim is to achieve a magnetization $\mathbf{M}^{(\omega)}(T) = \mathbf{M}_d^{(\omega)}$ within the time interval $\Omega = [0, T]$ for a list of offset frequencies $\omega_1, \dots, \omega_J$ using control values $u(t)$ from a discrete set

$$\mathcal{M} = \left\{ \begin{pmatrix} 0 \\ 0 \end{pmatrix}, \begin{pmatrix} \omega_0 \cos\theta_1 \\ \omega_0 \sin\theta_1 \end{pmatrix}, \dots, \begin{pmatrix} \omega_0 \cos\theta_M \\ \omega_0 \sin\theta_M \end{pmatrix} \right\}$$

for a fixed amplitude $\omega_0 > 0$ and $M > 2$ equi-distributed phases $0 \le \theta_1 < \ldots < \theta_M < 2\pi$.

Introducing the control space $U := L^2(0, T; \mathbb{R}^2)$, the control-to-state operator

$$S : U \to (\mathbb{R}^3)^J, \qquad u \mapsto \left[\mathbf{M}^{(\omega_1)}(T), \dots, \mathbf{M}^{(\omega_J)}(T)\right],$$

and the target vector $z := [\mathbf{M}_d^{(\omega_1)}, \dots, \mathbf{M}_d^{(\omega_J)}]^T \in (\mathbb{R}^3)^J$, this problem can be formulated as an optimal control problem

$$\min_{u \in U} \frac{1}{2}\|S(u) - z\|_2^2 + \int_0^T g(u(t))\,\mathrm{d}t. \tag{1}$$

Here, $g : \mathbb{R}^2 \to [0, \infty]$ is a vector-valued version of the *multi-bang penalty* from Clason and Kunisch (2014, 2016) that can be motivated as the convex hull of the non-convex penalty $\frac{\alpha}{2}|\cdot|_2^2 + \delta_{\mathcal{M}}$, where $\delta_{\mathcal{M}}$ denotes the indicator function in the sense of convex analysis, and can thus be expected to promote controls with values only in $\mathcal{M}$. The main advantage of this formulation is that it leads to a convex optimization problem that can be efficiently solved using a semismooth Newton method (Clason et al., 2016).

2. CONVEX ANALYSIS FRAMEWORK

Standard arguments from convex analysis and on the continuity and differentiability of S yield the following results.

Theorem 2.1. There exists a solution $\bar{u} \in U$ to (1)

Theorem 2.2. Let $\bar{u} \in U$ be a local minimizer of (1). Then there exists a $\bar{p} \in U$ satisfying

$$\begin{cases} -\bar{p} = S'(\bar{u})^*(S(\bar{u}) - z) =: \mathcal{F}'(\bar{u}), \\ \bar{u}(t) \in \partial g^*(\bar{p}(t)) \quad \text{a.e. } t \in [0, T]. \end{cases} \tag{2}$$

Here, $S'(u)^*$ denotes the adjoint of the Fréchet derivative of S, which can be computed as the solution of the adjoint Bloch equation, and ∂g^* denotes the convex subdifferential of the Fenchel conjugate of g, which will be specified below.

For the numerical solution, we also require the Moreau–Yosida regularization

$$\begin{cases} -p_\gamma = S'(u_\gamma)^*(S(u_\gamma) - z) = \mathcal{F}'(u_\gamma), \\ u_\gamma(t) = h_\gamma(p_\gamma(t)) \quad \text{a.e. } t \in [0, 1], \end{cases} \tag{3}$$

where

$$h_\gamma := (\partial g^*)_\gamma = \frac{1}{\gamma}(\mathrm{Id} - \mathrm{prox}_{\gamma g^*})$$

and $\mathrm{prox}_{\gamma g^*} = (\mathrm{Id} - \gamma \partial g^*)^{-1}$ denotes the (single-valued and Lipschitz-continuous) proximal mapping of g^*.

⋆ CC is supported by the German Science Fund (DFG) under grant CL 487/1-1. CT gratefully acknowledges support by the DFG Research Training Group 2088 Project A1. BW's research was supported by the Alfried Krupp Prize for Young University Teachers awarded by the Alfried Krupp von Bohlen und Halbach-Stiftung. The work was also supported by the Deutsche Forschungsgemeinschaft (DFG), Cells-in-Motion Cluster of Excellence (EXC1003 – CiM), University of Münster, Germany.

3. MULTIBANG PENALTY

Letting $\bar{u}_i$, $i = 0, \dots, M$, denote the admissible control values in $\mathcal{M}$ (with $\bar{u}_0 = 0$), we obtain from the definition of the Fenchel conjugate and the maximum rule for the subdifferential by straightforward if tedious computation the following explicit characterization for $q := p(t)$:

$$\partial g^*(q) = \begin{cases} \{\bar{u}_i\} & q \in Q_i, \\ \operatorname{co}\{\bar{u}_{i_1}, \dots, \bar{u}_{i_k}\} & q \in Q_{i_1 \dots i_k}. \end{cases}$$

Together with (2) this yields that apart from singular cases corresponding to the second line, the optimal control $\bar{u}$ will indeed take on values from the admissible set. The sets Q_i can be characterized using polar coordinates; here we only illustrate their distribution in Fig. 1a.

Similarly, we obtain for the Moreau–Yosida regularization

$$h_\gamma(q) = \begin{cases} 0 & q \in Q_0^\gamma, \\ \bar{u}_i & q \in Q_i^\gamma, \\ \left(\frac{\langle q, \bar{u}_i \rangle}{\gamma \omega_0^2} - \frac{\alpha}{2\gamma}\right) \bar{u}_i & q \in Q_{0,i}^\gamma, \\ \frac{\bar{u}_i + \bar{u}_{i+1}}{2} + \frac{\langle q, \bar{u}_i - \bar{u}_{i+1} \rangle (\bar{u}_i - \bar{u}_{i+1})}{\gamma |\bar{u}_i - \bar{u}_{i+1}|_2^2} & q \in Q_{i,i+1}^\gamma, \\ \frac{q}{\gamma} - \frac{\alpha}{\gamma} \left(\frac{\omega_0}{|\bar{u}_i + \bar{u}_{i+1}|_2}\right)^2 (\bar{u}_i + \bar{u}_{i+1}) & q \in Q_{0,i,i+1}^\gamma, \end{cases}$$

with the subdomains Q_i^γ illustrated in Fig. 1b.

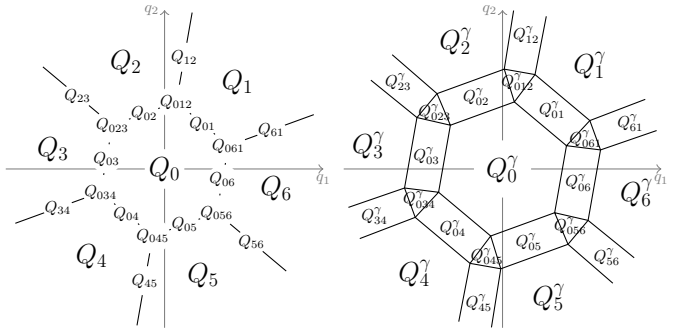

(a) ∂g^* (b) h_γ

Fig. 1. Subdomains for radially distributed $\mathcal{M}$, $M = 6$

4. NUMERICAL SOLUTION

Introducing the superposition operator $H_\gamma : U \to U$ via $[H_\gamma(p)](t) = h_\gamma(p(t))$, we can write (3) in reduced form as

$$u_\gamma - H_\gamma(\mathcal{F}'(u_\gamma)) = 0.$$

Since h_γ is Lipschitz continuous and piecewise differentiable and the range of $S'(u)^* \subset L^\infty(0, T; \mathbb{R}^2)$, this is a Newton-differentiable equation. Taking

$$D_N h_\gamma(q) = \begin{cases} 0 & q \in Q_i^\gamma, \\ \frac{\bar{u}_i \bar{u}_i^T 1}{\gamma \omega_0^2} & q \in Q_{0,i}^\gamma, \\ \frac{(\bar{u}_i - \bar{u}_{i+1})(\bar{u}_i - \bar{u}_{i+1})^T}{\gamma |\bar{u}_i - \bar{u}_{i+1}|_2^2} & q \in Q_{i,i+1}^\gamma, \\ \frac{1}{\gamma} \operatorname{Id} & q \in Q_{0,i,i+1}^\gamma, \end{cases}$$

the corresponding superposition operator $D_N H_\gamma(p)$ leads to a superlinearly convergent semismooth Newton method

$$\left(\operatorname{Id} - D_N H_\gamma(\mathcal{F}'(u^k)) \mathcal{F}''(u^k)\right) \delta u = -u^k + H_\gamma(\mathcal{F}'(u^k)),$$

which can be realized using a matrix-free Krylov method such as GMRES (where $\mathcal{F}''(u)$ can be computed using the solution of two linearized (adjoint) Bloch equations).

5. NUMERICAL EXAMPLES

Figure 2 illustrates the above approach for the simultaneous control of $J = 4$ isochromats with from $\mathbf{M}_0 = (0, 0, 1)^T$ to $\mathbf{M}_d^{(\omega_j)} = (0, 0, 1)$ for $j = 3$, $\mathbf{M}_0$ else, and $M = 6$ admissible values with equidistant phases (marked with dashed lines in Fig. 2a), where the implementation of the discrete (linearized) Bloch and adjoint equations is taken from Aigner et al. (2015). For more details and examples, see Clason et al. (2016).

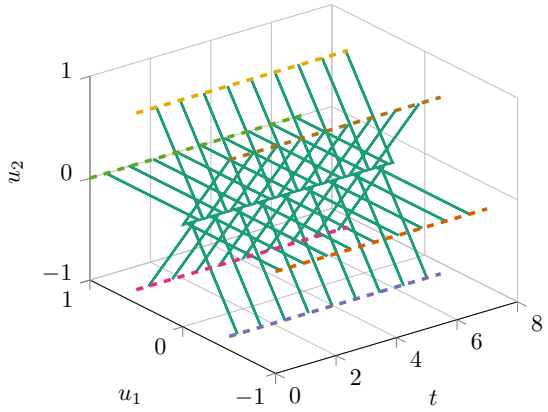

(a) control $\tilde{u}(t)$

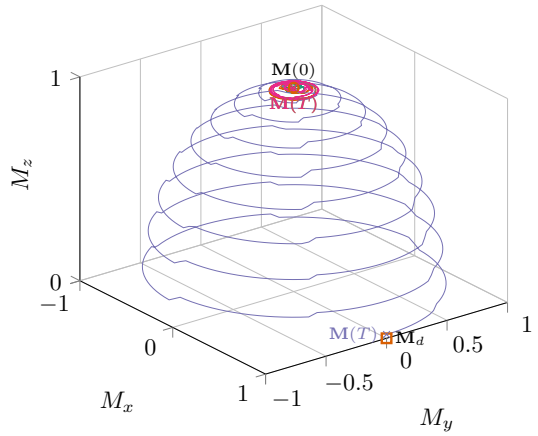

(b) state $\mathbf{M}_u^{(\omega_j)}(t)$

Fig. 2. Optimal control and state for $M = 6$, $J = 4$

REFERENCES

Aigner, C.S., Clason, C., and Rund, A. (2015). rfcontrol. doi:10.5281/zenodo.31187.

Clason, C. and Kunisch, K. (2014). Multi-bang control of elliptic systems. *Annales de l'Institut Henri Poincaré (C) Analyse Non Linéaire*, 31(6), 1109–1130. doi:10.1016/j.anihpc.2013.08.005.

Clason, C. and Kunisch, K. (2016). A convex analysis approach to multi-material topology optimization. *ESAIM: Mathematical Modelling and Numerical Analysis*, 50(6), 1917–1936. doi:10.1051/m2an/2016012.

Clason, C., Tameling, C., and Wirth, B. (2016). Vector-valued multibang control of differential equations. *arXiv*. URL `https://arxiv.org/abs/1611.07853`.

Dridi, G., Lapert, M., Salomon, J., Glaser, S.J., and Sugny, D. (2015). Discrete-valued-pulse optimal control algorithms: Application to spin systems. *Physical Review A*, 92(4), 043417. doi:10.1103/PhysRevA.92.043417.

Industrial Group Production Program under market uncertainty ⋆

Dorota Bochnacka *

* *Faculty of Management and Computer Modelling*
Kielce University of Technology Poland, 25-314 Kielce, Poland
(e-mail: dbochnacka@tu.kielce.pl).

Keywords: optimal control, industrial group

1. INTRODUCTION

The effects of globalization, such as the development of economies, free movement of capital, whether the increase in competitiveness is forcing companies to adjust strategy to rapidly changing environmental conditions. One of the ways to achieve market success and maintain a competitive position is cooperating with others enterprises.

In this work, we are concentrated on an industrial group with vertical cooperation in which, legally and economically independent companies of different stages of the technological chain are working together in the direction of production cost reduction, setting transfer price for goods and services, and impact on the final consumer (see Fernandez-Olmos et al. (2016)).

The goal of the work is to define of those conditions of cooperation of the group members which could ensure their stable functioning and economic development and could maximize economic efficiency on the long-term planning horizon under uncertain behavior of consumers.

2. OPTIMAL COOPERATION PROBLEM

Let us consider some industrial group on a cooperation interval $[t_0, t_1]$, where t_0 and t_1 are the initial and final moments of cooperation ($t_0 \leq t_1, [t_0, t_1] \subset \mathbb{R}_+$). Let $j \in \{1, 2, ..., K\}$. This structure includes the vertical cooperation of k members. Each member acquires the necessary resources and has production facilities. The manufacturing activity of the group is considered on product and consumer markets. We assume that the production does not bring the loss to j^{th} member of the group, $j \in \{1, 2, ..., K\}$, when its selling price covers the manufacturing costs as well as that the overall production does not exaggerate the market demand.

Each member of the group tries to improve own economic situation and to increase profit. Analyzing the internal and external characteristics, we have noticed the following. There exist some parameters, for example, the products internal transfer prices, which present the antagonistic interests of the members of the group, and therefore these values have an effect not only on the profit of each group's member but also on the decision of cooperation and economic efficiency on the planning horizon. Moreover, the uncertainty of market characteristics constrains the economic activities of the group as well as of each its member.

The problem of the maximizing of economic efficiency on long-term planning horizon $[t_0, t_1]$ can be formulated as the task of the functional maximization with respect to control variables $u(t)$ ($x_j \in \varepsilon, u \in U$, ε and U are some spaces)

$$\pi_j(t_1) = \max_{\mathbf{u} \in U} \sum_{j=1}^{K} [J_j(x_j(\cdot), u(\cdot))] \tag{1}$$

s.t.

$$x_j(t) = \mathbb{T}(t, x_j(t), u(t)) \tag{2}$$

$$\Psi_j^1(x_j(t_0), x_j(t_1)) \leq 0 \tag{3}$$

$$\Psi_j^2(x_j(t_0), x_j(t_1)) = 0 \tag{4}$$

$$g_j^k(t, x_j(t)) \leq 0, k = 1, 2, ..., \ell_1^{(j)} \tag{5}$$

$$\phi_j^m(t, u(t)) \leq 0, m = 1, 2, ..., \ell_2^{(j)} \tag{6}$$

where $\mathbb{T}(t, x_j(t), u(t))$ is a differential operator of the mathematical model describing the economic situation $x_j(t) \in \mathbb{R}$ of j^{th} member of group, $\Psi_j^1 : \mathbb{R} \times \mathbb{R} \to \mathbb{R}^{n_1^{(j)}}$ and $\Psi_j^2 : \mathbb{R} \times \mathbb{R} \to \mathbb{R}^{n_2^{(j)}}$ are the terminal constraints; $g_k^{(j)} : \mathbb{R} \times \mathbb{R} \to \mathbb{R}^{\ell_1^{(j)}}$ are phase constraints; $\phi_m^{(j)} : \mathbb{R} \times \mathbb{R}^r \to \mathbb{R}^{\ell_2^{(j)}}$ are the control constraints; $n_1^{(j)}, n_2^{(j)}, \ell_1^{(j)}, \ell_2^{(j)}, r \in \mathbb{N}$.

The solution of the optimal control problem (1) – (6) depends on the model selection for each its expression. Bochnacka and Filatova (2017) studied the case of the two-enterprises group. The stochastic differential equation with fractional Brownian motion was used as the mathematical model describing the economic situation $x_j(t)$. Taking into account the theoretical results proposed by Filatova et al. (2010) the necessary optimality conditions were formulated. Since the real economic situation is more complex, the incorporation of the market uncertainty would allow to check the reaction (a kind of sensitivity) of the economic situation. For this purpose, we propose to take into account the consumers behavior.

3. MODEL OF CONSUMER BEHAVIOR

Having in mind the external influence of the product market, it is assumed that the value of total sales of the

⋆ This paper was supported by Ministry of Science and High Education of Poland, project 04.0.09.00/2.01.01.02.0015 MNSC.ZKEZ.17.

group during given period $[t_0, t_1]$ depends on demand and, by implication, on quantity of consumers willing to buy products, on their behavior and decision.

Filatova et al. (2016) proposed the model of consumer behavior, which can be implemented through the composition of individual choices over two alternative policies – Rawlsian maximin and Harsanyian utilitarianism. Analysis of similar conceptual and mathematical models describing the social preferences pointed out the possibilities of the consumer behavior dynamics' description omitting any specific analysis of decision-making mechanisms.

Here we suppose that the number of consumers willing to buy the products of the group at some moment of time $t \in [t_0, t_1]$ is $y(t) > 0$, $y(t) \in \mathbb{R}_+$. The consumers are subdivided into different classes according to the policy of its members. Each consumer can choose (and change or stay with his/her decision later) a situation that favors the less well-off possibly in detriment of the most well-off (first group, "maximin"), or wants to maximize the average distribution of wealth (second group, mean utilitarianism or "maximean"), or finally desires to maximize most well-off, possibly to the detriment of the less well-off, especially if it maximizes the general well-off (third group, which can label "maximax" and corresponds to some classical form of unqualified utilitarianism). In this case, consumers can be defined through:

$$y(t) = y^{(1)}(t) + y^{(2)}(t) + y^{(3)}(t) \tag{7}$$

where $y^{(\ell)}(t) \geq 0$, $y^{(\ell)}(t) \in \mathbb{R}_+$, represents the cardinality of ℓ^{th} group, $\ell = 1, 2, 3$.

As one can see, there exist six possibilities for change. Let the members of each group change their strategies with six different intensities. These intensities depend on social preference, risk aversion or other exogenous factors such as culture, etc.). We denote these parameters as γ_{ij}, which corresponds to exchange between i and j, $i, j = 1, 2, 3$. The passage of individuals from the group to group usually occurs as a result of interpersonal contacts among individuals or other factors which make an individual change the preferences. This phenomenon cannot be measured directly.

Taking into consideration the characteristics of the consumers mentioned above, the dynamic model of consumer behavior can be written as the system of ordinary differential equations:

$$\begin{aligned} dy^{(1)}(t) &= [-(\gamma_{21} - \gamma_{12})y^{(1)}(t)y^{(2)}(t) && (8)\\ &\quad +\gamma_{23}y^{(3)}(t) - \gamma_{32}y^{(1)}]dt, && (9)\\ dy^{(2)}(t) &= [(\gamma_{21} - \gamma_{12})y^{(1)}(t)y^{(2)}(t) && (10)\\ &\quad -(\gamma_{32} - \gamma_{23})y^{(2)}(t)y^{(3)}(t)]dt, && (11)\\ dy^{(3)}(t) &= [(\gamma_{32} - \gamma_{23})y^{(2)}(t)y^{(3)}(t) && (12)\\ &\quad -\gamma_{23}y^{(3)}(t) + \gamma_{32}y^{(1)}(t)]dt, && (13) \end{aligned}$$

with $y^{(\ell)}(t_0) = y_0^{(\ell)}$.

Associating with each class $y^{(\ell)}(t)$ some purchasing power $a_j^{(\ell)}$, $j = 1, 2, ..., K$, the demand on the production can be presented as some function

$$d_j(t) = \xi(t, \sum_{\ell=1}^{3} a_j^{(\ell)} y^{(\ell)}(t)), j = 1, 2, ..., K. \tag{14}$$

Under these assumptions the formulation of the problem of the maximizing of economic efficiency under conditions of dynamic demand on production is the same as in previous case, however one of groups of the phase constraints (5), which take a form

$$x_j(t) - d_j(t) \leq 0 \ \forall t \in [t_0, t_1], j = 1, 2, ..., K. \tag{15}$$

requires particular attention due to complex behavior near the equilibrium points of (8).

4. CONCLUSIONS

An industrial group, consisting of two enterprises with vertical cooperation, is considered. We assume that both enterprises, having necessary production capacities, act on the product markets once as the partners and once as the independent actors. The main problem of this kind of cooperation is to find the optimal conditions for the production programs for both enterprises, or in other words, it is necessary to find the solution of task (1) – (6) under different conditions of the consumer's behavior. The possible way of the mathematical problem formulation, as well as its relation to the optimal control problem, is the essence of this work. The theoretical backgrounds for the solution of the optimal cooperation production program are developed using the Dubovitski-Milyutin method.

In the further stages of the research, issues related to determining the determinants of vertical cooperation will be introduced, which should contribute to the formulation of more precise models of cooperating enterprises and their optimal management.

REFERENCES

Bochnacka, D. and Filatova, D. (2017). Necessary optimality conditions for enterprises production programs. In *The International Conference of Information and Digital Technologies 2017*, 61–65.

Fernandez-Olmos, M., Dejo-Oricain, N., and Rosell-Martinez, J. (2016). Product differentiation strategy and vertical integration: an application to the doc rioja wine industry. *Journal of Business Economics and Management*, 17(5), 796–809.

Filatova, D., Bourgeois-Gironde, S., Baratgin, J., Jamet, F., and Shao, J. (2016). Cycles of maximin and utilitarian policies under the veil of ignorance. *Mind & Society*, 15(1), 105–116.

Filatova, D., Grzywaczewski, M., and Osmolovskii, N. (2010). Optimal control problem with an integral equation as the control object. *Nonlinear Analysis: Theory, Methods and Applications*, 72(3), 1235 – 1246.

Structure-preserving Model Reduction of Hamiltonian Systems for Linear Elasticity

Patrick Buchfink *

* *Institute of Applied Analysis and Numerical Simulation, University of Stuttgart, Pfaffenwaldring 57, 70569 Stuttgart, Germany.*

Keywords: Symplectic model reduction, linear elasticity, Hamiltonian system, Proper Symplectic Decomposition.

1. INTRODUCTION

The goal of this paper is to apply model reduction techniques that preserve the Hamiltonian structure (see e.g. Maboudi Afkham and Hesthaven (2016)) to a high-dimensional, linear elasticity model. The Hamiltonian structure of a linear elasticity model is presented and the structure-preserving model reduction is introduced. Further, two structure-preserving model reduction techniques are compared to a technique that does not preserve the Hamiltonian structure in a numerical experiment.

2. HIGH-DIMENSIONAL MODEL

2.1 Second-order formulation

The model for two-dimensional linear elasticity is derived from a geometrically linear, small strain formulation. The Lamé constants $\lambda_\mathrm{L}, \mu_\mathrm{L} \in \mathbb{R}$ with $\mu_\mathrm{L} > 0$, $3\lambda_\mathrm{L}+2\mu_\mathrm{L} > 0$ are used to describe the linear elastic material behavior. Additionally, nondimensionalization is applied. This results in a dimensionless Lamé–Navier initial boundary value problem. Application of the Finite Element Method (FEM) with a triangular grid and linear shape functions yields the initial value problem of size $n \in \mathbb{N}$ which describes the evolution of the unknown, parameter-dependent, displacement field $\boldsymbol{q} : [t_0, t_\mathrm{e}] \times \mathcal{P} \to \mathbb{R}^n$ with

$$\boldsymbol{M}\frac{\mathrm{d}^2}{\mathrm{d}t^2}\boldsymbol{q}(t,\boldsymbol{\mu}) + \boldsymbol{K}(\boldsymbol{\mu})\boldsymbol{q}(t,\boldsymbol{\mu}) = \boldsymbol{f}(t), \tag{1}$$

with the initial value conditions

$$\boldsymbol{q}(t_0,\boldsymbol{\mu}) = \boldsymbol{q}_0, \qquad \frac{\mathrm{d}}{\mathrm{d}t}\boldsymbol{q}(t_0,\boldsymbol{\mu}) = \boldsymbol{v}_0 \tag{2}$$

where $\boldsymbol{\mu} = [\lambda_\mathrm{L}, \mu_\mathrm{L}]^\mathsf{T} \in \mathcal{P}$ are the parameters from the parameter space $\mathcal{P} \subset \mathbb{R}^2$, $\boldsymbol{M} \in \mathbb{R}^{n\times n}$ is the mass matrix, $\boldsymbol{K}(\boldsymbol{\mu}) \in \mathbb{R}^{n\times n}$ is the parameter-dependent stiffness matrix, $\boldsymbol{f}(t)$ is the force vector, $\boldsymbol{q}_0 \in \mathbb{R}^n$ is the initial displacement, and $\boldsymbol{v}_0 \in \mathbb{R}^n$ is the initial velocity at the initial time $t_0 \in \mathbb{R}$. The final time is denoted with $t_\mathrm{e} \in \mathbb{R}$. The parameters $\boldsymbol{\mu}$ are assumed fixed during a single simulation. The parameter-dependence is only denoted if required in the following which is why we abbreviate $\boldsymbol{K} = \boldsymbol{K}(\boldsymbol{\mu})$, $\boldsymbol{q}(t) = \boldsymbol{q}(t,\boldsymbol{\mu})$.

2.2 Hamiltonian formulation

In order to derive a Hamiltonian formulation of the system, the force vector $\boldsymbol{f}(t) = \boldsymbol{f}$ has to be constant. The second-order system (1) is rewritten in terms of a first-order system with the linear momentum $\boldsymbol{p}(t) = \boldsymbol{M}\frac{\mathrm{d}}{\mathrm{d}t}\boldsymbol{q}(t)$ and the state vector $\boldsymbol{x}(t) = [\boldsymbol{q}^\mathsf{T}(t), \boldsymbol{p}^\mathsf{T}(t)]^\mathsf{T}$. The corresponding *Hamilton's equation* reads

$$\frac{\mathrm{d}}{\mathrm{d}t}\boldsymbol{x}(t) = \mathbb{J}_{2n}\nabla_{\boldsymbol{x}}\mathcal{H}(\boldsymbol{x}(t)) = \mathbb{J}_{2n}(\boldsymbol{H}\boldsymbol{x}(t) + \boldsymbol{h}), \tag{3}$$

$$\boldsymbol{x}(t_0)) = \boldsymbol{x}_0 = [\boldsymbol{q}_0^\mathsf{T}, \boldsymbol{v}_0^\mathsf{T}]^\mathsf{T} \tag{4}$$

with the definitions

$$\mathbb{J}_{2n} = \begin{bmatrix} \boldsymbol{0}_n & \boldsymbol{I}_n \\ -\boldsymbol{I}_n & \boldsymbol{0}_n \end{bmatrix}, \quad \boldsymbol{H} = \begin{bmatrix} \boldsymbol{K} & \boldsymbol{0}_n \\ \boldsymbol{0}_n & \boldsymbol{M}^{-1} \end{bmatrix}, \quad \boldsymbol{h} = \begin{bmatrix} -\boldsymbol{f} \\ \boldsymbol{0}_{n\times 1} \end{bmatrix} \tag{5}$$

and the corresponding *Hamiltonian function*

$$\mathcal{H}(\boldsymbol{x}) = 1/2\ \boldsymbol{x}^\mathsf{T}\boldsymbol{H}\boldsymbol{x} + \boldsymbol{x}^\mathsf{T}\boldsymbol{h} \tag{6}$$

where $\boldsymbol{0}_n \in \mathbb{R}^{n\times n}$ is the matrix and $\boldsymbol{0}_{n\times 1} \in \mathbb{R}^n$ the vector of all zeros and $\boldsymbol{I}_n \in \mathbb{R}^{n\times n}$ is the identity matrix.

An essential feature of the definition of Hamilton's equation is that the Hamiltonian function is preserved along the solution, i.e. $\frac{\mathrm{d}}{\mathrm{d}t}\mathcal{H}(\boldsymbol{x}(t)) = 0$, where $\boldsymbol{x}(t)$ is the solution of the Hamiltonian system (3).

3. STRUCTURE-PRESERVING MODEL REDUCTION

3.1 Motivation

The size $2n$ of the system (3) is in general high which is why the model is called high-dimensional model. Multiquery scenarios or real-time application require model reduction techniques. The goal of the structure-preserving model reduction is to derive a reduced system that preserves the Hamiltonian structure of the system (3). To this end, the full state vector $\boldsymbol{x} \in \mathbb{R}^{2n}$ is approximated with a low-dimensional state $\widehat{\boldsymbol{x}} \in \mathbb{R}^{2k}$ of size $2k$ where $k \in \mathbb{N}$ and $k \ll n$. A reduced order basis (ROB) $\boldsymbol{V} \in \mathbb{R}^{2n\times 2k}$ is used for the approximation

$$\boldsymbol{x}(t) \approx \boldsymbol{V}\widehat{\boldsymbol{x}}(t). \tag{7}$$

The ROB is chosen to be *symplectic matrix*, i.e.

$$\boldsymbol{V}^\mathsf{T}\mathbb{J}_{2n}\boldsymbol{V} = \mathbb{J}_{2k}. \tag{8}$$

If the ROB is symplectic, the existence of its *symplectic inverse* $\boldsymbol{V}^+ = \mathbb{J}_{2k}^\mathsf{T}\boldsymbol{V}^\mathsf{T}\mathbb{J}_{2n} \in \mathbb{R}^{2k\times 2n}$ with $\boldsymbol{V}^+\boldsymbol{V} = \boldsymbol{I}_{2k}$ is guaranteed.

The approximation (7) is inserted into Hamilton's equation (3) while the system is projected with $\boldsymbol{W}^\mathsf{T} = \boldsymbol{V}^+$.

This yields the low-dimensional initial value problem as the *reduced Hamiltonian's equation*

$$\frac{\mathrm{d}}{\mathrm{d}t}\widehat{\boldsymbol{x}}(t) = \mathbb{J}_{2k}\nabla_{\widehat{\boldsymbol{x}}}\widehat{\mathcal{H}}(\widehat{\boldsymbol{x}}(t)) = \mathbb{J}_{2k}(\widehat{\boldsymbol{H}}\widehat{\boldsymbol{x}}(t) + \widehat{\boldsymbol{h}}), \tag{9}$$

$$\widehat{\boldsymbol{x}}(t_0) = \boldsymbol{W}^{\mathsf{T}}\boldsymbol{x}_0 = \boldsymbol{V}^{+}\boldsymbol{x}_0 \tag{10}$$

with the definitions

$$\widehat{\boldsymbol{H}} = \boldsymbol{V}^{\mathsf{T}}\boldsymbol{H}\boldsymbol{V}, \qquad \widehat{\boldsymbol{h}} = \boldsymbol{V}^{\mathsf{T}}\boldsymbol{h} \tag{11}$$

with the corresponding *reduced Hamiltonian function*

$$\widehat{\mathcal{H}}(\widehat{\boldsymbol{x}}) = 1/2\ \widehat{\boldsymbol{x}}^{\mathsf{T}}\widehat{\boldsymbol{H}}\widehat{\boldsymbol{x}} + \widehat{\boldsymbol{x}}^{\mathsf{T}}\widehat{\boldsymbol{h}}. \tag{12}$$

3.2 Snapshot-based basis generation

A snapshot-based basis generation is used. This means several simulations with the high-dimensional model (3) are used to provide $n_\mathrm{s} \in \mathbb{N}$ state vectors $\boldsymbol{x}_i^\mathrm{s} = \boldsymbol{x}(t_i, \boldsymbol{\mu}_i)$, $i = 1, \ldots, n_\mathrm{s}$ which are referred to as snapshots. The ROB is computed based on the ensemble of all snapshots, e.g. with the snapshot matrix $\boldsymbol{X}^\mathrm{s} = [\boldsymbol{x}_1^\mathrm{s}, \ldots, \boldsymbol{x}_{n_\mathrm{s}}^\mathrm{s}] \in \mathbb{R}^{2n \times n_\mathrm{s}}$.

The Proper Symplectic Decomposition (PSD) (see Peng and Mohseni (2016)) chooses the ROB to minimize the residual of the symplectic projection $(\boldsymbol{I} - \boldsymbol{V}\boldsymbol{V}^{+})\boldsymbol{X}^\mathrm{s}$ of the snapshot matrix, i.e.

$$\underset{\boldsymbol{V} \in \mathbb{R}^{2n \times 2k}}{\text{minimize}} \left\| (\boldsymbol{I} - \boldsymbol{V}\boldsymbol{V}^{+})\boldsymbol{X}^\mathrm{s} \right\|_F, \tag{13}$$

$$\text{subject to} \quad \boldsymbol{V}^{\mathsf{T}}\mathbb{J}_{2n}\boldsymbol{V} = \mathbb{J}_{2k}, \tag{14}$$

while the side condition (14) requires the ROB to be symplectic (cf. (8)). An explicit solution for the minimization problem (13)-(14) is yet not known and can only be provided under restrictive assumptions on the structure of the ROB. Peng and Mohseni (2016) for example present the *Cotangent Lift* and the *Complex SVD* whereas Maboudi Afkham and Hesthaven (2016) present a greedy procedure to solve the minimization problem.

4. NUMERICAL RESULTS

In this section, two structure-preserving model reduction techniques are compared with a technique that does not preserve the Hamiltonian structure. A relative, mean over time, state space error measure is considered to compare the model reduction techniques numerically

$$e(2k) = \sum_{i=1}^{n_\mathrm{t}} \frac{1}{n_\mathrm{t}} \frac{\|\boldsymbol{x}(t_i) - \boldsymbol{V}\widehat{\boldsymbol{x}}(t_i)\|_2}{\|\boldsymbol{x}(t_i)\|_2} \tag{15}$$

where $t_1, \ldots, t_{n_\mathrm{t}} \in [t_0, t_\mathrm{e}]$ are the discrete times and the variable $2k$ is the size of the ROB $\boldsymbol{V}$.

The example scenario is a beam that is clamped on one side and loaded with a force on the other side. The force acts on the boundary and pushes orthogonal to the beam. The finite element model has $2n = 1152$ degrees of freedom. The ROB is created from snapshots computed with one simulation with $\boldsymbol{\mu}_1 = [1.21\,10^{11}\mathrm{N/m}, 8.08\,10^{10}\mathrm{N/m}]^{\mathsf{T}}$. The reduction techniques are compared for the same parameter $\boldsymbol{\mu}_1$. In all cases, a symplectic integration scheme, namely the implicit midpoint rule, is used for time integration.

The Cotangent Lift and the greedy approach from Maboudi Afkham and Hesthaven (2016) are considered as structure-preserving model reduction techniques in the following. Both are compared with the Proper Orthogonal Decomposition (POD) which does not necessarily preserve the Hamiltonian structure. For more details on the POD, see e.g. Volkwein (2013).

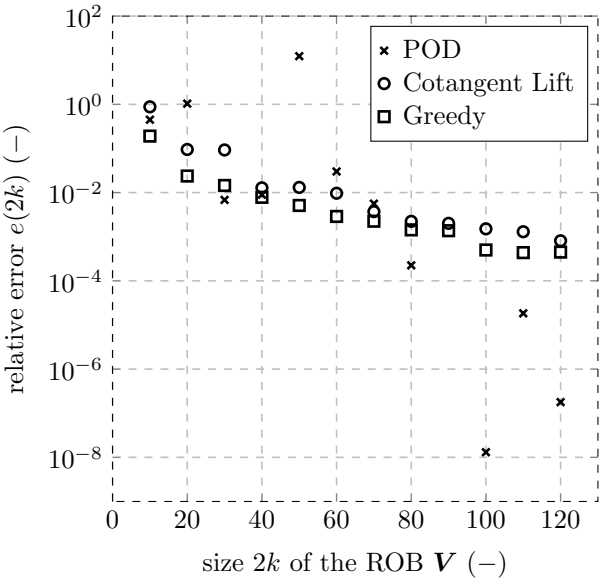

Fig. 1. Relative, mean over time, state space error $e(2k)$ for different ROB sizes $2k$ in a semi-logarithmic plot.

The results of the comparison are displayed in Figure 1 in terms of the error measure from (15). It shows that the POD is able to compute the best ROB with $2k = 100$. But the POD also yields the highest error with $e(90) > 10^2$ which was excluded from Figure 1 for the sake of a better overview. Overall, the results of both structure-preserving PSD techniques show less peaks and thus are more reliable. The greedy approach is in all considered cases better than the Cotangent Lift.

5. CONCLUSION

The structure-preserving model reduction was introduced and the Proper Symplectic Decomposition was presented as corresponding snapshot-based model reduction technique. The numerical results showed that the considered structure-preserving model reduction techniques provide bases that are more reliable than the ones created with the Proper Orthogonal Decomposition.

ACKNOWLEDGEMENTS

The author expresses a special thanks to the supervisors of his master thesis (A. Bhatt, B. Haasdonk, and J. Fehr).

REFERENCES

Maboudi Afkham, B. and Hesthaven, J.S. (2016). Structure Preserving Model Reduction of Parametric Hamiltonian Systems.

Peng, L. and Mohseni, K. (2016). Symplectic Model Reduction of Hamiltonian Systems. *Siam Journal on Scientific Computing*, 38, A1–A27.

Volkwein, S. (2013). Proper Orthogonal Decomposition: Theory and Reduced-Order Modelling. Lecture notes, Universität Konstanz.

Modeling and analyzing the long-time behavior of random chemostat models ⋆

Tomás Caraballo * **María J. Garrido-Atienza** *
Javier López-de-la-Cruz * **Alain Rapaport** **

* *Dpto. Ecuaciones Diferenciales y Análisis Numérico, Facultad de Matemáticas, Universidad de Sevilla, Calle Tarfia s/n, Sevilla 41012, Spain*
E-mails: {caraball,mgarrido,jlopez78}@us.es.

** *MISTEA (Mathematics, Informatics and Statistics for Environmental and Agronomic Sciences), INRA, Montpellier SupAgro, Univ. Montpellier, 2 place Pierre Viala, 34060 Montpellier cedex 01, France*
E-mail: alain.rapaport@inra.fr

Keywords: Chemostat model, random dynamical system, random attractor, input flow, brownian motion, standard Wiener process, Ornstein-Uhlenbeck process

Chemostat refers to a laboratory device used for growing microorganisms in a cultured environment and has been regarded as an idealization of nature to study competition modeling in mathematical biology, since they can be used to study genetically altered microorganisms, waste water treatment and play an important role in theoretical ecology, to mention a few applications.

The simplest form of chemostat consists of three interconnected tanks called *feed bottle*, *culture vessel* and *collection vessel*, respectively. The substrate or nutrient is pumped from the first tank to the culture vessel and another flow is also pumped from the culture vessel to the third tank such that the volume of the second one remains constant. It leads us to consider the following deterministic chemostat model with Monod kinetics

$$\frac{ds}{dt} = D(s_{in} - s) - \frac{msx}{a+s}, \tag{1}$$

$$\frac{dx}{dt} = -Dx + \frac{msx}{a+s}, \tag{2}$$

where $s(t)$ and $x(t)$ denote concentrations of the nutrient and the microbial biomass, respectively; s_{in} denotes the volumetric dilution rate, a is the half-saturation constant, D is the dilution rate and m is the maximal consumption rate of the nutrient and also the maximal specific growth rate of microorganisms. We notice that all parameters are supposed to be positive and a function Holling type-II, $\mu(s) = ms/(a+s)$, is used as functional response of the microorganisms describing how the nutrient is consumed by the species.

Some standard assumptions are usually imposed when setting up the simplest chemostat model (1)-(2), for instance, it is usually supposed that the availability of the nutrient and its supply rate are both fixed. Nevertheless, this kind of restrictions are really strong since the real world is non-autonomous and stochastic and this is one of the reasons which encourage us to study stochastic and/or random chemostat models.

There are many different ways to introduce stochasticity and/or randomness in some deterministic model, see e.g. Campillo et al. (2011, 2014, 2016); Grasman et al. (2005); Imhof and Walcher (2005); Wang and Jiang (2017); Wang et al. (2016); Xu and Yuan (2015); Zhao and Yuan (2016, 2017). Concerning the chemostat model, the authors in Caraballo et al. (2017a) have already analyzed the simplest chemostat model (1)-(2) in which a stochastic perturbation of the payoff function in continuous-time replicator dynamics is introduced, following the idea developed in Fudenberg and Harris (1992) or in Foster and Young (1990).

Even though there are many different ways to introduce some stochastic perturbation in the chemostat model, it is made on the growth function in most of cases. It could be interesting when the number of individual bacteria is small and there exists some risk of extinction of the biomass in finite time, however this kind of situations hardly ever take place in a nominal regime which is well supervised. Nevertheless, fluctuations on the input flow that brings permanently resources to the bacterial population in continuous cultures are much likely to be observed. In this way, Caraballo and some co-authors already considered a stochastic perturbation on the input flow in the simplest chemostat model (1)-(2) by making use of the standard Wiener process, also called brownian motion or white noise, see e.g. Caraballo et al. (2016) and Caraballo et al. (2017b). Unfortunately, some drawbacks can be found when considering this unbounded stochastic process, for instance, some state variables can take negative values, since the fluctuations could be large enough, what would

⋆ Partially supported by FEDER and Ministerio de Economía y Competitividad under grant MTM2015-63723-P, Junta de Andalucía under the Proyecto de Excelencia P12-FQM-1492 and VI Plan Propio de Investigación y Transferencia de la Universidad de Sevilla.

also mean that there is some reverting flow which is a completely unrealistic situation from the biological point of view. In addition, it is not possible to prove the persistence of the microorganisms when perturbing the input flow with the standard Wiener process.

In order to solve the previous problem, another kind of random perturbation on the simplest chemostat model (1)-(2) is analyzed in Caraballo et al. (2017c) by using the well-known Orsntein-Uhlenbeck process, which is a stationary mean-reverting Gaussian stochastic process given by the solution of the Langevin equation

$$dz_t + \beta z_t dt = \nu d\omega_t, \tag{3}$$

where ω_t represents the Wiener process at time $t \geq 0$, $\beta > 0$ is a mean reversion constant that represents how *strongly* our system reacts under some perturbation and $\nu > 0$ is a volatility constant which represents the variation or the size of the noise.

The O-U process can be used to describe the position of some particle by taking into account the friction, which is the main difference with the standard Wiener process and will make our models to be a much better approach to the real ones, in fact, it can be understood as a kind of generalization of the standard Wiener process, which would correspond to take $\beta = 0$ and $\nu = 1$ in (3). Thanks to that, the O-U process consists on a really interesting tool when perturbing the input flow in the chemostat model (1)-(2), since it will allow us to control the perturbations in a suitable way such that the input flow is bounded in some interval to be previously determined by the practitioner.

In conclusion, it can be easily deduce that the O-U process provides us a useful tool to model stochasticity and randomness in the chemostat model since it allows us to lead in models which are a much better approach to the real ones. In addition, this new framework could also be extended to analyze other kinds of models, for instance, those ones with several species and competition and this is currently our main point of interest.

In this work, the simplest chemostat model (1)-(2), perturbing the input flow by means of the O-U process, will be presented. We will make use of the techniques involved in the theory of random dynamical systems (see e.g. Arnold (1998); Caraballo and Han (2016)) to provide some results concerning the existence and uniqueness of global solution just like that the existence and uniqueness of random pullback attractor, which will allow us to obtain detailed information about the long-time behavior of our model. In particular, some conditions on the different parameters of our model will be given to ensure the persistence of the microbial biomass in the *strong* sense

$$\lim_{t \to +\infty} x(t) \geq \rho > 0.$$

Finally, several numerical simulations comparing the results with the ones obtained when perturbing the input flow by using the standard Wiener process will be also shown.

REFERENCES

Arnold, L. (1998). *Random Dynamical Systems*. Springer Berlin Heidelberg.

Campillo, F., Joannides, M., and Larramendy-Valverde, I. (2011). Stochastic modeling of the chemostat. *Ecological Modelling*, 222(15), 2676–2689.

Campillo, F., Joannides, M., and Larramendy-Valverde, I. (2014). Approximation of the fokker–planck equation of the stochastic chemostat. *Mathematics and Computers in Simulation*, 99, 37–53.

Campillo, F., Joannides, M., and Larramendy-Valverde, I. (2016). Analysis and approximation of a stochastic growth model with extinction. *Methodology and Computing in Applied Probability*, 18(2), 499–515.

Caraballo, T., Garrido-Atienza, M.J., and López-de-la-Cruz, J. (2016). *Some Aspects Concerning the Dynamics of Stochastic Chemostats*, volume 69, 227–246. Springer International Publishing, Cham.

Caraballo, T., Garrido-Atienza, M.J., and López-de-la-Cruz, J. (2017a). Dynamics of some stochastic chemostat models with multiplicative noise. *Communications on Pure and Applied Analysis*, 16(5), 1893–1914.

Caraballo, T., Garrido-Atienza, M.J., López-de-la-Cruz, J., and Rapaport, A. (2017b). Corrigendum to "Some aspects concerning the dynamics of stochastic chemostats". *arXiv:1710.00774 [math.DS]*.

Caraballo, T., Garrido-Atienza, M.J., López-de-la-Cruz, J., and Rapaport, A. (2017c). Modeling and analysis of random and stochastic input flows in the chemostat model (submitted).

Caraballo, T. and Han, X. (2016). *Applied Nonautonomous and Random Dynamical Systems, Applied Dynamical Systems*. Springer International Publishing.

Foster, D. and Young, P. (1990). Stochastic evolutionary game dynamics. *Theor. Pop. Bio.*, 38(2), 219–232.

Fudenberg, D. and Harris, C. (1992). Evolutionary dynamics with aggregate shocks. *Journal of Economic Theory*, 57(2), 420–441.

Grasman, J., Gee, M.D., and Herwaarden, O.A.V. (2005). Breakdown of a chemostat exposed to stochastic noise. *Journal of Engineering Mathematics*, 53(3-4), 291–300.

Imhof, L. and Walcher, S. (2005). Exclusion and persistence in deterministic and stochastic chemostat models. *Journal of Differential Equations*, 217(1), 26–53.

Wang, L. and Jiang, D. (2017). Periodic solution for the stochastic chemostat with general response function. *Physica A: Statistical Mechanics and its Applications*, 486, 378–385.

Wang, L., Jiang, D., and O'Regan, D. (2016). The periodic solutions of a stochastic chemostat model with periodic washout rate. *Communications in Nonlinear Science and Numerical Simulation*, 37, 1–13.

Xu, C. and Yuan, S. (2015). An analogue of break-even concentration in a simple stochastic chemostat model. *Applied Mathematics Letters*, 48, 62–68.

Zhao, D. and Yuan, S. (2016). Critical result on the break-even concentration in a single-species stochastic chemostat model. *Journal of Mathematical Analysis and Applications*, 434(2), 1336–1345.

Zhao, D. and Yuan, S. (2017). Break-even concentration and periodic behavior of a stochastic chemostat model with seasonal fluctuation. *Communications in Nonlinear Science and Numerical Simulation*, 46, 62–73.

Hybridization of Aim Point Optimization Methods for Solar Tower Power Plants

D. Maldonado Quinto*. R. Flesch**
P. Schwarzbözl***

**Institute of Solar Research, German Aerospace Center (DLR), Linder Höhe, Cologne 51147 Germany*
(Tel: 0049-2203-6013981; e-mail: Daniel.MaldonadoQuinto@dlr.de)
***Institute of Solar Research, German Aerospace Center (DLR), Prof. Rehm-Strasse 1, Juelich 52428 Germany*
(e-mail: Robert.Flesch@dlr.de)
**** Istitute of Solar Research, German Aerospace Center (DLR), Linder Höhe, Cologne 51147 Germany*
(e-mail: Peter.Schwarzboezl@dlr.de)

Keywords: Solar Tower Power Plant, Aim Point Optimization, Heuristic Programming, Searching Problems, Hybrid Modes, Discrete Optimization.

1. INTRODUCTION

In solar tower power plants a large number of heliostats concentrate the solar irradiation onto a receiver, which is mounted on the top of a tower. The two-axis tracking systems allow an individual alignment for each heliostat in order to reflect the irradiation to a so called aim point. The aim point is located on the receiver surface or an off receiver point, e.g. as a safety position. The aiming strategy defines the aim point of each heliostat for a specific operating point over the day. The concentrated solar power is absorbed by the receiver and a heat transfer medium is used to pipe the heat to the connected process, e.g. a Rankine power cycle. Different receivers are currently employed or are under development using air, water/steam, molten salt, particles or liquid metals as heat transfer medium.

1.1 Aiming Strategy

A good aiming strategy is of great importance for an efficient operation of solar power towers. Most of the radiation will most likely hit the receiver if all heliostats aim to its centre. Unfortunately, this aiming strategy cannot be applied as temperature and/or stress limits of the receiver, which can be expressed in a limit for the flux density, will be exceeded. Therefore, the aim points of the heliostats have to be distributed over the receiver surface in order to lower the peak flux densities. But this will presumably reduce the amount of radiation hitting the receiver. The aiming strategy can be characterized as a constraint optimization problem, in which the optical or thermal performance is optimized with respect to all limits for the receiver.

2. OPTIMIZATION

2.1 Optimization Problem

The flux distribution for each heliostat and each aim point is calculated with a Monte Carlo ray tracing approach. For this calculation model a discrete optimization approach is appropriate. Allowing only a finite number of aim points defines the optimization as a discrete problem with combinatorial characteristics. As described by Belhomme et al. (2014) the size of the solution space S and therefore the number of possible heliostat aim-point combinations is equal to the number of fixed aim points n_Z to the power of the number of heliostats n_H, as in (1). In solar tower power plants n_H is typically larger than 5000.

$$|S| = {n_Z}^{n_H} \tag{1}$$

This combinatorial optimization problem belongs to the NP-complete class. A trivial solution method, the complete enumeration of the solution space, is obviously unrealistic for typical heliostat field sizes. Heuristic methods are needed. Belhomme et al. (2014) therefore adapted the ant colony optimization metaheuristic (ACO) for the specific optimization problem.

2.2 ACO

The ACO method is a probabilistic technique that benefits from the principles of swarm intelligence and imitates the behaviour of ant colonies during foraging. The aiming optimization is transferred to a suitable problem for the ACO by defining the aim point configuration as the trail of an ant. The entire trail is divided in edges, which represents the aim point assignment for a specific heliostat. One trail represents one possible heliostat aim point assignment for the entire concentrator field. A suboptimal trail at the beginning is improved according heuristic information. The heuristic information, namely intercept factor and receiver performance, are calculated with a Monte-Carlo-Raytracer (Belhomme et al. (2009)) and a Finite-Element-Method, respectively. The raytracer calculates the flux density distribution on the receiver surface and the FEM model determines the receiver performance, the model is described by Flesch et al. (2017). The FEM model is a black box for the optimization procedure and determines the so called global quality value. If receiver constraints like flux density limits are exceeded the quality value is penalized by the FEM model. The result serves the ACO to update the attractiveness

of the edges, which affect the choice of a new trail in the following optimization step.

The optimization procedure was tested on a realistic power plant scenario by Maldonado et al. (2017). The results show, that in heavily constrained cases the performance of the ACO drops. This is because of the drawback that in case of a limit exceedance the entire path is penalized even if only one heliostat/edge is responsible. To overcome this drawback a second optimization algorithm called local search (LS) was implemented. In this study several optimization parameters were examined using the scenario of Maldonado et al. (2017) in order to find fast convergence behaviour.

2.4 LS

The LS starts from a solution and moves towards an improvement, equally to the ACO. In contrast to the ACO, it only manipulates the aim point configuration in a local region; this means that the calculation of the local quality at a single edge is restricted to a so called neighbourhood. For a single LS run all heliostats' assignments are examined one by one in a certain sequence. In each examination step the assignment for a single heliostat can change by shifting to one of the neighbouring aim points. The overall receiver performance is calculated after each shift until an improved solution is found in the neighbourhood. Otherwise the initial solution is maintained. Compared to the ACO a local change of a single heliostat aim point assignment is evaluated and local exceedances of allowable flux can be prevented without affecting the entire aim point configuration.

3. EVALUATION OF BOTH METHODS

For the comparison of the different optimization methods the thermal output of the receiver during the optimization is plotted in dependence of the evaluations of the thermal model. One exemplary plot is shown in figure 1. The black curve represents the ACO. The remaining plots represent LS optimization runs with different parameter.

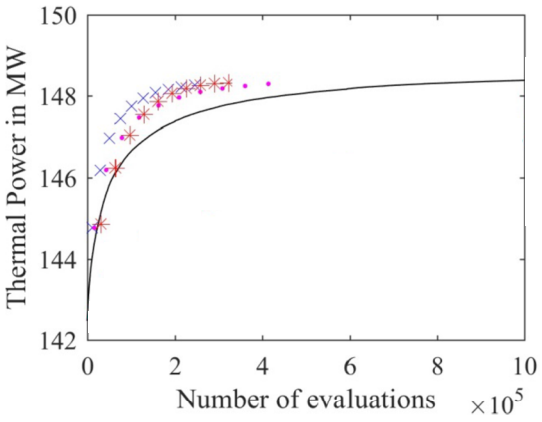

Fig. 1. Results of the optimization for an exemplary time point with high flux density constraints.

The curve with the blue crosses is parameterized with a small neighbourhood, whereas the curve with the red stars represents an enlarged neighbourhood. The purple dotted curve represents a case with the larger neighbourhood, but in comparison to the other cases the entire neighbourhood is examined in each evaluation. Figure 1 shows that the LS can outperform the ACO in the first $4 \cdot 10^5$ evaluation steps. The progresses for the LS are steeper at the very beginning and stagnate strongly afterwards. The black curve stagnates less and can outperform the LS after $6 \cdot 10^5$ evaluation steps.

5. HYBRIDIZATION

The evaluation of optimization processes for different time and operating points strongly suggests to combine the methods. Furthermore, the number of evaluations for a single method is too large for many cases. The computational time for an online optimization where boundary conditions, e.g. solar irradiation, can change quickly must be minimized.

Hybridization should be done automatically with a dynamic adjustment of the optimization parameters. The mathematical model of the receiver and the heliostat field should supply output quantities that decide on the optimization parameters and when to switch optimization strategy.

The LS performs well if the case is highly constrained and the initial solution is within the analysed neighbourhood. On the other hand it can get stuck in a local optimum or even cannot find a valid solution. The ACO in contrast performs fairly well for most cases and better than the LS if the initial solution is far away from the global optimum and not heavily constrained.

One hybridization approach is to start always with the ACO and to find a valid solution after very few runs. Afterwards switch to the LS to benefit from a possible steeper climb. The approach monitors a possible stagnation of the LS to decide if the ACO should continue proceeding. At the end of the optimization process the ACO should bring us close to the global optimum and the LS as a hill climber can do the rest.

REFERENCES

Belhomme, B., Pitz-Paal, R., Schwarzbözl, P. and Ulmer, S. (2009). *Journal of Solar Energy Engineering*. A New Fast Ray Tracing Tool for High-Precision Simulation of Heliostat Fields, volume 131, 031002-031002-8.

Belhomme, B., Pitz-Paal, R. and Schwarzbözl, P. (2014). *Journal of Solar Energy Engineering*. Optimization of Heliostat Aim Point Selection for Central Receiver Systems Based on the Ant Colony Optimization Metaheuristic. Name of paper, volume 136, 011005-011005-7.

Flesch, R., Frantz, C., Maldonado, D., Schwarzbözl, P. (2017). *Solar Energy*. Towards an optimal aiming for molten salt power towers, volume 155, 1273-1281.

Maldonado Quinto, D., Flesch, R., Reinholz, A., Schwarzbözl, P. (2017). *Proceedings of the SolarPACES International Symposium on Concentrated Solar Power and Chemical Energy Technologies*, Santiago de Chile. Evaluation of Aim Point Optimization Methods.

Dynamic Modelling of Molten Salt Central Receiver Systems

Robert Flesch*. Daniel Maldonado Quinto. Peter Schwarzbözl *****

**German Aerospace Center (DLR), Juelich, 52428 Germany (Tel: +49-2203-601-4172; e-mail: robert.flesch@dlr.de).*
***German Aerospace Center (DLR), Cologne, 51147 Germany (e-mail:daniel.maldonadoQuinto@dlr.de)*
****German Aerospace Center (DLR), Cologne, 51147 Germany (e-mail:peter.schwarzboezl@dlr.de).*

Keywords: Solar energy, concentrated solar power, central receiver, molten salt, finite element method, coupled simulation, control system

1. INTRODUCTION

Molten salt central receiver (MSCR) systems are a very promising option for the large-scale production of electricity from solar radiation. A central receiver system consists of a field of thousands of mirrors which reflect the sunlight to the top of a tower, at which the receiver is located. The receiver is built of tubes where molten salt is flowing through as the heat transfer fluid. The salt is heated up due to the concentrated solar radiation. The hot salt can be easily stored in large unpressurized tanks driving a convectional steam plant afterwards. The efficiency and the easy storage option have made the MSCR system to the predominant concentrating solar technology in the recent years.

Like every other technology which uses direct solar radiation, MSCR systems have to deal with a highly dynamic resource. Clouds which move over the heliostat field and shade heliostats result in a highly non-uniform and transient flux density distribution on the receiver surface. The task of the control system is to ensure a safe and efficient operation under the described dynamic boundary conditions. Due to the usage of molten salt used as fluid in the receiver the safety aspect during operation is especially challenging. Temperatures below 240°C must be avoided because of crystallization in the tubes (Zavoico, 2001). If not radiated for a short period, the system has to be drained. The upper temperature is restricted to approximately 600°C to avoid degradation of the salt and corrosion of tubes (Zavoico, 2001). With regards to the typical design temperature range from 290°C to 565°C, the control system has to regulate the temperature with just a small deviation.

The DLR has created a dynamic simulation environment for MSCR systems which includes a detailed model of the heliostat field and the receiver. The simulation environment can be used to simulate and evaluate control strategies of the receiver system under realistic boundary conditions.

First, we briefly describe the approach and provide some validation data. Then, initial results of our current work are shown and an outlook to our planned activities is given.

2. METHODS

A MSCR system can be divided into subunits. In the present analysis the heliostat field and the receiver are the two units of interest. For a realistic analysis of the receiver dynamics it is necessary to have a model of the heliostat field which calculates the flux density distribution on the receiver. We used the in-house developed ray tracing tool STRAL (Belhomme et al, 2009) for this task. The receiver, however, is modelled by using the modelling language Modelica within Dymola. Both tools are connected with the third party tool TISC (Kossel et al, 2006), which exchanges data in a predefined synchronization rate. In the following the two models are described in little more detail.

2.1 Heliostat field model

STRAL is a simulation tool which can be used to calculate the flux density produced by a heliostat field on any arbitrary surface in high calculation speed. In our case, the cylindrical or polygonal shape of the receiver is used. STRAL has proven its high accuracy in several tests (Belhomme et al, 2009). To reproduce the flux of an existing field, heliostat surface information obtained from deflectometry measurements can be included (Belhomme et al, 2009). STRAL itself does not offer a method to include shading data of clouds, but it can be controlled from Matlab: in Matlab a tool was created which can be used to include DNI maps which are created as described in (Schenk et al, 2015). In the model a heliostat is switched off if the flux density in its centre falls under a given threshold. This is a simplification as in reality a heliostat can obviously be partly shaded, but the influence is assumed to be small in a field with typically several ten-thousands of heliostats.

2.2 Receiver model

The model of the receiver is implemented in Dymola with the modelling language Modelica. A receiver consists of panels through which the fluid flows sequentially. The panels are built of parallel tubes. To reduce the computational effort in the simulation several tubes can be bundled and represented by a single tube which is simulated. The fluid in the tubes is

discretized one dimensionally with a finite volume approach using a staggered grid. The tube is divided in a front side and back side element. To calculate the temperature of the front element the differential equation

$$\pi \Delta z\, k\left((T_{\mathrm{O}}-T_{\mathrm{C}})/\ln(d_{\mathrm{O}}/d_{\mathrm{C}})-(T_C-T_I)/\ln(d_{\mathrm{C}}/d_{\mathrm{I}})\right) + A_{\mathrm{FB}}\, 2k/(d_C\pi)(T_{\mathrm{B}}-T_{\mathrm{C}}) = mc\,\partial T_C/\partial t \quad (1)$$

is solved with the mass of the element m, the heat capacity c, the length Δz, the conductivity k, the contact surface between front and back A_{FB} and the temperature T and diameter at the outer (O), central (C) and inner (I) position. As boundary for the outer temperature the relation

$$d_O\Delta z\left(aI-\varepsilon\sigma\left(T_O^4-T_\infty^4\right)-\alpha(T_O-T_\infty)\right)=\pi\Delta z\,k\,(T_{\mathrm{O}}-T_{\mathrm{C}})/\ln(d_{\mathrm{O}}/d_{\mathrm{C}}) \quad (2)$$

is used with the absorptivity a, the emissivity ε, the convective heat transfer coefficient α, the incoming radiation I and the ambient temperature T_∞. The boundary for the inner temperature is similar, except it connects the heat transfer through the tube to the fluid temperature with a heat transfer correlation. The equation for the backside element is similar to (1) and uses the same inner boundary. The outer surface is assumed to be adiabatic.

Validation was performed with more detailed CFD and FEM simulations and additionally with experimental data as described in Flesch et al (2017). A comparison of the fluid temperature at several locations in the receiver for one case is given in Fig. 1. The model predicts the dynamics of the temperature very well.

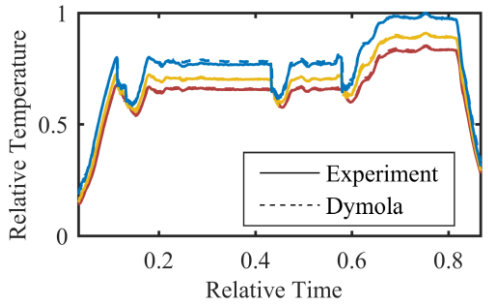

Fig.1. Validation with experimental data. The different colours indicate different position in the receiver.

3 RESULTS

As example simulation result the temperature response of the system on a cloud shading the southern part of the heliostat field of a plant located in South Africa is shown in Fig 2. The cloud moves from west to east. In the plots the results for three different control systems is shown: the first system corresponds to the one used in the Solar Two plant (Pacheco, 2002). It includes a so-called cloud standby (CSB) which increases the mass flow in case of a skewed flux distribution caused by clouds. The second system equals the Solar Two approach without CSB. The third system is as well similar to the Solar Two system but instead of a CSB it uses limits for the mass flow which are calculated from a model which uses an estimate of the current radiation on the receiver. The CSB in the Solar Two system is activated little too late to fully prevent the system from excessive temperatures, though it does avoid hazardous temperature peaks as one can see in case of the deactivated cloud standby. The system with the limits based on the current conditions performs better during cloud entry, but temperature overshoots when the cloud leaves. In that situation the control system requests a mass flow which is higher than the maximum mass flow of the system. This can be prevented by increasing the maximum mass flow rate or by using some kind of cloud forecast. Further results will be shown on the conference.

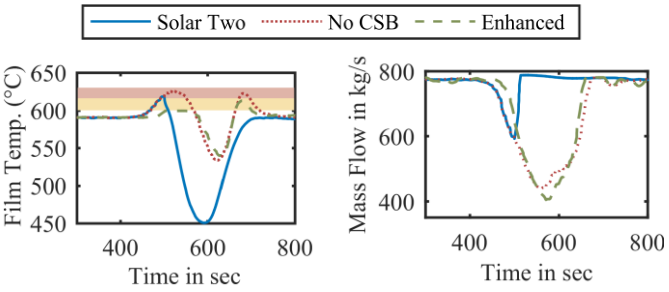

Fig. 2. Film temperature and mass flow of the receiver during cloud passage: The yellow colour indicates the temperature range which is allowed for short period. A temperature within the red range should be strictly avoided.

4. SUMMARY AND OUTLOOK

A coupled simulation approach has been developed to simulate the dynamics of a MSCR system e.g. during clouds. The state-of-the-art control system as used in the Solar Two plant with and without CSB was analysed and an enhanced system developed based on the lessons learned. In a recently started project we work on further improvements in the control of the normal operation by using a model predictive control. Besides we are working on an operation assistant system, which aims to improve and support the operators during receiver start-up and shutdown.

REFERENCES

Belhomme, B., Pitz-Paal, R., Schwarzbözl, P. and Ulmer, S. (2009). A New Fast Ray Tracing Tool for High-Precision Simulation of Heliostat Fields. *Journal of Solar Energy Engineering,* 131 (3), 031002.

Flesch, R., Högemann, D., Hackmann, J., Uhlig, R., Schwarzbözl, P., Augsburger, G. and Clark, M. (2017). Dynamic modeling of molten salt power towers. *AIP Conference Proceedings*, 1850, 030016.

Kossel R., Tegethoff W., Bodmann M. and Lemke N. (2006). Simulation of complex systems using Modelica and tool coupling. *5th Modelica Conference,* 2, 485

Pacheco J.E. (2002). *Final Test and Evaluation Results from the Solar Two Project,* Sandia National Laboratories, Albuquerque, New Mexico and Livermore, California.

Schenk, H., Hirsch, T., Wittmann, M., Wilbert, S., Keller, L. & Prahl, C. (2015). Design and Operation of an Irradiance Measurement Network. *Energy Procedia*, 69, 2019.

Zavoico A.B. (2001). *Solar Power Tower Design Basis Document,* Sandia National Laboratories, Albuquerque, New Mexico and Livermore, California.

Efficient Simulation of Variability and Heterogeneity in Bioprocess Engineering ⋆

Dennis Pischel * **Kai Sundmacher** *,** **Robert J. Flassig** **

* *Otto-von-Guericke-University Magdeburg, Process Systems Engineering, 39106 Magdeburg, Germany*
** *Max Planck Institute for Dynamics of Complex Technical Systems, Process Systems Engineering, 39106 Magdeburg, Germany*

Keywords: chemical master equation, Gillespie algorithm, unscented transformation, stochastic differential equation, systems biology.

1. INTRODUCTION

The individual character of microbial systems is very dominant, since cells vary in plenty of properties, such as morphology, cell cycle state and many more. To accurately capture biological variability by simulations *in silico* several sources of noise must be considered. In this contribution we refer to intrinsic noise as an inherent stochastic process, extrinsic noise as cell-to-cell variability and external noise as external perturbations, see Fig. 1A. In order to clarify our understanding of the different sources of noise we investigate in Fig. 1B-D their impact on a simple decay process $\mathrm{P} \rightarrow \emptyset$ Pischel et al. (2017). We modeled intrinsic noise *via* the Gillespie algorithm Gillespie et al. (2013), which captures stochastic biochemical reactions. In contrast extrinsic noise was computed *via* Monte Carlo sampling of the distributed initial conditions accounting for cell-to-cell variability. Both effects lead to a probability density function describing the abundance of the protein P for every time point. The synergy of intrinsic and extrinsic noise yields a further spread of the probability density function.

The interaction of different sources of noise and their impact on the overall variability of bioprocesses is hardly investigated due to computational and experimental challenges Lencastre Fernandes et al. (2011); Delvigne and Goffin (2014). A popular approach to model stochastic biochemical reaction systems is by means of the chemical master equation, which governs the temporal evolution of the probability P to find the system in a certain state $\boldsymbol{x}$

$$\frac{\mathrm{d}}{\mathrm{d}t}P(\boldsymbol{x}(t),t) = \sum_{k=1}^{m} a_k(\boldsymbol{x}(t)-\boldsymbol{N}_k)P(\boldsymbol{x}(t)-\boldsymbol{N}_k,t) - a_k(\boldsymbol{x}(t))P(\boldsymbol{x}(t),t). \quad (1)$$

We denote by $\boldsymbol{a}$ the reaction propensities and by $\boldsymbol{N}$ the stoichiometric matrix. The index k indicates the chemical reaction. In general it is not possible to solve the chemical master equation analytically, wherefore approximate methods are used, *e.g.* the Gillespie algorithm and its derivations, the methods of moments, the system size expansion or the finite state projection algorithm Kazeroonian et al. (2016). All of these methods have several drawbacks and cannot capture different sources of noise. Thus, we present a recent developed method, which is capable to simulate intrinsic, extrinsic and external noise simultaneously Pischel et al. (2017).

⋆ This work was supported by the Federal Ministry of Education and Research in Germany [031A304 to D.P.].

2. EFFICIENT MODELING OF VARIOUS SOURCES OF NOISE

The simplest approach to model different sources of noise simultaneously is by Monte Carlo sampling of uncertain parameters combined with the temporal system evolution *via* a stochastic process Wilkinson (2009). In our application the stochastic process is governed by the chemical master equation, which is why we use the Gillespie algorithm through this study. The combined approach is asymptotically exact and yields an accurate solution of the chemical master equation, which goes along with a huge computational load. To accelerate this proceeding we approximate the Monte Carlo sampling of the uncertain parameters by the unscented transformation, which chooses only $2n_\sigma + 1$ samples (sigma points) of the n_σ uncertain parameters deterministically Julier et al. (2000). The sigma points are propagated through time *via* the τ-leaping algorithm, which is an efficient approximation of the Gillespie algorithm. For every time point t the mean and covariance of the system can be estimated from the propagated sigma points. Since the temporal evolution was computed using a stochastic process this procedure is repeated n times. With assumptions, *e.g.* normality or log-normality, the underlying distribution $\hat{\boldsymbol{\rho}}_i(t)$ can be reconstructed from the mean and covariance for each run i. By weighted superposition of the distributions

$$\tilde{\boldsymbol{\rho}} = \sum_{i=1}^{n} \omega_i \boldsymbol{\rho}_i = \frac{1}{n}\sum_{i=1}^{n} \hat{\boldsymbol{\rho}}_i \quad (2)$$

we obtain an approximate solution $\tilde{\boldsymbol{\rho}}$ of the chemical master equations with uncertain parameters. This algorithm is outlined in Fig. 2. We applied our method to several examples of systems biology and observed accelerated convergence regarding the statistical moments and the probability density function compared to the combined Monte Carlo approach Pischel et al. (2017). Although our

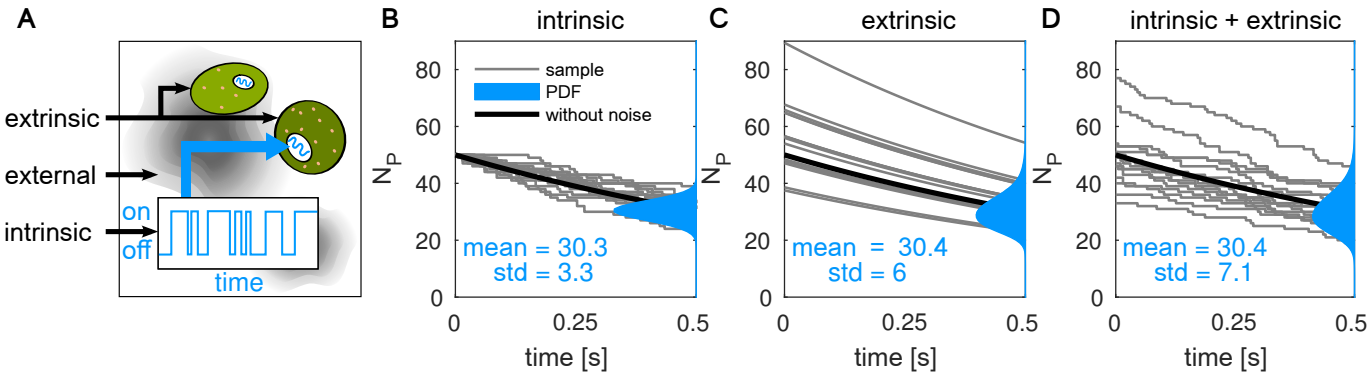

Fig. 1. Noisy biochemical reaction systems: (A) Several sources of noise impact biological variability. Intrinsic (B), extrinsic (C), and intrinsic combined with extrinsic noise perturb a decay process Pischel et al. (2017).

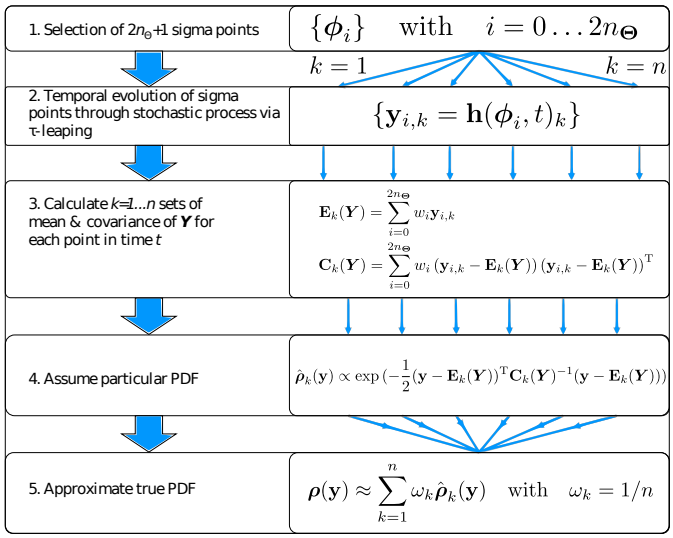

Fig. 2. Algorithm outline Pischel et al. (2017).

approximate method might in some cases not converge to the exact solution we observe qualitative conformance.

3. CONCLUSION

In this study an efficient approach to model different sources of noise in biochemical reaction systems simultaneously was proposed. Our method converges very fast to an approximate solution compared to straightforward Monte Carlo methods. Hence, it is well suited to speed up costly optimization tasks, *e.g.* parameter estimation problems of distributed, stochastic biochemical systems Pischel et al. (2017). Since optimization of stochastic systems is rarely performed due to its huge computational load Poovathingal and Gunawan (2010); Fröhlich et al. (2016) our approach paves the way to further understanding of uncertainty in complex dynamical systems.

REFERENCES

Delvigne, F. and Goffin, P. (2014). Microbial heterogeneity affects bioprocess robustness: Dynamic single-cell analysis contributes to understanding of microbial populations. *Biotechnology Journal*, 9(1), 61–72. doi: 10.1002/biot.201300119.

Fröhlich, F., Thomas, P., Kazeroonian, A., Theis, F., Grima, R., and Hasenauer, J. (2016). Inference for stochastic chemical kinetics using moment equations and system size expansion. *PLoS Computational Biology*, 12(7). doi:10.1371/journal.pcbi.1005030.

Gillespie, D.T., Hellander, A., and Petzold, L.R. (2013). Perspective: Stochastic algorithms for chemical kinetics. *Journal of Chemical Physics*, 138(17). doi: 10.1063/1.4801941.

Julier, S., Uhlmann, J., and Durrant-Whyte, H.F. (2000). A new method for the nonlinear transformation of means and covariances in filters and estimators. *IEEE Transactions on Automatic Control*, 45(3), 477–482. doi: 10.1109/9.847726.

Kazeroonian, A., Fröhlich, F., Raue, A., Theis, F.J., and Hasenauer, J. (2016). Cerena: Chemical reaction network analyzer–a toolbox for the simulation and analysis of stochastic chemical kinetics. *PLoS ONE*, 11(1), e0146732. doi:10.1371/journal.pone.0146732.

Lencastre Fernandes, R., Nierychlo, M., Lundin, L., Pedersen, A.E., Puentes Tellez, P.E., Dutta, A., Carlquist, M., Bolic, A., Schäpper, D., Brunetti, A.C., Helmark, S., Heins, A.L., Jensen, A.D., Nopens, I., Rottwitt, K., Szita, N., van Elsas, J.D., Nielsen, P.H., Martinussen, J., Sørensen, S.J., Lantz, A.E., and Gernaey, K.V. (2011). Experimental methods and modeling techniques for description of cell population heterogeneity. *Biotechnology Advances*, 29(6), 575–599. doi: 10.1016/j.biotechadv.2011.03.007.

Pischel, D., Sundmacher, K., and Flassig, R.J. (2017). Efficient simulation of intrinsic, extrinsic and external noise in biochemical systems. *Bioinformatics*, 33(14), i319–i324. doi:10.1093/bioinformatics/btx253.

Poovathingal, S.K. and Gunawan, R. (2010). Global parameter estimation methods for stochastic biochemical systems. *BMC Bioinformatics*, 11. doi:10.1186/1471-2105-11-414.

Wilkinson, D.J. (2009). Stochastic modelling for quantitative description of heterogeneous biological systems. *Nature Reviews Genetics*, 10(2), 122–133. doi: 10.1038/nrg2509.

Modelling of the Self-Propelled Vibro-Impact Capsule in Small Intestine ⋆

Y. Yan * **Y. Liu** ** **S. Prasad** ***

* *School of Aeronautics and Astronautics, University of Electronic Science and Technology of China, Chengdu, 611731, China (e-mail: y.yan@uestc.edu.cn).*
** *College of Engineering, Mathematics and Physical Sciences, University of Exeter, North Park Road, Exeter, EX4 4QF, UK (e-mail: y.liu2@exeter.ac.uk)*
*** *The Royal Devon and Exeter NHS Foundation Trust, Barrack Road, Exeter, EX2 5DW, UK (e-mail: shyamprasad@nhs.net)*

Keywords: Vibro-impact; Non-smooth dynamical system; Self-propulsion; Capsule endoscopy; Small intestine.

1. INTRODUCTION

The technology of capsule endoscopy, which employs a swallowable device propelled by gastrointestinal peristalsis through small intestinal tract to transmits video images, has been used in the past decade for evaluating gastrointestinal bleeding, inflammation, tumours, and some other diseases, see McCaffrey et al. (2008); Koulaouzidis et al. (2013) However, the bottleneck issue of such technology is the lack of motion control, i.e. the capsule cannot settle down at a suspected area for longer period or take a reverse travel within the tract, causing missing images of symptom, which has consumed massive doctor's time and oversight of diseases.

This work concerns this issue by employing the so-called vibro-impact capsule technique (see e.g. Chernousko (2002); Liu et al. (2013); Jiang and Xu (2017)), which utilizes internal vibration and impact forces for bidirectional rectilinear self-propelled driving. Mathematical modelling of the vibro-impact capsule system will be considered in the environment of small intestinal tract, and a complete analysis of the capsule's performance in terms of its progression speed and energy efficiency will be carried out.

2. MATHEMATICAL MODELLING

In this work, we consider the two-degrees-of-freedom dynamical capsule system as shown in Fig. 1(a), where a movable internal mass m_1 is driven by a harmonic force with magnitude P_d and frequency Ω. The internal mass interacts with a rigid capsule m_2 via a linear spring with stiffness k and a viscous damper with damping coefficient c. The capsule has a cylindrical body with a hemispherical head and tail. Impact between the internal mass and a weightless plate connected to the capsule through a secondary spring with stiffness k_1 may occur, once their relative displacement $x_1 - x_2$ is larger or equal to the gap g_1, where x_1 and x_2 are the absolute displacements of the internal mass and the capsule, respectively.

⋆ Y. Liu would like to acknowledge the financial support from EPSRC for his First Grant (Grant No. EP/P023983/1).

2.1 Resistance

As the diameter of the capsule is larger than the inner diameter of the small intestine, the capsule stretches the intestinal tract to yield hoop stress. This hoop stress causes normal and frictional forces on the capsule yielding environmental resistance which prevents the motion of the capsule. In addition, the gravity of the capsule which exerts normal pressure on the intestinal tract also adds additional value to the resistance. It is therefore that the overall resistance on the capsule can be written as

$$F_r = F_{\text{hoop}} + F_{\text{gravity}}, \tag{1}$$

where F_{hoop} and F_{gravity} represent the resistances introduced by hoop stress and capsule gravity, respectively. As depicted in Fig. 1(b), the resistance due to the hoop stress can be given as

$$F_{\text{hoop}} = -\operatorname{sign}(v_2)(F_{Hp} + F_{Tp} + F_{Hf} + F_{Bf} + F_{Tf}), \tag{2}$$

where v_2 is the capsule speed, F_{Hp} and F_{Tp} are the normal pressures of the intestine on the capsule head and tail, and F_{Hf}, F_{Bf} and F_{Tf} are the frictional forces exerted on the head, the body, and the tail of the capsule, along the axial direction of the capsule, respectively. As the cross section of the small intestine is expanded by the capsule yielding tensile stress, the hoop stress depends on the geometric deformation of the intestinal wall. The geometric parameters of the capsule are shown in Figure. 1(b), where L is the length of the capsule, R_c is the radius of the head, the body, and the tail, R_i is the original inner radius of the intestinal tract, ϕ_c is the angle of the point from where the intestine tract starts to surround the capsule, and x_c is the distance from the contact point to the centre of the head (or the tail).

2.2 Equations of motion

As depicted in Fig. 1, a periodic external excitation, $P_d \cos(\Omega t)$, is applied on the inner mass m_1 to drive the capsule m_2. The inner mass interacts with the capsule via a damped spring at the tail and a secondary spring at the head of the capsule. Due to the gap between the mass

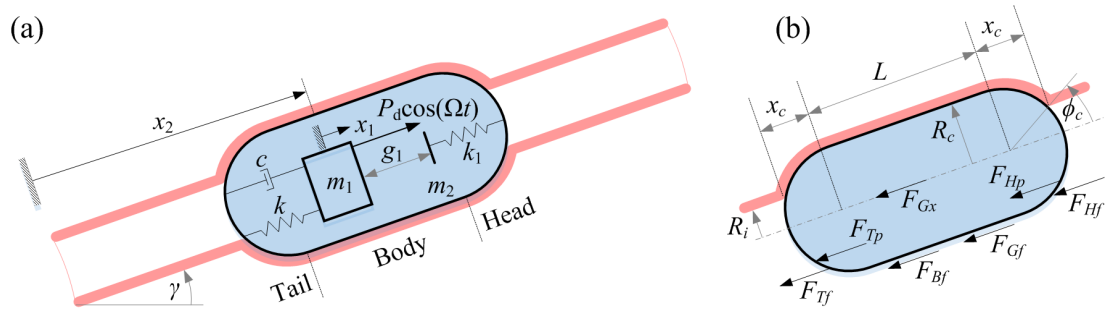

Fig. 1. (a) Physical model of the vibro-impact capsule in small intestine. (b) Resistance forces and geometric parameters of the capsule. The capsule is depicted in cyan, and the intestinal tract is presented in light red.

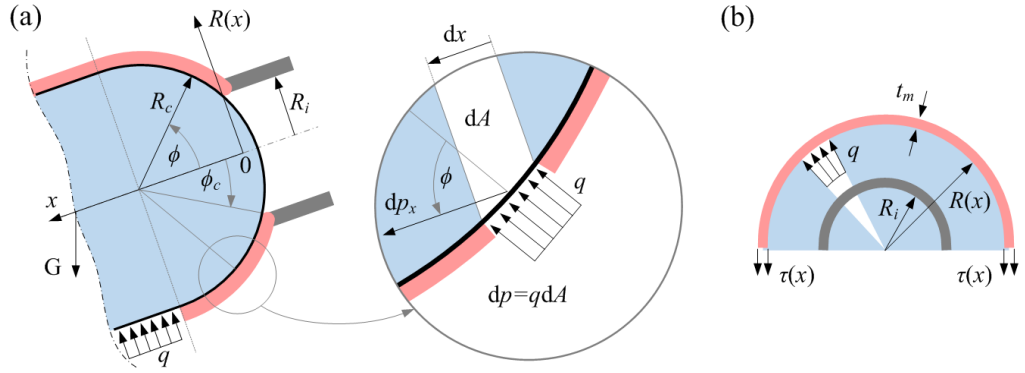

Fig. 2. (a) Hoop stress on the head and the body of the capsule. (b) Cross section of the intestinal tract. The intestinal tract without stretch is depicted in grey, and the one with stretch is shown in light red.

and the secondary spring, g_1, the interaction between m_1 and m_2 keeps switching between two phases: no contact $(x_1-g_1-x_2<0)$ and contact $(x_2-g_1-x_1\geq 0)$. Therefore, the mutual interactive force between the inner mass and the capsule can be written as

$$F_i = -c(\dot{x}_1-\dot{x}_2)-k(x_1-x_2)-H_1k_1(x_1-g_1-x_2), \quad (3)$$

where H_1 is the Heaviside function given by

$$H_1 = H(x_1-g_1-x_2). \quad (4)$$

Here, a detailed consideration of these switching phases can be found in Liu et al. (2013). Finally, the comprehensive equations of motion for the vibro-impact capsule system are written as

$$\begin{aligned}
\dot{x}_1 &= v_1,\\
\dot{v}_1 &= \tfrac{1}{m_1}[P_d\cos(\Omega t)+F_i]-g\sin\gamma,\\
\dot{x}_2 &= v_2,\\
\dot{v}_2 &= -\tfrac{1}{m_2}[F_i-F_{\text{hoop}}-F_{\text{gravity}}]-g\sin\gamma.
\end{aligned} \quad (5)$$

3. CONCLUDING REMARKS

Modelling of the self-propelled vibro-impact capsule system moving in a small intestinal tract was studied in this paper. Our studies focused on exploring the dynamics of the system and its performance in terms of average velocity and energy efficiency under variations of different system and control parameters, such as the forcing frequency and magnitude, the natural frequency of the inner mass, the contact gap between the inner mass and the secondary spring, and the capsule's radius and length.

Future works include prototype design and fabrication, test rig design, and experimental testing of the capsule prototype. Numerical studies in this paper will support the design and fabrication of the capsule prototype, and an artificial intestinal environment will be created for model validation. Research findings along this direction will be reported in a separate publication in due course.

ACKNOWLEDGEMENTS

Dr Yang Liu would like to acknowledge the financial support from EPSRC for his First Grant (Grant No. EP/P023983/1).

REFERENCES

Chernousko, F.L. (2002). The optimum rectilinear motion of a two-mass system. *J Appl Math Mech*, 66, 1–7.

Jiang, Z. and Xu, J. (2017). Analysis of worm-like locomotion driven by the sine-squared strain wave in a linear viscous medium. *Mechanics Research Communications*, 85, 33–44.

Koulaouzidis, A., Rondonotti, E., and Karargyris, A. (2013). Small-bowel capsule endoscopy: A ten-point contemporary review. *World Journal of Gastroenterology*, 19, 3726–3746.

Liu, Y., Wiercigroch, M., Pavlovskaia, E., and Yu, H. (2013). Modelling of a vibro-impact capsule system. *Int J Mech Sci*, 66, 2–11.

McCaffrey, C., Chevalerias, O., O'Mathuna, C., and Twomey, K. (2008). Swallowable-capsule technology. *Pervasive Computing IEEE*, 7, 23–29.

A Comparison of Co-Simulation Interfaces between Trnsys and Simulink: A Thermal Engineering Case Study

Georg Engel [*], **Gerald Schweiger** [**]

[*] *AEE - Institute for Sustainable Technologies, Gleisdorf, Austria (e-mail: g.engel@aee.at).*
[**] *AEE - Institute for Sustainable Technologies, Gleisdorf, Austria (e-mail: g.schweiger@aee.at).*

Keywords: Co-Simulation, Trnsys, Simulink, Type155, Compact Thermal Energy Storage

1. INTRODUCTION

Complex systems are usually decomposed into sub-systems, which are often modelled using different tools and methods. Co-simulation is a novel approach which aims at a cooperative simulation of several such tools. This paper presents a discussion of different co-simulation interfaces between Trnsys and Simulink. The interfaces are compared with respect to user-friendliness and flexibility, computational costs and accuracy. For this purpose, a thermal engineering case study is considered, which includes a compact thermal energy storage modelled in Trnsys and a heat sink modelled in Simulink. The interfaces considered include the Functional Mockup Interface (FMI), the Building Controls Virtual Test Bed (BCVTB) and a Component Object Model (COM), based on Trnsys' Type155.

2. CO-SIMULATION INTERFACES

FMI (Blochwitz et al., 2009) is a tool independent standard that has been developed in the ITEA2 European Advancement project MODELISAR. FMI supports both model exchange and co-simulation of dynamic models using a combination of xml-files and executables. FMI is currently supported by 95 tools and is used by various industries and universities. The available implementation of FMI between Trnsys and Simulink based on (Widl, 2015) and (Modelon, 2017) currently allows for a loose coupling scheme only.
BCVTB is a software environment developed at Lawrence Berkeley National Laboratory (Wetter, 2011). BCVTB is based on Ptolemy II, an open-source software framework supporting experimentation with actor-oriented design. BCVTB allows in general for a loose coupling scheme only.
Type155 is available in Trnsys' standard library, and establishes a communication between Trnsys and Matlab. In order to build a coupling between Trnsys and Simulink, a Matlab-script was developed to start and stop Simulink simulations at each iteration to ensure a strong coupling scheme, see (Engel et al., 2017a) and (Engel et al., 2017c).

3. METHOD

We introduce a case study where a sorption-based compact thermal energy storage is coupled thermally to a simple heat sink. The corresponding system design is shown in Figure 1. We discuss continuous time co-simulation only,

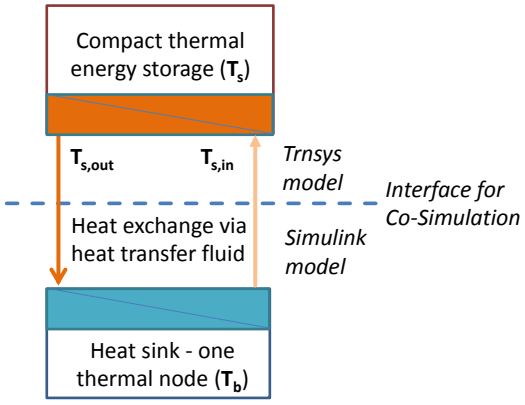

Fig. 1. The case study: A compact thermal energy storage is connected to a heat sink via a heat transfer fluid. The storage is modelled in Trnsys, while the heat sink is modelled in Simulink.

which is why discrete events like control switches are avoided. The compact thermal energy storage is modelled in Trnsys as detailed in (Engel et al. 2017b), results were presented also in (Engel et al., 2016). The heat sink including one thermal node is modelled in Simulink, as detailed in (Engel et al., 2017a).
The interface of the co-simulation is situated physically in the circuit of the heat transfer fluid. Correspondingly, the inlet and outlet temperatures $T_{\mathrm{s,in}}$ and $T_{\mathrm{s,out}}$ of the sorption reactor heat exchanger are the variables communicated via the interface between Trnsys and Simulink.
The different interfaces are compared with respect to user-friendliness and flexibility, accuracy and computational costs. The user-friendliness and the flexibility is judged only on a qualitative basis. The model is implemented also entirely in Trnsys, referred to as "reference simulation", employed with improved solver parameters to ensure high accuracy results. These serve for a discussion of the accuracy of the various co-simulations. The variables communicated via the co-simulation interface (inlet and outlet temperature of the heat transfer fluid) as well as the temperatures of the heat storage and the body are compared to the corresponding time-series results obtained in the reference simulation. The maximum deviation is considered as measure for the accuracy.

4. RESULTS

The behaviour trace of the system is shown as time series in Figure 2. The inaccuracies of the various interfaces are shown in Figures 3 and 4.

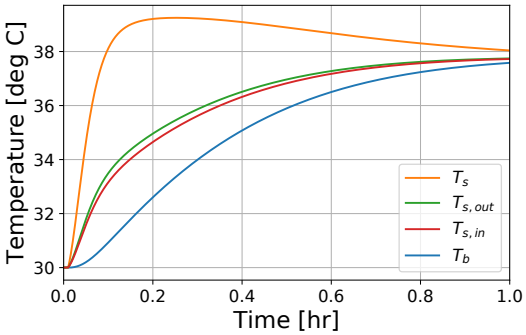

Fig. 2. Results for the temperatures of the heat sink T_b, the heat storage T_s, the outlet of the heat storage $T_{s,out}$ and the inlet of the heat storage $T_{s,in}$. The reaction increases the temperature of the heat storage up to roughly 39°C, which is in the further progress cooled through the thermal coupling to the heat sink, until the different temperatures eventually converge.

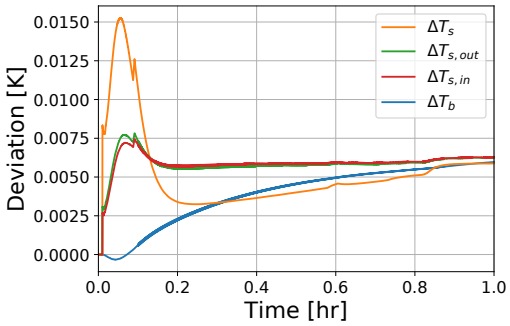

Fig. 3. Deviation of the different temperatures from the co-simulation based on the Type155 (strong coupling) compared to the ones of the reference simulation. The deviations of the monolithic simulation are in the same ballpark. For declaration of the variables see Figure 2.

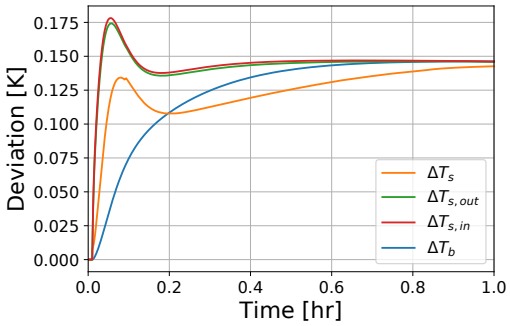

Fig. 4. Like Figure 3, but for the interface based on BCVTB or FMI (loose coupling).

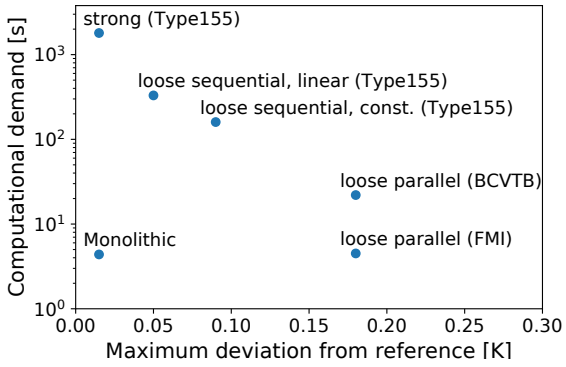

Fig. 5. An overview of different co-simulation interfaces, confronting accuracy and computational demand.

5. CONCLUSIONS

Considering the handling of the interface, the Type155-based interface offers a lot of flexibility to the user, allowing to implement loose and strong coupling co-simulation, and also various extrapolation schemes for the input variables. BCVTB offers out-of-the-box models for the various interfaces, while it is limited to loose coupling with a constant extrapolation of the input variables. FMI is a general and flexible approach, however, the implementation available specifically for Trnsys and Simulink is limited to loose coupling, due to restrictions imposed by Trnsys.
The accuracy and the computational demand of the implemented strong and loose coupling co-simulations differ significantly, as shown in Figure 5.

REFERENCES

Blochwitz, T. et al. (2009). The Functional Mockup Interface for Tool independent Exchange of Simulation Models. In *8th International Modelica Conference 2011*, 173–184. doi:10.3384/ecp12076173.

Engel, G., Chakkaravarthy, A., and Schweiger, G. (2017a). A methodology to compare different co-simulation interfaces: A thermal engineering case study. In *SIMULTECH 2017* . doi:10.5220/0006480204100415.

Engel, G. et al.(2016). Demonstration of a Real-scale Hardware-in-the-loop Seasonal Solar Sorption Storage System. In *10th International Renewable Energy Storage Conference*.

Engel, G., Asenbeck, S., Köll, R., Kerskes, H., Wagner, W., and van Helden, W. (2017b). Simulation of a seasonal, solar-driven sorption storage heating system. *Journal of Energy Storage*, 13, 40–47. doi: 10.1016/j.est.2017.06.001.

Engel, G., Chakkaravarthy, A.S., and Schweiger, G. (2017c). Co-Simulation between Trnsys and Simulink based on Type155. In *International Conference on Software Engineering and Formal Methods*.

Modelon (2017). FMI toolbox for Matlab/Simulink.

Wetter, M. (2011). Co-simulation of building energy and control systems with the Building Controls Virtual Test Bed. *Journal of Building Performance Simulation*, 4(3), 185–203. doi:10.1080/19401493.2010.518631.

Widl, E. (2015). TRNSYS FMU Export Utility: https://sourceforge.net/projects/trnsys-fmu/.

Hierarchies of Modeling Infections: Comparison of Reaction-Diffusion System and Cellular Automaton

Cordula Reisch * **Ihno Schrot** **

* *Inst. Computational Mathematics, Technische Universität Braunschweig, Germany (e-mail: c.reisch@tu-bs.de).*
** *Universität Heidelberg, Germany.*

Keywords: Model family, partial differential equations, cellular automaton, liver infection.

1. INTRODUCTION

Various mathematical models reproducing similar observations have different advantages and disadvantages. Consequently, the question evolves how to compare and relate models in a hierarchical order. We present two approaches for modeling viral liver infections such as hepatitis C, a world wide disease which chronifies in up to 75% of the cases, cf. Schwab (2011). The first model using reaction-diffusion equations allows analytical longterm behavior predictions. The second model, a cellular automaton, describes the interactions of virus and T cells in a smaller dimension and includes new mechanisms.

2. MODELING HEPATITIS

We list properties of the liver as well as of viral liver infections. Based on this, we present a reaction-diffusion system in Sec. 2.2 and a cellular automaton in Sec. 2.3.

2.1 Liver infections

The liver lobes consist of hepatic lobules connected to the veins. This results in a ramified small-scale system.

After the infection, the immune system reacts to the virus. First, dendritic cells report the presence of the virus. As a reaction, T cells are produced in the lymphocytes. Different kinds of T cells are involved in the primary immune reaction. T helper cells induce B lymphocytes to produce antigens. The killer T cells identify infected cells and trigger the programmed cell death. Killer T cells cause most of the damage caused by a liver infection, cf. Bowen et al. (2002). The incubation time between the infection and the attack of the killer T cells is several weeks.

The inflammation starts with an acute phase in which the killer T cells try to eliminate the virus. Then, either the virus is eliminated and the immune reaction fades, or in case of a chronic course, the virus remains in remote areas of the liver and a diminished immune reaction persists.

2.2 Reaction-diffusion model

In the model, first presented by Kerl (2012), the immune reaction is summarized in a term of T cells v. The interactions of the virus u and the T cells v are based on Lotka-Volterra equations with a logistic growth $w(u) = (1-u)\frac{u-\epsilon}{u+\kappa}$ of the virus, including the Allee effect, and an inflow term $j[u]$ which describes the inflow of T cells through the vein depending on the total virus population in the liver. For $\mathbf{x} \in \Omega$ and $t > 0$, the equations

$$\begin{aligned} \dot{u} &= uw(u) - \gamma uv + \alpha \Delta u\,, \\ \dot{v} &= j[u] - \eta(1-u)v + \beta \Delta v - \mu \Delta u \end{aligned} \tag{1}$$

describe the reactions between the virus and T cells, the diffusion spread of the populations (α, β) and the chemotactic effects (μ), which direct T cells to the virus. Initial values $u_0(\mathbf{x})$ and $v_0(\mathbf{x})$ and homogenous Neumann boundary conditions are used.

The occurrence of chronifications depends on the minimal eigenvalue λ of the negative Laplacian in Ω with Neumann boundary conditions, the maximal diffusion coefficient $d = \max\{\alpha, \beta\}$ and the maximal change rate of the reactions M. If these parameters fulfill $\sigma = \lambda d - M > 0$, chronic courses can be ruled out, see Smoller (1994).

2.3 Cellular automaton

We use a rectangular geometry with $n \times m$ cells and an additional cut with regard to the small-scale liver structure. The possible states of a cell are obstacle (-1), dead (0), healthy (1), infected (2) and attacked by T cells (3), see Fig. 1. We use these discrete states and a coupled map lattice for the amount of T cells in each cell. The automaton is inhomogeneous because we model an inflow area as described in Sec. 2.1. The update uses a Neumann neighborhood with radius 1. The chemotactic effects are gained from a Moore neighborhood with radius 3.

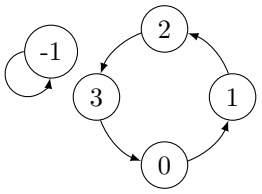

Fig. 1. Change of cell states: Obstacles (-1) remains, healthy cells (0) change over infected (1), and attacked by T cells (2) to dead (3). Dead cells may get healthy.

3. RESULTS

In this section, we compare the simulations of both models and highlight similarities and differences.

3.1 Reaction-diffusion model

The area Ω has a cut at $x_1 = 0.5$ with regard to the small-scale liver structure and an inflow area around $(x_1, x_2) = (1, 1)$. Depending on the parameters in Eq. (1), both main courses, healing and chronification, are reproducible. For parameters with $\sigma < 0$, we may observe spatial inhomogeneous, stationary solutions, which we interpret as chronic infections, see Fig. 2. The virus persists in an area remote from the inflow area. The immune reaction does not fade out.

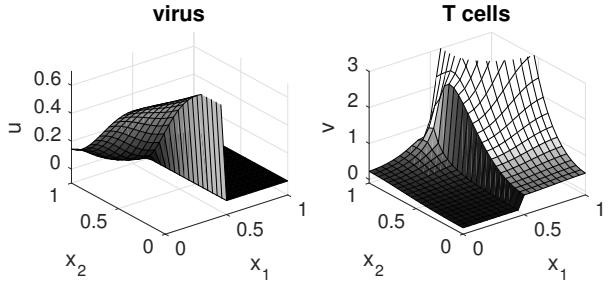

Fig. 2. Stationary virus and T cell distribution in a chronic infection course, modeled with Eq. (1).

3.2 Cellular automaton (CA)

The numerical simulation by hands of the cellular automaton reproduces both disease courses as well as the model in Eq. (1). For small chemotaxis parameters μ, it shows a behavior which is equivalent to the reaction-diffusion model. The system behavior of a chronic infection is comparable to the simulation in Fig. 2. For healing courses with strong chemotactic effects, we observe a new mechanism. A group of T cells follows the virus behind the cut. As an effect, there is a gap between the separated group and the inflow area without any virus and T cells. The group of T cells eliminates the virus and dies thereafter. The separated group of T cells in an active phase is shown in Fig. 3, in the lower right, behind the obstacle.

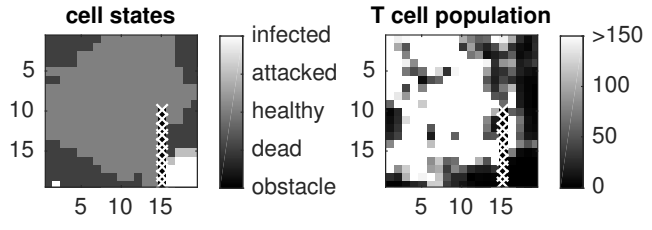

Fig. 3. Isolation of T cells in an active phase, simulation by hands of the cellular automaton. The barrier of obstacles is marked with white crosses.

3.3 Model family

Mathematical modeling starts with the observation of the object to be modeled. We presented the most relevant observations in Sec. 2.1. They form our constructed reality, the observed liver. From a philosophical point of view, the observations are already a first model of the real world or, in our case, of the real liver. In the next modeling step, we chose a way of modeling, e.g. partial differential equations, cellular automata or stochastic models. For each modeling approach, we select mechanisms for describing the constructed reality, i.e. the interaction of virus and T cells or chemotactic effects. Both presented models used an area with a cut as a model for the small-scale liver structure.

As a joint result, both models show healing and chronic courses, in dependency of the size of the area Ω, the chosen parameters and the initial conditions. The cellular automaton inherits the longterm behavior of system (1). This is reasonable because the average of the cellular automaton fits to the finite differences of the reaction diffusion system, cf. Weimar (1994). Besides this similarity, the numerical simulation of the cellular automaton shows a separation of some T cells, see Fig. 3. This effect is not included in the reaction diffusion model. Due to this, the question evolves, wether a reaction diffusion model including this additional effect exists, see Fig. 4.

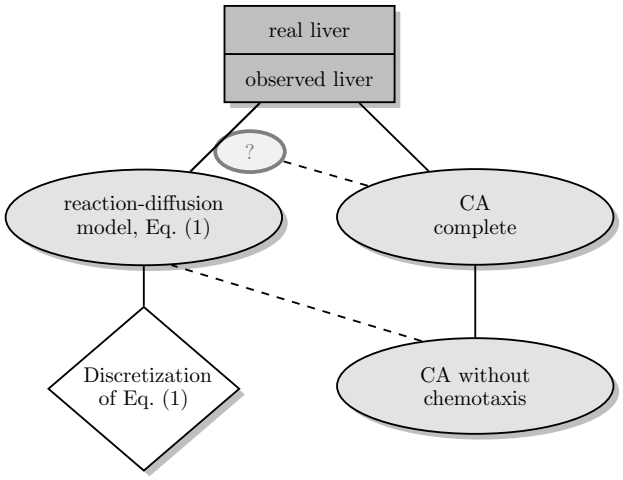

Fig. 4. Model hierarchy. Downwards: sub-models, upwards: model refinements. The discretization of Eq. (1) is equivalent to the CA without chemotaxis. This one is a discrete sub-model of the continuous Eq. (1) and a simplification of the CA described in Sec. 3.2. It is questionable whether there is a refined PDE model reproducing the separated T cell group.

REFERENCES

D.G. Bowen, A. Warren, T. Davis, M.W. Hoffmann, G.W. McCaughan, D.F. De St Groth and P. Bertonlino: Cytokine-dependent bystander hepatitis due to intrahepatic murine CD8 T-cell activation by bone marrow-derived cells. *Gastroenterology* 12, 1252-1264, 2002.

H.-J. Kerl, D. Langemann and A. Vollrath: Reaction-diffusion equations and the chronification of liver infections. *Math. Comput. Simulat.* 82, 2145-2156, 2012.

M. Schwab: *Encyclopedia of Cancer* Springer, 2011.

J. Smoller: *Shock waves and reaction-diffusion equations.* Springer, 1994.

J.R. Weimar, J.-P. Boon: Class of cellular automata for reaction-diffusion systems. *Phys. Rev.* 49, 1749-1752, 1994.

Efficient Ray Tracing with Real Weather Data

Pascal Richter * **Janna Tinnes** * **Peter Schwarzbözl** **
Amadeus Rong **

* *RWTH Aachen University, Department of Mathematics, MathCCES, Schinkelstraße 2, 52062 Aachen, Germany (e-mail: richter@mathcces.rwth-aachen.de).*
** *German Aerospace Center (DLR), Institute for Solar Research, Linder Höhe, 51147 Cologne, Germany.*

Keywords: Solar energy, Mathematical models, Optimization, Simulation, Sampling, Quadrature, Software Performance

1. INTRODUCTION

The optimized layout of a central receiver power plants requires an accurate but fast simulation of the plant operation depending on its design parameters. Ray tracing models are commonly used to calculate the solar flux concentrated by the heliostat field. The computation time for an annual performance simulation is critical for the usage in an optimization procedure.

The main influences on run-time are the spatial (number of rays) and temporal (number of time points) discretization. For the annual simulation, usually weather data from clear sky models is used, e.g. the meteorological radiation model (MRM), see Badescu (2008). Using non-symmetric measured weather data (e.g. from a TMY file) the temporal sample points have to be chosen in a different way.

In this paper, different temporal integration approaches are presented and discussed for the case of measured weather data.

2. TEMPORAL INTEGRATION

The annual energy production E_{year} of the solar tower power plant can be computed with the sum over all days d and the integral of the daily power production,

$$E_{\text{year}} = \sum_{d=1}^{365} \underbrace{\left(\int_{\text{sunrise}}^{\text{sunset}} P(t,d)\ \mathrm{d}t \right)}_{=:E(DNI(d))}, \tag{1}$$

where $E(DNI(d))$ describes the direct normal irradiation at day d. The computation of the annual energy production can be accelerated by reducing the number of samples per day by quadrature rules and reducing the number of days by clustering.

2.1 Quadrature methods for intraday sampling

Quadrature methods can be used to approximate the integral of the daily energy $E(DNI(d))$ by using specific sampling points and their according temporal weight. Because hourly data is provided by the weather files, so far just quadrature methods with a constant time step of one hour are used, e.g. the summed midpoint and summed trapezoidal rule. But to apply quadrature rules with higher order (e.g. Gauss-Legendre quadrature rule) and reduce the number of sampling points, a higher temporal resolution than just hourly constant data is helpful and would further increase the accuracy. It is possible to achieve a higher resolution from the hourly averaged measured data by using data reconstruction, see Fig. 2.1.

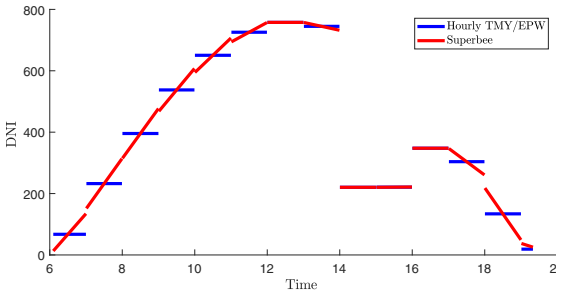

Fig. 1. Reconstruction of the hourly averaged measured DNI data (blue) using the conservative and TVD superbee limiter (red).

DNI value at day d around the time t_i changes as follows:

$$DNI(t,d) = DNI(t_i,d) + \sigma(t_i)\cdot(t-t_i),$$
$$t \in [t_i - \frac{\Delta t}{2}, t_i + \frac{\Delta t}{2}], \tag{2}$$

with its originally measured value $DNI(t_i,d)$, and reconstructed slope $\sigma(t_i)$.

Calculating the reconstructed slope with the superbee limiter, which fulfills the required properties of conservativ and TVD, see Leveque (1986), the error between the hourly averaged measured values and the real values can be reduced by 32% for a cloudy day. For a clear sky, e.g. the data from the MRM model, the error can be reduced by 85%.
With the reconstructed values three different quadrature-rules, midpoint, trapezoidal and Gauss-Legendre with a changing number of quadrature points are investigated

for computing the daily energy, see Fig. 2.1. For Mumbai around 7 sample points per day are needed for a sufficient accuracy.

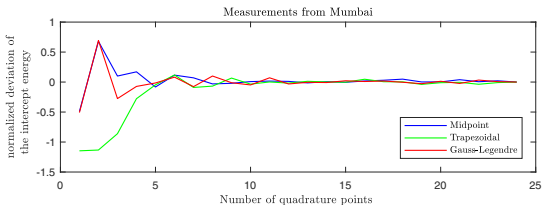

Fig. 2. Comparison of the three quadrature-rules with a changing number of quadrature points for Mumbai.

2.2 Clustering of days

Considering the different, day dependent weather conditions an averaged DNI value of the neighboring days can be computed by

$$D\tilde{N}I(d_k) = \sum_{i=\frac{d_{k-1}+d_k}{2}}^{\frac{d_k+d_{k+1}}{2}} \frac{2}{d_{k+1}-d_{k-1}} DNI(d_i). \qquad (3)$$

Using this averaged DNI for the simulated, representing day the annual energy can be computed with the summed trapezoidal-rule

$$E_{\text{year}} \approx \sum_{k=1}^{m-1} \frac{d_{k+1}-d_k}{2} \left(E(D\tilde{N}I(d_{k+1})) + E(D\tilde{N}I(d_k)) \right). \qquad (4)$$

Comparing the annual energy computed with the aggregated approach with the usually used constant day sampling, the new approach allows to reduce the number of sample points to only 38 points, see Fig. 2.2.

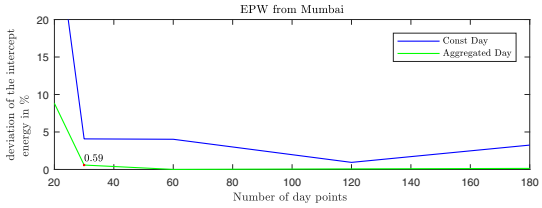

Fig. 3. Comparison of the constant day sampling with the aggregated day sampling approach for a changing number of sample points.

3. ANGULAR INTEGRATION

The annual energy production E_{year} can also be computed by considering the sun path in the domain of the solar angles instead of the time domain. Therefore, the DNI needs to be transformed from the time domain into the angular domain. Then, two-dimensional quadrature rules are used to compute the annual energy, e.g. midpoint-rule, trapezoidal-rule, Gauss-Legendre quadrature-rule. The underlying quadrature method defines a region in the angular-solar domain. All DNI values of this region are aggregated to one average DNI value, while the number of data points resemble the temporal weight of this region, see Fig 3.

Using the integration in the azimuth-altitude domain the number of sampling points for the computation of the annual energy for Mumbai can be reduced to 18.

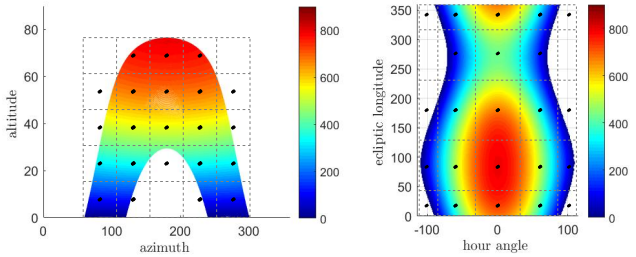

Fig. 4. Integration domain for the transformation to azimuth and altitude with a midpoint grid (left) and to ecliptic longitude hour angle with a Gauss-Legendre grid (right).

A transformation to the hour angle and the ecliptic longitude gives further enhancements, such as the almost rectangular shape of the integration domain, see V. Grigoriev and Blanco (2015). For Mumbai the number of sample points could be reduced further to just 16 sample points per year.

4. FIELD EFFICIENCY MAP

Looking at the equation for the power of one heliostat P_i with the number of considered losses n,

$$P_i(t,d) = A_i \cdot I_{\text{DNI}}(t,d) \cdot \sum^{n} \eta_{n,i}(t,d) \qquad (5)$$

the power depends linearly on the intensity of the sun $I_{\text{DNI}}(t,d)$. This allows to uncouple the DNI values and the efficiency of the power plant. A field efficiency map is computed, including the efficiency of the power plant for all possible sun positions, by using e.g polynomial interpolation or spline functions. With this field efficiency map the energy of the power plant can be computed extremely fast by only multiplying the efficiency with the corresponding DNI value.

5. CONCLUSION

For industrial performance computations, real measured weather data should be used. For that case, smarter integration methods and a field efficiency map are successfully used, such that the simulation time is strongly reduced.

ACKNOWLEDGEMENTS

The authors acknowledge the financial support by the Federal Ministry for Economic Affairs and Energy of Germany in the project SolFieOpt (project number 0324039) for the RWTH Aachen University and the project ISAPT (project number 0325655) for the German Aerospace Center (DLR).

REFERENCES

Badescu, V. (2008). *Modeling Solar Radiation at the Earth's Surface*. Springer Berlin Heidelberg.

Leveque, R. (1986). *Theory and Numerics for Hyperbolic Conservation Laws*. Teubner, Stuttgart.

V. Grigoriev, C.C. and Blanco, M. (2015). Fourier sampling of sun path for applications in solar energy. *Solar PACES South Africa*.

Modeling Actomyosin Clustering depending on Medium ATP-Concentrations ⋆

Christian Wölfer * **Robert J. Flassig** * **Michael Mangold** *,**

* *Max Planck Institute for Dynamics of Complex Technical Systems, 39106 Magdeburg, Germany*
** *TH Bingen, 55411 Bingen am Rhein, Germany*

Keywords: Actin-Myosin Cortex, Dynamic Modeling, Distributed Model, System Analysis, Synthetic Biology

1. INTRODUCTION

The cell cortex, formed by membrane linked actin filaments, is an important functional unit of almost all eukaryotic cells and involved in a variety of major cellular processes like cell division, motility, formation and stabilization of cell shape(Alberts et al., 1994). Hence, modeling and understanding of the cell cortex is of great interest in the context of bottom-up synthetic biology (Schwille, 2011).
The polymeric and filamentous protein F-actin forms the mesh-like and therefore viscoelastic material. Together with the myofilament myosin II, a filamentous protein with a variety of motor domain (Fig. 1b), the cortex has active gel properties.
An experimental study with a synthetic 'minimal actin cortices' (Vogel and Schwille, 2012) showed that spatial cluster formation of actin cortices only occur in a range of 0.1 to 10 μM and surprisingly not for high ATP concentrations (Vogel et al., 2013).

2. THE ACTOMYOSIN MODEL

To explain the experimental findings qualitatively a two dimensional continuum model was developed in polar coordinates to represent a cut through a spherical cell or vesicle. Additionally, the actomyosin cortex properties were mimicked by assuming that the actin and myosin species remain close to the membrane in a very thin layer. Thus, the actomyosin cortex can be described as a one dimensional ring system with periodic boundary conditions. In contrast, the energy source ATP, which is consumed by the cortex, diffuses from the inside through the whole two dimensional system (A.1). The spatial distribution of the cortex species obeys an advection-diffusion equation with additional mass action reaction rates (A.2-A.4).
The underlying force generating biochemical circuit is the well described myosin cross bridge cycle (Rayment et al., 1993). We used a simplified spatial distributed myosin cross bridge model (Fig. 1a) where energy provided by ATP hydroxylation causes a conformational change of the myosin head (M). The active myosin head is able to interact with F-actin forming an active actomyosin complex (A-M). The unstable active actomyosin complex performs a further conformational change of the myosin head triggering an acceleration of the F-actin filament due to the mechanical coupling. To close the cycle, ATP is needed to release the myosin head from the F-actin filament.
We assumed that the binding and releasing of the myosin head are the rate-determining steps. Thus, force generation and the ATP hydroxylation take place during myosin binding (r_1) and detachment (r_2).
The momentum equation with viscoelastic material behaviors is described by

$$\frac{D(\rho \boldsymbol{v})}{Dt} = \frac{\partial}{\partial \varphi}(\sigma_v + \sigma_e + \sigma_m), \tag{1}$$

consisting of the material derivation for F-actin momentum $\rho \boldsymbol{v}$, and terms for viscous stress σ_V as one dimensional representation of the viscous stress tensor $\tau_{\varphi\varphi}$ (Bird et al., 1960), elastic stress $\sigma_e = \alpha A^2(1-e)$ derived by Lewis et al. (2014) with the related evolution of network deformation e (A.5) and the contractile stress σ_m generated by the myosin pulls.
As a new approach, the contractile stress is modeled by the force generating mass action rate r_1 times a force transmission state χ:

$$\sigma_m = \psi \cdot r_1 \cdot \chi \tag{2}$$

The fundamental idea is that the myosin can only bend, break or compact filaments when on both sides of the myofilament (Fig. 1b) enough heads are connected to the F-actin mesh (Wölfer et al., 2016). Otherwise, the power stroke would not be transmitted sufficiently and instead move the myosin molecule along the actin filament. The force transmission should increase the more myosin heads are bound to the actin filament. Thus, in our formulation the local force transmission is determined by the concentration of inactive actomyosin scaled by the total amount of myosin.

$$\chi = \frac{A\text{-}M}{A\text{-}M + M} \tag{3}$$

In contrast to other actin models (Jülicher et al., 2007; Ramaswamy and Jülicher, 2016) polymerization, depolymerization and, as a consequence, polarity of F-actin filaments were not taken into account because of an insignificant role of those processes in the underlying *in vitro* experiment Vogel et al. (2013).

⋆ This work is a part of the MaxSynBio consortium, which is funded by the German Federal Ministry of Education and Research and the Max Planck Society.

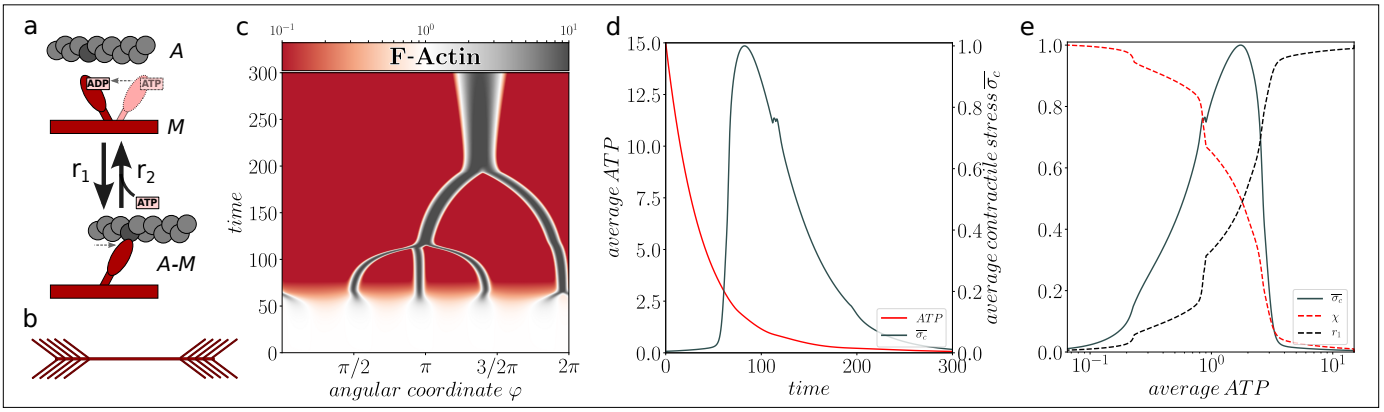

Fig. 1. a: Myosin cross bridge model b: myofilament c: clustering actin cortex d: average ATP concentration and normalized contractile stress over time e: normalized curves force generation r_1, transmission χ and contractile stress against average ATP conc.

3. RESULTS AND DISCUSSION

Simulation of the nondimensionalized and discretizised model showed that clustering occurs even when the ATP concentration (consumed in r_2) drops under 5 units according with an increase of the contractile stress σ_m (Fig. 1c,d). The network clustered gradually by merging of smaller clusters, pursuant to the periodic initial conditions, consistent to the experimental observations. Finally, the contraction ceases after ATP depletion, recognizable by diminishing of the cluster due to diffusion.

As expected, for high ATP level concentrations the generated force by r_1 is very high . Thus, the majority of myosin heads are in the unbound state resulting in a poor transmission of force χ and therefore small contractile stress σ_m or rather a movement of the myofilament along the actin fiber. With decreasing ATP concentration the force transmission is improved accompanied by a decreasing force generation, resulting in a nearly bell-shaped dose-response curve for σ_m (Fig. 1e).

Accordingly, we are able to generate the desired dose-response relation for ATP and resulting contraction, with the suggested formulation for contractile stress. In addition *in vitro* studies, which observed a movement of myosin proteins along actin filaments, support our new formulation (Sheetz and Spudich, 1983; Vogel et al., 2013).

REFERENCES

Alberts, B., Bray, D., Lewis, J., Raff, M., Roberts, K., and Watson, J.D. (1994). Molecular biology of the cell. 3rd. *New York: Garland Pub*, 43(1294), 67.

Bird, R.B., Stewart, W.E., and Lightfoot, E.N. (1960). *Transport Phenomena*. John Wiley and Sons.

Jülicher, F., Kruse, K., Prost, J., and Joanny, J.F. (2007). Active behavior of the cytoskeleton. *Physics Reports*, 449, 3–28.

Lewis, O.L., Guy, R.G., and Allard, J.F. (2014). Actin-myosin spatial patterns from a simplified isotropic viscoelastic model. *Biophysical journal*, 107, 863–870.

Ramaswamy, R. and Jülicher, F. (2016). Activity induces traveling waves, vortices and spatiotemporal chaos in a model actomyosin layer. *Scientific Reports 6*.

Rayment, I., Holden, H.M., Whittaker, M., Yohn, C.B., Lorenz, M., Holmes, K.C., and Milligan, R.A. (1993). Structure of the actin-myosin complex and its implications for muscle contraction. *Science*, 261, 58–65.

Schwille, P. (2011). Bottom-up synthetic biology: Engineering in a tinkerers world. *Science*, 333, 1252–1254.

Sheetz, M.P. and Spudich, J.A. (1983). Movement of myosin-coated fluorescent beads on actin cables in vitro. *Nature*, 303, 31–35.

Vogel, S.K., Petrasek, Z., Heinemann, F., and Schwille, P. (2013). Myosin motors fragment and compact membrane-bound actin filaments. *Cytoskeleton (Hoboken)*, 70, 706–717.

Vogel, S.K. and Schwille, P. (2012). Minimal systems to study membrane-cytoskeleton interactions. *Curr Opin Biotechnology*, 23, 758–765.

Wölfer, C., Vogel, S.K., and Mangold, M. (2016). A curvilinear model approach: Actin cortex clustering due to atp-induced myosin pulls. *IFAC-PapersOnLine*, 49(26), 103–108.

Appendix A. PDE SYSTEM

$$\frac{\partial ATP}{\partial t} = D_T \left(\frac{1}{R}\frac{\partial}{\partial R}\left(R\frac{\partial ATP}{\partial R}\right) + \frac{1}{R^2}\frac{\partial^2 ATP}{\partial \varphi^2}\right) \quad \text{(A.1)}$$

$$\frac{\partial A}{\partial t} = -\frac{\partial (A\cdot V)}{\partial \varphi} + D_A \frac{\partial^2 A}{\partial \varphi^2} - r_1 + r_2 \quad \text{(A.2)}$$

$$\frac{\partial M}{\partial t} = -\frac{\partial (M\cdot V)}{\partial \varphi} + D_M \frac{\partial^2 M}{\partial \varphi^2} - r_1 + r_2 \quad \text{(A.3)}$$

$$\frac{\partial A\text{-}M}{\partial t} = -\frac{\partial (A\text{-}M\cdot V)}{\partial \varphi} + D_A \frac{\partial^2 A\text{-}M}{\partial \varphi^2} + r_1 - r_2 \quad \text{(A.4)}$$

$$\frac{\partial e}{\partial t} = -\frac{\partial (e\cdot V)}{\partial \varphi} + \lambda(1-e) \quad \text{(A.5)}$$

Optimal Asset Allocation with Heterogeneous Persistence of Shocks ⋆

Domenica Di Virgilio * **Fulvio Ortu** ** **Federico Severino** ***
Claudio Tebaldi ****

* *Bank of Slovenia (e-mail: domdivirgilio@gmail.com).*
** *Università Bocconi and IGIER, (e-mail: fulvio.ortu@unibocconi.it)*
*** *Università della Svizzera Italiana, SFI and Università Bocconi (e-mail: federico.severino@usi.ch)*
**** *Università Bocconi and IGIER, (e-mail: claudio.tebaldi@unibocconi.it)*

Keywords: optimal portfolio, Epstein-Zin preferences, multiple horizons, persistence of returns, shocks heterogeneity.

1. INTRODUCTION

There is wide evidence that financial time series are the outcome of the superposition of processes with heterogeneous frequencies. This is true, in particular, for market return. Indeed, log market return can be decomposed into uncorrelated components that explain the reaction to shocks with different persistence. The instrument that allows us to do so is the Extended Wold Decomposition of Ortu, Severino, Tamoni and Tebaldi (2017). Hence, we construct portfolios of these components in order to maximize the utility of an agent with a fixed investment horizon. In particular, we build upon Campbell and Viceira (1999) solution of the optimal consumption-investment problem with Epstein-Zin utility, by using a rebalancing interval of 2^J periods. It comes out that the optimal asset allocation involves all the persistent components of market log return up to scale J. Such components play a fundamental role in characterizing both the myopic and the intertemporal hedging demand. Moreover, the optimal policy prescribes an increasing allocation on more persistent assets when the investor's relative risk aversion rises. Finally, portfolio reallocation every 2^J periods is consistent with rational inattention. Indeed, observing assets value is costly and transaction costs make occasional rebalancing optimal.

2. SUMMARY

Given a zero-mean weakly stationary time series $\mathbf{x} = \{x_t\}_t$, the Classical Wold Decomposition allows us to write any x_t as an infinite sum of uncorrelated innovations:

$$x_t = \sum_{k=0}^{\infty} \alpha_h \varepsilon_{t-h}, \tag{1}$$

where $\boldsymbol{\varepsilon} = \{\varepsilon_t\}_t$ is a unit variance white noise and α_h are the so-called impulse response functions. The Extended Wold Decomposition introduced by Ortu, Severino, Tamoni and Tebaldi (2017), instead, decomposes x_t into uncorrelated *persistent components* $x_t^{(j)}$ associated with specific scales j:

$$x_t = \sum_{j=1}^{+\infty} x_t^{(j)}, \qquad x_t^{(j)} = \sum_{k=0}^{+\infty} \beta_k^{(j)} \varepsilon_{t-k2^j}^{(j)}. \tag{2}$$

Here each *detail process* $\boldsymbol{\varepsilon^{(j)}} = \left\{\varepsilon_t^{(j)}\right\}_t$ is an $MA(2^j - 1)$ with respect to the fundamental innovations of $\mathbf{x}$ and $\beta_k^{(j)}$ is the *multiscale impulse response* associated with scale j and time-shift $k2^j$. Specifically,

$$\varepsilon_t^{(j)} = \frac{1}{\sqrt{2^j}} \left(\sum_{i=0}^{2^{j-1}-1} \varepsilon_{t-i} - \sum_{i=0}^{2^{j-1}-1} \varepsilon_{t-2^{j-1}-i} \right) \tag{3}$$

and

$$\beta_k^{(j)} = \frac{1}{\sqrt{2^j}} \left(\sum_{i=0}^{2^{j-1}-1} \alpha_{k2^j+i} - \sum_{i=0}^{2^{j-1}-1} \alpha_{k2^j+2^{j-1}+i} \right) \tag{4}$$

for any $j \in \mathbb{N}$ and $k \in \mathbb{N}_0$. Moreover, fixed a maximum scale J, it is possible to write the orthogonal decomposition

$$x_t = \sum_{j=1}^{J} x_t^{(j)} + m_t^{(J)}, \tag{5}$$

where $m_t^{(J)}$ constitutes a *residual component*. With a small abuse of notation we denote $x_t^{(J+1)} = m_t^{(J)}$. The support $\{t - k2^j\}$ of details $\varepsilon_t^{(j)}$ is sparser and sparser as the scale raises, conveying the intuition of increasing duration, together with the higher order of MA. Therefore, scale-specific impulse responses $\beta_k^{(j)}$ capture the sensitivity of x_t with respect to underlying shocks with increasing durations of 2, 4, 8, ... periods.

We apply the previous decomposition to the process of market log returns associated, for instance, to S&P 500 index. We consider an Epstein-Zin investor that chooses how to distribute her wealth among $J+1$ risky assets and a riskless security, with a periodic rebalancing every 2^J periods. Log returns of these risky assets are supposed to mimic the persistent components $x_t^{(1)}, \ldots, x_t^{(J+1)}$ of

⋆ This abstract is for the Minisymposium *Dynamic models in economics and management.*

market log returns. Moreover, each $x_t^{(j)}$ is assumed to follow an $AR(1)$ process on its own scale:

$$x_{t+2^j}^{(j)} = \mu_j (1-\phi_j) + \phi_j x_t^{(j)} + s_j \varepsilon_{t+2^j}^{(j)}. \quad (6)$$

Finally, the fundamental innovations ε_t are i.i.d. and distributed as standard normal.

By denoting portfolio loadings by $\pi_t(j)$, the return over 2^J periods is, then,

$$R_{p,t+2^J} = \sum_{j=1}^{J+1} \pi_t(j) e^{x_{t+2^J}(j)} + \left(1 - \sum_{j=1}^{J+1} \pi_t(j)\right) e^{2^J r_f}. \quad (7)$$

The previous assumptions allow the vector of returns $\mathbf{z}_t = \left[x_t^{(1)}, \ldots, x_t^{(J+1)}\right]'$ to follow the VAR dynamics

$$\mathbf{z}_{t+2^J} = \Phi_0 + \Phi \mathbf{z}_t + \mathbf{v}_{t+2^J}, \quad (8)$$

where Φ_0 is a vector, Φ is a diagonal matrix and $\mathbf{v}_t$ is a multivariate white noise on the time grid $\{t - k2^J\}$ with $k \in \mathbb{Z}$. The orthogonality properties of the Extended Wold Decomposition are crucial for obtaining a white noise here.

Our investor has recursive preferences but her utility depends on the current consumption and the certainty equivalent associated with the utility 2^J periods ahead:

$$\max_{\{C_t, \boldsymbol{\pi}_t\}_{t=k2^J}} U_t = \left((1-\beta) C_t^{(1-\gamma)/\theta} + \beta E_t \left[U_{t+2^J}^{1-\gamma}\right]^{1/\theta}\right)^{\theta/(1-\gamma)}$$
$$sub \qquad W_{t+2^J} = R_{p,t+2^J}(W_t - C_t),$$

where $0 < \beta < 1$ is the preference discount factor, $\gamma > 0$ is the coefficient of relative risk aversion, ψ denotes the intertemporal elasticity of substitution (IES) and $\theta = (1-\gamma)/\left(1-\psi^{-1}\right)$. Consumption C_t and wealth W_t are scalars, while the vector $\boldsymbol{\pi}_t$ contains portfolio weights associated with the $J+1$ securities into consideration.

The previous VAR representation of returns allows us to embed our optimal consumption-investment problem into Campbell, Chan and Viceira (2003) strategic allocation theory. In particular, we exploit the affine guess

$$\boldsymbol{\pi}_t = A_0 + A_1 \mathbf{z}_t, \quad (9)$$

paired with the quadratic log consumption-wealth ratio

$$c_t - w_t = b_0 + B_1' \mathbf{z}_t + \mathbf{z}_t' B_2 \mathbf{z}_t, \quad (10)$$

where b_0 is a scalar, A_0 and B_1 are vectors and B_2 is a square matrix.

After approximating log return, budget constraint and Euler equation following the standard derivation with pace 2^J, we determine the approximate optimal asset allocation, which is driven by myopic and hedging motives:

$$\boldsymbol{\pi}_t = A_{0,myopic} + A_{0,hedging} + (A_{1,myopic} + A_{1,hedging})\,\mathbf{z}_t. \quad (11)$$

The orthogonality of the Extended Wold Decomposition ensures that the *myopic part of* $\pi_t(j)$ depends only on $x_t^{(j)}$. Moreover, if $\gamma = 1$ - because, for instance, the investor has logarithmic utility - the *hedging part* of $\boldsymbol{\pi}_t$ disappears. Then, for a myopic investor the weight $\pi_t(j)$ depends only on $x_t^{(j)}$.

Instead, if $\gamma \neq 1$, the resulting capital allocation on the j-th component of market returns depends also on the other components. In particular, $\pi_t(j)$ depends on $x_t^{(i)}$ with $i \neq j$ through the term $A_{1,hedging}\mathbf{z}_t$. Hence, the share $\pi_t(j)$ invested in the component $x_t^{(j)}$ depends on the components at scales $i \neq j$ just for hedging purposes.

Finally, although the investor's horizon is 2^J, the optimal capital allocation involves all the components of market returns, not only the one at scale J.

Once A_0 and A_1 are determined, we assess that the log consumption-wealth ratio is actually quadratic in the state vector $\mathbf{z}_t$ and we are able to find the optimal b_0, B_1 and B_2.

We corroborate our analysis by estimating optimal weights of a portfolio investing in persistent components of S&P 500 index. By employing daily data, we can capture the impact of two-day shocks on time scale $j = 1$, (roughly) weekly shocks on scale $j = 2$ and so on and so forth. Moreover, we consider investors with different values of risk aversions. If $\gamma = 1$ the agent is fully myopic and the weights are all equal across scales. When γ increases, instead, the investor diversifies within persistent assets and portfolio loadings to high scales become prominent.

REFERENCES

[1] Campbell J.Y., Chan Y.L, Viceira L.M. (2003), "A multivariate model of strategic asset allocation", *Journal of financial economics*, 67, 1, 41-80.

[2] Campbell J.Y., Viceira L.M. (1999), "Consumption and portfolio decisions when expected returns are time varying", *Quarterly Journal of Economics*, 114, 433-495.

[3] Ortu F., Severino F., Tamoni A., Tebaldi C. (2017), "A persistence-based Wold-type decomposition for stationary time series", *Available at https* : *//papers.ssrn.com/sol3/papers.cfm?abstract_id* = 1973049.

A solution to shape optimization problems using time evolution equations

Daisuke Murai * **Atsushi Kawamoto** * **Tsuguo Kondoh** *

* *Toyota Central Research and Development Laboratories Institute, 41–1, Yokomichi, Nagakute, Aichi, Japan (e-mail: Daisuke-Murai@mosk.tytlabs.co.jp).*

Keywords: Shape optimization problems, Time evolution equations, Adjoint variable method

1. INTRODUCTION

This paper deals with a numerical analysis method based on time evolution equations for solving nonparametric boundary shape optimization problems of domain boundaries. Shape optimization problems often appear at the final stage of design.

2. SHAPE OPTIMIZATION PROBLEM

Let $\Omega \subset \mathbb{R}^d,\ d = 2, 3$ be a design domain with boundary $\partial\Omega = \Gamma_{\rm N} \cup \Gamma_{\rm D}$ where $\Gamma_{\rm N}$ is a Neumann boundary and $\Gamma_{\rm D}$ is a Dirichlet boundary, $D = \cup\Omega$ be a set of design domains. We denote that $\boldsymbol{n} = (n_1, \cdots, n_d)$ is an outward normal unit vector on the boundary $\partial\Omega$, $\mathbf{0}$ is a zero vector and $\boldsymbol{\nabla} = (\partial/\partial x_1, \cdots, \partial/\partial x_d)$ for a point $\boldsymbol{x} = (x_1, \cdots, x_d)$ in Ω. We define the steady-state heat conduction problem:

$$\begin{aligned} &-\boldsymbol{\nabla}\cdot(q\boldsymbol{\nabla}u) = b, \quad \text{in} \quad \Omega, \\ &-(q\boldsymbol{\nabla}u)\cdot\boldsymbol{n} = p, \quad \text{on} \quad \Gamma_{\rm N}, \\ &u = u_{\rm D}, \quad \text{on} \quad \Gamma_{\rm D}, \end{aligned} \tag{1}$$

where $b \in \mathbb{R}$, $p \in \mathbb{R}$ and $u_{\rm D} \in \mathbb{R}$ are given functions, $q > 0$ is a given constant. In the problem (1), b presents a heat source in Ω, p presents a heat flux on $\Gamma_{\rm N}$, $u_{\rm D}$ presents a temperature defined on the boundary $\Gamma_{\rm D}$ and q presents a thermal conductivity. Using the solution u to the problem (1), we define the objective function as a thermal resistance presented by

$$f_0(\Omega) = \int_\Omega bu{\rm d}\boldsymbol{x} + \int_{\Gamma_{\rm N}} pu{\rm d}\gamma - \int_{\Gamma_{\rm D}} u_{\rm D}\,(q\boldsymbol{\nabla}u)\cdot\boldsymbol{n}{\rm d}\gamma \tag{2}$$

and the constraint function as a volume for domain measure such as

$$f_1(\Omega) = \int_\Omega 1{\rm d}\boldsymbol{x}. \tag{3}$$

A shape optimization problem is defined by

$$\min_\Omega \left\{ f_0(\Omega);\, f_1(\Omega) \le f_1(\Omega_0),\ u \text{ is a solution to (1)} \right\}, \tag{4}$$

where $\Omega_0 \in D$ is a given initial domain with boundary $\partial\Omega_0 = \Gamma_{\rm M} \cup \Gamma_{\rm F}$ and $f_1(\Omega_0)$ is the initial value of f_1 given as

$$f_1(\Omega_0) = \int_{\Omega_0} 1{\rm d}\boldsymbol{x}.$$

Here $\Gamma_{\rm M}$ is a moving boundary, i.e., $\Gamma_{\rm M}$ is deformed in the computational steps of optimization process and $\Gamma_{\rm F}$ is a fixed boundary, i.e., $\Gamma_{\rm F}$ is fixed in the computational steps of optimization process.

A Lagrangian function of the problem (4) is given as

$$\mathscr{L}(\Omega, u, v_0, v_1, \lambda_1) = \mathscr{L}_0(\Omega, u, v_0) + \lambda_1 \mathscr{L}_1(\Omega, u, v_1), \tag{5}$$

where $\mathscr{L}_i(\Omega, u, v_i),\ i = 0, 1$ are Lagrangian functions for $f_i,\ i = 0, 1$, defined as

$$\mathscr{L}_i(\Omega, u, v_i) = f_i + \int_\Omega \left\{ \boldsymbol{\nabla}\cdot(q\boldsymbol{\nabla}u) + b \right\} v_i {\rm d}\boldsymbol{x}. \tag{6}$$

respectively. Here $v_i,\ i = 0, 1$ are the Lagrange multipliers for the problem (1).

3. SHAPE DERIVATIVE

In order to solve the problem (4) by gradient based method, the shape gradient for the objective function f_0 and the constraint function f_1 with respect to the variation of Ω are requested. The shape gradient $\boldsymbol{g}_i,\ i = 0, 1$ can be obtained using the stationary conditions of $\mathscr{L}_i,\ i = 0, 1$. The shape gradient of $f_i,\ i = 0, 1$ are represented as

$$\frac{{\rm d}\mathscr{L}_i(\Omega, u, v_i)}{{\rm d}\Omega} = \frac{\partial\mathscr{L}_i}{\partial u}\frac{\partial u}{\partial\Omega} + \frac{\partial\mathscr{L}_i}{\partial v_i}\frac{\partial v_i}{\partial\Omega} + \frac{\partial\mathscr{L}_i}{\partial\Omega} \tag{7}$$

where $\partial u/\partial\Omega = \delta u$ is a variation of u, $\partial v_i/\partial\Omega = \delta v_i$ are variations of $v_i,\ i = 0, 1$.

The stationary condition of $\mathscr{L}_i,\ i = 0, 1$ for all variations δv_i of $v_i,\ i = 0, 1$, such that

$$\frac{\partial\mathscr{L}_i}{\partial v_i}\frac{\partial v_i}{\partial\Omega} = \int_\Omega \left\{ \left(\boldsymbol{\nabla}\cdot(q\boldsymbol{\nabla}u) + b \right)\delta v_i \right\} {\rm d}\boldsymbol{x} = 0, \quad i = 0, 1$$

are equivalent to the condition that u is the solution to the problem (1).

The stationary condition of $\mathscr{L}_i,\ i = 0, 1$ for all variations δu, $\delta u = 0$ on $\Gamma_{\rm D}$ of u such that

$$\begin{aligned} \frac{\partial\mathscr{L}_0}{\partial u}\frac{\partial u}{\partial\Omega} &= \int_\Omega \left\{ \boldsymbol{\nabla}\cdot(q\boldsymbol{\nabla}v_0) + b \right\}\delta u {\rm d}\boldsymbol{x} \\ &\quad - \int_{\Gamma_{\rm N}} \delta u \left\{ p + (q\boldsymbol{\nabla}v_0)\cdot\boldsymbol{n} \right\} {\rm d}\gamma \\ &\quad + \int_{\Gamma_{\rm D}} \left\{ v_0 - u_{\rm D} \right\} \delta\,(q\boldsymbol{\nabla}u)\cdot\boldsymbol{n}{\rm d}\gamma = 0, \\ \frac{\partial\mathscr{L}_1}{\partial u}\frac{\partial u}{\partial\Omega} &= \int_\Omega \left\{ \boldsymbol{\nabla}\cdot(q\boldsymbol{\nabla}v_1)\,\delta u \right\} {\rm d}\boldsymbol{x} \\ &\quad - \int_{\Gamma_{\rm N}} \delta u\,(q\boldsymbol{\nabla}v_1)\cdot\boldsymbol{n}{\rm d}\gamma \\ &\quad + \int_{\Gamma_{\rm D}} v_1\delta\,(q\boldsymbol{\nabla}u)\cdot\boldsymbol{n}{\rm d}\gamma = 0 \end{aligned}$$

are equivalent to the condition that $v_i,\ i = 0, 1$ are the solutions to the following adjoint problems, respectively:

$$\begin{aligned} &-\boldsymbol{\nabla}\cdot(q\boldsymbol{\nabla}v_0) = b, \quad \text{in} \quad \Omega, \\ &-(q\boldsymbol{\nabla}v_0)\cdot\boldsymbol{n} = p, \quad \text{on} \quad \Gamma_{\mathrm{N}}, \\ &v_0 = u_{\mathrm{D}}, \quad \text{on} \quad \Gamma_{\mathrm{D}}, \end{aligned} \tag{8}$$

$$\begin{aligned} &-\boldsymbol{\nabla}\cdot(q\boldsymbol{\nabla}v_1) = 0, \quad \text{in} \quad \Omega, \\ &-(q\boldsymbol{\nabla}v_1)\cdot\boldsymbol{n} = 0, \quad \text{on} \quad \Gamma_{\mathrm{N}}, \\ &v_1 = 0, \quad \text{on} \quad \Gamma_{\mathrm{D}}. \end{aligned} \tag{9}$$

Here, we fix u and $v_i,\ i = 0, 1$ with the solutions of problems (1), (8) and (9). By (7), we have the shape gradients for $f_i,\ i = 0, 1$:

$$\frac{\mathrm{d}\mathscr{L}_0}{\mathrm{d}\Omega} = \frac{\partial\mathscr{L}_0}{\partial\Omega} = \{2bu - (q\boldsymbol{\nabla}u)\cdot\boldsymbol{\nabla}u\}\,\boldsymbol{n} = g_0\boldsymbol{n},$$
$$\frac{\mathrm{d}\mathscr{L}_1}{\mathrm{d}\Omega} = \frac{\partial\mathscr{L}_1}{\partial\Omega} = \boldsymbol{n} = g_1\boldsymbol{n}.$$

See Azegami (1994).

4. SOLUTION TO THE PROBLEM (4) USING TIME EVOLUTION EQUATIONS

In order to obtain the solution to the problem (4), we introduce following time evolution equations:

$$\begin{aligned} &\frac{\partial\boldsymbol{v}(t,\boldsymbol{x})}{\partial t} = \boldsymbol{\nabla}\cdot(c\boldsymbol{\nabla}\boldsymbol{v}(t,\boldsymbol{x})) - \alpha\boldsymbol{v}(t,\boldsymbol{x}), \quad \text{in} \quad \Omega_0\times[0,T], \\ &\boldsymbol{v}(0,\boldsymbol{x}) = \boldsymbol{0} \quad \text{in} \quad \Omega_0, \\ &-(c\boldsymbol{\nabla}\boldsymbol{v}(t,\boldsymbol{x}))\cdot\boldsymbol{n} = -\left(g_0(t) + \lambda_1 g_1(t)\right)\boldsymbol{n} \text{ on } \Gamma_{\mathrm{M}}\times[0,T], \\ &\boldsymbol{v}(t,\boldsymbol{x}) = \boldsymbol{0} \quad \text{on} \quad \Gamma_{\mathrm{F}}\times[0,T], \end{aligned} \tag{10}$$

$$\frac{\partial\boldsymbol{\rho}(t,\boldsymbol{x})}{\partial t} = \boldsymbol{v}(t,\boldsymbol{x}) \quad \text{in} \quad [0,T]\times\Omega_0. \tag{11}$$

where $c > 0$, $\alpha \geq 0$ and $T > 0$ are given constants. We chose sufficiently large T so that

$$|f_0(\Omega(T)) - f_0(\Omega(T-\delta t))| \,/\, |f_0(\Omega(T-\delta t))| \leq \varepsilon_0$$

holds for a small time step δt and given small constant $\varepsilon_0 > 0$. λ_1 denotes a Lagrange multiplier for f_1. In this paper, we set λ_1 as

$$\lambda_1 = -\frac{\|g_0(t)\boldsymbol{n}\|}{\|g_1(t)\boldsymbol{n}\|}\exp(\beta f_1), \quad \|\cdot\| = \sqrt{\langle\cdot,\cdot\rangle}, \tag{12}$$

so that KKT condition $g_0(T)\boldsymbol{n}+\lambda_1 g_1(T)\boldsymbol{n} = \boldsymbol{0},\ \lambda_1 f_1(T) = 0,\ \lambda_1 \geq 0,\ f_1(T) \leq 0$ holds at the end of optimization process. Here $\beta > 0$ is the given constant for controlling the violation of constraint function during the optimization process (See Kawamoto (2013)). We consider the violation of f_1 in the optimization process of computation and chose $\beta > 0$ so that $f_1 \leq 0$ holds for all $t \in [0,T]$. The solution to the problem (4) is obtained by $\Omega = \Omega_0 + \boldsymbol{\rho}$.

5. NUMERICAL EXAMPLE

We analyze a two-dimensional problem related to a steady-state heat conduction problem (1). Fig. 1 shows the initial domain Ω_0 with boundary $\partial\Omega_0 = \Gamma_{\mathrm{M}}\sup\Gamma_{\mathrm{F}}$. Fig. 2 shows a design domain Ω with boundary $\partial\Omega = \Gamma_{\mathrm{N}}\cup\Gamma_{\mathrm{D}}$ where $\Gamma_{\mathrm{N}} = \Gamma_{\mathrm{N1}}\cup\Gamma_{\mathrm{N2}}$. Table 1 shows problem settings of the problem (10) and (1). Fig. 3 shows the solution u to the problem (1) in the initial domain Ω_0 and the mesh used in this analysis. Fig. 4 shows the solution u to the problem (1) in the optimized domain Ω. Fig. 5 shows the history of objective function and constraint function during the optimization process. In fig. 5, objective function and constraint function are normalized by using each initial values.

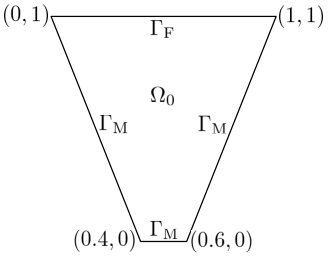

Fig. 1. The original domain Ω_0 with boundary $\partial\Omega_0$

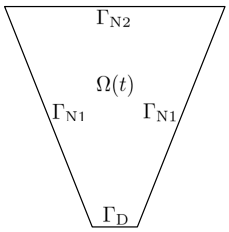

Fig. 2. A design domain Ω with boundary $\partial\Omega$

Table 1. Problem settings of the problem (10) and (1)

Problem	Settings
problem (10)	$T = 1.5$, $c = 1$, $\alpha = 0$, $v_2 = 0$ on $\Gamma_{\mathrm{M}}\times[0,T]$
problem (1)	q=1, b=0, p=0 on Γ_{N1}, p=−1 on Γ_{N2}, u_{D}=0
equation (12)	$\beta = 100$

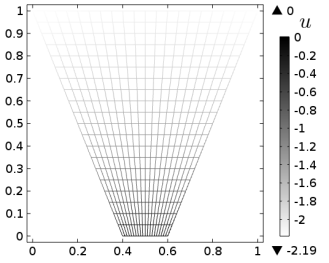

Fig. 3. The solution to the problem (1) in Ω_0

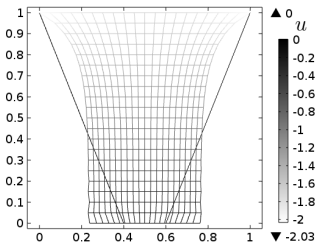

Fig. 4. The solution to the problem (1) in Ω

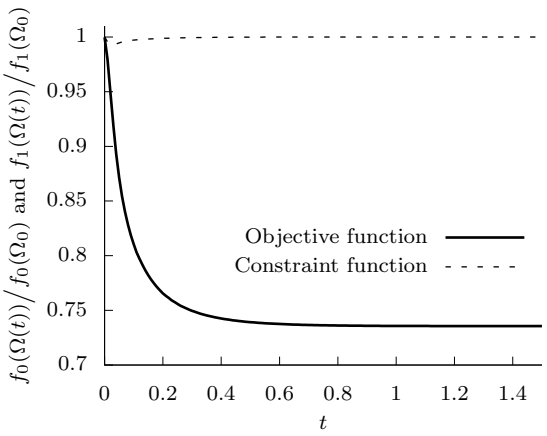

Fig. 5. The history of objective function and constraint function

REFERENCES

H. Azegami. Solution to domain optimization problems. *Trans. Japan Society Mechanics and Engineering* 60(574): pages 1479–1994, 1994.

A. Kawamoto, T. Matsumori, T. Nomura, T. Kondoh, S. Yamasaki, S. Nishiwaki. Topology optimization by a time-dependent diffusion equation. *International Journal for Numerical Methods in Engineering* 93(8): pages 795–817, 2013.

Biologically inspired topology optimization model with a local density penalization ⋆

Misaki Sakashita * **Tsuguo Kondoh** ** **Atsushi Kawamoto** **
Emmanuel Tromme ** **Shigeru Kondo** *

* *Osaka University, Suita, Osaka 565-0871, Japan*
(e-mail: sakashitamsk@gmail.com)
** *Toyota Central R&D Labs., Inc., Nagakute, Aichi 480-1192, Japan*
(e-mail: atskwmt@mosk.tytlabs.co.jp)

Keywords: Topology Optimization, Wolff's law, Vertebra, Local density penalization

1. INTRODUCTION

Wolff's law states that bone morphology evolves according to their external mechanical loading. Following this law, researchers have tried to simulate bone shape formation, especially for trabecular bone, using topology optimization (Huiskes et al., 2000). Less attention has been given to the bone outer shape, composed of cortical bone. However, trabecular bone and cortical bone are both mainly formed by osteoblasts and osteoclasts. Therefore, we hypothesize that the bone outer shape also adapts to the external forces. The aim of this research is to understand the mechanism that generates the bone outer shape by reproducing the latter using topology optimization.

The mathematical model we developed is inspired by the fish vertebra. The fish vertebra can be divided into two parts (Fig. 1): an inner hourglass-like structure and an outer lateral structure (blue-colored part). Based on our observations, it turns out that numerous species present a similar hourglass-like structure but that the lateral structure strongly depends on the fish species (Fig. 2). Lateral structures can be classified into two types. The first type exhibits a ridge structure with one or more thick bone plates and the second type exhibits a network structure in which fine bones are randomly oriented. These differences seem related to the fish motion, i.e. the swimming type of the fish, and therefore, it is assumed that lateral structures also evolve based on external loading conditions. Because fish has the variety of swimming type, the model we built can produce the structure resistant to the various movements respectively as well as explain the bone formation.

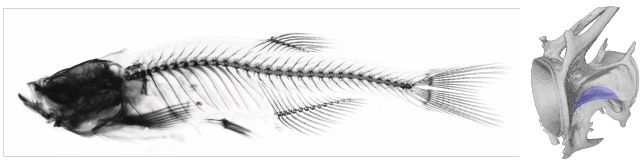

Fig. 1. Zebrafish skeleton (left) and a single vertebra scanned with micro-CT (right). The zebrafish is a model organism.

⋆ The authors acknowledge CREST and Toyota Central R&D Labs for their support.

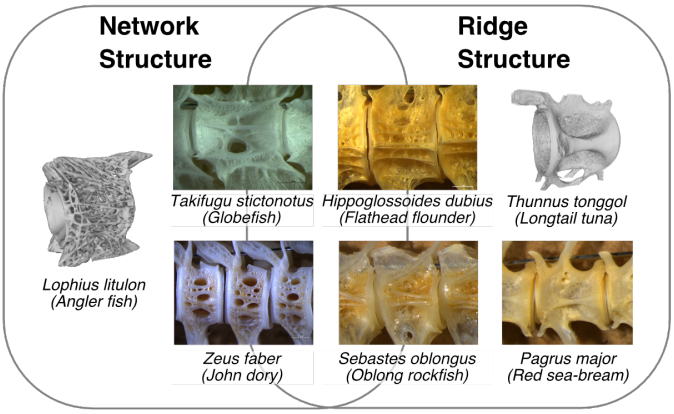

Fig. 2. Varieties of fish vertebra shape.

In standard topology optimization, the density at each material point is only constrained by the total volume of material. However, the activity of osteoblast and osteoclast is more a local phenomenon. Hence, the standard topology optimization problem is supplemented with a local density penalization to mimic this local phenomenon. The developed mathematical model to study the fish vertebra formation is hereafter detailed.

2. MATHEMATICAL MODELING

The adopted optimization problem governing the bone density $\rho = \rho(\boldsymbol{x})$ distribution is stated as

$$\begin{aligned} \min_{\rho(\boldsymbol{x})} \; & f[\rho] \equiv f_0[\rho] + f_{\text{stab}}[\rho] + f_{\text{local}}[\overline{\rho}[\rho]] \\ \text{s.t. } & g[\rho] \equiv \int_\Omega \rho \, d\Omega - \bar{V} \leq 0, \end{aligned} \tag{1}$$

where Ω is the design domain and $\bar{V}$ the upper bound of the total volume constraint $g[\rho]$. The objective function $f[\rho]$ is composed of three functions that read,

$$f_0[\rho] \equiv \int_\Omega \tilde{\sigma}[\rho] : \tilde{\varepsilon}[\rho] \, d\Omega, \tag{2}$$

$$f_{\text{stab}}[\rho] \equiv C_{\text{stab}} \int_\Omega (\boldsymbol{\nabla}\rho)^2 \, d\Omega, \; C_{\text{stab}} > 0, \tag{3}$$

$$f_{\text{local}}[\overline{\rho}[\rho]] \equiv C_{\text{local}} \int_\Omega \mathrm{H}(\overline{\rho}[\rho] - \overline{\rho}_{\text{local}}) \, d\Omega, \; C_{\text{local}} > 0. \tag{4}$$

$f_0[\rho]$ is the total strain energy in the design domain ($\tilde{\sigma}$ and $\tilde{\varepsilon}$ are the stress and strain tensors). $f_{\text{stab}}[\rho]$ is a diffusion term smoothing the distribution of ρ. $f_{\text{local}}[\overline{\rho}[\rho]]$ enforces a penalty to the objective function when the locally averaged density $\overline{\rho}$ exceeds the prescribed upper bound $\overline{\rho}_{\text{local}}$ (H is the Heaviside function). $\overline{\rho}$ is obtained by averaging $\rho = \rho(\boldsymbol{x})$ with the Helmholtz PDE based filter (Kawamoto et al., 2011) as:

$$\begin{aligned} \overline{\rho} = \overline{\rho}(\boldsymbol{x}): \quad & -R^2\boldsymbol{\nabla}^2\overline{\rho} + \overline{\rho} = \rho \quad \text{in} \quad \Omega, \\ & R^2\frac{\partial\overline{\rho}}{\partial n} = 0 \quad \text{on} \quad \Gamma \equiv \partial\Omega; \quad R > 0, \end{aligned} \tag{5}$$

where R is the filtering radius.

To solve the optimization problem (1), a method based on a time dependent reaction-diffusion equation (6) is employed (Kawamoto et al., 2013). Equation (6) is driven by the sensitivity S, in which the Lagrangian multiplier λ is introduced as follows:

$$\begin{aligned} \rho = \rho(\boldsymbol{x}, t): \quad & m\frac{\partial\rho}{\partial t} = -S \quad \text{in} \quad \Omega, \\ & C_{\text{stab}}\frac{\partial\rho}{\partial n} = 0 \quad \text{on} \quad \Gamma; \\ m > 0, \quad & S \equiv \frac{\delta F[\rho]}{\delta\rho}, \quad F[\rho] \equiv f[\rho] + \lambda g[\rho]. \end{aligned} \tag{6}$$

Solving this optimization problem gives an optimized structure with respect to the imposed boundary and loading conditions. The penalization term enables to control locally the feature size.

3. NUMERICAL EXAMPLES

The proposed mathematical model is implemented in the commercial software COMSOL Multiphysics®. The mathematics module as well as the solid mechanics module are used.

A 2-D cantilever beam problem is first solved to demonstrate the developed method. The results illustrate that finer features can be obtained by increasing the penalization on local densities (Fig. 3).

Fig. 3. Cantilever beam design problem (left) and the results with small effect (center) and large effect (right) of local density penalization.

The 3-D design domain of the fish vertebra is illustrated in Fig. 4. Since the hourglass-like structure is assumed to be identical for all fish species, the part of the design domain illustrated in Fig. 4 (on the left) is composed of bones ($\rho = 1$) regardless of external forces. The yellow parts, composed of two wedges of 30° spaced by 180°, contain nerves and blood vessels, thus no bone is allowed ($\rho = 0$). Finally, the design domain is thus composed of the two external blue parts. Compression forces are applied to the external surface of the hourglass structure (red-colored surfaces) in the axial direction (black arrows).

Without local density penalization, thick beams appear similarly to the ridge structure. Penalizing locally the density, thinner beams are promoted and they tend to form a network (Fig. 5).

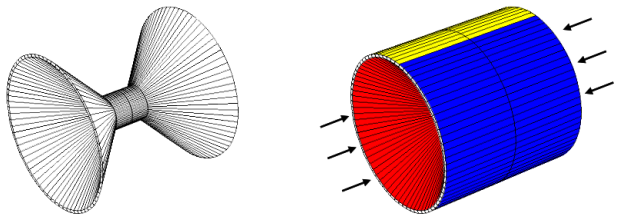

Fig. 4. Design domain of the fish vertebra.

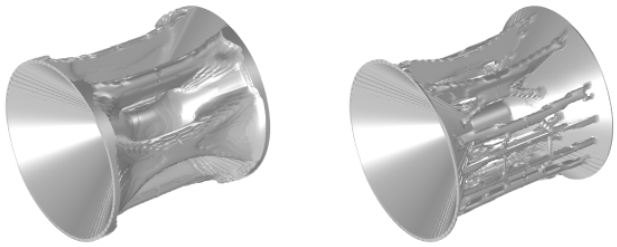

Fig. 5. Optimization result without local density penalization (left) and with local density penalization (right).

4. CONCLUSION

A mathematical model has been developed to generate fish vertebra using topology optimization combined with a local density penalization. Numerical results show that the proposed model can produce both types of lateral structures, i.e. ridge structure and network structure, which are similar to the actual fish bone. In the future, it would be interesting to be able to produce various forms of fish vertebra by only adjusting a few parameters of the penalization law.

REFERENCES

Huiskes, R., Ruimerman, R., van Lenthe, G.H., and Janssen, J.D. (2000). Effects of mechanical forces on maintenance and adaptation of form in trabecular bone. *Nature*, 405(6787), 704–706. doi:10.1038/35015116.

Kawamoto, A., Matsumori, T., Nomura, T., Kondoh, T., Yamasaki, S., and Nishiwaki, S. (2013). Topology optimization by a time-dependent diffusion equation. *International Journal for Numerical Methods in Engineering*, 93(8), 795–817. doi:10.1002/nme.4407.

Kawamoto, A., Matsumori, T., Yamasaki, S., Nomura, T., Kondoh, T., and Nishiwaki, S. (2011). Heaviside projection based topology optimization by a PDE-filtered scalar function. *Structural and Multidisciplinary Optimization*, 44(1), 19–24. doi:10.1007/s00158-010-0562-2.

Exact Sub-Systems and their Link to Modelling

Janina Dierkes * **Dirk Langemann** *

* *Institute of Computational Mathematics, Technische Universität Braunschweig, Germany (e-mail: j.dierkes@tu-bs.de).*

Keywords: mathematical modelling, model families, sub-models, approximation

1. INTRODUCTION

The approximation of a high-dimensional, discrete or continuous, quantified or even non-quantified system by a lower-dimensional well-quantified system occurs in multiscale numerics, cf. Ames (1969), in lower-dimensional representations and in modelling, cf. Murray (2008). In particular in modelling, the small system is interpreted as a model for the larger system, oftentimes a real-world problem. Here, we discuss basic ideas by hands of finite dimensional specifications.
We regard a system of ordinary differential equations

$$\dot{X} = F(X) \ , \ X(0) = X^{\text{ini}} \in \Omega \subseteq \mathbb{R}^N \tag{1}$$

in $X = X(t) \in \mathbb{R}^N$ with the initial value X^{ini}. In general, the N equations in (1) are coupled. We aim to approximate this system by a lower dimensional system in $Y \in \mathbb{R}^M$, $M < N$ and sometimes formally $M \leq N$, named

$$\dot{Y} = G(Y) \ , \ Y(0) = Y^{\text{ini}} \in \Theta \subseteq \mathbb{R}^M \tag{2}$$

with the initial value Y^{ini}. One essential question is wether $Y(t) \approx \varphi(X(t))$ with a link map $\varphi : \mathbb{R}^N \to \mathbb{R}^M$ is an appropriate approximation for certain $X^{\text{ini}} \in \Omega$, $Y^{\text{ini}} \in \Theta$ and $t \in [0, T]$.

Definition 1. We call the system $\dot{Y} = G(Y)$ an exact sub-system of $\dot{X} = F(X)$, if $Y(t) = \varphi(X(t))$ for all $t \in [0, T]$ results from $Y^{\text{ini}} = \varphi(X^{\text{ini}})$ for all $X^{\text{ini}} \in \Omega$.

Remark 2. Equation (2) needs not to be a sub-system in the sense that it is a part of (1). Here, we understand an exact sub-system as the existence of an exact link map φ.

Example 3. Let us regard the harmonic oscillator with $F : \mathbb{R}^2 \to \mathbb{R}^2$ and $\dot{X} = F(X) = (X_2, -X_1)^{\mathrm{T}}$. Even for this comparably simple system, we find surprisingly many exact sub-systems. By transition to complex variables, we find the two sub-systems $\dot{Y} = \pm \mathrm{i} Y = G(Y)$ with $\varphi : \mathbb{R}^2 \to \mathbb{C}$ by $\varphi(X) = \frac{1}{2}(1, \mp \mathrm{i})^{\mathrm{T}} \cdot X = Y$, which are independent from each other. By

$$\varphi : X \mapsto c(X_1^2 + X_2^2) = Y$$

with $\dot{Y} = G(Y) = 0$, we generate a sub-system containing the conservation of energy. In addition,

$$\varphi : X \mapsto t = Y = \arctan \frac{-X_2}{X_1}$$

and $G = 1$ pose an unexpected exact sub-system of the harmonic oscillator as long as $0 \leq t < 2\pi$ holds.
These four exact sub-systems are part of the model family of all models of the harmonic oscillator.

2. TERMS, DEFINITIONS AND PROPERTIES

A particularly simple sub-system is induced by a selection of components of X. Such a selection is a projection

$$\pi_J : X = (X_1, \ldots, X_N)^T \mapsto (X_{j_1}, \ldots, X_{j_k})^T = Y \tag{3}$$

with a set of indices $J = \{j_1, \ldots, j_k\}$. The projection $\pi_J : \mathbb{R}^N \to \mathbb{R}^M$ with $M = |J|$ defines the link $\varphi = \pi_J$ between the system in $X \in \mathbb{R}^N$ and a sub-system in $Y \in \mathbb{R}^M$.

2.1 Reducibility, separability, adjacency structure

Definition 4. A system (1) is called reducible, if there is a set $J \subset I = \{1, \ldots, N\}$, $J \neq I$, forming an exact sub-system with $\varphi = \pi_J$ and $G(\pi_J X) = \pi_J F(X)$. A system (1) is called separable, if $\varphi = \pi_{I \setminus J}$ forms an exact sub-system, too.

Reducibility and separability are recognized by the adjacency structure of ∇F. A system (1) is reducible if $\nabla F \in \mathbb{R}^{N \times N}$ is an identically reducible matrix for all $X \in \Omega$. It is separable if ∇F has block structure.
Furthermore, ∇F displays the causal dependency structure of the system (1), i.e. X_i causally depends on X_j, if the entry $(\nabla F)_{ji}$ in the j-th row and i-th column of the matrix ∇F is non-vanishing for some $X \in \Omega$.

2.2 Coordinates and concepts

The terms of reducibility and separability depend on coordinates. In order to achieve a causal structure, which is as simple as possible, coordinates are sought, in which the system is reducible or even separable. This search is formalised by a transformation $\mathcal{T} : \mathbb{R}^N \to \mathbb{R}^N$ with a bijective diffeomorphism $\mathcal{T} : X \mapsto X'$. The transformed system in $X' \in \mathbb{R}^N$ is

$$\dot{X}' = [\nabla \mathcal{T}^{-1} X'] \cdot F(\mathcal{T}^{-1} X') = \tilde{F}(X'). \tag{4}$$

If there is a transformation so that the system (4) is reducible or separable, we call the system (1) potentially reducible or separable, respectively.

2.3 Linear systems

Applied to linear systems $\dot{X} = AX = F(X)$ with $A \in \mathbb{R}^{N \times N}$, we look for a linear sub-system $\dot{Y} = BY = G(Y)$ with $B \in \mathbb{R}^{M \times M}$ and initial values as mentioned above.

A spectral decomposition induces a transformation $\mathcal{T} : R^N \to \mathbb{R}^N$ given by

$$X' = \mathcal{T}X := V^{-1}X,$$

where $V \in \mathbb{C}^{N\times N}$ contains the eigenvectors of A with $AV = V\Lambda$. Then, (4) is $\dot{X}' = \Lambda X'$, where $\Lambda \in \mathbb{C}^{N\times N}$ is the Jordan matrix of eigenvalues.

In case of a non-diagonalisable matrix A, the transformed system separates into Jordan blocks. Each Jordan block represents an exact sub-system, not further separable. Let us regard an upper tridiagonal $r \times r$-Jordan block between the rows $m - r + 1$ and m in Λ. Then, all projections

$$\varphi = \pi_J\mathcal{T} : X \mapsto (X'_{m-j}, \ldots, X'_m)^{\mathrm{T}} = Y$$

with $0 \le j \le r - 1$ induce exact sub-systems. An amount of k Jordan blocks is equivalent to k independent sub-systems. In particular the system $\dot{X}' = \Lambda X'$ is separable if Λ contains more than one Jordan block, because they depict sub-systems that can be described independently from each other.

In case of a diagonalisable A, the matrix Λ is diagonal. Hence, the system $\dot{X}' = \Lambda X'$ is completely separable. All projections $\varphi = \pi_I\mathcal{T} : X \mapsto Y$ with any set of indices $I = \{i_1, \ldots, i_m\} \subseteq \{1, \ldots, N\}$ induce exact sub-systems. In contrast to the non-diagonalisable Jordan case, any selection of components is admissible, and the system $\dot{X}' = \Lambda X'$ has a very simple causal structure.

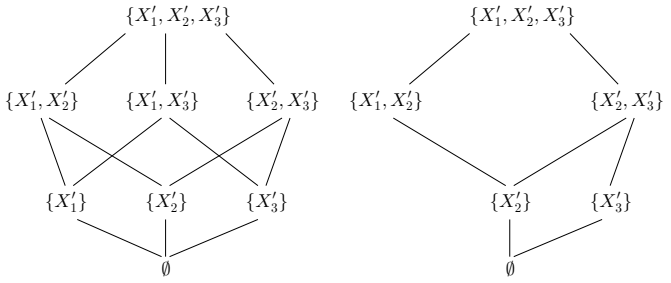

(a) diagonal (b) Jordan

Fig. 1. Families of exact linear sub-systems for $N = 3$. Left: diagonalisable A, full family. Right: Two Jordan blocks, one with $r = 2$, $m = 2$, and one with $r = 1$, $m = 3$ with separation in $\{X'_1, X'_2\}$ and $\{X'_3\}$. Thus $\{X'_1\}$ is not a stand-alone exact sub-system.

2.4 One-dimensional situation

In the one-dimensional case with $N = M = 1$, we have scalar quantities X and Y. Consequently, we find $F, G : \mathbb{R} \to \mathbb{R}$ and the link $\varphi : \mathbb{R} \to \mathbb{R}$. So the systems (1) and (2) are one-dimensional autonomous ordinary differential equations. Solutions of such equations always are monotonous. Furthermore, differentiable and monotonous functions $\mathbb{R} \to \mathbb{R}$ can be transformed into each other by a non-linear scaling of the domain and co-domain. Consequently, every one-dimensional system is an exact sub-system of every one-dimensional differential equation according to Def. 1. The impact of this surprising observation in modelling will be analysed in further research.

2.5 Noether's theorem and conserved quantities

Noether's theorem explains the connection between the existence of conserved quantities and the symmetry of a system under transformation of variables, cf. Boccaletti and Pucacco (2001). The invariance under spacial translations leads to momentum conservation, while the conservation of energy results from the invariance under time translation, as in Example 3. In the formalism introduced here, a conserved quantity Y of (1), like in Noether's theorem, is described by an exact sub-system in (2) with $M = 1$ and $G = 0$ what implies $Y \in \mathbb{R}$ with $\dot{Y} = 0$.

3. THE MODELLING POINT OF VIEW

We have introduced a conceptual framework that describes the approximation of $\dot{X} = F(X)$ by lower-dimensional sub-systems $\dot{Y} = G(Y)$. The modelling point of view takes the system (1) as a real-world system, we want to describe by a model (2). In the context of modelling, we interpret the transformation $\mathcal{T} : X \mapsto X'$ as a choice of terms or concepts, that induce a well-arranged causal structure that is as simple as possible. While describing physical or biological systems, scientists always search for simple causal dependencies and simple descriptions, cf. Machamer and Silberstein (2002). The projection π_J induced by (3) represents the selection of components to consider in the model. The presented conceptual framework fits into the process of modelling and forms an approach for its formalisation.

4. OUTLOOK

An intuitive approach to modelling starts with an identification of basic mechanisms. In order to model a system (1), we assume separated and independent mechanisms. These mechanisms are represented by functions $F_i : \mathbb{R}^N \to \mathbb{R}^N$ in $F = \alpha_1 F_1 + \ldots + \alpha_k F_k$ with fixed $\alpha_1, \ldots, \alpha_k \in \mathbb{R}$. This leads to the system equation

$$\dot{X} = \alpha_1 F_1(X) + \ldots + \alpha_k F_k(X). \tag{5}$$

It is determined, which mechanism leads to which change of the system (5). One question to analyse is, how the terms of reducibility and separability fit to the separation of mechanisms and the resulting linear combination of different F_i.

Another point of view might interpret the α_i as parameters, defining different models to identify. The resulting parameter identification is a model identification in order to find a best model of a real-world problem and thus a best approximation of the system (1).

REFERENCES

Ames, W.F. (1969). *Numerical Methods for Partial Differential Equations.* Nelson, London.

Boccaletti, D. and Pucacco, G. (2001). *Theory of Orbits: Integrable Systems and Non-Perturbative Methods.* Springer, Berlin.

Machamer, P. and Silberstein, M. (eds.) (2002). *The Blackwell Guide to the Philosophy of Science.* Blackwell Publishers, Oxford.

Murray, J. (2008). *Mathematical Biology.* Springer, New York.

On Flatness-based Control for Shape-Memory Alloy Actuators ⋆

L. Kiltz * **J. Rudolph** ** **D. Gerbet** **

* *Corporate Research and Development, ZF Friedrichshafen AG (e-mail: lothar.kiltz@zf.com)*
** *Chair of Systems Theory and Control Engineering, Saarland University (e-mail: {j.rudolph,d.gerbet}@lsr.uni-saarland.de)*

Keywords: Flatness-based control, Shape-memory alloys

1. INTRODUCTION

Mechanical actuators the operating principle of which is based on the deformation of a shape-memory alloy can create high forces while the overall actuator size is comparably small. Often these kinds of actuators are operated in an on-off mode, only. Nonetheless, a continuous operation is also possible, which is usually controlled using heuristic linear or nonlinear controllers. In this article a flatness-based open-loop control of this kind of actuators is proposed using a simple physically inspired model of the alloy.

The operating principle of shape-memory alloy actuators is the diffusionless transition between different metallic phases. Depending on the phase, the geometric shape of the actuator changes thus leading to relatively large deformations. What metallic phase the alloy prefers depends on the current temperature and the mechanical stress (there are magnetic alloys, too, but these are not considered here). For a nickel titanium alloy (NiTi), there is an austenitic phase, which is stable at high temperatures, and a martensitic phase, stable at low temperatures. Because of the shape of the crystal cells, martensite forms in twins of different orientation (Wang and Sehitoglu (2014)), when the alloy is cooled. Stretching the cold alloy results in a shift of the twin plane, which looks like a plastic deformation from the macroscopic point of view, but is a diffusionless process. The process can be reversed by heating the alloy, which turns the crystal in the austenitic phase again, so that the previous shape results.

To this end, actuators formed as thin wires are considered, which can only afford tension forces in one direction. Thus, the martensite cells will orientate in a way that minimizes the strain energy and different orientations are not subject to the considerations, here. This way, one can regard the phase fractions x_A of austenite and the fractions x_+ and x_- of representative martensite phases, only (Müller and Seelecke (2001)). In addition, the following simplified assumptions are made: The wire is always loaded by a tension force $f(l, \dot{l}, \ldots)$ that can be expressed by the wire length l and its derivatives. This function is given by the mechanical system attached to the wire. The mass, and therefore all inertial forces, of the wire can be neglected. The wire shall have a homogeneous temperature, spatially distributed effects are not considered yet. Thus, a wire of spatially constant cross section A, volume V, and length $l = l_0(1 + \epsilon)$ is considered, where l_0 is the length in the austenitic phase under no load and ϵ is the strain. Note that the cross section A depends on both the phase fraction and the strain, because of the volume preserving phase transition and the elastic tension of the compressible material, while the volume depends on the elastic component of the strain only. Polycrystalline effects are neglected and the wire is described by stacked layers of martensite and austenite with the fractions $x_+ = x$ and $x_\mathrm{A} = 1 - x$, respectively. Since the wire is assumed to be always loaded, only one martensitic phase is considered.

2. MATERIAL MODEL

To explain the hysteretic behavior of the shape-memory alloy, a free energy model was developed in Müller and Seelecke (2001), which has been used in many other works. In this model, the (Helmholtz) free energy $F = U - TS$ as a function of the temperature T and the strain ϵ is considered. Here, U denotes the internal energy and S the entropy. A thermodynamic system tends to minimize the free energy. Considering the material tension with respect to austenite, the martensitic phases can be regarded to have a strain $\epsilon_\pm$, so that the (linear) stress-strain relation is $\sigma_\mathrm{A} = E_\mathrm{A}\epsilon$ and $\sigma_\pm = E_\pm(\epsilon - \epsilon_\pm)$ for austenite and martensite, respectively, while E denotes the corresponding Young's modulus. Therefore, the free energy has minima at the specific strains, if the phases are stable at the temperature T. At high temperatures, the entropy term dominates and only the austenitic phase is stable (see Figure 1a)). As the temperature decreases, minima at the martensitic phases occur, but the energy barrier prevents a phase transition (Figure 1b)). If the temperature decreases further, the energy barrier gets smaller so that the alloy transforms to the martensitic phase (Figure 1c)). As the material is heated again, there is an energy barrier to the austenite phase, which explains the hysteresis.

For an alloy under tension stress σ, the free enthalpy $G = F - \partial_\epsilon U\epsilon$ is minimized. To find the term $\partial_\epsilon U$, the Gibbs fundamental equation $\mathrm{d}U = T\,\mathrm{d}S + \mathrm{d}W$ conforming to Kluge and Neugebauer (1994) with the work term

⋆ The explanation of the ideas behind the material model by Prof. Seelecke is gratefully acknowledged.

$$\mathrm{d}W = f\,\mathrm{d}l = \sigma A l_0\,\mathrm{d}\epsilon = \sigma\tfrac{V}{1+\epsilon}\,\mathrm{d}\epsilon$$

in combination with the total derivative $\mathrm{d}U = \partial_S U\,\mathrm{d}S + \partial_\epsilon U\,\mathrm{d}\epsilon$ can be used to find

$$\partial_\epsilon U = \sigma\tfrac{V}{1+\epsilon}.$$

The additional term $\partial_\epsilon U\epsilon$ in the free enthalpy explains why only one martensitic phase is formed when cooling a wire under tension.

This phase transformation process is assumed to have a rate that depends on the temperature and the height $\Delta G(\sigma, T)$ of the energy barriers, which are different for the different transitions A+ from austenite to martensite and +A from martensite to austenite. There, the quantities T and ΔG occur in the argument of an exponential function. For an explanation the reader is referred to Müller and Seelecke (2001). Thus, one has quasilinear differential equations

$$\tau\dot{x}_\mathrm{A} = x_+ p_{+\mathrm{A}}(T,\sigma) - x_\mathrm{A} p_{\mathrm{A}+}(T,\sigma)$$
$$\tau\dot{x}_+ = x_\mathrm{A} p_{\mathrm{A}+}(T,\sigma) - x_+ p_{\mathrm{A}+}(T,\sigma)$$

for the phase fractions, which obviously respect the algebraic condition $x_\mathrm{A} + x_+ = 1$ and can be reduced to

$$\tau\dot{x} = (1-x)p_{\mathrm{A}+}(\sigma,T) - x p_{+\mathrm{A}}(\sigma,T). \qquad (1)$$

Since the proposed time constant τ is very small, singular perturbation theory may be used to come up with algebraic equations instead, neglecting the very fast dynamics.

To complete the actuator model, an equation for the heating power P is required. The following considerations are easier to understand when working with the length l and force f of the wire. Since $\dot{U} = \dot{Q} + f\dot{l}$ for the change of the internal energy, for the enthalpy $H = U - fl$ one has $\dot{H} = \dot{Q} - l\dot{f}$. On the other hand $H = xH_\mathrm{M} + (1-x)H_\mathrm{A}$ holds for the enthalpy, where H_M and H_A is the enthalpy of the whole wire, as if it had only one metallic phase. Further

$$\dot{H}_{\mathrm{M,A}} = \partial_T H_{\mathrm{M,A}}\dot{T} + \partial_f H_{\mathrm{M,A}}\dot{f},$$

while $\partial_f H_{\mathrm{M,A}} = -l$. Comparing the two equations for the derivative $\dot{H}$, one finds

$$\begin{aligned}\dot{H} &= \dot{x}\,(H_\mathrm{M} - H_\mathrm{A}) - l\dot{f} + (x\partial_T H_\mathrm{M} + (1-x)\partial_T H_\mathrm{A})\,\dot{T}\\ &= \dot{Q} - l\dot{f},\end{aligned}$$

which yields

$$\dot{Q} = (x\partial_T H_\mathrm{M} + (1-x)\partial_T H_\mathrm{A})\,\dot{T} + (H_\mathrm{M} - H_\mathrm{A})\,\dot{x}. \qquad (2)$$

3. DIFFERENTIALLY FLAT SYSTEM

Combining the shape-memory alloy wire model with the mechanically system providing an external force (a spring for instance) results in a differentially flat system with the wire length l as a flat output, as will be shown next. Given the length l_0 of the unloaded wire in austenitic phase as a parameter, one has the relation $l = l_0\,(1+\epsilon)$ and that knowing l the strain is known, too. From the mechanical system itself one directly computes the tension force $f = f(l, \dot{l}, \ldots)$.

To compute the stress $\sigma = \frac{f}{A}$ and the phase fractions the cross section A of the wire is required first. Under the assumptions above, one has a volume preserving tension due to the phase transition next to an elastic tension due to stress. The latter effect contributes a strain

$$\bar{\epsilon} = \sigma\left(\tfrac{1-x}{E_\mathrm{A}} + \tfrac{x}{E_\mathrm{M}}\right)$$

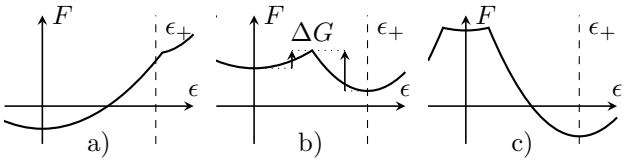

Fig. 1. Free energy $F(T,\epsilon)$. Sections are shown for different temperatures T.

so that $\epsilon = x\epsilon_+ + \bar{\epsilon}$ for the composite strain. The elastic tension scales the cross section by $(1-\nu\bar{\epsilon})^2 \approx 1 - 2\nu\bar{\epsilon}$ with the transverse deformation constant ν so that

$$A = A_0\tfrac{(1-\nu\bar{\epsilon})^2}{1+x\epsilon_+}$$

for the cross section. These equations can be solved for the phase fraction x and the stress σ, given the strain ϵ and the force f.

Now, in the rate equation (1) the quantities computed so far as well as the derivative $\dot{x}$ of the phase fraction are substituted to solve this equation for the temperature T. Using (2) and differentiating T then allows to express the control input, viz the heating power $P = \dot{Q}$. This way, given any sufficiently smooth trajectory $t \mapsto l(t)$, allows one to compute the corresponding control input $P(t)$.

The step of computing the temperature requires some attention. The monocrystalline model suggests that, due to the large negative exponents, there is almost no phase transition until a critical temperature or strain reached. Inverting the equations directly results in very large heating powers. In practice, such a behavior is not observed. A polycrystalline extension of this model as proposed in Heinze (2004) will allow to address this problem.

One should also note that the wire can be easily heated by forcing an electrical current through it, while there is usually no way to cool it actively. Negative values of $\dot{Q}$ are achieved by convection that depends on the temperature and geometry of the wire, which are known from $t \mapsto l(t)$.

Since the small wire is fixed at its ends, there are very large heat sinks, which call for a spatially distributed model. Such a model might lead to much better coincidence between simulation results and experiments, in return yielding more accurate control behavior.

REFERENCES

Heinze, O. (2004). *A computationally efficient free energy model for shape memory alloys - experiments and theory.* Ph.D. thesis, North Carolina State University.

Kluge, G. and Neugebauer, G. (1994). *Grundlagen der Thermodynamik.* Spektrum Akademischer Verlag, Heidelberg, Berlin, Oxford.

Müller, I. and Seelecke, S. (2001). Thermodynamic Aspects of Shape Memory Alloys. *Mathematical and Computer Modelling*, 34, 1307–1355.

Wang, J. and Sehitoglu, H. (2014). Martensite modulus dilemma in monoclinic NiTi-theory and experiments. *International Journal of Plasticity*, 61, 17–31.

Towards Bayesian Parametrization of national scale epidemics

Eriksson Robin * **Engblom Stefan** * **Widgren Stefan** *,**

* *Department of Information Technology, Uppsala University, 751 05 Uppsala, Sweden, (e-mail: robin.eriksson@it.uu.se, stefane@it.uu.se, stefan.widgren@it.uu.se)*
** *Department of Disease Control and Epidemiology, National Veterinary Institute, 751 89 Uppsala, Sweden, (e-mail: stefan.widgren@sva.se)*

Keywords: Simulation of stochastic systems, Discrete event modeling and simulation, Spatial stochastic models, Bayesian parameter estimation.

1. INTRODUCTION

Many infections or diseases that pose a public health threat have a *zoonotic* origin, i.e., are transmitted from animals to humans by contact with infected animals. Verotoxin-producing *Escherichia coli* (VTEC) is an example of a zoonotic foodborne pathogen where cattle can act as a reservoir, see Newell et al. (2010). Livestock movements are the primary transmission route for transferring VTEC infections between cattle herds, Nielsen et al. (2002). EU regulations require member states to keep national databases of all bovine animals and it is therefore possible to develop realistic large-scale disease spread models that incorporate the transport network to better understand the transmission of zoonotic infections in the cattle population. Although mainly inspired by zoonotic diseases and models driven by livestock data, our discussion is of entirely general character and applies to arbitrary epidemiological models. We have implemented a framework for stochastic disease spread simulator on networks in the software **SimInf**, see Widgren et al. (2016a), which is a C compiled extension to the programming language R available through the Comprehensive R Archive Network (CRAN). With **SimInf** and data with detailed information about the movement of the Swedish cattle population and bacterial testing at multiple sites we can perform Bayesian parameter inference on national scale epidemics.

2. EPIDEMIOLOGICAL MODELING

The SIS_E-model consists of the two compartments susceptible (S) and infected (I) and an environmental compartment (E) representing an infectious pressure from free-living pathogens. The infection transmits indirectly from infected to susceptible individuals through the local environment, contaminated by infected individuals. Within each herd i, the SIS_E model has the following two state transitions,

$$\left.\begin{array}{l} S_i \xrightarrow{\upsilon\varphi_i} I_i \\ I_i \xrightarrow{\gamma} S_i \end{array}\right\}, \tag{1}$$

where υ is the indirect transmission rate of the environmental infectious pressure, and γ is the recovery rate from the infection. Moreover, $\varphi_i(t)$ is the concentration of the local environmental-infectious pressure in herd i, evolved as

$$\frac{d\varphi_i(t)}{dt} = \frac{\alpha I_i(t)}{S_i(t) + I_i(t)} - \beta(t)\varphi_i(t), \tag{2}$$

where α is the average shedding rate of bacteria to the environment per infected individual, while the time-dependent function β captures the decay and removal of bacteria. The model can be extended to include multiple compartments, such as different age groups in the susceptible and infected compartments, see Bauer et al. (2016); Widgren et al. (2016b). With the inclusion of observations, we implement (1) and (2) as stochastic simulations on a connected network in **SimInf**, see Engblom and Widgren (2017); Bauer et al. (2016).

The data we have available contains a total of 18,649,921 reports with information about; first, the date and the node for birth events, second, the date, the source, and destination node for any movements, and third, the date for slaughter or death, Nöremark et al. (2011). Each unique node identifier (n = 37,221) in the data corresponds to a single geographical location where animals are kept, and could, e.g., correspond to a farm building or pasture distributed across the entire Sweden.

3. BAYESIAN PARAMETRIZATION

We consider a postulated truth in the form of a time-dependent stochastic process $X(t) = X(t, \theta)$, for some parameter θ. The density for this process is denoted by $P\big((x,t)|(x',t');\theta\big) = \mathbf{P}\big(X(t) = x|X(t') = x';\theta\big)$, and we consider throughout this work that the true density is computationally intractable but — mainly for convenience — is Markovian. We are given a set of observations $(x_i) = (x_i, t_i) \sim X(t_i)$, and the task is to estimate the unknown parameter θ.

In exploring the posterior density $\mathbf{P}(\theta|x) \propto \mathbf{P}(x|\theta)$, likelihood-based inference methods are not viable and other methods need to be advised. We consider two likelihood-free inference methods, first, Approximate Bayesian Computations (ABC), see Beaumont et al. (2002), and second, Synthetic Likelihood Markov chain

Monte Carlo (SLMCMC) as in Wood (2010). Both methods generate simulated data $(z_i(\theta')) \sim X(t_i, \theta')$ and compare it with the observed data as a substitute for the likelihood.

In ABC one compares the summarized versions of $\{(z_i), (x_i)\}$, the summary statistics $\{S(z), S(x)\}$, using a distance measure, e.g., the Euclidean norm. If the distance is smaller than a tolerance ϵ, the proposed parameter θ' is accepted. The ABC method thus gives the approximate posterior distribution defined as

$$\mathbf{P}_\epsilon(\theta|S(x)) \propto \int_{\mathcal{X}} \mathbf{P}(z|\theta')\mathbf{P}(\theta')\mathbb{I}_{A_{\epsilon,x}}(z)\mathrm{d}z \qquad (3)$$
$$A_{\epsilon,x}(z) = \{z \in \mathcal{X}; ||S(z) - S(x)|| < \epsilon\}.$$

The choice of the acceptance tolerance ϵ will define how close to the true posterior the approximation is. As $\epsilon \to \infty$ the sample distribution is the prior: $\mathbf{P}_\epsilon(\theta|S(x)) \to \mathbf{P}(\theta)$, and as $\epsilon \to 0$ the approximation will converge to the posterior $\mathbf{P}_\epsilon(\theta|S(x)) \to \mathbf{P}(\theta|S(x))$, see Wilkinson (2013).

The other method referred to as SLMCMC considers each set of simulated summary statistics to be an observation of a multivariate normal distribution $S(\cdot) = \boldsymbol{s} \sim \mathcal{N}(\boldsymbol{m}_\theta, \Sigma_\theta)$, where $\boldsymbol{m}_\theta$ is the mean and Σ_θ is the covariance. When assuming normality, we utilize an auxiliary model $\mathcal{Z}$ and will, in turn, be able to observe the auxiliary model's posterior density $\mathbf{P}_{\mathcal{Z},\eta}(\theta|\boldsymbol{s})$. The accuracy of the observed posterior density depends on the number of observation η of $\boldsymbol{s}$ and the validity of the assumption of the auxiliary model $\mathcal{Z}$ being descriptive of the postulated truth. We construct the synthetic log-likelihood as

$$\boldsymbol{p}_{\mathcal{Z},\eta}(\boldsymbol{s}|\theta) = -\frac{1}{2}(\boldsymbol{s} - \hat{\boldsymbol{m}}_\theta)^\top \hat{\Sigma}_\theta^{-1}(\boldsymbol{s} - \hat{\boldsymbol{m}}_\theta) - \frac{1}{2}\log|\hat{\Sigma}_\theta|, \quad (4)$$

where $\hat{\boldsymbol{m}}_\theta$ and $\hat{\Sigma}_\theta$ are estimates of the mean and covariance. We then explore the approximate posterior density using (4) in a likelihood-based Markov chain Monte Carlo method.

In Figure 1, we illustrate a proof of concept for the two methods. We conduct the parameter inference on a Geometric Brownian Motion, for which the likelihood function is known, and we present the results from ABC and SLMCMC together with the likelihood-based Metropolis-Hastings algorithm, Hastings (1970), i.e., the best attainable posterior in this setting. We are currently applying these likelihood-free methods to the SIS_E-model using series of measurements

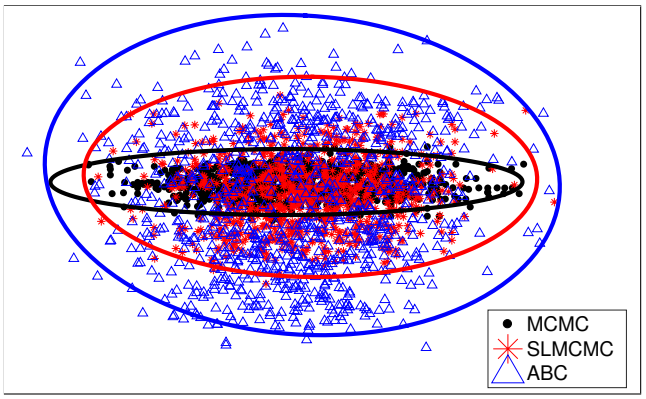

Fig. 1. Proof of concept for the likelihood-free methods, ABC and SLMCMC. Estimating parameters for a geometric Brownian motion together with a Metropolis-Hastings generated estimation present.

ACKNOWLEDGEMENTS

This work was financially supported by the Swedish Research Council Formas (S. Engblom, S. Widgren), by the Swedish Research Council within the UPMARC Linnaeus center of Excellence (S. Engblom, R. Eriksson), and by the Swedish strategic research program eSSENCE (S. Widgren).

REFERENCES

Bauer, P., Engblom, S., and Widgren, S. (2016). Fast event-based epidemiological simulations on national scales. *Int. J. High Perf. Comput. Appl.*, 30(4), 438–453. doi:10.1177/1094342016635723.

Beaumont, M.A., Zhang, W., and Balding, D.J. (2002). Approximate bayesian computation in population genetics. *Genetics*, 162(4), 2025–2035.

Engblom, S. and Widgren, S. (2017). Chapter 11 - data-driven computational disease spread modeling: From measurement to parametrization and control. In A.S.S. Rao, S. Pyne, and C. Rao (eds.), *Disease Modelling and Public Health, Part A*, volume 36 of *Handbook of Statistics*, 305 – 328. Elsevier.

Hastings, W.K. (1970). Monte carlo sampling methods using markov chains and their applications. *Biometrika*, 57(1), 97–109.

Newell, D.G., Koopmans, M., Verhoef, L., Duizer, E., Aidara-Kane, A., Sprong, H., Opsteegh, M., Langelaar, M., Threfall, J., Scheutz, F., et al. (2010). Food-borne diseases - the challenges of 20 years ago still persist while new ones continue to emerge. *International journal of food microbiology*, 139, S3–S15. doi: 10.1016/j.ijfoodmicro.2010.01.021.

Nielsen, E.M., Tegtmeier, C., Andersen, H.J., Grønbaek, C., and Andersen, J.S. (2002). Influence of age, sex and herd characteristics on the occurrence of verocytotoxin-producing *Escherichia coli* O157 in danish dairy farms. *Veterinary Microbiology*, 88(3), 245–257.

Nöremark, M., Håkansson, N., Lewerin, S.S., Lindberg, A., and Jonsson, A. (2011). Network analysis of cattle and pig movements in sweden: measures relevant for disease control and risk based surveillance. *Preventive veterinary medicine*, 99(2), 78–90.

Widgren, S., Bauer, P., and Engblom, S. (2016a). Siminf: An r package for data-driven stochastic disease spread simulations. *arXiv preprint arXiv:1605.01421*.

Widgren, S., Engblom, S., Bauer, P., Frössling, J., Emanuelson, U., and Lindberg, A. (2016b). Data-driven network modelling of disease transmission using complete population movement data: spread of VTEC O157 in Swedish cattle. *Veterinary Research*, 47(1), 81. doi: 10.1186/s13567-016-0366-5.

Wilkinson, R.D. (2013). Approximate bayesian computation (abc) gives exact results under the assumption of model error. *Statistical applications in genetics and molecular biology*, 12(2), 129–141.

Wood, S.N. (2010). Statistical inference for noisy nonlinear ecological dynamic systems. *Nature*, 466(7310), 1102–1104.

An Optimal Control Problem for Stereotactic Neurosurgery

Kathrin Flaßkamp * **Karl Worthmann** ***
Christoph Greiner-Petter ** **Christof Büskens** *
Thomas Sattel **

* *Center for Industrial Mathematics, University of Bremen (e-mail: kathrin.flasskamp@uni-bremen.de, bueskens@math.uni-bremen.de)*
** *Department of Mechanical Engineering, Technische Universität Ilmenau (e-mail: {christoph.greiner-petter/thomas.sattel}@tu-ilmenau.de)*
*** *Institute for Mathematics, Technische Universität Ilmenau (e-mail: karl.worthmann@tu-ilmenau.de)*

Keywords: Trajectory and Path Planning, Modeling for Control Optimization, Telerobotics, Robots manipulators, Control in Neuroscience, Mechatronic Systems Modeling

1. INTRODUCTION

In typical stereotactic neurosurgery, an entry point on the skullcap is determined from which the target region inside the brain is approached on a straight line, see, e.g. Rahman et al. (2009). MRT or CT data provide information on one or multiple target points in the brain, which the cannula has to reach during operation, as well as on critical regions inside the brain that should not be penetrated. Stereotactic neurosurgery requires careful a priori design and planning of cannula trajectories.

Here, we focus on a novel approach to mitigate negative side effects due to the penetration of brain tissue. To this end, we propose the usage of a cannula that is composed of several pre-curved nickel-titanium tubes with decreasing diameter such that their construction allows for intertwining, see Fig. 1. Then, surgery planning includes choosing an entry point on the skullcap, the cannula design, e.g. how many and which type of cannula, and the computation of control commands for the individual tubes of the cannula. Using actively deformable cannulas offers the possibility to reach multiple target points through one entry point and may even allow to reach a target point in view off critical regions inside the brain.

However, actively deformable cannulas give raise to an infinite number of possible tube trajectories, such that it is inevitable to support surgery planning by mathematical optimization.

2. MODELING & OPTIMIZATION

We model the design and planning problem as a *constrained optimization problem*. The optimization variables can be partitioned into design and control variables, see Fig. 1. While the former have to be fixed before the cannula is built, the latter can be adjusted later on, e.g. after parameter identification or by model-based control. Finding steering curves for the individual tubes of the cannula can be modeled as an *optimal control problem*; details are presented in the following.

Kinetic/Kinematic Model: We develop kinetic and kinematic models, in which the configuration of the cannula and its history is decisive while the actual speed of realizing that path can be ignored. Hence, time does not play a role. However, in order to take the configuration and its history properly into account, we artificially introduce a time parameter. Within robotics terminology, our planning problem is thus between a path and a trajectory planning problem. Ordinary differential equations are derived, whose solution trajectories are absolutely continuous, which ensures smoothness of the computed path for the cannula.

Additional Constraints: Both technical boundary conditions, such as parameter ranges, mechanical material characteristics (cf. Greiner-Petter and Sattel (2017)), and medical aspects, such as intolerable lateral movements of the cannula or the structure of the brain, have to be taken into account as equality or inequality constraints on tube trajectories.

Objective Function: We identified several different objective functions of interest. The length of the fully extended cannula, i.e. when the target region is reached, should be minimized, which corresponds to a classical Mayer-term in an optimal control problem. Moreover, torsion of the elastic tubes may cause violations of the follow-the-leader behavior, which leads to undesired lateral movements of the cannula and, thus, severe damage of tissue and therefore, has to be minimized. A similar behavior can be observed due to hysteresis.

These objectives are potentially conflicting optimization criteria. Thus, they have to be considered in a multi-objective optimization framework and e.g. handled by scalarization methods. A set of Pareto optimal solutions, i.e. optimal compromises of the considered optimization criteria, can greatly support decision making by allowing

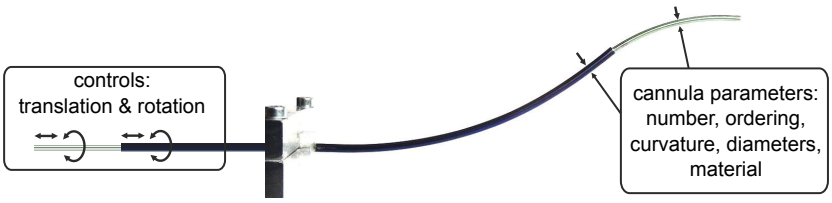

Fig. 1. Picture of surgical instrument with optimization variables indicated: parameters of the cannula and controls.

the surgeon to choose in dependence of the individual patient.

3. RELATED WORK

State-of-the-art surgery techniques are based on straight cannulas that are steered via a stereotactic frame. However, recently, research has been done on actively deformable cannulas which provide more degrees of freedom in design and control Burgner-Kahrs et al. (2015). In this case, the mechanical model gains complexity, since interaction between the tubes have to be considered Greiner-Petter and Sattel (2017).

Trajectory planning for medical applications is often addressed by stochastic, sampling-based, or heuristic optimization approaches, e.g. the Nelder-Mead method in Bergeles et al. (2015) or rapidly exploring roadmaps in Alterovitz et al. (2011); Torres and Alterovitz (2011). Further, Monte-Carlo Simulations have been used in Burgner-Kahrs et al. (2014) for workspace characterization. Approaches to collision avoidance for brain regions have been considered in Lyons et al. (2009, 2010); Alterovitz et al. (2011); Torres and Alterovitz (2011). In Anor et al. (2011), simultaneous trajectory planning and cannula design is presented. However, the approach does not use gradient information but pattern search methods. Global solutions are obtained via varied initial guesses. Optimal planning for actively deformable cannulas by gradient-based techniques has only been considered for simple kinematic cannula models in Lyons et al. (2009).

4. IMPLEMENTATION & OUTLOOK

Our approach to the design and planning problem of actively deformable cannula is to use model-based optimization, more concretely, gradient-based nonlinear optimization techniques. The optimal control problem is discretized by transcription methods, see, e.g. Gerdts (2011). Medical and technical constraints are added to the problem.

The development of structure-exploiting efficient optimization software, e.g. WORHP, Büskens and Wassel (2012), nowadays allows to use gradient-based optimization techniques, as opposed to sampling heuristics, even in highly complex applications with many variables and constraints. Here, local optimality of solutions can be guaranteed and the numerical solution offers further information in terms of sensitivities, which can be used to study robustness properties of solutions, for instance. Robustness is of utmost importance for the considered application in order to cope with modeling errors and external disturbances.

In future, this contribution will be part of a trajectory planning tool for a mechatronic instrument for stereotactic neurosurgery.

REFERENCES

Alterovitz, R., Patil, S., and Derbakova, A. (2011). Rapidly-exploring roadmaps: Weighing exploration vs. refinement in optimal motion planning. In *IEEE Int. Conf. on Rob. and Autom.*, 3706–3712.

Anor, T., Madsen, J.R., and Dupont, P. (2011). Algorithms for design of continuum robots using the concentric tubes approach: A neurosurgical example. In *IEEE Int. Conf. on Rob. and Autom.*, 667–673.

Bergeles, C., Gosline, A.H., Vasilyev, N.V., Codd, P.J., del Nido, P.J., and Dupont, P.E. (2015). Concentric tube robot design and optimization based on task and anatomical constraints. *IEEE Trans. Rob.*, 31(1), 67–84.

Burgner-Kahrs, J., Gilbert, H., Granna, J., Swaney, P., and Webster, R. (2014). Workspace characterization for concentric tube continuum robots. In *IEEE/RSJ Int. Conf. on Intell. Robots and Syst.*, 1269–1275.

Burgner-Kahrs, J., Rucker, D., and Choset, H. (2015). Continuum robots for medical applications: A survey. *IEEE Trans. Rob.*, 31(6), 1261–1280.

Büskens, C. and Wassel, D. (2012). The ESA NLP solver WORHP. In *Modeling and optim. in space eng.*, 85–110. Springer.

Gerdts, M. (2011). *Optimal Control of ODEs and DAEs.* De Gruyter.

Greiner-Petter, C. and Sattel, T. (2017). On the influence of pseudoelastic material behavior in planar shape-memory tubular continuum structures. *Smart Materials and Structures.*

Lyons, L., Webster, R., and Alterovitz, R. (2009). Motion planning for active cannulas. In *IEEE/RSJ Int. Conf. on Intell. Robots and Syst.*, 801–806.

Lyons, L., Webster, R., and Alterovitz, R. (2010). Planning active cannula configurations through tubular anatomy. In *IEEE Int. Conf. on Rob. and Autom.*, 2082–2087.

Rahman, M., Murad, G., and Mocco, J. (2009). Early history of the stereotactic apparatus in neurosurgery. *Neurosurg. Focus*, 27(3).

Torres, L. and Alterovitz, R. (2011). Motion planning for concentric tube robots using mechanics-based models. In *IEEE/RSJ Int. Conf. on Intell. Robots and Syst.*, 5153–5159.

Constant-free, randomized a posteriori error estimators for parameter-dependent partial differential equations

Kathrin Smetana * **Olivier Zahm** ** **Anthony T. Patera** ***

* *University of Twente, 7500 AE Enschede, The Netherlands (e-mail: k.smetana@utwente.nl).*
** *Massachusetts Institute of Technology, Cambridge, MA 02139-4307 USA, (e-mail: zahmo@mit.edu)*
*** *Massachusetts Institute of Technology, Cambridge, MA 02139-4307 USA, (e-mail: patera@mit.edu)*

Keywords: A posteriori error estimation, reduced basis method, parametrized partial differential equations, randomization, concentration inequalities, high dimensional probability, adjoint method

1. INTRODUCTION

During the last decades (numerical) simulations based on partial differential equations (PDEs) have considerably gained importance in engineering applications, life sciences, environmental issues, and finance. However, especially when multiple simulation requests or a real-time simulation response are desired, standard methods such as finite elements (FE) are prohibitive. Model reduction approaches such as the reduced basis (RB) method, which we will consider here, have been developed to tackle such situations (see for instance Haasdonk (2017); Quarteroni et al. (2016); Hesthaven et al. (2016) for an overview). The key concept of the RB method is to prepare a problem-adapted low-dimensional subspace of the high-dimensional (FE) discretization space in a possibly expensive offline stage to realize a fast simulation response by Galerkin projection on that low-dimensional space in the subsequent online stage.

To assess the approximation error caused by the RB method in the online stage a reliable and efficient a posteriori error estimator has been derived in Veroy et al. (2003). However, for inf-sup stable problems such as acoustics problems the estimation of the inf-sup constant still poses a challenge and the existing methods often result in rather pessimistic results and thus pessimistic error bounds. We propose a constant-free, probabilistic a posteriori error estimator that does not require to estimate any stability constants and is both reliable and efficient at (given) high probability. Here, we extend the approach in Cao and Petzold (2004); Homescu et al. (2005), where the solution of an adjoint problem with random conditions at the final time is employed to estimate the approximation error for ordinary differential equations.

2. THE REDUCED BASIS METHOD FOR INF-SUP STABLE PARAMETRIZED PDES

2.1 Problem setting

Let $D \subset \mathbb{R}^d$, $d = 1, 2, 3$ be a bounded Lipschitz domain, $\mathcal{P}$ denote the set of admissible parameters, and introduce a Hilbert space $H_0^1(D) \subset X \subset H^1(D)$. Moreover, we introduce a linear operator $A(\mu) : X \to X'$ that is inf-sup stable and bounded, i.e.

$$0 < \beta \leq \beta(\mu) := \inf_{v \in X} \sup_{w \in X} \frac{\langle A(\mu)v, w\rangle}{\|v\|_X \|w\|_X} \quad \text{and} \tag{1}$$

$$\gamma(\mu) := \sup_{v \in X} \sup_{w \in X} \frac{\langle A(\mu)v, w\rangle}{\|v\|_X \|w\|_X} \leq \gamma < \infty, \tag{2}$$

where X' denotes the dual space of X and $\langle \cdot, \cdot \rangle$ the duality pairing.

We consider the following parameter-dependent PDE: For any given $\mu \in \mathcal{P}$ find $u(\mu) \in X$ such that

$$A(\mu)u(\mu) = f(\mu) \quad \text{in } X', \tag{3}$$

where $f(\mu) \in X'$ is a given continuous linear form.

2.2 The high-dimensional discretization

Next, we introduce a conforming high-dimensional (FE) space $X^{\mathcal{N}} \subset X$ of dimension $\mathcal{N}$ and a so-called truth solution $u^{\mathcal{N}}(\mu)$ that is defined as the solution of

$$A(\mu)u^{\mathcal{N}}(\mu) = f(\mu) \quad \text{in } X^{\mathcal{N}\prime}. \tag{4}$$

Note that in order to simplify the presentation we do not introduce suitable discrete linear operators as we believe the respective definition to be clear from the actual setting.

2.3 The reduced basis method in a nutshell

We assume that we have constructed an RB space $X^N := \text{span}\{\phi_1, \ldots, \phi_N\}$ in the offline stage say via a greedy algorithm as introduced in Veroy et al. (2003), relying on

the high-dimensional discretization. We may then define an RB approximation $u^N(\mu) \in X^N$ as the solution of

$$A(\mu)u^N(\mu) = f(\mu) \quad \text{in } X^{N\prime}. \tag{5}$$

Note that thanks to a suitable offline/online-decomposition the computation of $u^N(\mu)$ in the online stage does not scale in the dimension $\mathcal{N}$ of the high-dimensional discretization (see for instance Haasdonk (2017); Quarteroni et al. (2016); Hesthaven et al. (2016) for details).

To assess the approximation error $\|u^{\mathcal{N}}(\mu) - u^N(\mu)\|_X$ one may introduce the residual

$$r(\mu) := f(\mu) - A(\mu)u^N(\mu) \in X^{\mathcal{N}\prime}. \tag{6}$$

It is then straightforward to show that we have

$$\|u^{\mathcal{N}}(\mu) - u^N(\mu)\|_X \leq \frac{1}{\beta(\mu)}\|r(\mu)\|_{X^{\mathcal{N}\prime}}. \tag{7}$$

While the dual norm of the residual can be efficiently computed via the Riesz representation, estimation of $\beta(\mu)$ remains a challenge. The Successive Constraint Method introduced in Huynh et al. (2007) yields a lower bound for $\beta(\mu)$ which may however be rather pessimistic.

3. A RANDOMIZED A POSTERIORI ERROR ESTIMATOR

To derive a randomized a posteriori error estimator we rely on results similar to the restricted isometry property employed in compressed sensing. In detail, we introduce a matrix $\underline{B} \in \mathbb{R}^{K\times\mathcal{N}}$ whose entries are mutually independent standard Gaussian random variables. Then, for a vector $\underline{x} \in \mathbb{R}^{\mathcal{N}}$ we have that for a given $\varepsilon \in \mathbb{R}, \varepsilon < 1$ the result

$$(1-\varepsilon)\|\underline{x}\|_2^2 \leq \|\underline{B}\underline{x}\|_2^2 \leq (1+\varepsilon)\|\underline{x}\|_2^2 \tag{8}$$

holds true at a (given) probability of at most $1-\delta$ if $K \geq \bar{K}(\delta,\varepsilon)$ (see for instance Vershynin (2012)). Here, $\|\cdot\|_2$ denotes the Euclidean norm. Note that in contrast to our approach the authors of Cao and Petzold (2004); Homescu et al. (2005) employ the small sample statistical method as proposed in Kenney and Laub (1994) that relies on random vectors which are uniformly distributed on the sphere $S^{\mathcal{N}-1}$.

Inspired by the results in Cao and Petzold (2004); Homescu et al. (2005) we introduce dual problems

$$\underline{A}^*(\mu)\underline{\psi}_i(\mu) = \underline{B}_{(i,:)}, \quad i = 1,\ldots,K, \tag{9}$$

where $\underline{A}^*(\mu)$ denotes the stiffness matrix associated with the adjoint operator $A^*(\mu)$ of $A(\mu)$ and $\underline{B}_{(i,:)}$ denotes the i-th row of the matrix $\underline{B}$. We may then use the dual solutions $\underline{\psi}_i(\mu)$ to define a probabilistic a posteriori error estimator that is a reliable and efficient bound of the error $\|u^{\mathcal{N}}(\mu) - u^N(\mu)\|_X$ at given probability $1-\delta$. However, as solving (9) for one i is as expensive as solving the primal truth problem (4) this estimator is not computationally feasible in the online stage.

In order to obtain an a posteriori error estimator that can be computed in the online stage in a complexity that does not depend on the dimension of the high-dimensional space $X^{\mathcal{N}}$, we also introduce an RB approximation of the dual problems (9). Here, we propose and compare different computational strategies for the generation of the dual RB space. If the RB approximation errors of the dual problems are small, the error $\|u^{\mathcal{N}} - u^N(\mu)\|_X$ can be bounded, with high probability, from below and above by this online-efficient a posteriori error estimator times a given constant. For more details see Smetana et al. (2018).

REFERENCES

Cao, Y. and Petzold, L. (2004). A posteriori error estimation and global error control for ordinary differential equations by the adjoint method. *SIAM J. Sci. Comput.*, 26(2), 359–374.

Haasdonk, B. (2017). *Reduced Basis Methods for Parametrized PDEs — A Tutorial Introduction for Stationary and Instationary Problems, in: Model Reduction and Approximation: Theory and Algorithms, Editors: P. Benner, A. Cohen, M. Ohlberger, and K. Willcox.* SIAM Publications, Philadelphia, PA.

Hesthaven, J.S., Rozza, G., and Stamm, B. (2016). *Certified Reduced Basis Methods for Parametrized Partial Differential Equations.* SpringerBriefs in Mathematics. Springer International Publishing.

Homescu, C., Petzold, L.R., and Serban, R. (2005). Error estimation for reduced-order models of dynamical systems. *SIAM J. Numer. Anal.*, 43(4), 1693–1714.

Huynh, D.B.P., Rozza, G., Sen, S., and Patera, A.T. (2007). A successive constraint linear optimization method for lower bounds of parametric coercivity and inf-sup stability constants. *C. R. Math. Acad. Sci. Paris*, 345(8), 473–478.

Kenney, C.S. and Laub, A.J. (1994). Small-sample statistical condition estimates for general matrix functions. *SIAM J. Sci. Comput.*, 15(1), 36–61.

Quarteroni, A., Manzoni, A., and Negri, F. (2016). *Reduced Basis Methods for Partial Differential Equations.* La Matematica per il 3+2. Springer International Publishing.

Smetana, K., Zahm, O., and Patera, A.T. (2018). Constant-free, randomized residual-based error estimators for parameter-dependent equations. Unpublished.

Veroy, K., Prud'homme, C., Rovas, D.V., and Patera, A.T. (2003). A posteriori error bounds for reduced-basis approximation of parametrized noncoercive and nonlinear elliptic partial differential equations. In *Proceedings of the 16th AIAA Computational Fluid Dynamics Conference*, volume 3847.

Vershynin, R. (2012). Introduction to the non-asymptotic analysis of random matrices. In *Compressed sensing*, 210–268. Cambridge Univ. Press, Cambridge.

Capsubot with an opposing spring: Simulation and experiments ⋆

A. Nunuparov * **F. Becker** ** **N. Bolotnik** *** **I. Zeidis** ** **K. Zimmermann** **

* *Moscow Institute of Physics and Technology, 9 Institutskiy per., Dolgoprudny, Moscow Region, 141700, Russia, e-mail: (anunuparov@me.com)*
** *Technische Universität Ilmenau, Technical Mechanics Group, Germany, e-mail: (felix.becker@tu-ilmenau.de)*
*** *Ishlinsky Institute for Problems in Mechanics RAS, 101-1 Vernadsky Ave, Moscow 119526 Russia, (e-mail:bolotnik@ipmnet.ru)*

Keywords: Mobile robot, Motion control, Capsubot, Locomotion

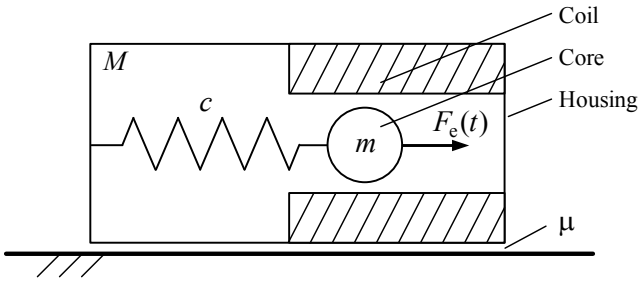

Fig. 1. Capsule-type robot. M – mass of the housing, m – mass of the core, c – spring rate, F_e – control force, μ – coefficient of dry friction

1. INTRODUCTION

A capsule robot (capsubot) is a locomotion system that can move in a resistive environment without external propelling devices (legs, wheels, caterpillars, fins, water screws, etc.) due to the motion of internal bodies and interaction of the housing with the environment.

The robot in current study consists of a rigid body (housing) and an electromagnetic (solenoid-type) drive located inside the housing. The drive involves an electromagnetic coil (solenoid) that is rigidly attached to the housing and an internal body(core); the core is made of a ferromagnetic material and can move inside the solenoid along its axis. The core is attached to the housing by a spring. The solenoid's axis is parallel to the axis of the housing. The housing interacts with a resistive environment in which the robot is moving. The robot is actuated by means of a magnetic force that acts on the core when an electric voltage is applied across the solenoid. The drive is designed so that the magnetic force acts in one direction and tends to pull the core inside the coil. The core returns to its initial position due to the spring. The robot moves on a horizontal plane along a straight line parallel to the axis of the robot's housing. The dynamics of the electric circuit of the solenoid is not taken into account. The schematic of the system described is shown in Fig. 1.

This model was suggested and derived in Bolotnik et al. (2016). The current study extends the cited paper with experimental investigations.

2. MATHEMATICAL MODEL

Let M denote the mass of the housing together with the solenoid, m the mass of the core, F_e the force applied to the core by the solenoid, F_fr the force with which the environment resists the motion of the housing, c the spring rate, x the coordinate that identifies the position of the housing's center of mass relative to a fixed (inertial) reference frame, ξ the coordinate that identifies the position of the core's center of mass relative to the housing. The variables x and ξ are measured along the line of motion of the robot. The coordinate ξ is chosen so that the spring is unstrained for $\xi = 0$. We assume that the resistance force F_fr acting between the housing and the environment is the dry friction force that obeys Coulomb's law and μ is the coefficient of dry friction of the housing against the supporting plane. Let X denote the center of mass:

$$X(t) = x(t) + \frac{m}{M+m}\,\xi(t), \tag{1}$$

By applying Newton's second law separately to the housing and to the core and using (1), we obtain the governing equations for the system under consideration in the following form:

$$\begin{aligned} &(M+m)\ddot{X} = F_\mathrm{fr}\left(\dot{X} - \frac{m}{M+m}\,\dot{\xi}\right), \\ &\frac{Mm}{M+m}\,\ddot{\xi} + c\,\xi = F_\mathrm{e} - \frac{m}{M+m}F_\mathrm{fr}\left(\dot{X} - \frac{m}{M+m}\,\dot{\xi}\right). \end{aligned} \tag{2}$$

Consider the force generated by the drive as a periodic piecewise continuous function:

$$F_\mathrm{e} = \begin{cases} F_0, & \left\{\dfrac{t}{T}\right\} < \tau, \\ 0, & \left\{\dfrac{t}{T}\right\} \geq \tau, \end{cases} \tag{3}$$

⋆ The research work reported here was partly supported by the Deutsche Forschungsgemeinschaft (Grant ZIM 540/19-2) and the Russian Foundation for Basic Research (Grant 17-51-12025)

where T is the period, F_0 is a positive constant that has a dimension of force, and τ is a dimensionless positive constant from the interval (0, 1). The parameter τ, called the duty cycle, identifies the fraction of the period, during which the control force is not equal to zero. Curly brackets denote the fractional part of the expression enclosed in them.

3. SIMULATION AND EXPERIMENTAL RESULTS

The basic content of this section is the analysis of the dependence of the average velocity of the robot on the excitation parameters T and τ.

The parameters of the experimental setup in terms of the mathematical model are provided in Table 1. These parameters are used for the simulation.

Table 1. Parameters of the system

Parameters	**Notatation and value**
Mass of the housing	$M = 0.193\,\mathrm{kg}$
Mass of the core	$m = 0.074\,\mathrm{kg}$
Stiffness of the spring	$c = 256.23\,\mathrm{Nm}^{-1}$
Maximum value of the force F_e	$F_0 = 1.25\,\mathrm{N}$
Dry friction coefficient	$\mu = 0.29$

The results will be presented in dimensionless variables. Instead of V, t, and T, we will use the variables $Vc/(F_0\omega)$, ωt, and ωT, respectively, preserving the previous notation for the normalized variables. The time scaling parameter is defined by $\omega = \sqrt{\frac{c(M+m)}{Mm}}$.

In the current study it is expected that the experimental and simulated data will not match quantitatively. This significant discrepancy could be accounted for by the fact that in the computational model, we ignored the dynamics of the electric circuit of the solenoid. However, the qualitative effects are expected to be observed.

3.1 Dependence of the average velocity of the robot on the parameter τ

The results of the investigation of the dependence of the average velocity V of the robot on the excitation parameter τ while the parameter T is fixed are depicted at Figure 2.

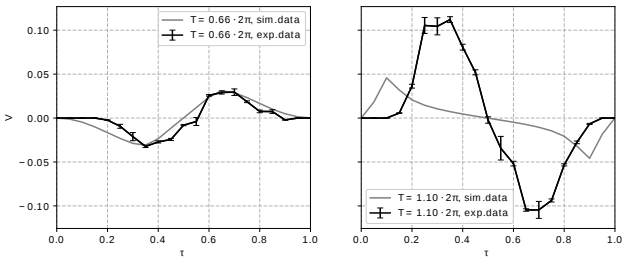

Fig. 2. The dependencies of average velocities on τ

The simulation and the experiment demonstrate that the average velocity of the steady-state motion of the robot depends significantly on the duty cycle of the pulse-width excitation signal, which indicates the possibility of controlling the motion of the robot by changing only the parameter τ. For $\tau = 0$, near $\tau = 1/2$, and $\tau = 1$, the average velocity of the robot is equal to zero. Based on this figure, one can assume that these curves possess a property of central symmetry about the point (1/2, 0) of the coordinate plane τV. For the mathematical model used for simulation this property was proved in Bolotnik et al. (2016). This implies that changing the duty cycle of the excitation signal from τ to $1 - \tau$ at the same period leads to the change in the direction of motion of the capsule robot, with the magnitude of its velocity being preserved.

3.2 Dependence of the average velocity on the period T

Figure 2 shows an essential qualitative difference between the curves for $T = 0.66 \cdot 2\pi$ and $T = 1.10 \cdot 2\pi$, which is reflected in the change in the sign of the average velocities for the same values of τ. For example, the sign of the average velocity in τ interval from 0 to 0.5 is non-negative for $T = 1.10 \cdot 2\pi > 1$ and non-positive for $T = 0.66 \cdot 2\pi < 2\pi$. This effect could be explained by the resonance phenomenon. The resonance-induced change in the direction of motion of a mobile vibration-driven system was observed previously in Zimmermann et al. (2009).

The resonant change in the sign of the average velocity of the robot can be seen from the curve plotting the average velocity V versus the excitation period T (Fig. 3).

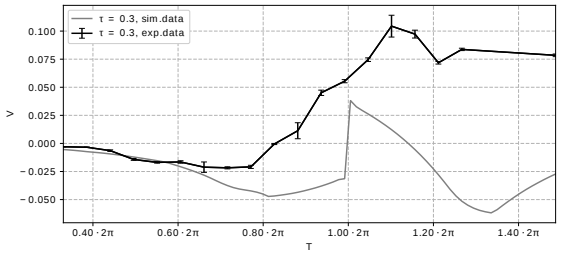

Fig. 3. The dependencies of average velocities on T

Both curves, the experiment and the simulation, record the change in the velocity, the first curve near $T = 0.82 \cdot 2\pi$, the second near $T = 2\pi$. Thus, the resonance effect is observed in the experiment and in the simulation.

4. CONCLUSION

This paper provides model-based and experimental investigations of a capsule-type robot motion with a periodic excitation force. The excitation force was controlled by two excitation parameters. It was demonstrated that the magnitude and the sign of the average velocity can be controlled by tuning any of the excitation parameters. The resonance-induced change in the direction of motion is shown.

REFERENCES

Bolotnik, N., Nunuparov, A., and Chashchukhin, V. (2016). Capsule-type vibration-driven robot with an electromagnetic actuator and an opposing spring: Dynamics and control of motion. *Journal of Computer and Systems Sciences International*, 55, 986–1000.

Zimmermann, K., Zeidis, I., Bolotnik, N., and Pivovarov, M. (2009). Dynamics of a two-module vibration-driven system moving along a rough horizontal plane. *Multibody System Dynamics*, 22, 199–219.

Modeling of Vertebrae Bone Growth by Topology Optimization ⋆

Atsushi Kawamoto * **Junpei Higashi** ** **Tsuyoshi Nomura** *
Tadayoshi Matsumori * **Shigeru Kondo** **

* *Toyota Central R&D Labs., Inc. Nagakute, Aichi 480-1192, Japan (e-mail: atskwmt@mosk.tytlabs.co.jp).*
** *Osaka University, Suita, Osaka 565- 0871, Japan (e-mail: shigerukondo@gmail.com)*

Keywords: Topology Optimization, Wolff's law, Vertebrae, Osteoblast, Osteoclast.

1. INTRODUCTION

It is widely known that trabecular bones of vertebrates are constantly being remodeled in response to the corresponding local stresses and strains Boyle (2011). This is called Wolff's law. On the other hand, it has yet to be understood how the outer shape of a vertebrae bone is formed. In this study, based on the observation of zebrafish vertebrae bones, we hypothesize that a vertebrae bone is composed of the two regions: one is formed a priori, while the other is formed a posteriori against external loading like trabecular bones. Assuming that Wolff's law can be expansively applied to the formation of the outer shape of a vertebrae bone, we introduce a mathematical model using topology optimization.

2. ZEBRAFISH AS A MODEL ORGANISM

In this research, we focus on zebrafish as a model organism. Zebrafish backbone is consist of 32 vertebrae (Fig. 1). The vertebrae bones significantly change their shapes as zebrafish is growing up from juvenile to adult (Fig. 2).

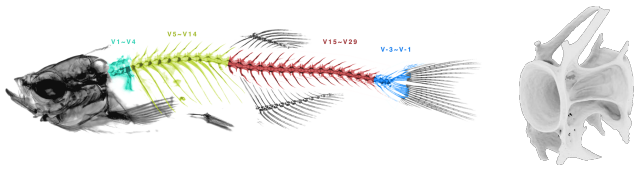

Fig. 1. Zebrafish skeleton (left) and V15 single vertebra(v15) scanned with micro-CT (right)

3. MATHEMATICAL MODELING

Based on the observation of zebrafish vertebrae bones, we hypothesize that a vertebrae bone is composed of two regions: one is formed a priori, while the other is formed a posteriori against external loading. To simulate the growth of such a vertebrae bone we first divide the computational domain into some subdomains as shown in Fig. 3. Regardless of external loading the white parts always have bones, while the green parts have no bones

⋆ The authors acknowledge that this research is supported by CREST and Toyota Central R&D.

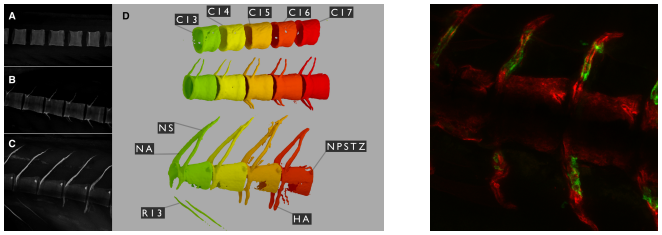

Fig. 2. Vertebra development (left) and visualization of osteoblast (right)

because the regions are occupied by nerves and blood vessels. These parts form a congenital basic structure. Assuming that loading acts on the two ends of the two cones, we apply distributed load on the red and orange parts with 1 and 0.5, respectively. In response to these mechanical stimuli, the bone shape in the purple parts is determined based on the following mathematical model.

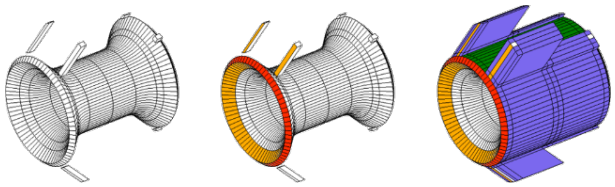

Fig. 3. Computational domain for simulating the growth of vertebrae bone.

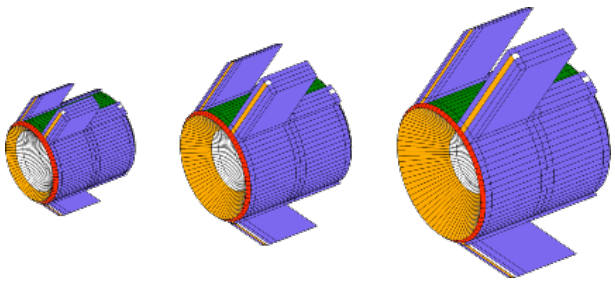

Fig. 4. Parameterization for the growth of computational domain

We first define bone density ρ by the following regularized Heaviside function of a scalar function ϕ:

$$\rho(\phi) = \begin{cases} d & (\phi < -h) \\ (1-d)H(\phi) + d & (-h \le \phi \le h) \\ 1 & (h < \phi) \end{cases} \quad (1)$$

where h is the half bandwidth between the bone domain ($h < \phi$) and the void domain ($\phi < -h$). d is a very small positive lower bound set for avoiding singularity of the stiffness matrix. $H(\phi)$ is defined as

$$H(\phi) = \frac{1}{2} + \frac{15}{16}\left(\frac{\phi}{h}\right) - \frac{5}{8}\left(\frac{\phi}{h}\right)^3 + \frac{3}{16}\left(\frac{\phi}{h}\right)^5 \quad (2)$$

With this representation, we assume that the bone structure in the purple part is obtained as a solution to the following optimization problem:

$$\begin{aligned} &\underset{\phi}{\text{minimize}} \quad f := \int_{\Gamma_N} \boldsymbol{t} \cdot \boldsymbol{u} \, \mathrm{d}\Gamma \\ &\text{subject to } g := \int_D \rho(\phi) \, \mathrm{dD} - \overline{V} \le 0, \end{aligned} \quad (3)$$

where $\overline{V}$ is the upper bound of total volume, $\boldsymbol{t}$ is the external surface traction, $\boldsymbol{u}$ is the displacement vector. Since the optimization problem (3) takes the nested form, the displacement vector $\boldsymbol{u}$ is given by solving the following force equilibrium problem.

Assuming the deformation is infinitesimal, the stress tensor σ and the strain $\boldsymbol{\epsilon}$ can be expressed with linear isotropic elasticity tensor $\mathbf{E}$ as

$$\sigma = \mathbf{E} : \boldsymbol{\epsilon}(\boldsymbol{u}), \qquad \boldsymbol{\epsilon}(\boldsymbol{u}) = \frac{1}{2}\left(\nabla \boldsymbol{u} + \nabla \boldsymbol{u}^\top\right). \quad (4)$$

Bone density ρ is embedded in the elasticity tensor as

$$\mathbf{E} = \rho^P \mathbf{E}_0, \quad (5)$$

where $\mathbf{E}_0$ is the elasticity tensor when $\rho = 1$. $P(= 3)$ is introduced for penalizing the intermediate values [0,1]. Finally, the force equilibrium problem is formulated as

$$\left.\begin{array}{ll} -\nabla \cdot \sigma = \mathbf{0} & \text{in } \mathrm{D} \\ \boldsymbol{u} = \mathbf{0} & \text{on } \Gamma_D \\ \sigma \cdot \boldsymbol{n} = \boldsymbol{t} & \text{on } \Gamma_N \end{array}\right\}. \quad (6)$$

In order to set up the time evolution equation for topology optimization (3), we introduce the Lagrangian $L := f + \lambda g$ and pursue the following optimality condition Kawamoto (2013):

$$\frac{\mathrm{d}L}{\mathrm{d}\phi} = \frac{\mathrm{d}f}{\mathrm{d}\phi} + \lambda \frac{\mathrm{d}g}{\mathrm{d}\phi} = 0, \quad \lambda g = 0, \quad \lambda \ge 0, \quad g \le 0, \quad (7)$$

where λ is the Lagrange multiplier. Finally, we update the scalar function ϕ by the following reaction diffusion equation:

$$\frac{\partial \phi}{\partial t} = \kappa \nabla^2 \phi - \alpha \frac{\mathrm{d}L}{\mathrm{d}\phi} \quad (8)$$

where, κ is the diffusion factor and α reaction factor.

4. NUMERICAL EXAMPLES

We implement the above mentioned method using COMSOL Multiphysics COMSOL (2015). The reaction diffusion equation (8) can be solved by the PDE mode (weak form) in the mathematics module in COMSOL Multiphysics. Also, the force equilibrium problem (6) can be solved by the solid mechanics module. The parametrized domain can be controlled by the parameter sweep function. When updating the parameter, the final configuration at the previous stage is used as the initial configuration for the next stage. At each stage, the upper bound of the volume fraction is set to 20%. Fig. 5 shows the representative five stages out of 10 stages. As the vertebrae bone growing, additional strengthening structures are formed on the both sides. Fig. 6 compares the measured shape of a zebrafish vertebrae bone and the shape produced by the proposed mathematical model. The calculated shape seemed to capture the basic structure but the shape has more roundish struts.

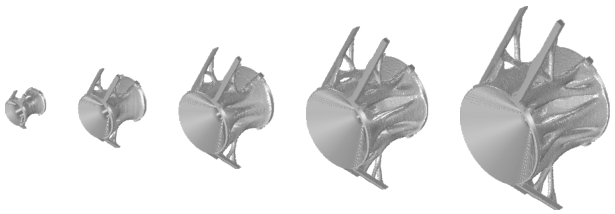

Fig. 5. Simulation of the growth of a vertebrae bone using topology optimization with a parametrized computational domain

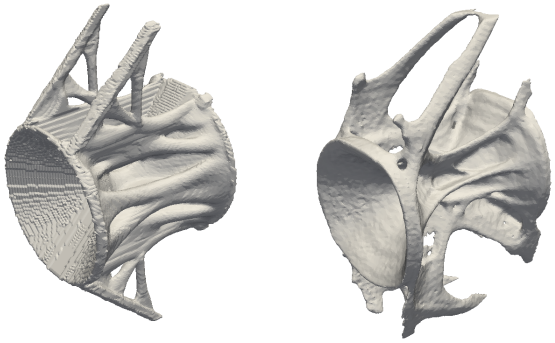

Fig. 6. Simulation (left) and measurement (right)

5. CONCLUSION

We have proposed a mathematical model for simulating the zebrafish vertebrae bone growth using topology optimization. Numerical results show the proposed model can capture the basic feature of vertebrae bone, while there still remain some discrepancies between the calculated shape and the measured shape.

REFERENCES

C. Boyle, Y.Y. Kim. Computational Simulation of Bone Remodeling using Design Space Topology Optimization. Proc. Appl. Math. Mech. 11, 97-98, 2011.

A. Kawamoto, T. Matsumori, T. Nomura, T. Kondoh, S. Yamasaki, S. Nishiwaki. Topology optimization by a time-dependent diffusion equation. International Journal for Numerical Methods in Engineering. 93(8):795-817, 2013.

COMSOL Multiphysics User's Guide, 2015. COMSOL AB.

Subsystem Interpolation for Parameterized Bilinear Dynamical Systems ⋆

A. Carracedo Rodriguez, Serkan Gugercin, Jeff Borggaard

Mathematics Department, Virginia Tech, Blacksburg, VA 24061 USA

(e-mail: {crandrea, gugercin, jborggaard}@vt.edu)

1. INTRODUCTION

Consider the following parametric bilinear system

$$\begin{cases} \dot{\mathbf{x}}(t) = \mathbf{A}(p)\mathbf{x}(t) + \mathbf{N}(p)\mathbf{x}(t)u(t) + \mathbf{b}(p)u(t), \\ y(t) = \mathbf{c}^\top(p)\mathbf{x}(t), \end{cases} \tag{1}$$

where $\mathbf{x}(t) \in \mathbb{R}^n$, $y(t) \in \mathbb{R}$, and $u(t) \in \mathbb{R}$ denote the states, output, and input, respectively. We assume that the parameter p is a scalar, i.e., $p \in \mathbb{R}$. We want to find a lower dimensional parametric bilinear system whose output is a good approximation to the output of the full order system for a wide variety of inputs $u(t)$ and parameter values p. We do so by means of a Petrov-Galerkin projection, i.e., given the reduction bases $\mathbf{V} \in \mathbb{R}^{n\times r}$ and $\mathbf{W} \in \mathbb{R}^{n\times r}$ with $\mathbf{W}^\top\mathbf{V} = \mathbf{I}_r$ where $r \ll n$. The reduced model has the same structure as in (1) with reduced matrices given by:

$$\begin{aligned} \widetilde{\mathbf{A}}(p) &= \mathbf{W}^\top\mathbf{A}(p)\mathbf{V} \in \mathbb{R}^{r\times r}, \quad \widetilde{\mathbf{b}}(p) = \mathbf{W}^\top\mathbf{b}(p) \in \mathbb{R}^{r\times 1} \\ \widetilde{\mathbf{N}}(p) &= \mathbf{W}^\top\mathbf{N}(p)\mathbf{V} \in \mathbb{R}^{r\times r}, \quad \widetilde{\mathbf{c}}(p) = \mathbf{V}^\top\mathbf{c}(p) \in \mathbb{R}^{r\times 1}. \end{aligned} \tag{2}$$

For the recomputations of the reduced model to be efficient, we assume an affine structure on the matrices in (1) with respect to the parameter. For example, $\mathbf{A}(p)$ is assumed to have the form

$$\mathbf{A}(p) = \mathbf{A}_0 + \sum_{i=1}^{\ell} f_i(p)\mathbf{A}_i, \tag{3}$$

where $\mathbf{A}_i \in \mathbb{R}^{n\times n}$ are constant matrices and $f_i(p)$ are scalar nonlinearities, for $i = 1, \ldots, \ell$. We will focus on building $\mathbf{V}$ and $\mathbf{W}$ so that interpolation of the two first transfer functions of (1) is guaranteed. Thus the goal is to extend the interpolatory parametric model reduction results of Baur *et al.* [2011] to the subsystem bilinear interpolation framework of Breiten&Damm [2010]. For more details on parametric and nonparametric model redution see Benner *et al.* [2015], Antoulas [2005], Antoulas *et al.* [2001], Baur *et al.* [2014], Benner *et al.* [2017], Benner *et al.* [2017], Hesthaven *et al.* [2016], Quarteroni *et al.* [2016], Benner and Breiten [2012], Flagg and Gugercin [2015], and references therein.

The two leading subsystem transfer functions of the bilinear system (1) are given by

$$\begin{aligned} \mathbf{H}_1(s;p) &= \mathbf{c}^\top(p)\mathbf{K}(s;p)\mathbf{b}(p), \quad \text{and} \\ \mathbf{H}_2(s_1,s_2;p) &= \mathbf{c}^\top(p)\mathbf{K}(s_2;p)\mathbf{N}(p)\mathbf{K}(s_1;p)\mathbf{b}(p) \end{aligned} \tag{4}$$

where

$$\mathbf{K}(s;p) = (s\mathbf{I}_n - \mathbf{A}(p))^{-1}. \tag{5}$$

The subsystem transfer functions of the reduced bilinear system are defined similarly and denoted by $\widetilde{\mathbf{H}}_1$ and $\widetilde{\mathbf{H}}_2$.

2. MAIN RESULTS

We now list the main results that show how to construct $\mathbf{V}$ and $\mathbf{W}$ for desired interpolation conditions:

Theorem 1. Let $\{\sigma_1, \sigma_2\} \subset \mathbb{C}$ and $\hat{p} \in \mathbb{R}$ such that $\mathbf{K}(\sigma_i;\hat{p})$ exists for all $i \in \{1, 2\}$. Define

$$\begin{aligned} &\mathbf{v}_1 = \mathbf{K}(\sigma_1;\hat{p})\mathbf{b}(\hat{p}), \quad \mathbf{v}_2 = \mathbf{K}(\sigma_2;\hat{p})\mathbf{N}(\hat{p})\mathbf{v}_1, \\ &\mathbf{w}_1 = \mathbf{K}(\sigma_2;\hat{p})^\top\mathbf{c}(\hat{p}), \quad \mathbf{w}_2 = \mathbf{K}(\sigma_1;\hat{p})^\top\mathbf{N}(\hat{p})^\top\mathbf{w}_1. \end{aligned} \tag{6}$$

If

$$\{\mathbf{v}_1, \mathbf{v}_2\} \subseteq \text{Ran}\mathbf{V}, \tag{7}$$

then

$$\begin{aligned} \mathbf{H}_1(\sigma_1;\hat{p}) &= \widetilde{\mathbf{H}}_1(\sigma_1;\hat{p}), \\ \mathbf{H}_2(\sigma_1,\sigma_2;\hat{p}) &= \widetilde{\mathbf{H}}_2(\sigma_1,\sigma_2;\hat{p}). \end{aligned} \tag{8}$$

If

$$\{\mathbf{w}_1, \mathbf{w}_2\} \subseteq \text{Ran}\mathbf{W} \tag{9}$$

then

$$\begin{aligned} \mathbf{H}_1(\sigma_2;\hat{p}) &= \widetilde{\mathbf{H}}_1(\sigma_2;\hat{p}), \\ \mathbf{H}_2(\sigma_1,\sigma_2;\hat{p}) &= \widetilde{\mathbf{H}}_2(\sigma_1,\sigma_2;\hat{p}). \end{aligned} \tag{10}$$

Theorem 2. Assume the conditions in Theorem 1. If both (7) and (9) hold, then not only do we have interpolation of the transfer functions

$$\begin{aligned} \mathbf{H}_1(\sigma_1;\hat{p}) &= \widetilde{\mathbf{H}}_1(\sigma_1;\hat{p}), \\ \mathbf{H}_2(\sigma_1,\sigma_2;\hat{p}) &= \widetilde{\mathbf{H}}_2(\sigma_1,\sigma_2;\hat{p}), \end{aligned} \tag{11}$$

but also of their sensitivities, i.e.,

$$\begin{aligned} \frac{\partial}{\partial s}\mathbf{H}_1(\sigma_1;\hat{p}) &= \frac{\partial}{\partial s}\widetilde{\mathbf{H}}_1(\sigma_1;\hat{p}), \\ \frac{\partial}{\partial s_i}\mathbf{H}_2(\sigma_1,\sigma_2;\hat{p}) &= \frac{\partial}{\partial s_i}\widetilde{\mathbf{H}}_2(\sigma_1,\sigma_2;\hat{p}), \\ \frac{\partial}{\partial p}\mathbf{H}_1(\sigma_1;\hat{p}) &= \frac{\partial}{\partial p}\widetilde{\mathbf{H}}_1(\sigma_1;\hat{p}), \\ \frac{\partial}{\partial p}\mathbf{H}_2(\sigma_1,\sigma_2;\hat{p}) &= \frac{\partial}{\partial p}\widetilde{\mathbf{H}}_2(\sigma_1,\sigma_2;\hat{p}). \end{aligned} \tag{12}$$

Remark. Interpolation of higher order derivatives can be attained by including derivative information in the

⋆ Supported in part by the National Science Foundation under contract DMS1522616 and the National Institute for Occupational Safety and Health under contract 200-2014-59669. The work of Gugercin was also supported in part by the Alexander von Humboldt Foundation.

reduction bases. We skip these details together with the proofs of above theorem for conciseness. The complete case of multi-input/multi-output systems together with a parameter vector $\mathbf{p}$ (as opposed to scalar p considered here) can be found in Carracedo *et al.* [2017].

3. EXAMPLE

Consider the following model of the transport and diffusion of the temperature of a fluid with thermal conductivity κ on the domain $\Omega = [-1, 1] \times [-1, 1]$:

$$\begin{aligned} \dot{T} &= \kappa \Delta T - \mathbf{v} \cdot \nabla T + u(t) f \\ T &= 0 \qquad \text{at } t = 0 \\ T &= 1 \qquad \text{on } \partial\Omega \end{aligned} \tag{13}$$

where

$$\mathbf{v}(x, y) = \sin t \begin{bmatrix} -y \\ x \end{bmatrix} + \frac{\cos t}{2}(\cos(\pi(x-y)) + 1) \begin{bmatrix} 1 \\ 1 \end{bmatrix} \tag{14}$$

and

$$f(x, y) = \exp(-(x^2 + y^2)) \tag{15}$$

is a source with strength controlled by the input $u(t)$. We can rewrite this model as a parametric bilinear system with input $u(t)$ and output (of our choice) the average temperature over $[0.5, 1] \times [0.5, 1]$. Then we can define a reduced-order model as in (2) with basis satisfying the conditions in Theorem 2. We do so for two different parameter sets: in the first set we only sample at 0.05; and in the second set we sample at 0.05, 0.06, 0.07, and 0.08. We show the performance of the reduced model for a non-sampled parameter value in Figures 1 and 2. Note that the full-order model has dimension 361 while the reduced-order model in Figures 1 and 2 has dimension 6 and 12, respectively. The figures show that a good approximation may be attained with this method by sampling the parameter space appropriately.

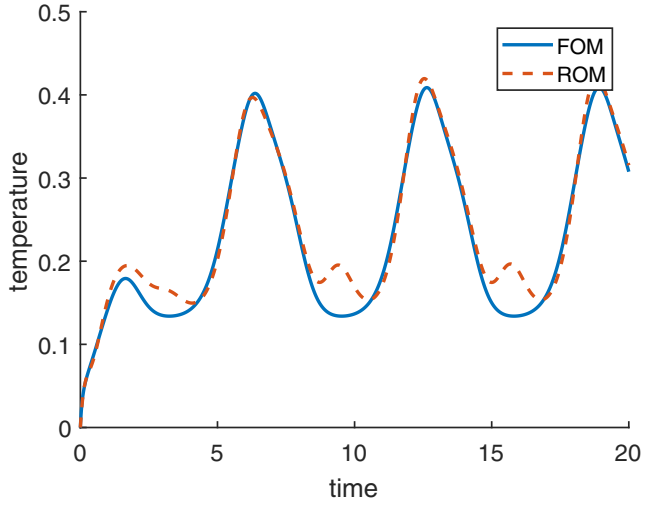

Fig. 1. Solution of the full order model and the reduced order model for parameter value $\kappa = 0.055$ and input $u(t) = 0.5$. Parameter sample: $\hat{\kappa} = 0.05$.

REFERENCES

Antoulas. Approximation of large-scale dynamical systems. *SIAM Publications*, Philadelphia, PA, 2005.

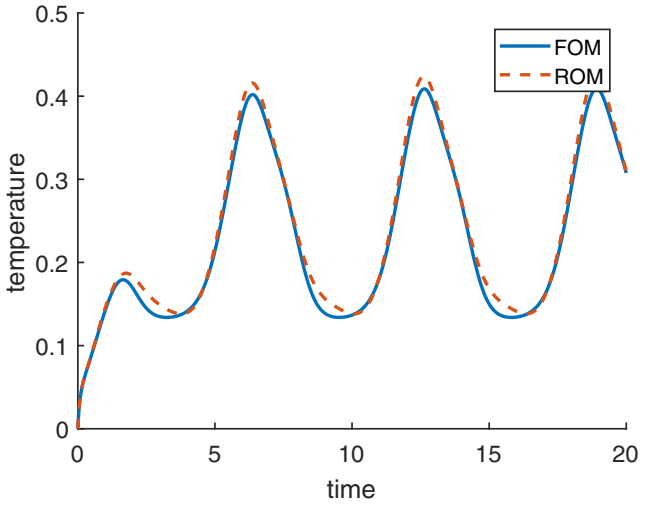

Fig. 2. Solution of the full order model and the reduced order model for parameter value $\kappa = 0.055$ and input $u(t) = 0.5$. Parameter samples: $\hat{\kappa}_1 = 0.05$, $\hat{\kappa}_2 = 0.06$, $\hat{\kappa}_3 = 0.07$, $\hat{\kappa}_4 = 0.08$.

Antoulas, Sorensen, and Gugercin. A survey of model reduction methods for large-scale systems. *Contemporary Mathematics* 280:193–219, 2001.

Baur, Beattie, Benner, and Gugercin. Interpolatory projection methods for parameterized model reduction. *SIAM Journal on Scientific Computing*, 33(5):2489–2518, 2011.

Baur, Benner, and Feng. Model order reduction for linear and nonlinear systems: A system-theoretic perspective. *Arch. Comput. Methods Eng.* 21(4):331–358, 2014.

Benner and Breiten. Interpolation-based $\mathcal{H}_2$-model reduction of bilinear control systems. *SIAM Journal on Matrix Analysis & Applications*, 33(3):859–885, 2012.

Benner, Gugercin, and Willcox. A survey of projection-based model reduction for parametric dynamical systems. *SIAM Review*, 57(4):483–531, 2015.

Benner, Cohen, Ohlberger, Willcox. Model reduction and approximation: theory and algorithms. *SIAM*, 2017.

Benner, Ohlberger, Patera, Rozza, Urban. Model Reduction of Parametrized Systems. *Springer*, 2017.

Breiten and Damm. Krylov subspace methods for model order reduction of bilinear control systems. *Systems & Control Letters*, 59:443–450, 2010.

Carracedo Rodriguez, Gugercin, and Borggaard. Interpolatory model reduction of parameterized bilinear dynamical systems. *Submitted to Advances in computational Mathematics*, 2017.

Flagg and Gugercin. Multipoint Volterra series interpolation and $\mathcal{H}_2$ optimal model reduction of bilinear systems. *SIAM Journal on Matrix Analysis and Applications*, 36(2):549–579, 2015.

Hesthaven, Rozza, and Stamm. Certified reduced basis methods for parametrized partial differential equations. *Springer*, 2016.

Quarteroni, Manzoni, Negri. Reduced Basis Methods for Partial Differential Equations. *Springer*, 2016.

Implicit Schur Complement for Model Order Reduction of Second Order Piezoelectric Energy Harvester Model

Chengdong Yuan [*,**] **Siyang Hu** [*,**]
Alessandro Castagnotto [***] **Boris Lohmann** [***]
Tamara Bechtold [*,**]

[*] *Department of Engineering, Jade University of Applied Sciences, Friedrich-Paffrath-Str. 101, D-26389 Wilhelmshaven. (e-mail: {chengdong.yuan, siyang.hu, tamara.bechtold}@jade-hs.de)*
[**] *Institute for Electronic Appliances and Circuits, University of Rostock, Albert-Einstein-Str. 2, 18059 Rostock.*
[***] *Chair of Automatic Control, Technical University of Munich, Boltzmannstr. 15, D-85748 Garching. (e-mail: {a.castagnotto, lohmann}@tum.de)*

Keywords: Multi-physical system, Model reduction, Krylov subspace, Schur complement.

1. INTRODUCTION

As energy efficiency becomes increasingly important in everyday life, different energy harvesting systems are being developed to recycle the energy wasted in the surrounding. By doing so, these devices act as independent power supplies for wireless micro-devices, as an alternative to batteries. In (Wang et al., 2012), the authors have introduced an energy harvester, which transforms vibrations into electrical energy, using the piezoelectric effect.

Kudryavtsev et al. (2015) showed that direct application of one-sided Krylov-subspace-based model order reduction (MOR) (Bai and Su, 2005; Salimbahrami and Lohmann, 2006; Gugercin et al., 2013) to the harvester model may lead to unstable reduced models. Therefore, the authors suggested a new approach called 'MOR after Schur' as they were able to obtain stable reduced models, when a Schur complement transformation was performed before MOR. However, they also stated that a Schur complement transformation increases the number of non-zero entries in the stiffness matrix and therefore the computational effort. To tackle this issue Benner et al. (2016) suggest to undo the Schur complement during the computation of the projection matrices to retake advantage of the sparse structure.

In this work, we consider an alternative approach for efficient one-sided reduction of the second-order piezoelectric energy harvester model, based on the work on first order systems in (Castagnotto et al., 2015), and establish an implicit Schur complement transformation.

2. MOR AFTER SCHUR

The system-level representation of the energy harvester model is shown in Fig. 1. It contains one mechanical input named **displ**, three mechanical outputs named **centre**, **south**, **north** and two electrical ports named **el1**, **el2**.

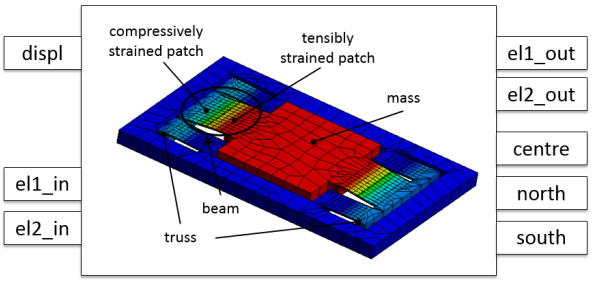

Fig. 1. System-level representation of piezoelectric energy harvester similar to (Kudryavtsev et al., 2015).

After the spatial discretization of governing partial differential equations, the piezoelectric model can be described as follows (Kudryavtsev et al., 2015):

$$\begin{cases} \underbrace{\begin{bmatrix} M_{11} & 0 \\ 0 & 0 \end{bmatrix}}_{M} \begin{bmatrix} \ddot{x}_1 \\ \ddot{x}_2 \end{bmatrix} + \underbrace{\begin{bmatrix} E_{11} & 0 \\ 0 & 0 \end{bmatrix}}_{E} \begin{bmatrix} \dot{x}_1 \\ \dot{x}_2 \end{bmatrix} + \underbrace{\begin{bmatrix} K_{11} & K_{12} \\ K_{21} & K_{22} \end{bmatrix}}_{K} \begin{bmatrix} x_1 \\ x_2 \end{bmatrix} = \underbrace{\begin{bmatrix} B_1 \\ B_2 \end{bmatrix}}_{B} u \\ y = \underbrace{\begin{bmatrix} C_1 & C_2 \end{bmatrix}}_{C} \begin{bmatrix} x_1 \\ x_2 \end{bmatrix} \end{cases} \tag{1}$$

$M, E \in \mathbb{R}^{(n+k)\times(n+k)}$ are the structural mass and damping matrix. $K_{11} \in \mathbb{R}^{n\times n}$ is the structural stiffness matrix, $K_{12} \in \mathbb{R}^{n\times k}$, $K_{21} \in \mathbb{R}^{k\times n}$ are the piezoelectric coupling matrices and $K_{22} \in \mathbb{R}^{k\times k}$ is the dielectric conductivity matrix. $x_1 \in \mathbb{C}^n$ and $x_2 \in \mathbb{C}^k$ are parts of the state vector representing nodal displacement and electrical potentials. $u \in \mathbb{R}^l$ is the vector of input load, $B_1 \in \mathbb{R}^{n\times l}$ and $B_2 \in \mathbb{R}^{k\times l}$ are parts of input matrix B. $y \in \mathbb{C}^m$ is the user defined output vector, $C_1 \in \mathbb{R}^{m\times n}$ and $C_2 \in \mathbb{R}^{m\times k}$ are parts of gathering matrix C.

When a Schur complement transformation is applied before the MOR process, the electrical domain related state vector x_2 can be eliminated by $x_2 = K_{22}^{-1}(B_2 u - K_{21} x_1)$, where given K_{22} is invertible, and the system is then transformed into:

$$\begin{cases} M_{11}\ddot{x}_1 + E_{11}\dot{x}_1 + \underbrace{(K_{11} - K_{12}K_{22}^{-1}K_{21})}_{=:K_s} x_1 = \underbrace{(B_1 - K_{12}K_{22}^{-1}B_2)}_{=:B_s} u \\ y = \underbrace{(C_1 - C_2K_{22}^{-1}K_{21})}_{=:C_s} x_1 + \underbrace{(C_2K_{22}^{-1}B_2)}_{=:D_s} u \end{cases} \tag{2}$$

For one-side reduction ($W = V$), the projection matrix V can be obtained from moment matching at the expansion point $\omega = 0$ (Salimbahrami and Lohmann, 2006). The reduced model resulting from the projection can then be written as:

$$\begin{cases} V^T M_{11} V \ddot{z} + V^T E_{11} V \dot{z} + V^T K_s V z = V^T B_s u \\ y = C_s V z + D_s u \end{cases} \tag{3}$$

3. MOR AFTER IMPLICIT SCHUR

In (Castagnotto et al., 2015), the authors show that an equivalent system for the first-order semi-explicit system can be established by projecting the input matrix onto the right deflating subspace corresponding to the finite eigenvalues. Using this new formulation, the Schur complement is implicitly performed during projection, as stated in the following result.

Theorem 1. The reduced model (3) can be obtained by reducing the equivalent system (4):

$$\begin{cases} \underbrace{\begin{bmatrix} M_{11} & 0 \\ 0 & 0 \end{bmatrix}}_{M} \begin{bmatrix} \ddot{x}_1 \\ \ddot{x}_2 \end{bmatrix} + \underbrace{\begin{bmatrix} E_{11} & 0 \\ 0 & 0 \end{bmatrix}}_{E} \begin{bmatrix} \dot{x}_1 \\ \dot{x}_2 \end{bmatrix} + \underbrace{\begin{bmatrix} K_{11} & K_{12} \\ K_{21} & K_{22} \end{bmatrix}}_{K} \begin{bmatrix} x_1 \\ x_2 \end{bmatrix} = \underbrace{\begin{bmatrix} B_s \\ 0 \end{bmatrix}}_{\widetilde{B}} u \\ y = \underbrace{\begin{bmatrix} C_1 & C_2 \end{bmatrix}}_{C} \begin{bmatrix} x_1 \\ x_2 \end{bmatrix} + D_s u \end{cases} \tag{4}$$

where the Schur complement transformation is only performed on the input matrix $\widetilde{B}$ and the feed-through matrix D_s is added.

The equality of the reduced models to (3) can then easily be shown by straightforward projection of (4) with its one-side Krylov subspace projection matrix. Note that (4) and (1) share the same transfer function, hence preserving the moment matching property.

4. NUMERICAL RESULTS AND CONCLUSION

Fig. 2 illustrates the full model's frequency response of the electrical outputs to the mechanical displacement excitation, which is visibly well matched by the frequency responses of the reduced models (reduce order $r = 30$) from both MOR after normal and implicit Schur. Both reduced models are obtained using first order one-sided Arnoldi at the expansion point $\omega = 0$ and with proportional damping (Rudnyi et al., 2004). Furthermore, Table 1 shows that the computational time of the MOR process can be significantly reduced (six times quicker) using implicit Schur, since the structure of the stiffness Matrix is preserved.

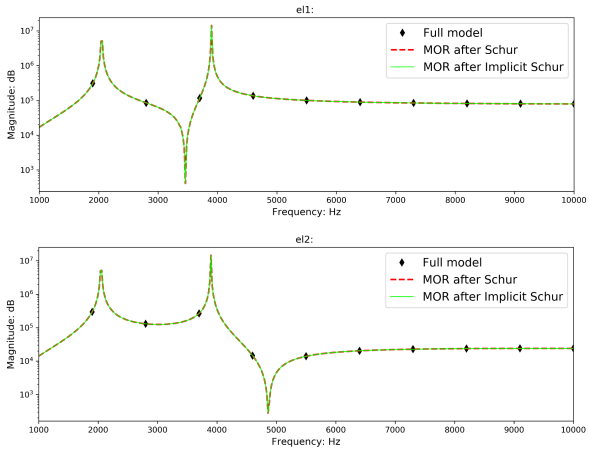

Fig. 2. Frequency response of the electrical outputs **el1_out** and **el2_out** with displacement excitation **displ** of full and reduced models.

Table 1. Computational time of MOR for normal and implicit Schur complement transformed system.

	MOR after Schur	MOR after Implicit Schur
Computational Time (s)	213.241	33.827

REFERENCES

Bai, Z. and Su, Y. (2005). Dimension reduction of large-scale second-order dynamical systems via a second-order Arnoldi method. *SIAM Journal on Scientific Computing*, 26(5), 1692–1709.

Benner, P., Saak, J., and Uddin, M.M. (2016). Reduced-order modeling of index-1 vibrational systems using interpolatory projections. In *Computer and Information Technology (ICCIT), 2016 19th International Conference on*, 134–138. IEEE.

Castagnotto, A., Panzer, H.K., Reinsch, K.D., and Lohmann, B. (2015). Stability-preserving, adaptive model order reduction of daes by Krylov-subspace methods. *arXiv preprint arXiv:1508.07227*.

Gugercin, S., Stykel, T., and Wyatt, S. (2013). Model reduction of descriptor systems by interpolatory projection methods. *SIAM Journal on Scientific Computing*, 35(5), B1010–B1033.

Kudryavtsev, M., Rudnyi, E.B., Korvink, J.G., Hohlfeld, D., and Bechtold, T. (2015). Computationally efficient and stable order reduction methods for a large-scale model of mems piezoelectric energy harvester. *Microelectronics Reliability*, 55(5), 747–757.

Rudnyi, E.B., Lienemann, J., Greiner, A., and Korvink, J.G. (2004). mor4ansys: Generating compact models directly from ansys models. In *Technical Proceedings of the 2004 Nanotechnology Conference and Trade Show, Nanotech*, volume 2, 279–282.

Salimbahrami, B. and Lohmann, B. (2006). Order reduction of large scale second-order systems using Krylov subspace methods. *Linear Algebra and its Applications*, 415(2-3), 385–405.

Wang, Z., Matova, S., Elfrink, R., Jambunathan, M., De Nooijer, C., van Schaijk, R., and Vullers, R. (2012). A piezoelectric vibration harvester based on clamped-guided beams. In *Micro Electro Mechanical Systems (MEMS), 2012 IEEE 25th International Conference on*, 1201–1204. IEEE.

Neurotransmitter Release from a Retinal Ribbon Synapse, a Modelling Study

Hassan Bassereh, Frank Rattay
Institute for Analysis and Scientific Computing, Vienna University of Technology, Wiedner Hauptstrasse 8-10, 1040 Vienna, Austria
(e-mail: Hassanbassereh@gmail.com)
(e-mail: frank.rattay@tuwien.ac.at)

Keywords: differential equation, retinal bipolar cell, Monte Carlo calculation, random numbers, average values, spike, ribbon synapse

1. INTRODUCTION

The chemical synapse is a structure that permits information transfer from neuron to neuron via neurotransmitter release. Synapses of specialized cells in the retina and inner ear, e.g. retinal photoreceptor and bipolar cells or cochlear hair cells, have an extra electron-dense structure in comparison to ordinary synapses. This structure, called "ribbon", plays a vital role on modulating vesicle release in response to time dependent input signals. This input, in the following investigation the terminal membrane voltage Vm of a retinal bipolar cell, is related to the variation of light intensity at a specific small region in the retina. Neurotransmitter release in axon terminals starts when the terminal membrane is depolarized which leads to open the voltage-gated calcium channels. Opening of calcium channels increases intracellular calcium concentration which triggers transient vesicle release. Transient vesicle release refers to contrast adaption (Oesch and Diamond, 2011). In case of long pulse stimulation, transient release is replaced by a tonic or sustained release, which occurs at slower rate and refers to luminance adaption (Oesch and Diamond, 2011). On the other hand, role of different periodic pulses on transient neurotransmitter release is investigated. The pulses make the terminal membrane depolarized in different levels which leads to different amount of neurotransmitter release.

2. RIBBON SYNAPSE

We simulated a bipolar cell terminal that contains one ribbon and we computed the number of vesicles released from this ribbon for time dependent input. Vesicles combine to the ribbon as soon as any vesicle site is empty on the ribbon. Voltage-dependent calcium channels close to the ribbon support the release, Fig. 1. The open probability increases for these channels according to the increase of membrane voltage allowing calcium ions to come into the terminal. Intracellular calcium concentration $[Ca^{2+}]$ is the key component in the release process as calcium ions make the vesicles ready to be released by binding to them. When the transmembrane voltage increases, the internal calcium concentration increases (with some delay caused by the ion channel gating kinetics) which consequently leads to increment in the number of released vesicles. The vesicle release continues until the transmembrane voltage reaches about -25mV (Oesch, and Diamond, 2011). On the other hand, the vesicle release has a stochastic component simulated as Monte-Carlo process.

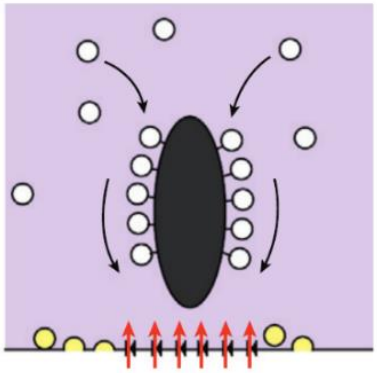

Fig, 1. Scheme of a ribbon synapse. The black oval-shaped part represents the ribbon and white spheres connected to the ribbon are 'ribbon vesicles'. Cytoplasmic vesicles are white spheres which are not connected to the ribbon. Red arrows show direction of incoming calcium ions. Picture taken from (Baden, et. al. 2013).

3. NEUROTRANSMITTER RELEASE

The calcium concentration is governed by

$$\frac{d[Ca^{2+}]}{dt} = -\frac{i_{ion}A}{2FV} - \frac{[Ca^{2+}] - [Ca^{2+}]_{rest}}{\tau} \quad (1)$$

Where i_{ion} is the calcium current which represents L-type calcium channels, A and V are surface and volume of the terminal, respectively, F=96485.33 $Cmol^{-1}$ is the Faraday constant, $[Ca^{2+}]_{rest}$ is the initial calcium concentration and τ

is the time constant of a passive extrusion process. The calcium current is explained by the Hodgkin-Huxley formalism (Hodgkin and Huxley, 1952). used in (Werginz, and Rattay, 2016) as follows: $i_{Ca} = \overline{g}_{Ca} m^3 (V - E_{Ca})$ where $\overline{g}_{Ca}$ is the maximum conductivity, m is the gating variable which represents open probability of the channel, V is the membrane voltage and E_{Ca} is the reversal potential and depends on the ratio of intracellular and extracellular calcium concentrations where the intracellular variations dominate.

A Monte-Carlo random process exerts the following condition on releasing: an equally distributed random integer number between 1 to 6 (number of initial vesicles) is selected and if there is any vesicle in that site, the neurotransmitter releasing occurs.

4. DISCUSSION

We fitted model parameter according to a synaptically two-paired pulse experiment in ref. (Oesch and Diamond, 2011, Graydon, et.al. 2014). The recorded data of a double pulse experiment demonstrates a nonlinear characteristic in vesicle release, Fig. 2, left. Our simulated results show averaged responses of 100 synapses, Fig. 2, right, which is fitted to the experimental data. In the next step, we simulated the vesicle release rate for periodic stimuli with frequencies of 2 and 8 Hz, Fig 3. Note, some spontaneous vesicle release occurs, that is without any stimulation. Frequencies up to 20Hz had the same characteristic features as the 8Hz case (simulated but not shown). The model again calculated for an ensemble with 100 memberships and the pulses starts from 100ms and continues to 1000ms.

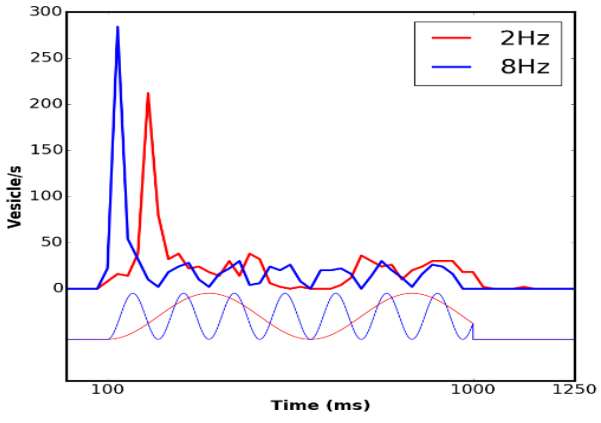

Fig. 3. Simulated vesicle release rate for two periodic input signals with frequencies of 2Hz and 8Hz. The stimulus starts at 100ms and continues to 1000ms. Some spontaneous vesicle release occurs, that is without any stimulation. Frequencies up to 20Hz had the same characteristic features as the 8Hz case (simulated but not shown).

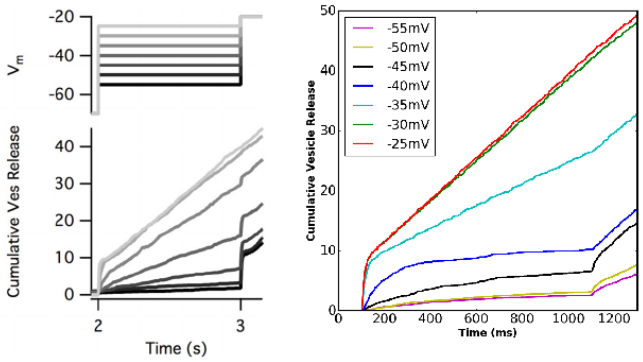

Fig. 2 (Left) Cumulative vesicle release (average of several experiments) vs. time in a single ribbon synapse (bottom) as response to a step function (top) Transmembrane voltage Vm was hold for one second at a constant value (e.g. -55mV (darkest line) or -25mV (bright line). A following higher voltage (-20mV) causes a sudden increase of release as long as the maximum release rate is not reached. (Graydon, et.al. 2014). (Right) The results from the model.

5. CONCLUSIONS

We used a calcium concentration dependent approach for neurotransmitter release for retinal bipolar cells. Direct use of membrane voltage as input to the ribbon model can be used instead of calcium concentration approach for slow events. However, there are different input output characteristics when graded potentials are interrupted by spikes in bipolar cells. When a spike reaches the terminal of a cell, calcium channels open and neurotransmitter will be released as consequence of an increase of intracellular calcium concentration. The presented model predicts the changing release rate as function of transmembrane voltage in the synaptic terminal both for spike trains and for graded potentials which can be assumed as arbitrary functions of time.

REFERENCES

Baden, T., Euler, T., Weckström, M., Lagnado, L. (2013) Spikes and ribbon synapses in early vision. *Trends. Neurosci,* 36, 480–488.

Graydon, CW. et. al. (2014) Passive diffusion as a mechanism underlying ribbon synapse vesicle release and resupply. *J. Neurosci*, 34, 8948–8962.

Hodgkin, A. L. and Huxley, A. F. (1952) A quantitative description of membrane current and its application to conduction and excitation in nerve. *J. Physiol*, 117, 500–544.

Oesch, N.W., Diamond, J.S. (2011) Ribbon synapses compute temporal contrast and encode luminance in retinal rod bipolar cells. *Nat. Neurosci*, 14, 1555–1561.

Werginz, P. and Rattay, F. (2016) The impact of calcium current reversal on neurotransmitter release in the electrically stimulated retina. *J. Neural. Eng*, 13(4), 046013.

An agent-based variant of the standard hidden-action model

Stephan Leitner * **Friederike Wall** **

* *Department of Management Control and Strategic Management, Alpen-Adria-Universität Klagenfurt, Universitätsstr. 65-67, 9020 Klagenfurt, Austria (e-mail: stephan.leitner@aau.at).*
** *Department of Management Control and Strategic Management, Alpen-Adria-Universität Klagenfurt, Universitätsstr. 65-67, 9020 Klagenfurt, Austria (e-mail: friederike.wall@aau.at).*

Keywords: Simulation, numerical simulation, economics, learning, dynamic system, management.

1. INTRODUCTION

In the context of incomplete information and environmental uncertainty, normative agency theory focuses on finding the most efficient contract between the principal and the agent, that aligns the two parties' interests but also maximizes the principal's utility. Typical classes of problems investigated within the framework of agency theory are concerned with hidden-characteristics, hidden-information and hidden-action (e.g., Eisenhardt, 1989).

Normative agency models have a set of assumptions incorporated. These assumptions are mainly concerned with (the distribution of) information and the involved individuals' behaviour (e.g., Müller, 1995) and might be regarded as a virtue as they allow for deriving optimal contracts in closed-form modeling. At the same time, these assumptions might also be a fundamental weakness as they might limit the theory's predictive validity.

The positive agency literature calls for relaxing these assumptions to map real-world situations. There are some conceptual papers that make aware of the limitations of normative agency literature (e.g., Shapiro, 2005). In addition, there is some empirical research that shows that mechanisms derived from normative agency models fail to work in real-world situations (e.g., Cuevas-Rodriguez et al., 2012). This is where we particularly place our research: We aim at contributing to closing the gap between positive and normative agency literature by providing a systematic analysis of selected assumptions in the standard hidden-action model.

In this paper, we transfer the standard hidden-action model into an agent-based variant of the hidden-action problem. In order to do so, we employ the so-called agentization approach which allows us to relax selected assumption incorporated in the standard hidden-action model. In the current paper, the process of agentization particularly concentrates on assumptions regarding the information available for both the principal and the agent. While the standard model allows to find the optimal contract in one timestep, the agent-based model variant requires the involved parties to search for the optimal contract over time. In addition to relaxed assumptions, the proposed agent-based model variant endows the principal and the agent with learning capabilities and a memory in which the learnings can be stored. The principal is additionally endowed with an exploration propensity which drives the selection of the strategy employed to search for 'better' contracts.

2. THE MODEL IN A NUTSHELL

We refer to the following model as standard hidden-action model: The principal offers the agent a contract (inter alia consisting of a task to be executed and a compensation scheme). In case the agent accepts the contract, she autonomously selects an effort level to execute the task. Together with an exogenous factor the selected effort level defines the outcome, which is observable by both the principal and the agent. The principal can neither observe the selected effort level, nor does he have information on the exogenous factor. Thus, the agent's compensation can only be based on the outcome. The standard hidden-action model gives information on how the contract should be designed so that the principal's utility maximizes (cf. Lambert, 2001).

The principal's utility function can be formalized by

$$U_P\left(\overbrace{\underbrace{X\left(a,\rho,\theta\right)}_{x=a\cdot\rho+\theta}}^{\text{production function}}\;,\;\overbrace{\underbrace{S\left(c_f,x,p\right)}_{s=c_f+x\cdot p}}^{\text{compensation function}}\right)\;, \qquad (1)$$

while the agent's utility function can be formalized by

$$U_A\left(s,a\right)=\overbrace{V\left(s\right)}^{\substack{\text{utility from}\\ \text{compensation}}}-\overbrace{G\left(a\right)}^{\substack{\text{disutility from}\\ \text{exerting effort}}}\;, \qquad (2)$$

where $a \in A$ represents the set of possible actions the agent can select from to carry out the delegated task, ρ stands for the agent's productivity, $\theta \in \Theta$ indicates the exogenous factor, c_f stands for the agent's fixed compensation component, and p indicates a premium level. For further elaborations, the agent's reservation utility is indicated by $\underline{U}$.

The principal is modeled to seek to maximize his expected utility (see Eq. 3) subject to the participation (see Eq. 4) and incentive compatibility constraint (see Eq. 5): [1]

$$\max \quad \mathbb{E}\left(U_P\left(x,s\right)\right) \tag{3}$$

$$s.t. \quad \mathbb{E}\left(U_A\left(s,a\right)\right) \geq \underline{U} \tag{4}$$

$$\int V(s)\, f_a\left(x|a\right) dx - G\left(a\right)' = 0 \tag{5}$$

The agent is also modeled to seek to maximize the expected utility,

$$\max \mathbb{E}\left(U_A\left(s,a\right)\right) \ . \tag{6}$$

Agency theory allows the principal to solve the optimization problem (i.e., to find the 'optimal' premium level, p, cf. Eq. 3–5) within one timestep, which (sometimes implicitly) includes very specific assumptions about the availability of information as well as about the involved parties capabilities. It is, e.g., assumed that the principal has full information about the agent's characteristics $(U_A, \underline{U}, \rho)$, is able to observe the outcome (x), knows the entire set of actions (A) the agent can select from to carry out the delegated task, and has information about the distribution of exogenous factors (Θ). The agent is assumed to have information on the distribution on exogenous factors (Θ), and the outcome (x). In addition, the agent is modeled to have private information on the selected action (a) and the realized exogenous factor (θ). [2]

Using the so-called agentization approach, the standard model is transferred into an agent-based model variant. [3] The agent-based model variant represents a multi-period version of the standard hidden-action model. A special feature of the agent-based model variant is that the principal and the agent are no longer able to find the optimal solution in one time-step but rather have to search for the optimal solution over time. During the process of agentization, particular focus is put on assumptions regarding the principal's and the agent's information about the distribution of exogenous factors and the principal's information about the set of actions. In particular, regarding the information about the action space and the distribution of exogenous factors, the following (presumably more realistic) assumptions are included in the agent-based model variant:

Assumptions regarding the principal's information

- Principal has limited information about the set of actions
- Principal is endowed with a mental horizon which defines the fraction of A that can be overseen
- Principal has no information about the distribution of exogenous factors
- Principal is endowed with the capability to learn about the distribution of exogenous factors over time and with a memory in which learnings are stored
- Principal is endowed with an exploration propensity which drives the strategy employed to search for 'the optimal solution' over time

Assumptions regarding the agent's information:

- Agent has no information about the distribution of exogenous factors
- Agent is endowed with the capability to learn about the distribution of exogenous factors over time and with a memory in which learnings are stored

All other assumptions remain unaffected by the agentization approach and are carried over from the standard model to the agent-based model variant.

3. SELECTED RESULTS

We find that the impact of the exogenous factor on the task's outcome significantly affects the efficiency of the contract offered to the agent, i.e., performance decreases as the impact of the exogenous factor on the task's outcome increases. Our results also indicate that the principal's exploration propensity does not significantly affect the efficiency of the derived contract if the impact of the exogenous factor is kept stable. We do, however, observe significant differences (caused by the principal's exploration propensity) across scenarios in which the impact of the exogenous factor is varied. We find that, in our model, a lower level of exploration propensity is particularly beneficial when the environment has a strong impact on the task's outcome. Moreover, we aim at identifying additional factors that drive our results (like, e.g., the principal's mental horizon). Based on our results we aim at characterizing critical factors and their interrelations in the context of hidden-action problem and at providing decision support on how to optimally shape delegation relationships.

REFERENCES

Cuevas-Rodriguez, G., Gomez-Mejia, L.R., and Wiseman, R.M. (2012). Has agency theory run its course?: Making the theory more flexible to inform the management of reward systems. *Corporate Governance: An International Review*, 20(6), 526–546.

Eisenhardt, K.M. (1989). Agency theory: An assessment and review. *Academy of Management Review*, 14(1), 57–74.

Guerrero, O.A. and Axtell, R. (2011). Using agentization for exploring firm and labor dynamics: A methodological tool for theory exploration and validation. In S. Osinga, G.J. Hofstede, and T. Verwaart (eds.), *Emergent Results of Artificial Economics*, volume 652 of *Lecture Notes on Economics and Mathematical Systems*, 139–150. Springer, Berlin, Heidelberg.

Lambert, R.A. (2001). Contracting theory and accounting. *Journal of Accounting and Economics*, 32(1-3), 3–87.

Leitner, S. and Behrens, D.A. (2014). On the efficiency of hurdle rate-based coordination mechanisms. *Mathematical and Computer Modelling of Dynamical Systems*, 1–19.

Müller, C. (1995). Agency-Theorie und Informationsgehalt. *Die Betriebswirtschaft*, 1995(1), 61–76.

Shapiro, S.P. (2005). Agency theory. *Annual Review of Sociology*, 31, 263–284.

[1] For more details on the standard model and the included constraints the reader might consult Lambert (2001).

[2] A detailed discussion of these assumptions is provided in Müller (1995).

[3] For details on the agentization approach the reader is referred to Leitner and Behrens (2014) and Guerrero and Axtell (2011).

Diffraction of plane wave on a periodic layer with arbitrary permittivity distribution ⋆

Dmitri Knyazkov

A.Ishlinsky Institute for Problems in Mechanics of the Russian Academy of Sciences, Moscow, Russia (e-mail: knyaz@ipmnet.ru)

Keywords: Diffraction, scattering, method of projections, sea surface radiometry

1. INTRODUCTION

A problem of modeling diffraction of a plane electromagnetic wave on a layer is considered. The layer is periodic by two directions and is bounded by two surfaces along the third one. These surfaces are also periodic and can have any form along those two directions. The permittivity of the layer is given by an arbitrary function. This function can even be discontinuous. Thus, in the framework of this model, a number of diffraction problems can be solved, e.g. diffraction on a grating or on a hologram, diffraction on earth or sea surfaces, problems of propagation of an electromagnetic wave in a waveguide, etc.

It is needed to calculate the diffracted electromagnetic field. The reflected and the propagated through the layer fields should be found. Coefficients of reflection, transmission and absorption (in the case of an absorbing medium) should also be computed. Therefore, in the described formulation, the following direct and inverse (see Kirsch (2011)) problems of diffraction can be solved:

- the tomography or the holography, where it is necessary to calculate the wave that passed through the media, or to synthesize a hologram with desired properties;
- the inverse scattering or the tomography of the inside of the layer, that requres to find the reflected from layer wave, for example, detection of underground objects as in Fiaz et al. (2012), or identifying the layer surface shape, for example, the active radar probing of the ocean surface;
- the determination of a shape of a layer based on information about its self-radiation, for example, the passive radio probing of the sea surface as in Gavrikov et al. (2016), where it is necessary to calculate the absorption coefficient.

The latter is possible thanks to the reciprocity principle, see Tsang et al. (2000). According to this principle, the self-radiation of a medium in a given direction is in the proportion to an energy absorbed by the medium under irradiation by a plane wave from this direction.

Solution of the outlined above problem of diffraction of the wave on the layer was described earlier for the two dimensional cases of H-polarization and E-polarization (see Knyazkov (2017b,a)). In the current paper, the substantially three dimensional case is considered. The method of projections proposed in Il'inskiy (1998) is used to calculate the result of diffraction. This approach allows us to reduce the original problem to a system of ordinary differential equations (ODEs) of the first order.

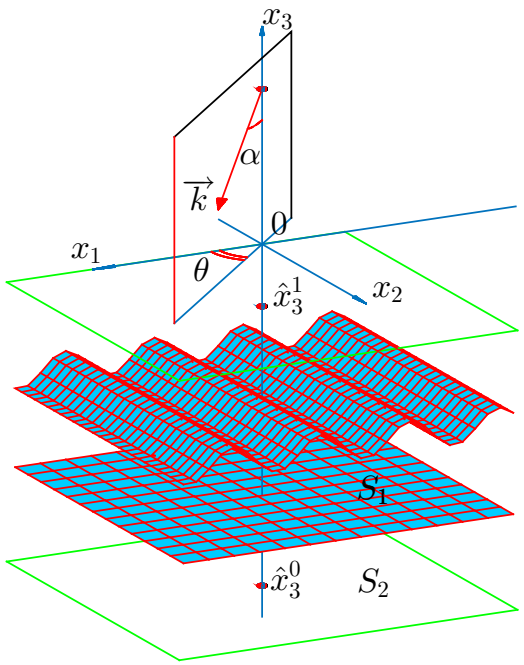

Fig. 1. Scheme of the wave incidence

2. PROBLEM STATEMENT

The wave comes at arbitrary inclination to the layer's surface. Its wave-vector $\vec{k}$ has the angle α with the axis Ox_3 (see Fig. 1). The projection of this vector to the Ox_1x_2 plane forms the angle θ with the Ox_1 axis. The layer is bounded by two surfaces defined by the functions $S_1(x_1, x_2)$ and $S_2(x_1, x_2)$. The permittivity of the layer is given by the function $\varepsilon(x_1, x_2, x_3)$. Functions S_1, S_2, ε are periodic along Ox_1 and Ox_2 axes with corresponding periods a_1 and a_2.

The Maxwells equations for the case of time-harmonic waves can be used. In the three dimensional space they lead to the following system for the components of the

⋆ The reported study was funded by RFBR, according to the research project No. 16-31-60096 mol-a-dk.

complex phasor amplitude electric field intensity vector $\overrightarrow{E} = (E_1, E_2, E_3)$:

$$\begin{cases} E_{1,22} + E_{1,33} - E_{3,13} - E_{2,12} + \varepsilon k_0^2 E_1 = 0, \\ E_{2,11} + E_{2,33} - E_{1,21} - E_{3,23} + \varepsilon k_0^2 E_2 = 0, \\ E_{3,11} + E_{3,22} - E_{1,31} - E_{2,32} + \varepsilon k_0^2 E_3 = 0, \end{cases} \quad (1)$$

where $E_{i,jk} = \frac{\partial}{\partial x_k}\frac{\partial}{\partial x_j}E_i(x_1, x_2, x_3)$. The goal is to solve the problem (1) with the corresponding radiation conditions in the domain $\Omega = [0, a_1] \times [0, a_2] \times [\hat{x}_3^0, \hat{x}_3^1]$.

3. THE METHOD OF PROJECTIONS

The system (1) can be solved with the use of the method of projections proposed in Il'inskiy (1998). The vector function $\overrightarrow{E}(x_1, x_2, x_3)$ can be represented as

$$E_i(x_1, x_2, x_3) = \sum_{s=1}^{N} B_{is}(x_3)\psi_s(x_1, x_2), \quad i = 1, 2, 3. \quad (2)$$

Here, functions ψ_s have the following property

$$\int_0^{a_2}\int_0^{a_1} \psi_{s_1}(x_1, x_2)\psi_{s_2}^*(x_1, x_2)dx_1dx_2 = \delta_{s_1,s_2}, \quad (3)$$

where $s_1, s_2 = 1, \ldots, N$, f^* is the conjugate of f, δ_{ij} is Kronecker delta, $\delta_{ij} = 1$ for $i = j$, $\delta_{ij} = 0$ for $i \neq j$.

After substituting the solution expansion (2) to the equations from (1), multiplying them by $\psi_s^*(x_1, x_2)$, $s = 1, \ldots, N$ and integrating on $[0, a_1] \times [0, a_2]$ we will have the following system of $4N$ first order ODEs:

$$\begin{cases} p' = Qb, \\ b' = Cp, \end{cases} \quad (4)$$

where Q and C are some matrixes with piece-wise continuous coefficients, p and b are the vectors of unknown variables. The boundary conditions can be written as

$$\begin{cases} Cp + iGb|_{x_3=\hat{x}_3^0} = 0, \\ Cp - iGb|_{x_3=\hat{x}_3^1} = v, \end{cases} \quad (5)$$

where G is the diagonal matrix and the vector v is defined by the initial wave:

$$\begin{aligned} v &= (v_1, \ldots, v_n, \ldots, v_{2N})^T \\ &= (-2i\gamma_1\sqrt{a_1a_2}E_{01}e^{-i\gamma_1\hat{x}_3^1}\delta_{n,1}, 0, \\ &\quad \ldots, 0, -2i\gamma_1\sqrt{a_1a_2}E_{02}e^{-i\gamma_1\hat{x}_3^1}\delta_{n,N+1}, 0, \ldots, 0)^T, \end{aligned} \quad (6)$$

where $\gamma_1 = |\overrightarrow{k}| \cdot cos(\alpha)$.

After solving the resulting system of ODEs (4) with the boundary conditions (5), we obtain the functions B_{ns}, $n = 1, 2, 3$, $s = 1, \ldots, N$. Substitution of these function to (2) gives us the desired solution. When knowing the solution, the reflection, transmission and absorption coefficients could easily be calculated.

4. COMPUTATIONAL PROGRAM

The computer program is written, that implements the described procedure. It is verified by comparison with an analytical solution in the simple cases of an oblique incidence on a homogeneous plane layer. In the other series of computations, the results are compared with the results obtained by another program for the case of H-polarized or E-polarized wave and homogeneous cylindrical layer with a sinusoidal surface (see Knyazkov (2017b,a)). Numerical experiments show the high accuracy. The error is less than 0.1% for computational meshes, that has 200-300 points along each of the coordinate axes. Some calculations for the needs of sea surface radiometry are performed. The good sensitivity and good selectivity to sea surface disturbances is shown for the inverse problem of sea surface form identification.

5. CONCLUSIONS AND OUTLOOK

In this paper, the diffraction of plane wave on a periodic layer is considered. The layer has arbitrary permittivity distribution and is bounded by two surfaces, that have arbitrary shape. The method of projections is used which allows to reduce the initial problem to the system of first order ordinary differential equations.

The developed computer program can be used in the mentioned applications. To decrease calculation time, the program can be rewritten for the hybrid cluster architecture. The described above programs are available free of charge on the internet. The source code can be downloaded from https://bitbucket.org/Jclash/dpproj. Small calculations can be performed with the use of web-interface http://ipmnet.ru/ knyaz/diffraction.html (see Knyazkov (2017c)) at Hybrilit HPC cluster installed at the Laboratory of Information Technologies of the Joint Institute for Nuclear Research, Dubna, Russia.

REFERENCES

Fiaz, M.A., Frezza, F., Pajewski, L., Ponti, C., and Schettini, G. (2012). Scattering by a circular cylinder buried under a slightly rough surface: the cylindrical-wave approach. *IEEE Transactions on antennas and propagation*, 60(6), 2834–2842.

Gavrikov, A., Knyazkov, D., Romanova, A., Chernik, V., and Shamaev, A. (2016). Simulation of influence of the surface disturbance on the ocean self radiation spectrum. *Program systems: theory and applications*, 7(2), 73–84. doi:10.25209/2079-3316-2016-7-2-73-84.

Il'inskiy, A.S. (1998). A method of investigating wave diffraction problems on a periodic structure. *USSR Computational Mathematics and Mathematical Physics*, 14(4), 242–246.

Kirsch, A. (2011). *An Introduction to the Mathematical Theory of Inverse Problems*, volume 120 of *Applied Mathematical Sciences*. Springer, 2nd edition edition.

Knyazkov, D. (2017a). Simulating diffraction of plane wave on periodic layer with the use of the method of projections. *IEEE Proc. of Days on Diffraction 2017, Saint-Petersburg, Russia*, 180–185. doi: 10.1109/DD.2017.8168019.

Knyazkov, D. (2017b). Simulation of diffraction on a layer using the method of projections. *AIP Conference Proceedings*, 1863, 370006. doi:10.1063/1.4992553.

Knyazkov, D. (2017c). Web-interface for hpc computation of a plane wave diffraction on a periodic layer. *Lobachevskii Journal of Mathematics*, 38(5), 936–939. doi:10.1063/1.4992553.

Tsang, L., Kong, J.A., and Ding, K.H. (2000). *Scattering of Electromagnetic Waves*, volume Vol. 1: Theory and Applications. Wiley Interscience.

Numerical simulations for fractional variable–order difference eigenfunctions

Piotr Oziabło

Faculty of Computer Science
Bialystok University of Technology, Wiejska 45A, Białystok, Poland
(e-mail: p.oziablo@student.pb.edu.pl)

Keywords: Difference equations; Dynamic systems; Eigenfunction; Fractional variable-order.

1. INTRODUCTION AND PRELIMINARIES

Recently fractional calculus is under strong attention as useful tool in modelling. In many cases fractional derivatives and difference operators proved their usefulnes and effectiveness in describing many real-life processes and phenomenas. For a review of theory and applications of fractional calculus, we refer the reader to (Hilfer, 2000; Kaczorek, 2009; Mozyrska & Wyrwas, 2015; Ostalczyk, 2016; Podlubny, 1999). For variable-order applications the reader can see more in Mozyrska & Ostalczyk (2017). In the paper we investigate discrete time operators with variable orders. We define variable-, fractional order backward difference of the Grünwald-Letnikov-type which means that the order is a single-variable, positive-valued function. Our goal is to start investigations of fitting data for noised eigenvalue function for initial value problem for fractional difference with variable-order.

Definition 1. For $k, l \in \mathbb{Z}$ and a given order function $\nu(\cdot)$ we define the oblivion function, as a discrete function of two variables, by its values $a^{[\nu(l)]}(k)$ given as

$$a^{[\nu(l)]}(k) = (-1)^k \frac{\nu(l)\,[\nu(l)-1]\cdots[\nu(l)-k+1]}{k!}\,,\ \text{for } k>0 \tag{1}$$

and $a^{[\nu(l)]}(k) = 0$ for $k < 0$, $a^{[\nu(l)]}(0) = 1$.

Formula (1) in Definition 1 is equivalent to the following recurrence with respect to $k \in \mathbb{N}$:

$$\begin{aligned} &a^{[\nu(l)]}(0) = 1\,,\\ &a^{[\nu(l)]}(k) = a^{[\nu(l)]}(k-1)\left[1-\frac{\nu(l)+1}{k}\right] \ \text{for } k \geqslant 1\,. \end{aligned} \tag{2}$$

Definition 2. Let f be a discrete-variable bounded real valued function. The Grünwald-Letnikov variable-, fractional-order backward difference (GL-VFOBD) with an order function $\nu : \mathbb{Z} \to \mathbb{R}_+ \cup \{0\}$ of function $x(\cdot)$ is defined as a finite sum

$$\left(\Delta^{[\nu(k)]}x\right)(k) = \sum_{i=0}^{k} a^{[\nu(k)]}(i)x(k-i) = \begin{bmatrix}1 & a^{[\nu(k)]}(1) & \cdots & a^{[\nu(k)]}(k)\end{bmatrix}\begin{bmatrix}x(k)\\ x(k-1)\\ \cdots\\ x(1)\\ x(0)\end{bmatrix}. \tag{3}$$

Let

$$\mathbf{A}^{[\nu(k)]} := \begin{bmatrix}1 & a^{[\nu(k)]}(1) & \cdots & a^{[\nu(k)]}(k)\\ 0 & 1 & \cdots & a^{[\nu(k-1)]}(k-1)\\ \vdots & \vdots & & \vdots\\ 0 & 0 & \cdots & 1\end{bmatrix}. \tag{4}$$

We consider the simple equation with variable-order for $k_0 = 0$.

$$\left(\Delta^{[\nu(k)]}x\right)(k) = \lambda x(k-1)\,,\ k \geq 1 \tag{5}$$

with initial condition $x(0) = x_0$ and constant coefficient $\lambda \in \mathbb{R}$. Then we can solve equation (5) by recurrence

$$x(k) = -\sum_{i=1}^{k} a^{[\nu(k)]}(i)x(k-i) + \lambda x(k-1)\,,\ k \geq 1\,. \tag{6}$$

Instead of working with recurrence we can use matrix form of defined matrices $\mathbf{A}_k^{[\nu(k)]}$. Moreover, let us use the following notation

$$\mathbf{x}(k) = \begin{bmatrix}x(k)\\ x(k-1)\\ \vdots\\ x(1)\\ x(0)\end{bmatrix}. \tag{7}$$

Then, equation (5) can be written in the matrix form

$$\mathbf{A}^{[\nu(k)]}\mathbf{x}(k) = \begin{bmatrix}\lambda\mathbf{x}(k-1)\\ x(0)\end{bmatrix},\quad k \geq 1$$

and its solution looks like the series of algebraic solutions:

$$\mathbf{x}(k) = \left(\mathbf{A}^{[\nu(k)]}\right)^{-1}\begin{bmatrix}\lambda\mathbf{x}(k-1)\\ x(0)\end{bmatrix}. \tag{8}$$

⋆ The work was supported by Polish founds of National Science Center, granted on the basis of decision DEC-2016/23/B/ST7/03686 and COST Action CA15225.

2. FRACTIONAL VARIABLE-ORDER EQUATIONS APPROXIMATION

Fitting experimental data is one of the most important issue for modeling. Efficient methods of finding fractional order equations which could describe real life phenomena would help us to develop better and more accurate mathematical models. In the first stage of our research we are trying to find a way to determine a value of λ knowing the order function. Additionally, we add noise signal to the data sets, which are used as an input data for our calculation to simulate "real life" measurement data. This approach emulates finding mathematical model which describes some real process.

We calculate GL-VFOBD values based on (8) matrix definition for different order functions and the different levels of noise. At the beginning we are trying to estimate λ using Mean Squared Error as a qualitative criterion of the estimation. Let $\mathbf{y}_k = \mathbf{x}(k) + \epsilon$, where $\epsilon \sim N(0, \sigma)$ is added noise. We assume, that we know order function, so we know also matrices given by formula (4). Then, the simplest criterion to fit λ is to minimize the following function

$$S_k(\lambda) := E_k^T E_k \,,$$

where

$$E_k = \mathbf{y}_k - \lambda \left(\mathbf{A}^{[\nu(k)]}\right)^{-1} \begin{bmatrix} \mathbf{y}_{k-1} \\ y_0 \end{bmatrix} .$$

The formula is slightly different as in equations (8), which gives us simpler formulation of the minimizer.

Then, λ_0 minimizing S_k for the set of $k+1$ values is given by the formula

$$\lambda_0 = \frac{1}{2d} \left(\mathbf{y}_k^T A^{-1} \begin{bmatrix} \mathbf{y}_{k-1} \\ y_0 \end{bmatrix} + \left[\mathbf{y}_{k-1}^T y_0\right] (A^T)^{-1} \mathbf{y}_k \right) , \quad (9)$$

where

$$d = \left[\mathbf{y}_{k-1}^T y_0\right] (A^T)^{-1} A^{-1} \begin{bmatrix} \mathbf{y}_{k-1} \\ y_0 \end{bmatrix}$$

and $A = \mathbf{A}^{[\nu(k)]}$.

Then, theoretical values $\hat{\mathbf{y}}_k$ we have from formula:

$$\hat{\mathbf{y}}_k = \left(\mathbf{A}^{[\nu(k)]}\right)^{-1} \begin{bmatrix} \lambda_0 \mathbf{y}_{k-1} \\ y_0 \end{bmatrix} . \quad (10)$$

In figures 1 and 2 we show some examples of order functions, noised data and the theoretical data from approximation given by (10). During our research we found out that λ estimation quality may be different for given order function even for the same level (variance and mean value) of noise. For some of the random noise values λ was not estimated properly (estimation error was significant). This was particularly evident when added noise values were high.

3. CONCLUSION

In future plans we are going to extend our investigations to matrix-eigenvalue form and also for situations, where we do not know parameters of order-function. Moreover, we are expecting some results in fitting real data by fractional models with variable order.

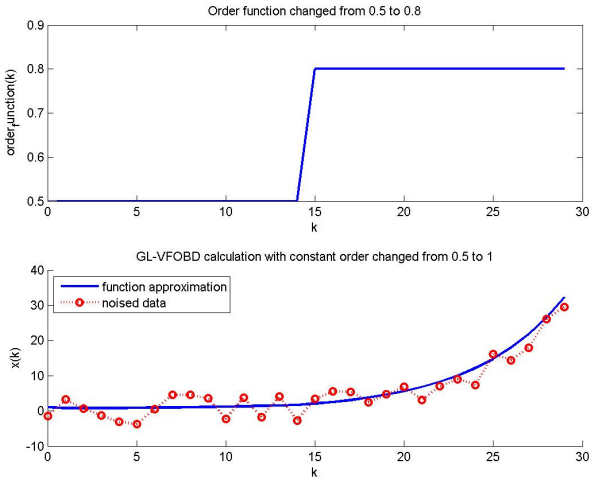

Fig. 1. Order function $\nu(\cdot)$ changed values from 0,5 to 0,8, original $\lambda = 0.3$, approximated $\lambda = 0.3035$

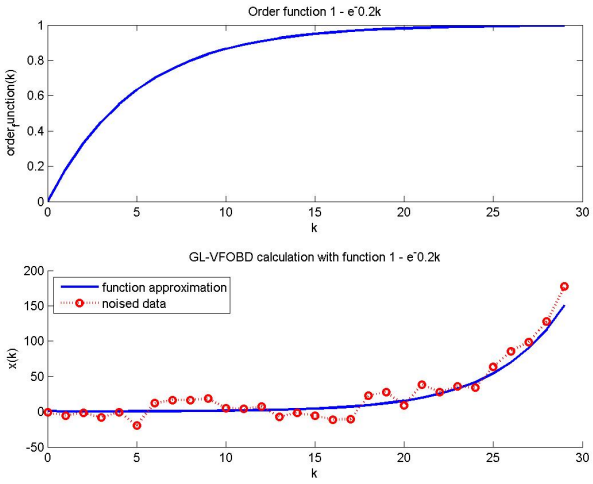

Fig. 2. Order function $\nu(k) = 1 - e^{-0,2k}$, original $\lambda = 0.3$, approximated $\lambda = 0.2923$

REFERENCES

Hilfer, R. (2000). *Applications of Fractional Calculus in Physics*. World Scientific Publishing Company, Singapore.

Kaczorek, T. (2009). Fractional positive linear systems. *Kybernetes*, 38(7/8):1059–1078.

Mozyrska, D. & Wyrwas, M. (2015). The Z-transform method and delta type fractional difference operators. *Discrete Dynamics in Nature and Society*, 2015:25 pages.

Mozyrska, D. & Ostalczyk, P. (2017). Generalized Fractional-Order Discrete-Time Integrator. *Complexity*, Volume 2017, Article ID 3452409, 11 pages.

Ostalczyk, P. (2016). *Discrete fractional calculus. Applications in control and image processing*. World Scientific Publishing Co Pte Ltd, vol. Series in Computer Vision - Vol. 4.

Podlubny, I. (1999). *Fractional Differential Equations. Mathematics in Sciences and Engineering*. 198. Academic Press, San Diego.

Impacts of Filter-Nonlinearities and Voltage Limitations on a Wide-Bandgap Inverter with Actively Damped LC-Filter

F. Maislinger * **H. Ertl** * **E. Gerstbauer** *

* *Institute of Energy Systems and Electrical Drives, TU Wien, Gusshausstraße 27-29, 1040 Vienna, Austria (franz.maislinger@tuwien.ac.at)*

Keywords: Inverter drives, multi-loop-control, active damping, system input limitation, nonlinear filters.

1. INTRODUCTION

Today, motor inverters in the kW domain typically are implemented using silicon (Si) based insulated gate bipolar transistors (Si-IGBT) operating in pulse width modulation (PWM) mode at switching frequencies up to 20 kHz. During the past few years, however, wide-bandgap switching devices like GaN- and SiC-MOSFETs have been significantly improved, especially concerning voltage capability of GaN devices. Due to the low switching- and also low on-state losses of GaN MOSFETs in comparison to Si-IGBTs, motor inverters with rather high switching frequencies but also high efficiency rates can be achieved (Shirabe and Swamy, 2012). However, the occurring high switching speed of the transistors with rise times in the range of 10 ns also create some crucial issues for motor applications caused by high du/dt rates.

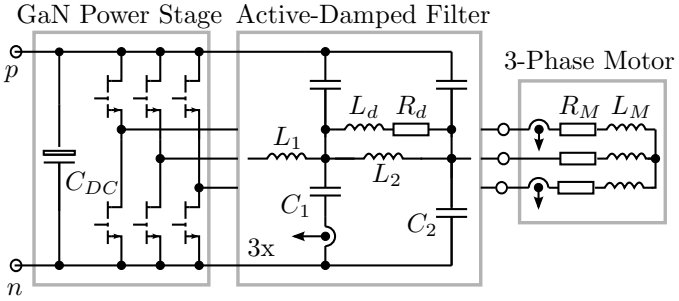

Fig. 1. Schematic concept of the proposed motor inverter with GaN power stage (switching frequency 100 kHz), active damped filter and a 3-phase motor as load.

To avoid and reduce negative effects of high-speed switching, the GaN inverter has to be extended by a filter system, which suppresses all switching noise at the inverter's output such that motor and cabling are fed by "sinusoidal-like" voltages (Fig.1). A two-stage LC output filter is used to achieve sufficient attenuation of the switching frequency harmonics. To obtain higher inverter efficiencies, an active damping concept of the LC-filter by feedback of the capacitor filter currents is applied instead of dissipative damping paths (which would result in additional losses). A closed-loop control concept using a simple PI-type controller employing additional feedback of the capacitor currents is performed. The determination of fitting controller parameters will be discussed in an upcoming paper, because here, the focus lies on the active damping scheme. Therefore, a mathematical model which represents the the physical properties of the filter and the motor as a load is implemented. Nevertheless, as illustrated in the following section inverter voltage limitations and nonlinearities of passive filter elements have negative influence on the chosen active damping scheme.

2. MATHEMATICAL MODEL

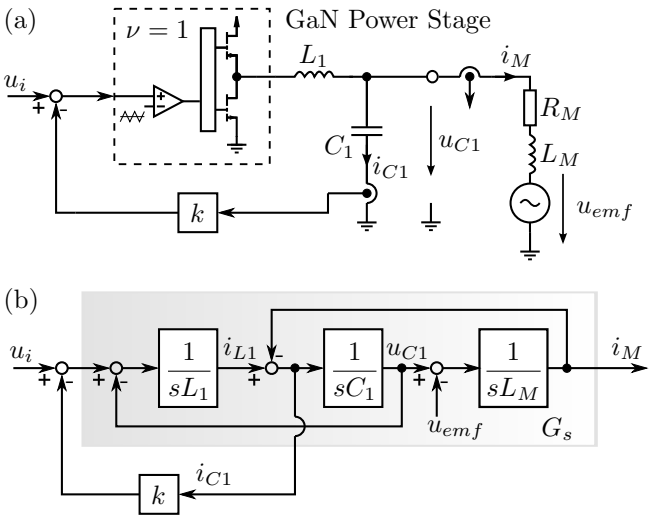

Fig. 2. (a) Single equivalent circuit of the inverter. (b) Plant dynamic model.

As described in (Maislinger et al., 2017), a single equivalent circuit can be found, (c.f., Fig. 2a), which shows the influence of the feedback of the capacitor current on the transfer function of the inverter. Therefore, the GaN power stage block has an assumed transfer function of gain $\nu = 1$. Furthermore, only a single stage filter is considered. The feedback gain k can be adjusted to obtain a desired filter behavior. The motor, which operates as inverter load, is considered by its resistance R_M, inductance L_M (which is at least ten times higher than L_1) and by the rotational speed proportional induced voltage u_{emf}, which acts in the system as a disturbance value. In case of a motor inverter

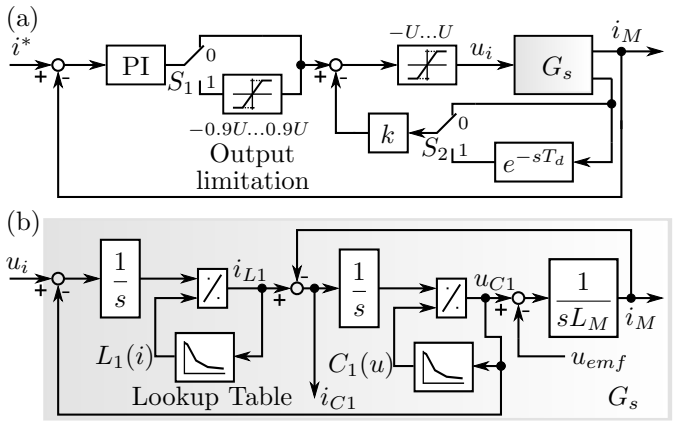

Fig. 3. (a) Closed-loop control concept. (b) Nonlinear plant dynamic model.

with constant values of L_1 and C_1, the transfer function in terms of the phase current i_M to the converter input voltage u_i can be written as (see Fig. 2b)

$$G(s) = \frac{1}{s\left(C_1 L_1 L_M s^2 + C_1 L_M k s + L_1 + L_M\right)}, \quad (1)$$

where the motor resistance R_M is set to zero (worst case scenario). A comparison of the transfer function to a conventional PT2 in the form

$$G_{PT2} = \frac{1}{s^2/\omega_0^2 + 2\xi s/\omega_0 + 1}, \quad (2)$$

leads to an expression of the active damping parameter

$$k = \frac{2\xi}{\omega_0}\frac{L_1 + L_M}{C_1 L_M} = 2\xi\sqrt{\frac{(L_1 + L_M)\,L_1}{C_1 L_M}}, \quad (3)$$

which guarantees a well damped system behavior.

2.1 System Input Limitation

For the investigated inverter, in case of a large step-change in the desired motor current i^* the system input u_i is limited to $\pm U$ (whereby U corresponds to the half of the DC-link voltage) as illustrated in Fig. 3a (switch S_1 is in position $S_1 = 0$). Therefore, the implemented active damping scheme is ineffective, since no control margin is available to counteract the excitation of the filter resonance. This phenomenon can be decreased if an additional output limiter is adapted next to the controller ($S_1 = 1$), which guarantees a buffer for the active damping part. Fig. 4a depicts the influence of the system input limitation on the filter current through the inductor i_{L1} as well as the resulting motor current, for both cases. As can be seen, the additional output limiter decreases the current in the passive filter elements, but also reduces the system dynamic.

2.2 Nonlinearities of Passive Filter Elements

To consider nonlinearities of the passive filter elements in the model, the function G_s of Fig. 2b has to be replaced by Fig. 3b. The values of the lookup tables come from data sheets that correspond to a Sendust powder core with a permeability of 60 for $L_1(i)$ and an Arcshield ceramic capacitor with 330 nF, 500 V for $C_1(u)$ (KEMET, 2017). As mentioned above in (3), the optimal active damping parameter k is a function of the passive filter elements L_1 and C_1. However, by measuring the capacitor filter current i_{C1} nonlinearities of L_1 and C_1 seem to have only small influences on the active damping mechanism of the proposed inverter as illustrated in Fig. 4b. But, if the effect of a time delay caused by measuring the filter current is also considered ($S_2 = 1$), the impact of nonlinear filter elements is crucial. In Fig. 4b, a time delay T_d of 5us is assumed, which corresponds to half a period at a switching frequency of 100 kHz. For higher time delays in the range of a full switching period the system becomes unstable.

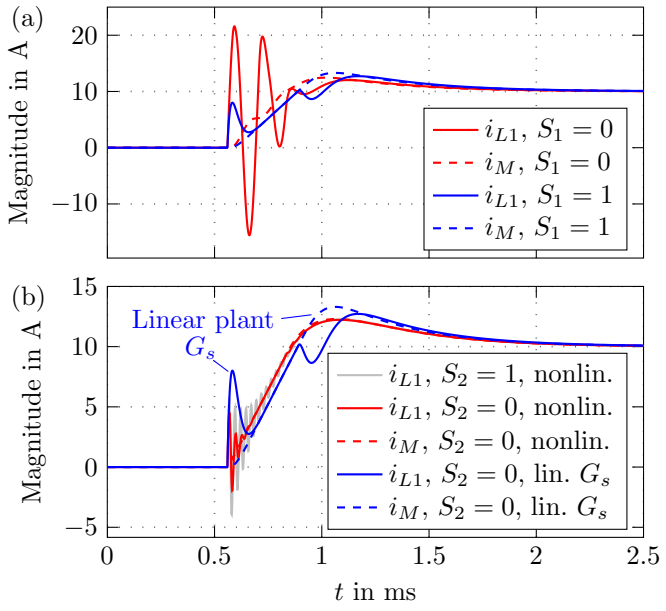

Fig. 4. (a) Influence of system input limitation. (b) Impact of nonlinearities on filter- and motor currents (red) as well as influence of time delay in capacitor current measurement (gray). In all cases: $S_1 = 1$.

3. CONCLUSION

The paper gives a brief overview about the impacts of nonlinearities and input limitations on wide-bandgap inverters with an active damped LC-filter. It is shown that by using a further limiter after the controller output, the functionality of the active damping scheme remains present, independent of the controller output. Furthermore, nonlinearities and time delays in capacitor current measurement can lead to an unstable behavior of the dynamic plant. The negative time delay effect can be neglected, if a linear observer-based model is used to calculate the capacitor filter current instead of the measurement. The effect of nonlinear filter elements on the control concept with the observer-based model is under investigation.

REFERENCES

KEMET (2017). K-sim version 2.0.17.8. Internet, 2017. Ksim.kemet.com.

Maislinger, F., Ertl, H., Stojcic, G., and Holzner, F. (2017). Control loop design for closed-loop class-d amplifiers with 4th order output filter. *PCIM Europe 2017*.

Shirabe, K. and Swamy, M. (2012). Advantages of high frequency pwm in ac motor drive applications. *Energy Conversion Congress and Exposition (ECCE)*.

Synchronization properties of Voltage Source Converters when seen as Coupled Oscillators based on the Kuramoto Model

Noe Barrera Gallegos * **Victoria Gasca Segura** **
Marta Molinas ***

* *Department of Engineering Cybernetics, Norwegian University of Science and Technology, 7491 Trondheim, Norway (e-mail: noebg20@gmail.com).*
** *Faculty of Electrical Engineering, Electronics and Computer Systems, Universidad Tecnolgica De Pereira, Pereira, Colombia, (e-mail: mvgasca@utp.edu.co)*
*** *Department of Engineering Cybernetics, Norwegian University of Science and Technology, 7491 Trondheim, Norway (marta.molinas@ntnu.no)*

1. INTRODUCTION

Microgrids are present in electrical networks and are becoming more important in the conventional AC distribution networks. Microgrids are composed by converters which transfer the power produced in the microgrids to the loads. It is crucial to control properly the converters in order to ensure stability of the voltage magnitude and frequency on the grid.

The general scheme of the voltage source converter (VSC) is presented in Fig. 1. Using modulated signals to control the pulses for opening and closing the switching devices, the converter is able to transfer back and forth the energy form the DC side to AC grid.

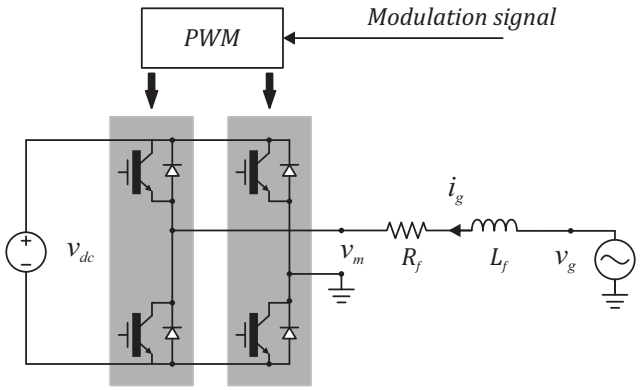

Fig. 1. Voltage source converter

The aim of this paper is to compare the properties of synchronization, here we present the comparison between two control strategies with very different conceptions. One is the synchronous reference frame control (SRFC), which is set by assuming that the converter exhibits a linear behavior [Yazdani and Iravani (2010) Teodorescu et al. (2011)]. The second controller is the virtual oscillator control (VOC). This is a new control approach for the AC/DC converters developed by Johnson et al. (2012). This control strategy uses a nonlinear oscillator that provides a modulation signal for the converter. This comparison is meaningful because both approaches have the same purpose in a microgrid: the control of the power in the converter.

2. SYNCHRONOUS REFERENCE FRAME CONTROL

Born for the control of electrical machinery (Kundur (1994)), the rotational framework $dq0$ helps to transform the sinusoidal values into constant values. This transformation simplify the control of the AC current in the inverters. This transformation is commonly used in three phase circuits. For the single-phase converter an additional step is needed for the phase angle detection. A fictitious $\alpha - \beta$ signal is produced by using the second order generalized integrator (SOGI). The resultant signals in quadrature provide a proper way to transform the single phase voltage and current into the $dq0$ framework.

2.1 Droop control

Under the assumption that the current control is tuned, and the PLL has a faster time response than the current control, then the power angle of the converter δ_i is small (De Brabandere et al. (2004)). It is also assumed that the resistance in the output filter R_s is negligible. Therefore, the power expression for the converter is,

$$S_i = P_i + jQ_i \tag{1}$$

Assuming that δ_i is small, the active power P_i is approximated by,

$$P_i \approx \frac{V_g V_m \delta_i}{X_L} \tag{2}$$

and the approximated reactive power Q_i is,

$$Q_i \approx \left(\frac{V_g - V_m}{X_L}\right) V_g \tag{3}$$

These relationships allow the proportional control for the voltage and frequency in the converter terminals by applying the following proportional control laws.

$$V_m = V_m^* + m_{Qi} Q_i \tag{4}$$

$$\omega = \omega^* + m_{Pi} P_i \tag{5}$$

Where m_{Qi} and m_{Pi} are the proportional droop gains for voltage and frequency respectively.

2.2 Kuramoto equivalent model

The equivalent Kuramoto model is the representation of the oscillatory characteristics of coupled oscillators (also called Kuramoto oscillators). Consider the phase of the i^{th} converter connected in parallel to the utility grid, which follows the dynamic.

$$\frac{d\theta_i}{dt} = \omega_i - \sum_{j=1}^{n} a_{ij} \sin(\theta_i - \theta_j) \tag{6}$$

Each converter connected to the utility grid has a degree of coupling a_{ij} to the utility grid frequency. The coupling parameter a_{ij} for each converter is by definition (Simpson-Porco et al. (2012)),

$$a_{i0} \triangleq \frac{V_g V_m}{X_L} \tag{7}$$

Where V_g and V_m are the RMS values of the voltages in the utility grid and the converter AC side.

3. VIRTUAL OSCILLATOR CONTROL

The virtual oscillator control works using a resonant circuit with equations similar to the nonlinear van Der pol oscillator.

The dynamic is that of a parallel RLC circuit and a nonlinear voltage dependent current source (Johnson et al. (2016)). Where the resonant circuit and the dependent current source $g(v_c)$ are implemented in a programmable device (computer, FPGA, etc.), the program provides the modulation signals to the converter. The current and voltage equations are,

$$L\frac{di_L}{dt} = v_c \tag{8}$$

$$C\frac{dv_c}{dt} = \sigma v_c - k_l v_c^3 - \frac{v_c}{R} - i_L + k_l u\,(t) \tag{9}$$

Where the term $(\sigma v_c - k v_c^3)$ describe the nonlinear dynamic of the voltage dependent current source, v_c is the voltage in the capacitor of the RLC circuit. For simplicity the following terms are defined

$$\epsilon = \sqrt{\frac{L}{C}}, \qquad \alpha = \sigma - \frac{1}{R}, \qquad \beta = \frac{3k_l}{\alpha}$$

where σ, k are positive constants. With the natural frequency of oscillation $\omega = \sqrt{LC}$. For the synchronization analysis the equations (8) and (9) need to be transformed into polar coordinates (Johnson et al. (2014a)). This transformation gives an explicit expression of the phase angle of the converter θ and amplitude r related to the voltage amplitudev_c. The equations in polar coordinates are,

$$\frac{dr_i}{dt} = \frac{1}{C}\left(\alpha h\left(r\cos(\omega t - \theta)\right) + k_l u\,(t)\right)\cos(\omega t - \theta) \tag{10}$$

$$\frac{d\theta_i}{dt} = \omega - \left(\frac{\alpha}{rC} h\left(r\cos(\omega t - \theta)\right) + \frac{k_l u\,(t)}{rC}\right)\sin(\omega t - \theta) \tag{11}$$

Where $h(y)$ is the function $h(y) = y - \frac{\beta}{3}y^3$.

Notice that equations (10) and (11) depend on the term $ku\,(t)$ which is the input current (sinusoidal) for the RLC circuit. Equation (11) also depend on the term α. As proposed by Johnson et al. (2014b), to ensure a stable limit cycle in the system, α has to be positive and small. This implies that a simplified form for equation (11) can take the form of the equivalent Kuramoto model.

3.1 Kuramoto equivalent

From equation (11), if α can be considered as a small, equation (11) becomes,

$$\frac{d\theta_i}{dt} = \omega - \left(\frac{k_l u\,(t)}{rC}\right)\sin(\omega t - \theta) \tag{12}$$

Such equivalent reduced nonlinear model has the same structure as the Kuramoto model. Being a_{ij} equal to,

$$\frac{k_l u\,(t)}{rC} = a_{ij} \tag{13}$$

The comparison of the two equivalent Kuramoto models for different control techniques represents a simplified task compared to the work presented by Johnson et al. (2017), in which the use of the measured current and the protector matrix (Johnson et al. (2014b)), the synchronization error is computed.

3.2 Discussion

To the authors understanding, the methods used nowadays for the analysis of synchronization characteristics in the SRFC does not include the complete PLL dynamics for the analysis. An explicit form for the phase angle is needed for the modeling of the PLL dynamics. Such mathematical expression could be used to understand the problematic of the synchrony of converters under adverse circumstances like

- The converters coupled by exchanging power.
- Converters connected to a "weak" utility grid.
- Converters controlling the DC voltage.

This paper presents the fact that there is no formal way to compare converters with different control objectives and structures. It presents the need for a formulation of the equivalent (Kuramoto) model that represent the dynamic of the synchronization.

ACKNOWLEDGEMENTS

This work was carried out during the tenure of an ERCIM "Alain Bensoussan" Fellowship Programme.

Model predictive control of a time-varying convection-diffusion equation with state constraints

Lars Grüne * **Simon Pirkelmann** **

* *Chair of Applied Mathematics, University of Bayreuth, 95447 Bayreuth, Germany (e-mail: lars.gruene@uni-bayreuth.de)*
** *Chair of Applied Mathematics, University of Bayreuth, 95447 Bayreuth, Germany (e-mail: simon.pirkelmann@uni-bayreuth.de)*

Keywords: Time-varying systems, model predictive control, partial differential equations

1. INTRODUCTION AND OUTLINE

In this discussion paper we consider the convection-diffusion equation with time-varying boundary conditions as a simple model of a room whose temperature shall be controlled in an energy efficient way. This model serves as an example for which we want to investigate whether results from a recent paper (Grüne and Pirkelmann, 2017) also hold for a more involved model.
In the first part we introduce the model and formulate a constrained optimization problem. The following section outlines how an approximate solution to the problem can be obtained using Model Predictive Control (MPC). The method is briefly described and we also mention results about the relation between the MPC solution and the solution of the original problem. The final part gives a brief overview of selected aspects of the implementation.

2. PROBLEM STATEMENT

Consider the heat equation

$$\frac{\partial y}{\partial t} - \alpha\nabla^2 y + w\nabla y = 0 \text{ on } Q := \Omega \times [0,T], \tag{1}$$

$$y(0) = y_0 \text{ on } \Omega, \tag{2}$$

where $y : Q \to \mathbb{R}$ is the temperature, $\alpha > 0$ is the diffusion coefficient, $w : [0,T] \times \Omega \to \mathbb{R}$ is a velocity field and $y_0 : \Omega \to \mathbb{R}$ is the initial condition.
As a domain Ω we consider the unit interval. The boundary Γ is partitioned into a controlled boundary Γ_c and an uncontrolled boundary Γ_{out}, see Figure 1. On the controlled part of the boundary a function u is applied representing heating and cooling. This is modelled by the condition

$$\beta\frac{\partial y}{\partial n} + \gamma_c y = \gamma_c u \text{ on } \Sigma_c := \Gamma_c \times [0,T]. \tag{3}$$

On the uncontrolled part we have

$$\beta\frac{\partial y}{\partial n} + \gamma_{out} y = \gamma_{out} y_{out} \text{ on } \Sigma_{out} := \Gamma_{out} \times [0,T]. \tag{4}$$

In the above equations $\frac{\partial y}{\partial n}$ is the derivative of y in normal direction, y_{out} is the outside temperature, and $\beta : \Sigma \to \mathbb{R}$, $\gamma_c : \Sigma_c \to \mathbb{R}$ and $\gamma_{out} : \Sigma_{out} \to \mathbb{R}$ are coefficient functions. Defining $\gamma := \begin{cases} \gamma_{out} & \text{on } \Gamma_{out} \\ \gamma_c & \text{on } \Gamma_c \end{cases}$ and $z := \begin{cases} y_{out} & \text{on } \Gamma_{out} \\ u & \text{on } \Gamma_c \end{cases}$ the two above boundary conditions can be written in a more consise way:

$$-\beta\frac{\partial y}{\partial n} = \gamma(y - z) \text{ on } \Sigma. \tag{5}$$

Fig. 1. Illustration of domain Ω and subdomain Ω_y, as well as controlled (Γ_c) and uncontrolled (Γ_{out}) parts of the boundary.

In addition to controlling the temperature at the boundary we may control the velocity field w. For simplicity we assume that for any fixed time point w is constant on the whole domain, i.e. does not depend on space.
The presented model is motivated by a practical application: energy efficient building control. We would like to influence the temperature of a room (Ω) by controlling the temperature at one wall of the room (Γ_c) and the airflow inside the room. The temperature at the other wall cannot be controlled and may be changing over time (e.g. due to changing weather). However, we assume that the outside temperature y_{out} is known in advance via the weather forecast, at least for a certain time span into the future.
Our goal is to keep the temperature in some part of the room Ω_y within certain upper and lower bounds $\underline{y}$ and $\overline{y}$, and doing so using as little control effort (or energy) u and w as possible. In addition, we may also want to penalize the deviation from some reference temperature y_Ω.
This is expressed by the following optimal control problem:

$$\min_{y,u} J(y,u) = \frac{\varepsilon_y}{2}\|y(T) - y_\Omega(T)\|^2_{L^2(\Omega)} + \frac{\varepsilon_y}{2}\|y - y_\Omega\|^2_{L^2(Q)} + \frac{\varepsilon_u}{2}\|u\|^2_{L^2(\Sigma)} + \frac{\varepsilon_w}{2}\|w\|^2_{L^2(0,T)} \tag{6}$$

subject to equations (2), (5) and the constraints

$$\underline{u} \le u \le \overline{u} \text{ on } \Sigma_c, \tag{7}$$

$$\underline{y} \le y \le \overline{y} \text{ on } \Omega_y \times [0,T], \tag{8}$$

with (possibly time-varying) lower and upper bounds for state and control.

⋆ This work was supported by DFG-Grant GR 1569/16-1

3. MODEL PREDICTIVE CONTROL

For large or possibly infinite time horizon T the problem becomes very difficult to solve numerically. Also, reliable weather forecast data will only be available for relatively short periods. To deal with this issue Model Predictive Control (MPC) is used. For an in-depth introdution to MPC we refer to Grüne and Pannek (2017).
Briefly, the idea is as follows: Starting at time $t = 0$ given the state $y(0) = y_0$ we consider the problem on a shorter horizon $[0, T_{MPC}]$ with $T_{MPC} < T$ and solve the reduced open-loop problem instead. As a solution we obtain the control u on the smaller horizon which is then applied to the system up to $t = h$ with some sampling rate $h < T_{MPC}$. At time $t = h$ the state is measured again and the procedure is repeated. Continuing this way we obtain the *closed-loop* of the controlled system.
The natural question now is whether the MPC closed-loop approximates the solution of the original problem. Our recent results for time-varying systems show that at least the cost of an infinite horizon optimal solution is approximated by the MPC algorithm, cf. Grüne and Pirkelmann (2017). In that paper we used a rather simple example to illustrate the results.
The model presented in the current paper is more involved and will serve to demonstrate that approximate optimality can also be observed in the infinite-dimensional setting.

4. IMPLEMENTATION DETAILS

MPC reduces the problem in time but we still need to solve an open-loop optimal control problem in each step of the MPC algorithm. We use a First-Discretize-Then-Optimize approach to solve the problem.
Discretizing the optimal control problem (6), (8) in time and space we obtain a finite-dimensional optimization problem with a quadratic cost functional

$$\min_{y_h,u,w} J(y_h,u,w) = \sum_{k=0}^{N-1} \Big(\frac{\varepsilon_y}{2}(y_{h,k}-y_{\Omega,k})^T Q(y_{h,k}-y_{\Omega,k}) + \frac{\varepsilon_u}{2} u_k^T R u_k + \frac{\varepsilon_w}{2} w_k^T W w_k \Big) + \frac{\varepsilon_y}{2}(y_{h,N}-y_{\Omega,N})^T Q(y_{h,N}-y_{\Omega,N})$$

subject to the nonlinear constraints

$$\begin{aligned} A y_{h,k+1} + w_k B_w y_{h,k+1} &= B_y y_{h,k} + b_u u_k + b_{y,out} y_{out,k} && \text{for } k \in \{0,\dots,N-1\}, \\ \underline{y}_{h,k,i} \le y_{h,k,i} \le \overline{y}_{h,k,i} && \text{for } k \in \{0,\dots,N\}, i \in \mathcal{I}_{\Omega_y}, \\ \underline{u}_k \le u_k \le \overline{u}_k && \text{for } k \in \{0,\dots,N-1\}, \end{aligned}$$

where the matrices A, B_w, B_y and the vectors b_u and $b_{y,out}$ stem from the finite element discretization and Q, R and W are weighting matrices and $\mathcal{I}_{\Omega_y}$ is an index set corresponding to finite element nodes inside the subdomain Ω_y.
The implementation is carried out using FEniCS, cf. Alnæs et al. (2015), Logg et al. (2012), for the finite element discretization and MATLAB's `fmincon` solver for the optimization. The source code for our implementation of the MPC algorithm can be found on GitHub, see references.
Our numerical simulations show that the costs of the closed-loops seem to converge for increasing horizon lengths (see Fig. 2). In addition, it was investigated whether the open-loop trajectories of the optimization have the turnpike property which is the key property of the optimal trajectories needed for proving near optimality of the MPC solutions. The corresponding numerical results will be presented in detail in the talk.

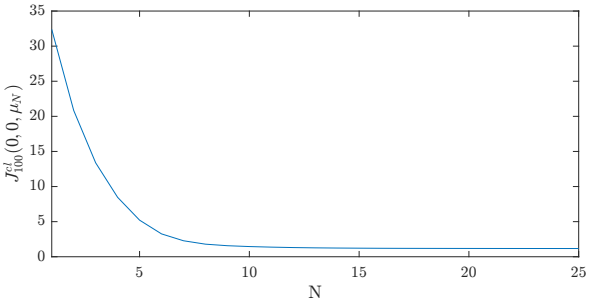

Fig. 2. Closed-loop cost of the MPC loop for a simulation over a time period of $T = 1$.

5. OUTLOOK

While the convergence of closed-loop costs can be explained by our theoretical results, it is not yet proven that the state and control trajectories also converge. This will be the subject of further investigations.
Another challenge is that the current implementation scales poorly with the degrees of freedom of the finite element discretization and therefore larger problems in multidimensional domains have not yet been addressed. A first approach to deal with this issue is the use of Proper Orthogonal Decomposition as described in (Mechelli and Volkwein, 2017). We are currently working with the authors on a more efficient implementation of our problem.

REFERENCES

Alnæs, M.S., Blechta, J., Hake, J., Johansson, A., Kehlet, B., Logg, A., Richardson, C., Ring, J., Rognes, M.E., and Wells, G.N. (2015). The fenics project version 1.5. *Archive of Numerical Software*, 3(100). doi:10.11588/ans.2015.100.20553.

Grüne, L. and Pannek, J. (2017). *Nonlinear Model Predictive Control. Theory and Algorithms*. Springer, second edition.

Grüne, L. and Pirkelmann, S. (2017). Closed-loop performance analysis for economic model predictive control of time-varying systems. Proceedings of the 56th IEEE Conference on Decision and Control (CDC).

Logg, A., Mardal, K.A., Wells, G.N., et al. (2012). *Automated Solution of Differential Equations by the Finite Element Method*. Springer. doi:10.1007/978-3-642-23099-8.

Mechelli, L. and Volkwein, S. (2017). Pod-based economic optimal control of heat-convection phenomena. Konstanzer Schriften in Mathematik 365, University of Konstanz.

Pirkelmann, S. (2018). Convection-diffusion-equation-pde-control. `https://github.com/Telos4/convection-diffusion-equation-fdto`.

Tröltzsch, F. (2010). *Optimal control of partial differential equations: theory, methods and applications*. American Mathematical Society, Providence, Rhode Island.

Using IEC 61499 Models for Automatic Network Configuration of Distributed Automation Systems

Ben Schneider, Sebastian Voss, Monika Wenger, Alois Zoitl

fortiss, An-Institut Technische Universität München, Guerickestr. 25, 80805 München, Germany (e-mail: schneider/voss/wenger/zoitl@fortiss.org).

Keywords: distributed industrial automation, IEC 61499, Time-Sensitive Networking, real-time, deterministic networking, schedule synthesis

1. INTRODUCTION

Industrie 4.0 and IIoT introduce new challenges for distributed automation systems regarding the network. These requirments include the distribtion of control logic, a high degree of interoperability, the need for dynamic reconfiguration and software reusability. All these requirements can be fulfilled by the IEC 61499 which is a modeling language for distributed control systems and can be seen as the successor of IEC 61131. This trend towards highly distributed control systems also causes new challenges for the network, as the fastly growing number of network devices rises the complexity of their configuration. Also, mixed-criticality systems become more and more important which require a convergent network (4) i.e., the transmission of traffic with different characteristics on the same network cable, like deterministic real-time traffic for motion control next to traffic for data acquisition into the cloud. These new requirements can be fulfilled by the new Time-Sensitive Networking (TSN) Ethernet standard which is currently standardized by the IEEE 802.1 Working Group. However, the configuration of TSN devices is time consuming and error-prone because each networking device has to be configured separately (1). The first step towards automatic configuration of asynchronous, real-time capable networks is the analysis of IEC 61499's models (6) and their support for network modeling (w.r.t. timing behavior, criticality and complexity) and the identification of missing information, that is needed to generate network configurations.

2. MODELING IN IEC 61499

Figure 1 shows the Application and System Model and the relation between both which is represented by the Distribution Model. The Application Model contains the Function Block Network (FBN) representing the control code. The execution of FBs is triggered by the event connections (black lines between FBS in Figure 1). Multiple connected FBs form an event chain which defines the execution order of the FBs.

The System Model contains information about the physical composition of the distributed control system. This includes devices, network segments and the interface to the controlled industrial process. A device is for example

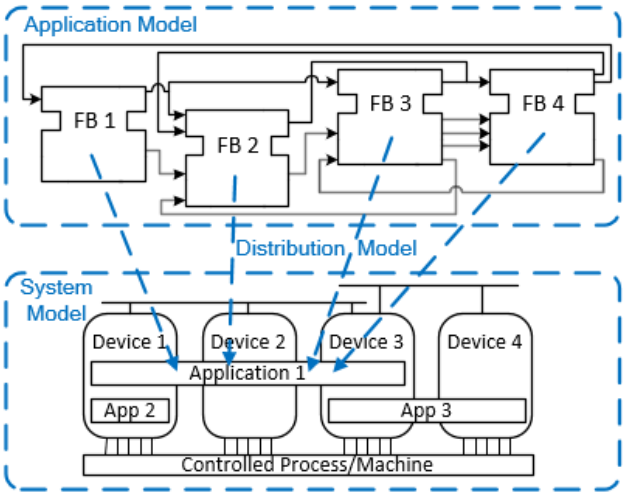

Fig. 1. Application, System and Distribution Model of IEC 61499

a specific Programmable Logic Controller (PLC) or an embedded computer and the network segment could specify the usage of Ethernet or a fieldbus like CAN or Profinet for communication.

After defining available devices and implementing the control algorithm as a Function Block Network (FBN), the application is mapped by the engineer to the control devices that are responsible for their execution. This mapping is the Distribution Model of IEC 61499 which is represented by the applications that are mapped to single or multiple devices like shown in Figure 1. During this process the network communication between the different devices and their application has to be modeled manually by the engineer using network Service Interface Function Blocks (SIFB) (3).

Each of these SIFBs has to be created separately, first by choosing the appropriate communication pattern such as publish-subscribe or client-server, second by choosing the protocol that shall be used for the communication e.g., UDP, MQTT or OPC UA and third by manually setting up the communication parameters such as IP address and port. After that the network devices need to be configured

such that they meet the requirements of the distributed application.

3. NETWORK MODELLING IN IEC 61499

This configuration process is very time consuming and error-prone and can be automated by generating the necessary parameters for industrial communication directly from the models of IEC 61499. The first steps of modelling the network using concepts of IEC 61499 is shown in the next sections.

3.1 Available Data for Network Modeling

The **Application Model** provides the execution order of FBs which are defined by event chains. The type of the event source of a chain can also be derived to a cyclic source which periodically triggers the event chain or an asynchronous source without any periodic behavior. It is also possible to model deadline for real-time FBs (2). Furthermore, the communication pattern can be derived from the FBN where event connections between FBs refer to a publish-subscribe and adapters refer to a client-server pattern.

The **System Model** provides an overview of all available devices which are able to execute IEC 61499 compliant control software and the connection of different devices through network segments and corresponding links. Additional capabilities of entities (not only devices, also for segments, resources, etc.) can be modeled with Attributes described in IEC 61499 Annex G (6). Attributes are typically expressing vendor specific data like CPU type, supported communication protocols or runtime environment and more.

The **Distribution Model** provides the end-to-end connections of traffic streams and can be used to derive the appropriate parameters like IP address and port.

3.2 Missing Data for Network Modeling

The following paragraphs summarize requirements for missing data in the models of IEC 61499 needed to generate real-time capable network configurations.

The **Application Model** lacks a way to model the criticality of events between FBs. This mixed-criticality is necessary to model network determinism and can be used to derive network parameters like VLAN and priority for a stream in a TSN network. The sending times of events are optional information which can only be used in cyclic applications. The network transmission of events can be used to optimize the TSN schedule.

The current **System Model** does not give precise information of the network segments. The definition of a network segment in the IEC 61499-1 (6) is a "physical partition of a communication network". A higher accuracy of the description of network segments was not necessary when the standardization started, because most automation systems used a shared bus and where usually directly wired to a ring of devices. With new emerging networking technologies in the field of industrial automation such as TSN, a more precise segment needs to be defined. The only approach that seems suitable for a segment is to model it like a single networking device e.g., a switch, router or firewall. Segments and devices are connected via links which results in the network topology. Modeled data of a segment can for example be number of ports, link speed, bandwidth etc. The logical modeling of a segment, for example as a subnet containing one or more networking devices, is not applicable, because the standard already defines it as a physical partition.

The **Distribution Model** is not providing any possiblity to model the worst case execution time (WCET) of FBs which are mapped on different devices. This data is amongst others dependent on a more sophisticated device model.

4. CONCLUSION AND FUTURE WORK

This paper showed an analysis of network modeling capabilities in the Application, System and Distribution Model of IEC 61499. The goal is to provide an automatic configuration for networks including real-time schedules (e.g., for TSN). The next steps are to evaluate which already existing modeling languages in the automation domain (e.g., FDCML, EDDL, AML etc.) can be reused for network modelling in IEC 61499, implement a first prototype in 4diac [1] and finally contribute to an extension of the IEC 61499 standard for network modeling based on the results of the prototype.

ACKNOWLEDGEMENTS

This work is partially funded by the German Federal Ministry of Education and Research (BMBF) under grant no. 01IS16022N through the project BaSys 4.0.

REFERENCES

[1] Marina Gutirrez, Astrit Ademaj, Wilfried Steiner, Radu Dobrin, Sasikumar Punnekkat, Self-Configuration of IEEE 802.1 TSN Networks, IEEE Emerging Technologies and Factory Automation (ETFA), Limassol, 2017

[2] Alois Zoitl, Real-Time Execution for IEC 61499, ISA, 1st Edition, 2009

[3] L. Lednicki and J. Carlson A framework for generation of inter-node communication in component-based distributed embedded systems, IEEE Emerging Technology and Factory Automation (ETFA), Barcelona, 2014, pp 1-8

[4] Sebastian Voss and Bernhard Schätz Deployment and Scheduling Synthesis for Mixed-Critical Shared-Memory Applications, IEEE International Conference on Engineering of Computer based Systems (ECBS), Budapest, 2013, pp. 100-109

[5] R. Froschauer, F. Auinger, A. Schimmel and A. Zoitl, Engineering of communication links with AADL in IEC 61499 automation and control systems, International Conference on Industrial Informatics (INDIN), Cardiff, 2009, pp. 582-587

[6] IEEE IEC 61499, Function blocks - part 1: architecture, 2012, 2nd Edition

[1] https://www.eclipse.org/4diac/

Parametric Nonlinear Model Reduction
for Structural Dynamics

Christopher Lerch * **Christian H. Meyer** **

* *Technical University of Munich, Chair of Automatic Control, Boltzmannstr. 15, 85748 Garching b. München, Germany (e-mail: christopher.lerch@tum.de).*
** *Technical University of Munich, Chair Applied Mechanics, Boltzmannstr. 15, 85748 Garching b. München, Germany (e-mail: christian.meyer@tum.de).*

Keywords: Nonlinear model reduction; Subspace methods; Real-time control;

1. INTRODUCTION

The finite element method has grown to the standard way to solve partial differential equations numerically. In the area of structural dynamics this method discretizes the partial differential equation

$$\nabla \cdot \boldsymbol{\sigma} + \hat{\boldsymbol{b}} - \varrho\, \ddot{\boldsymbol{u}} = \boldsymbol{0} \quad \text{on } \Omega$$

with boundary and initial conditions $\boldsymbol{u} = \hat{\boldsymbol{u}}$ on $\partial\Omega_u$, $\boldsymbol{\sigma} \cdot \boldsymbol{n} = \hat{\boldsymbol{t}}$ on $\partial\Omega_\sigma$, $\boldsymbol{u}(t_0) = \boldsymbol{u}_0$ and $\dot{\boldsymbol{u}}(t_0) = \dot{\boldsymbol{u}}_0$. $\boldsymbol{u}$ are the displacements of the structure. If the analyzed structure undergoes large deflections, the outcoming discretized equation of motion

$$\boldsymbol{M}\, \ddot{\boldsymbol{u}}(t) + \boldsymbol{f}(\boldsymbol{u}(t)) = \boldsymbol{B}\boldsymbol{F}(t) \tag{1}$$

is nonlinear with respect to the restoring force $\boldsymbol{f}(\boldsymbol{u})$.

In applications such as design or control, the equation of motion can depend on parameters that concern the shape, material and boundary conditions as illustrated in Fig. 1. These parameters can either be changed by the engineer during construction (usually shape and material) or due to operation conditions and control (usually boundary conditions).

The dependence of Eq. (1) on these parameters can be expressed by

$$\boldsymbol{M}(\boldsymbol{p})\, \ddot{\boldsymbol{u}}(t) + \boldsymbol{f}(\boldsymbol{p}, \boldsymbol{u}(t)) = \boldsymbol{B}(\boldsymbol{p})\boldsymbol{F}(t) \tag{2}$$

where $\boldsymbol{p} \in \mathbb{P}$ is a set of variable parameters.

Finite element models of complex geometries that appear in engineering can have million degrees of freedoms which

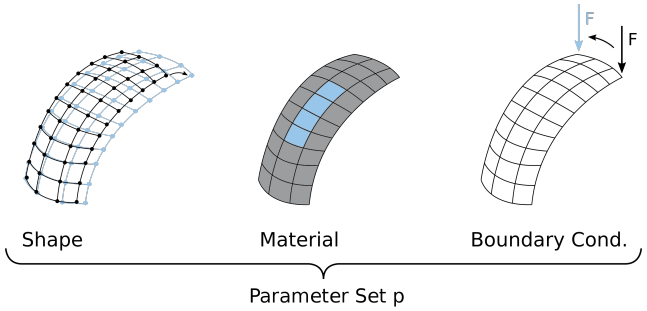

Fig. 1. Parameterization of Structural Finite Element Models.

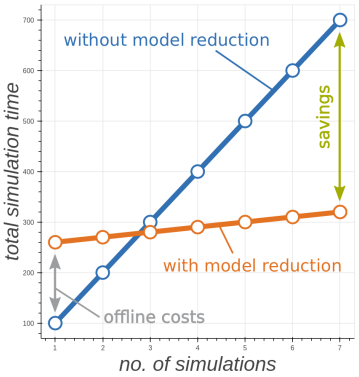

Fig. 2. Computational savings with model reduction.

can lead to high computation costs when solving Eq. (1). In applications such as design iterations or realtime control where the equation of motion have to be solved several times, a short simulation time is highly demanded. One approach to satisfy this demand is model reduction. It reduces the computation time by reducing the problem dimension in a reduction step (offline) and then computing the reduced smaller model (online). After a certain number of simulations or calculated timesteps the total simulation time can be reduced as illustrated in Fig. 2.

2. MODEL REDUCTION FOR FINITE ELEMENT MODELS IN STRUCTURAL DYNAMICS

For equations of type (1) the model reduction is performed in two steps. First, the number of unknowns is reduced by a Galerkin projection. Second, the evaluation of the nonlinear force term is sped up by hyperreduction.

2.1 Galerkin Projection

In order to reduce the dimension of the problem, i.e. the number of unknowns, a Galerkin projection is performed. Therein a lower-dimensional approximation of the relevant system dynamics is done by

$$\boldsymbol{u} = \boldsymbol{V}\boldsymbol{q} + \boldsymbol{\varepsilon} \approx \boldsymbol{V}\boldsymbol{q}$$

with the nonlinear reduction basis $\boldsymbol{V} = [\boldsymbol{V}_{\text{lin}} \mid \boldsymbol{V}_{\text{nl}}]$ consisting of a linear part $\boldsymbol{V}_{\text{lin}}$ augmented with an additional nonlinear part $\boldsymbol{V}_{\text{nl}}$. The linear part is calculated

Table 1. Possible combinations of methods for calculation of the nonlinear reduction basis.

	Linear part $\boldsymbol{V}_{\text{lin}}$	*Nonlinear part* $\boldsymbol{V}_{\text{nl}}$
Modal truncation	Vibration modes	Modal derivatives Static derivatives
Moment matching	Krylov directions	Krylov derivatives Static derivatives
Other linear methods	Linear basis vectors	Exact derivatives Static derivatives

using linear methods together with a linearized model (e.g. Salimbahrami and Lohmann (2006)). The additional nonlinear part consists of exact or static derivatives of the linear basis vectors accounting for the nonlinear behavior (e.g. Idelsohn and Cardona (1984)). Tab. 1 lists basic combinations of methods that are used.

This leads to the projected and reduced system dynamics

$$\boldsymbol{V}^{\mathsf{T}}\boldsymbol{M}\boldsymbol{V}\ddot{\boldsymbol{q}}(t) + \boldsymbol{V}^{\mathsf{T}}\boldsymbol{f}(\boldsymbol{V}\boldsymbol{q}(t)) = \boldsymbol{V}^{\mathsf{T}}\boldsymbol{B}\boldsymbol{F}(t)\,.$$

The quality of the reduction basis and the associated reduced system are evaluated and optimized via a specific $\mathcal{H}_2$-norm for the error system.

2.2 Hyperreduction

Although the projection reduces the dimension of the problem, its reduction of computation time is quite poor. This originates from the evaluation of the reduced nonlinear restoring force $\boldsymbol{V}^{\mathsf{T}}\boldsymbol{f}(\boldsymbol{V}\boldsymbol{q})$, because it still has to be evaluated in the full element domain, i.e. for the physical displacements $\boldsymbol{u} = \boldsymbol{V}\boldsymbol{q}$. Hyperreduction methods have been developed to overcome this issue.

The ansatz of Hyperreduction is to evaluate the elemental restoring forces $\boldsymbol{f}_e$ of a subset of all elements and extrapolate their contribution to the global restoring force vector $\boldsymbol{f}$ instead of assembling the contibution of all elements:

$$\begin{aligned}\boldsymbol{V}^{\mathsf{T}}\boldsymbol{f}(\boldsymbol{V}\boldsymbol{q}) &= \sum_{e\in E} \boldsymbol{V}^{\mathsf{T}}\boldsymbol{B}_e^{\mathsf{T}}\boldsymbol{f}_e(\boldsymbol{B}_e\boldsymbol{V}_e\boldsymbol{q}) \\ &\approx \sum_{e\in \widetilde{E}\subset E} \boldsymbol{V}^{\mathsf{T}}\boldsymbol{L}_e\boldsymbol{B}_e^{\mathsf{T}}\boldsymbol{f}_e(\boldsymbol{B}_e\boldsymbol{V}_e\boldsymbol{q})\,.\end{aligned}$$

Different Hyperreduction methods differ in the way the element subset $\widetilde{E}$ and the operator $\boldsymbol{L}_e$ are chosen. One of the most popular Hyperreduction methods for structural problems is called the Energy Conserving Sampling and Weighting (ECSW) method. It has advantageous properties when applied to mechanical problems, such as stability and passivity (Farhat et al. (2014, 2015)).

3. PARAMETRIC REDUCTION

The consideration of parameter changes only needs a prior suitable sampling of the parameter space $\mathbb{P}$. Then the same methods can be applied for each parameter sampling point $\boldsymbol{p}_i \in \mathbb{P}$ $(i = 1, 2, \ldots, N)$ resulting in N different reduction bases $\boldsymbol{V}(\boldsymbol{p}_i)$ and if necessary reduced systems $\mathcal{S}_{\text{r}}(\boldsymbol{p}_i)$ (e.g. Benner et al. (2015)). Tab. 2 summarizes basic approaches used within this framework.

Table 2. Methods used for parametric reduction.

Local approaches	*Global approaches*
Basis updating $\boldsymbol{V}(\boldsymbol{p}_i)$	Concatenation to global basis $\left[\boldsymbol{V}(\boldsymbol{p}_1)\ \boldsymbol{V}(\boldsymbol{p}_2)\ \cdots\ \boldsymbol{V}(\boldsymbol{p}_N)\right]$
Basis interpolation $\boldsymbol{V}(\boldsymbol{p}_i)$	Global parameter-dependent basis $\boldsymbol{V}(\boldsymbol{p})$
Matrix/system interpolation $\mathcal{S}_{\text{r}}(\boldsymbol{p}_i)$	

4. RESEARCH CODE AMFE

Nonlinear model reduction methods have not been implemented in commercial code so far. Furthermore, the implementation of new developed methods is very tedious in conjunction with commercial finite element code. Therefore, an open source research code, called AMfe (Rutzmoser (2017)), has been implemented that makes prototyping new model reduction methods easy. The code is written in Python and provides easy access to internal computations due to its modular structure. Several reduction methods have been implemented such as methods for calculating reduction bases and hyperreduction methods e.g. ECSW.

5. OUTLOOK

At current state only non-parametric nonlinear model order reduction methods have been implemented in the research code. The goal of current research of the authors is to develop and implement new reduction techniques for parameter dependent systems for applications such as design, optimization and control systems.

ACKNOWLEDGEMENTS

The authors thank the German Research Foundation (DFG) for supporting this research project within the priority programm (SPP) 1897 "Calm, Smooth and Smart: Novel Approaches for Influencing Vibrations by Means of Deliberately Introduced Dissipation".

REFERENCES

Benner, P., Gugercin, S., and Willcox, K. (2015). A survey of projection-based model reduction methods for parametric dynamical systems. *SIAM Review*, 57(4), 483–531.

Farhat, C., Avery, P., Chapman, T., and Cortial, J. (2014). Dimensional reduction of nonlinear finite element dynamic models with finite rotations and energy-based mesh sampling and weighting for computational efficiency. *Int. J. for Numerical Methods in Engineering*, 98(9), 625–662.

Farhat, C., Chapman, T., and Avery, P. (2015). Structure-preserving, stability, and accuracy properties of the energy-conserving sampling and weighting method for the hyper reduction of nonlinear finite element dynamic models. *International Journal for Numerical Methods in Engineering*, 102(5), 1077–1110.

Idelsohn, S. and Cardona, A. (1984). Recent advances in reduction methods in non linear structural dynamics. In *Proceedings of the 2nd International Conference on Recent Advances in Structural Dynamics 1984*, 475–482. University of Southampton, England.

Rutzmoser, J. (2017). Amfe – finite elements with simplicity in mind. `https://github.com/AppliedMechanics/AMfe`.

Salimbahrami, S. and Lohmann, B. (2006). Order reduction of large scale second-order systems using Krylov subspace methods. *Linear Algebra and its Applications*, 415(2), 385–405.

Model order reduction in thermoacoustic stability analysis

Max Meindl *, **Maria Cruz Varona** *,
Alessandro Castagnotto *, **Felix Thomann** *,
Wolfgang Polifke *, **Boris Lohmann** *

* *Technical University of Munich, Germany*
(e-mail: meindl@tfd.mw.tum.de)

Keywords: Model order reduction, state-space models, thermoacoustics, stability analysis, linear coupled systems.

1. INTRODUCTION

Modern gas-turbines are typically operated under lean, premixed combustion conditions due to emission restrictions. In this operating range, the flame is susceptible to acoustic perturbations. Once perturbed, the heat-release fluctuates, which acts as a monopole sound-source. Due to interaction with the compressor, the turbine and the combustor housing, these acoustic waves can be reflected back to the flame, which establishes a feedback cycle. When constructive interference occurs, the amplitudes of this mechanism can grow and a thermoacoustic instability develops that might limit the operating range, increase material wear and even cause fatal damage.

In order to predict and avoid these instabilities, linear time-invariant (LTI) models consisting of an acoustic part (AC) for the wave propagation and an acoustic-flame interaction model are often used. Due to the complex geometries found in gas-turbines, the models for the acoustic propagation, e.g. based on the finite element method, can become very large. In this contribution, a pilot study is conducted in which model order reduction (MOR) techniques are applied to a simple acoustic model. After the reduction, a flame transfer function (FTF) is coupled to the reduced acoustic system in order to account for the acoustic-flame interaction. This *a posteriori coupling* allows to change the FTF for parameter studies with only one MOR of the acoustic system. The linear thermoacoustic stability analysis is conducted on both, the full- (FOM) and the reduced-order model (ROM), by computing the eigenvalues of the coupled systems. The suitability of three MOR algorithms – modal reduction, truncated balanced realization and the iterative rational Krylov algorithm – is investigated based on the stability prediction of the reduced models.

2. THERMOACOUSTIC MODEL

In this study, the thermoacoustic stability of a swirl burner is investigated. The model for the acoustic wave propagation is based on the 1D thermoacoustic network modeling tool *taX* [1], while the acoustic-flame interaction is governed by an FTF identified from a large eddy simulation of the burner. The state-space representation is used for both parts of the model, which facilitates easy coupling and robust computations.

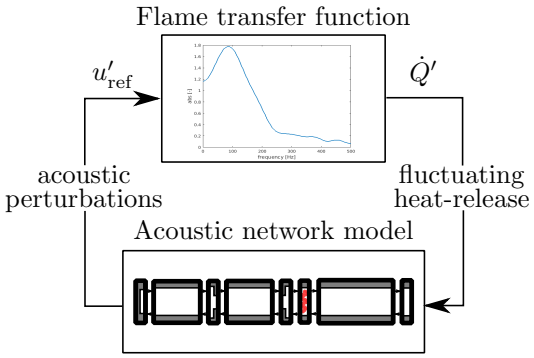

Fig. 1. Coupling between the acoustic and the flame-response model.

2.1 Acoustic network model

Within the scope of this pilot study, a low order, 1D network model is used for the propagation of the acoustic waves. Although the size of this model is rather small – 78 degrees of freedom – the basic principles learned from MOR should be applicable to larger models as well.

The network model consists of simple elements, for which the analytical solution of the wave propagation is known, e.g. a duct with constant cross-section or an area jump. By matching the wave amplitudes at the interfaces of these elements, a network that represents the whole burner can be established (see Fig. 1). In order to provide an interface to the FTF, inputs and outputs of the acoustic state-space model have to be chosen. Due to the velocity-sensitive premixed flame, the acoustic perturbation in axial flow velocity at a reference position u'_{ref} is chosen as an output. To account for the fluctuating heat-release $\dot{Q}'$ of the flame, an input is provided which translates these fluctuations to acoustic waves.

⋆ The work related to this contribution is supported by the German Research Foundation (DFG), Grant LO408/19-1.

[1] The code for the software package taX can be found at `http://gitlab.lrz.de/tfd/tax` and its documentation at `http://tax.wiki.tum.de`.

2.2 Flame transfer function

The flame transfer function has a low-pass filter behavior and relates axial velocity perturbations to heat-release fluctuations. In state-space representation, the input of the FTF is u'_{ref} and the output is $\dot{Q}'$. This allows for coupling between the FTF and the acoustic network model. Through the coupling, a monolithic state-space model is retrieved which incorporates the whole thermoacoustic dynamics.

3. MODEL ORDER REDUCTION OF THE ACOUSTIC SUBSYSTEM

Our pursued workflow consists of first reducing the acoustic part of the thermoacoustic model before coupling the acoustic ROM to the FTF. Another approach could be to reduce the coupled system (AC+FTF) as a whole. The former technique, however, is more advantageous, since it allows to perform parameter studies of the FTF without having to reduce the whole system after each parameter variation. To reduce the acoustic model, three linear MOR techniques from the *sssMOR* toolbox [2] are applied (Castagnotto et al. (2017)). These techniques employ a projection of the FOM onto a respective subspace to obtain a corresponding ROM (Antoulas (2005)).

We compute the projection subspaces with different reduction methods, namely *modal reduction* (Davison (1966)), *truncated balanced realization* (Moore (1981)) and the *iterative rational Krylov algorithm* (Gugercin et al. (2008)). Note that modal reduction – i.e. the preservation of some eigenmodes – is state of the art in the reduction of acoustic models, since these can be usually extracted directly from FE solvers.

4. COUPLING THE REDUCED ACOUSTIC SYSTEM WITH THE FLAME TRANSFER FUNCTION

After the model order reduction, the reduced acoustic network model is coupled to the FTF. The eigenvalues of this reduced coupled model are compared to the eigenvalues of the full coupled model (full acoustic network model connected to FTF). The complexity of this task lies in the fact, that a good approximation of the eigenmodes of the acoustic subsystem will not guarantee a good fit of the coupled, thermoacoustic modes between the FOM and the ROM. This is due to the fact that the FTF significantly changes the system dynamics. The investigated model exhibits a low-frequent *intrinsic thermoacoustic* (ITA) eigenmode which is marginally stable. This mode only occurs in the coupled system (Hoeijmakers et al. (2014); Emmert et al. (2016)). Due to its prime importance for thermoacoustic stability, the quality of the ROM will be judged based on the approximation of this mode.

A robust and efficient MOR algorithm is desired, which produces a ROM that converges to the correct thermoacoustic eigenmodes, when coupled to the FTF. This study investigates the convergence behavior of the three before mentioned methods with respect to increasing ROM order.

[2] sss and sssMOR are open-source MATLAB toolboxes available under `www.rt.mw.tum.de/?morlab` or in GitHub under `https://github.com/MORLab`.

It is known that the acoustic feedback mechanism between the fluctuating heat-release and the velocity perturbations at the reference position is of major importance for the intrinsic eigenmode. It is therefore expected that the model reduction algorithms focusing on exactly this transfer behavior from $\dot{Q}'$ to u'_{ref} (TBR and IRKA) will yield better results than the modal MOR (cf. Fig. 2). This and further aspects will be discussed at the conference.

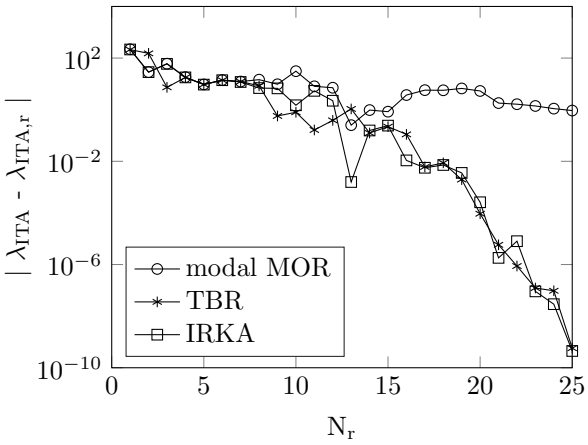

Fig. 2. Error between the ITA eigenfrequency of the FOM (λ_{ITA}) and the ROMs ($\lambda_{\mathrm{ITA,r}}$) with the three different reduction algorithms depending on the order N_r of the reduced acoustic system.

5. OUTLOOK: LARGE-SCALE ACOUSTIC SYSTEMS

Based on the experience gained from the small-scale network model case, suitable ROM techniques need to be developed for large-scale (aero-)acoustic models with up to 10^6 degrees of freedom. Major challenges are the 3D effects and hydrodynamic-acoustic interactions, which are not included in the network model.

REFERENCES

Antoulas, A.C. (2005). *Approximation of Large-Scale Dynamical Systems*. SIAM. doi:10.1137/1.9780898718713.

Castagnotto, A., Cruz Varona, M., Jeschek, L., and Lohmann, B. (2017). sss & sssmor: Analysis and Reduction of Large-Scale Dynamic Systems in MATLAB. *at-Automatisierungstechnik*, 65(2).

Davison, E. (1966). A method for simplifying linear dynamic systems. *IEEE TAC*, 11(1), 93–101.

Emmert, T., Bomberg, S., Jaensch, S., and Polifke, W. (2016). Acoustic and Intrinsic Thermoacoustic Modes of a Premixed Combustor. In *36th Int'l Symposium on Combustion*. Combustion Institute, Seoul, Korea. doi: 10.1016/j.proci.2016.08.002.

Gugercin, S., Antoulas, A.C., and Beattie, C. (2008). $\mathcal{H}_2$ Model Reduction for Large-Scale Linear Dynamical Systems. *SIAM Journal on Matrix Analysis and Applications*, 30(2), 609–638. doi:10.1137/060666123.

Hoeijmakers, M., Kornilov, V., Lopez Arteaga, I., de Goey, P., and Nijmeijer, H. (2014). Intrinsic Instability of Flame-Acoustic Coupling. *Combustion and Flame*, 161(11), 2860–2867.

Moore, B.C. (1981). Principal component analysis in linear systems: controllability, observability and model reduction. *IEEE TAC*, 26, 17–32.

Taylor series based solution of nonlinear-quadratic ODE systems

V. Šátek [*,**] **P. Veigend** [*] **G. Nečasová** [*]

[*] *Brno University of Technology, Faculty of Information Technology, Božetěchova 2, 612 66 Brno, Czech Republic, (e-mail: satek@fit.vutbr.cz)*

[**] *IT4Innovations, VŠB Technical University of Ostrava, 17. listopadu 15/2172, 708 33 Ostrava-Poruba, Czech Republic*

Keywords: Continuous systems, Ordinary differential equations, Initial value problems, Taylor series, MATLAB

1. INTRODUCTION

The "Modern Taylor Series Method" (MTSM) is the numerical integration method that can numerically solve ordinary differential equations (ODEs). The method calculates terms of the Taylor series recurrently for each integration step. The number of calculated terms is generally different for every step and it depends on a defined accuracy of the calculation. Model implementation of MTSM (TKSL software package, Kunovský (1994)), is limited by maximal number of equations and double accuracy.Therefore the method is currently being tested and reimplemented in MATLAB.

Several papers focus on computer implementation of the Taylor series method in a variable-order and variable-step context (see, for instance, Abad et al. (2015), the TIDES software or in Jorba and Zou (2005)). The reduction of rounding errors Rodríguez and Barrio (2012) and utilization of multiple arithmetic Barrio et al. (2011) improves the applicability of Taylor series based algorithms.

This paper demonstrates that the MTSM, specialized to directly solving nonlinear-quadratic ODE systems, solves non-stiff and in some cases stiff systems very fast (in comparison with MATLAB implementation of explicit and implicit ode solvers) and outperforms standard solvers in the considered benchmark problems. This paper is closely connected with Šátek et al. (2015) where effective solution of linear ODE systems using MSTM was introduced.

2. SCHEME FOR QUADRATIC ODES

In this article, we have focused on effective solution of special case of nonlinear-quadratic systems of ODEs. The nonlinear-quadratic systems of ODEs is any first-order ODE that is quadratic in the unknown function. For such system Taylor series based numerical method can be implemented in very effective way.

The best-known and most accurate method of calculating a new value of a numerical solution of ordinary differential equation $y' = f(t, y),\ \ y(0) = y_0$ is to construct the Taylor series Hairer et al. (1987).

The $n-$th order method uses n Taylor series terms in the explicit form

$$y_{i+1} = y_i + hf(t_i, y_i) + \frac{h^2}{2!} f^{[1]}(t_i, y_i) + \cdots + \frac{h^n}{n!} f^{[n-1]}(t_i, y_i). \tag{1}$$

Equation (1) for nonlinear-quadratic systems of ODEs can be rewritten in the form

$$\boldsymbol{y}' = \mathbf{A}\boldsymbol{y}^2 + \mathbf{B}\boldsymbol{y_{jk}} + \mathbf{C}\boldsymbol{y} + \mathbf{b}\,, \tag{2}$$

where $\mathbf{A} \in \mathbb{R}^{ne\times ne}$ is the matrix for pure quadratic term, $\mathbf{B} \in \mathbb{R}^{ne\times ne(ne-1)/2}$ is the matrix for mixed quadratic term, $\mathbf{C} \in \mathbb{R}^{ne\times ne}$ is the Jacobian matrix for linear part of the system and $\mathbf{b} \in \mathbb{R}^{ne}$ is the right-hand side for the forces incoming to the system. The unknown function $\boldsymbol{y}^2$ represents the vector of multiplications $(y_1y_1, y_2y_2, \ldots, y_{ne}y_{ne})^T$; the unknown function $\boldsymbol{y_{jk}}$ represents the vector of mixed terms multiplications $(y_{j_1}y_{k_1}, y_{j_2}y_{k_2} \ldots, y_{j_{ne(ne-1)/2}}y_{k_{ne(ne-1)/2}})^T$. The indices j, k come from combinatorics $C(ne, 2)$ and symbol ne stands for the number of equations in ODE system. For simplification we suppose that the constant matrices $\mathbf{A}, \mathbf{B}, \mathbf{C}$ and the constant vector $\mathbf{b}$ are used in system (2).

Higher derivatives of such systems (2) can be effectively computed in MATLAB software MathWorks (2017) using matrix-vector multiplication, e.g. higher derivative $\boldsymbol{y}^{[p]}$ for pure quadratic term with matrix $\mathbf{A}$ should be expressed as

$$\boldsymbol{y}^{[p]} = \mathbf{A}\left(\sum_{i=0}^{p-2} \boldsymbol{y}^{[p-1-i]} .* \boldsymbol{y}^{[i]} \binom{p-1}{i} + \boldsymbol{y} .* \boldsymbol{y}^{[p-1]}\right), \tag{3}$$

where the operation '.∗' stands for *element-by-element* multiplication, i.e. $\boldsymbol{y}^{[p_1]} .* \boldsymbol{y}^{[p_2]}$ is vector $(y_1^{[p_1]}y_1^{[p_2]}, \ldots, y_{ne}^{[p_1]}y_{ne}^{[p_2]})^T$. The binomial coefficients $\binom{p-1}{i}$ can be effectively precomputed using Pascal triangle, for more information see *pascal* function in MATLAB software.

3. NUMERICAL EXPERIMENTS

All algorithms are implemented in Matlab 2015a and computations are partially performed on SALOMON supercomputer at IT4Innovations VŠB-TU Ostrava

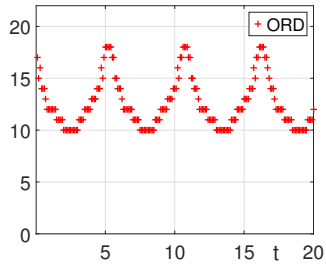

Fig. 1. Order of MTSM for B1 non-stiff problem

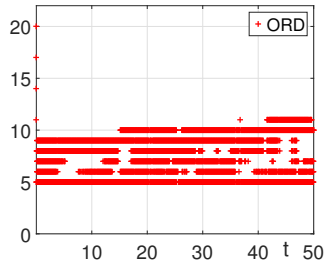

Fig. 2. Order of MTSM for D4 stiff problem

IT4Innovations (2017). Relative and absolute tolerance for all computations was set to 10^{-7}. Classical double precision arithmetic has been used in our examples and maximum order of Taylor series was set to $ORD = 60$.

Vectorized MATLAB code of explicit Taylor series **expTay** with a variable order and variable step size scheme for nonlinear-quadratic systems of ODEs (2) has been implemented. This algorithm was compared on a set of "non-stiff" nonlinear-quadratic systems (see Enright and Pryce (1987)) with vectorized MATLAB explicit **ode** solvers. Benchmark results are shown in table 1 (each reported runtime is taken as a median value of 100 computations). Ratios of computation times $ratio = \boldsymbol{ode}/\boldsymbol{expTay} > 1$ indicate faster computation of the MTSM in all cases (see used orders in Fig. 1).

Table 1. Time of solutions (non-stiff systems): explicit Taylor **expTay** and MATLAB explicit **ode** solver comparison

	ode23	**ode45**	**ode113**	**expTay**
problem	*ratio*	*ratio*	*ratio*	[s]
B1	30.67	2.05	1.57	0.0323
B3	14.79	1.65	1.34	0.00965
B5	29.54	2.17	1.28	0.0201
E4	17.1	2.12	2.19	0.00276

The MTSM, due to the higher order, has some positive properties for stability of the solution. Thanks to these properties it can be effectively used for solution of moderately stiff problems. In table 2 one can see the comparisons **expTay** method with implicit MATLAB **ode** solvers (see used orders in Fig. 2).

Table 2. Time of solutions (stiff systems): explicit Taylor **expTay** and MATLAB implicit **ode** solver comparison

	ode15s	**ode23s**	**ode23t**	**ode23tb**	**expTay**
problem	*ratio*	*ratio*	*ratio*	*ratio*	[s]
C1	1.07	21.21	14.99	14.53	0.0849
C2	1.03	20.05	14.05	13.34	0.0823
D1	0.23	24.75	2.9	2.33	0.569
D3	2.12	19.55	19.4	17.28	0.065
F3	1.2	15.31	13.14	11.75	0.0359

4. CONCLUSION

The Taylor series scheme (after MATLAB vectorization) seems to be very efficient for solution of some types of nonlinear-quadratic ODEs. In many cases it significantly outperforms standard solvers on the considered benchmark problems.

Detailed information and more results will be presented at the conference.

ACKNOWLEDGEMENTS

This research was financially supported by the Ministry of Education, Youth and Sports from the National Program of Sustainability (NPU II) project IT4Innovations excellence in science LQ1602. The paper also includes the results of the international AKTION research project Number 76p11 and the internal BUT FIT project FIT-S-17-4014.

REFERENCES

Abad, A., Barrio, R., Marco-Buzunariz, M., and Rodríguez, M. (2015). Automatic implementation of the numerical taylor series method: a mathematica and sage approach. *Applied Mathematics and Computation*, 268, 227–245.

Barrio, R., Rodríguez, M., Abad, A., and Blesa, F. (2011). Breaking the limits: The taylor series method. *Applied Mathematics and Computation*, 217, 7940–7954.

Enright, W.H. and Pryce, J.D. (1987). Two fortran packages for assessing initial value methods. In *ACM Trans. Math. Softw.*, volume 13, 1–27. ACM.

Hairer, E., Nørsett, S.P., and Wanner, G. (1987). *Solving Ordinary Differential Equations I.* vol. Nonstiff Problems. Springer-Verlag Berlin Heidelberg. ISBN 3-540-56670-8.

IT4Innovations (2017). *"National Supercomputing Center, VŠB-Technical University of Ostrava, Salomon Cluster Documentation - Matlab Overview"*. URL `https://docs.it4i.cz/`.

Jorba, A. and Zou, M. (2005). A software package for the numerical integration of ODE by means of high-order Taylor methods. In *Exp. Math.*, volume 14, 99–117.

Kunovský, J. (1994). *Modern Taylor Series Method.* FEI-VUT Brno. Habilitation work.

MathWorks, T. (2017). *MATLAB and Simulink software.* URL `http://www.mathworks.com/products/matlab/[online]`.

Rodríguez, M. and Barrio, R. (2012). Reducing rounding errors and achieving brouwers law with taylor series method. *Applied Numerical Mathematics*, 62, 1014–1024.

Šátek, V., Kocina, F., Kunovský, J., and Schirrer, A. (2015). Taylor series based solution of linear ode systems and matlab solvers comparison. In *MATHMOD VIENNA 2015 - 8th Vienna Conference on Mathematical Modelling*, ARGESIM REPORT No. 44, 693–694. ARGE Simulation News.

Optimum Spacing of Solar Modules for Two Axis Tracking

Elmer, Gy.*. Perjési-Hámori, I.**

*University of Pécs, 7624, Pécs,
Hungary (Tel: 36 72 503650; e-mail:elmer@mik.pte.hu)
**University of Pécs, 7624, Pécs,
Hungary (Tel: 36 72 503650; e-mail:perjesi@mik.pte.hu)

Keywords: Solar field, tracking, computer algebra, visualization

1. INTRODUCTION

In Middle-Europe a significant increase in solar energy production can be achieved by applying solar tracking in photovoltaic (PV) farms. According to the technical literature between 20% (Zsiborás) and 40% (www.astrasun.hu) plus energy has been measured with solar tracking compared to energy production of fixed PV farms e.g. in Hungary. However this high achievement is only true if a single module arrangement is rotated as a unit with no neighbouring modules.

How much plus energy can be expected in case of several rotated modules placed near to each-other compared to fixed panels occupying the same surface? There are papers in the technical literature partly answering this question, e.g. how to optimize solar field design for single axis tracking (Appelbaum) and for stationary collectors (Weinstock).

If the basis for the comparison is the total surface occupied by a solar field made up of PV modules placed densely near to each-other, then the plus energy can be less than the expected maximum, since the modules begin to shadow their neighbouring panels when being rotated. This shadowing can be reduced by applying gaps between the rotated units, however than a part of the total surface is inactive for energy production thus lowering the resulted energy yield.

This paper proposes a mathematical method to determine the optimum gap dimensions between the rotated modules both in East-West and North-South direction which arrangement assures maximum solar energy produced by two-axis tracking on a certain area.

2. DIMENSIONS AND PRECONDITIONS

Dimension of the PV module rotated as one unit is a in East-West direction with a gap c between the neighbouring modules and b in North-South direction with a gap d between them (Fig. 1). Thus the total area occupied by one module is $A = (a+c)(b+d)$ and this area serves as basis for the comparison of energy yields in case of different c and d values. The active part of the basis area is $A_a = ab$ producing PV energy.

For the first step of developing the mathematical method the following preconditions are taken into account: 1. Modules are placed on a horizontal surface. 2. An internal module will be analysed surrounded by other modules in every directions, i.e. to the north, north-east, east, south-east, south, south-west, west and north-west. 3. Modules face always perpendicular to the direct solar radiation, so they rotate and tilt continuously. 4. Only clear weather is taken into account without any clouds. 5. Shadows have always sharp edges on the panels in any distances only core shadow is taken into account. 6. The method is valid only locations with latitudes between the north polar circle and the Tropic of Cancer.

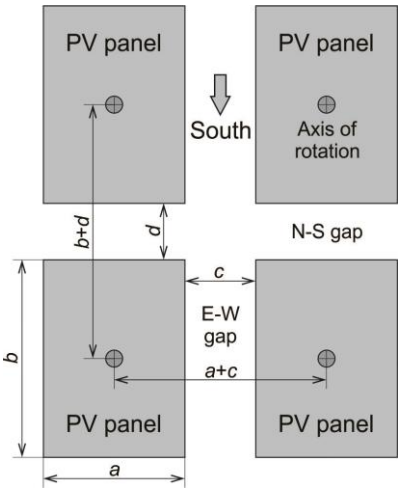

Fig. 1. Dimensions of the PV modules laying horizontally.

3. EQUATIONS OF THE CALCULATION

3.1 Equations of the Sun's path

Since the Sun's path is symmetrical to the solar south direction it is enough to analyse one half of its path. Thus the panels are rotated from their position facing south to their direction at sunrise increasing the so called β hour angle. The dependence of α solar elevation angle on the β hour angle is

$$\sin\alpha = \sin\Phi\sin\delta + \cos\Phi\cos\delta\cos\beta \qquad (1)$$

where Φ is the latitude of the location of the PV panels (48.21° in case of Vienna) and δ is the declination at the given day which can be calculated with

$$\delta = -23.44\cos\left(\frac{360}{365}(N+10)\right) \qquad (2)$$

where N is the number of the given day. $N = 172$ in case of the 21st of June. On this day the declination is maximum, i.e. $\delta_{06.21} = 23.44°$. Then with the help of (1) the hour angle of the sunrise is $\beta_{Sr} = 119.02°$ for the latitude of Vienna.

3.2 Equations for calculating the shadowed area

The shadow thrown by a neighbouring panel onto the PV panel under investigation has a horizontal dimension e and a vertical dimension f. Geometry of the panels is shown in Fig. 2 for hour angles $90° \le \beta \le \beta_{Sr}$ for the calculation of dimension e and in Fig. 3 for the calculation of f.

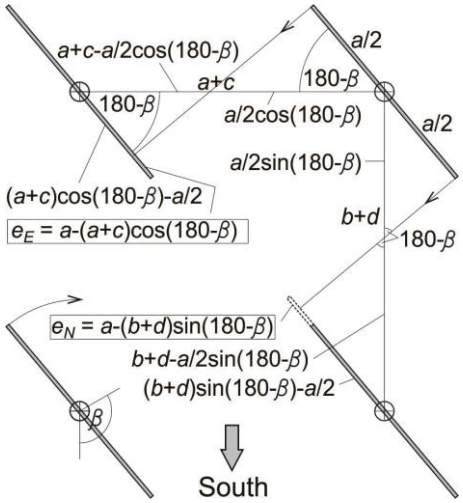

Fig. 2. Upper view of the panels for $90° \le \beta \le \beta_{Sr}$.

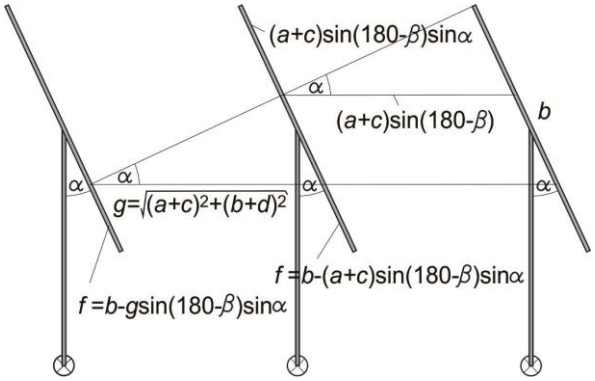

Fig. 3. Lateral view for calculating f for $90° \le \beta \le \beta_{Sr}$

Within the frame of this extended abstract only the shadow thrown by the Eastern neighbour and the gap dimension c is analysed. Horizontal dimension of the shadow thrown by the Eastern panel for hour angles $90° \le \beta \le \beta_{Sr}$ is

$$e_{E2} = a - (a + c)\cos(180 - \beta) \quad (3)$$

and for hour angles $0° \le \beta < 90°$

$$e_{E1} = a - (a + c)\cos(\beta). \quad (4)$$

Vertical dimension of the shadow thrown by the Eastern panel in the range of $90° \le \beta \le \beta_{Sr}$ is

$$f_{E2} = b - (a + c)\sin(180 - \beta)\sin\alpha \quad (5)$$

and the vertical dimension of the shadow thrown by the Eastern panel in the range of $0° \le \beta < 90°$ is

$$f_{E1} = b - (a + c)\sin\beta\sin\alpha. \quad (6)$$

4. CALCULATION OF THE OPTIMUM GAP SIZE

For this first step of analysis dimensions a and b of the panel result unit surface, i.e. $A_a = ab = 1$ not taking account dimensions. The part of the surface of the panel exposed to direct sunlight produces unit power and the shadowed surface part only $0.1ef$ power (https://wikipedia.org.wiki.Solar-tracker). Then this value is divided by the total area A occupied by the panel. Thus the resulted normalized power produced by the panel at a certain angle β is

$$P(\beta) = \frac{ab - 0.1\, e(\beta) f(\beta)}{(a+c)(b+d)}, \quad (7)$$

where $d = 0$ for this analysis. Then the power values are summarized for every integer β angle values being proportional to time. This result is signed with letter W, referring to the PV energy production.

Calculations has been performed with the mathematical software MAPLE. In Fig. 4 dependence of W on the gap dimension c is shown. The found maximum value belongs to $c = 0.45$ (approximately), i.e. 0.45 times a.

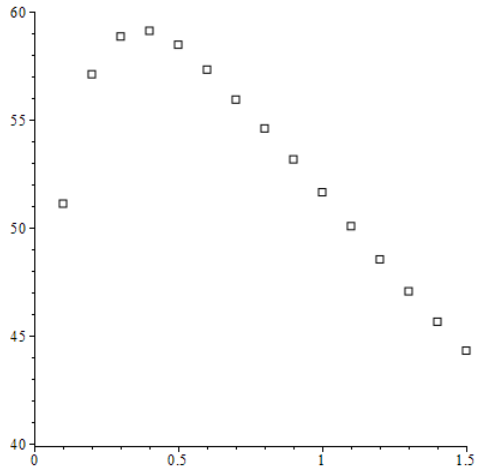

Fig. 4. Plot of W vs gap dimension c.

5. CONCLUSIONS AND FURTHER WORK

Results of the calculation verify the expectation that there is an optimum gap size between PV panels even in case of taking into account only two panels. As next steps the other neighbouring panels and the dependence of the irradiation intensity on the hour angle will be taken into account.

REFERENCES

Appelbaum, J., Weinstock, D. (2007). Optimization of Solar Field Design for Single Axis Tracking Collectors *Proceedings of the 14th Sede Boqer Symposium on Solar Electricity Production* 103-106.

https://en.wikipedia.org/wiki/Solar_tracker

Weinstock, D., Appelbaum, J. (2007). Optimization of Economic Solar Field Design of Stationary Thermal Collectors. *Journal of Solar Energy Engineering,* Vol. 127, 363-370.

www.astrasun.hu.

Zsiborás, H., Dr. Pályi, B. (2014). Solar tracking relations in summer in Hungary (on Hungarian language). *LVI. Georgikon Days,* Keszthely.

Reduction of a Cabin Thermal Bond Graph Model

Youssef Hammadi*, David Ryckelynck and Amin EL-BAKKALI*****

** Methods and Tools for Numerical Simulation Department, Renault Group, Guyancourt, France, (e-mail: youssef.hammadi@renault.com, youssef.hammadi@mines-paristech.fr).*
*** Simulations of Materials and Structures Department, MINES ParisTech Center of Material, Evry, France, (e-mail: david.ryckelynck@mines-paristech.fr).*
**** Methods and Tools for Numerical Simulation Department, Renault Group, Guyancourt, France, (e-mail: amin.el-bakkali@renault.com).*

Keywords: model reduction, automotive control, machine learning, singular value decomposition, bond graphs, differential equations

1. INTRODUCTION

In order to describe the transient thermal behavior of an automotive cabin, we need to model the energy and mass exchanges between the *cabin system* and the *environment* as well as these exchanges inside the cabin system itself.

Given that the cabin model and its environment are intended to be integrated into a control loop, we have adopted a system level modelling (0D) based on the *Bond Graph* approach [Paytner 1961]. The simulator, thus built, results in a set of nonlinear *Differential Algebraic Equations* (DAE). As part of this work, we will use the *Discrete Empirical Interpolation Method* (DEIM) [Chaturantabut 2010] to solve DAE only for a selection of explanatory variables. This is a way to build a Reduced Bond Graph by decreasing the number of solved differential equations.

2. CABIN THERMAL MODEL AND REDUCTION METHODOLOGY

2.1 Cabin thermal model

In bond graph approach applied to thermal domain, two elements exchanging an energy are linked by a line (*Bond*). The heat flux exchanged between the two elements is expressed as the product of the temperature θ (effort variable) and the entropy flux $\dot{s}$ (flow variable). The line is also completed with a half-headed arrow indicating the positive direction of heat transfer, and a causal line indicating which of the two elements receives the effort variable and returns the flow one.

Figure 1 shows the bong graph associated to the thermal conduction through a wall represented by an internal and an external thermal capacitance connected through an equivalent thermal conductance. θ_{wi} and θ_{we} are respectively the temperatures of the internal and external surfaces of the wall. $\dot{s}_{int}$ and $\dot{s}_{ext}$ are respectively the internal and external entropy fluxes.

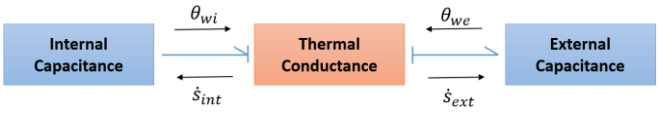

Fig. 1. Bond graph modelling of thermal conduction through a wall.

For a cabin system containing a number Nw of walls and a number Na of air zones, the global thermal bond graph leads to the nonlinear first order DAE system (1):

$$\begin{cases} \boldsymbol{\theta}(t=0) = {}_{ini} \\ \dfrac{d\boldsymbol{\theta}}{dt} + \boldsymbol{\varphi}(\boldsymbol{\theta}, \boldsymbol{u}; \boldsymbol{\mu}) = \boldsymbol{\theta} \quad \forall t \in [0, t_f] \end{cases} \tag{1}$$

$$\boldsymbol{\theta} = \begin{bmatrix} \boldsymbol{\theta_w} \\ \boldsymbol{\theta_a} \end{bmatrix} \quad \mathbb{R}^N \text{ with } \begin{cases} \boldsymbol{\theta_w} = \begin{bmatrix} \theta_{wi_1} \\ \theta_{we_1} \end{bmatrix} \cdots \begin{bmatrix} \theta_{wi_{Nw}} \\ \theta_{we_{Nw}} \end{bmatrix}^T \\ \boldsymbol{\theta_a} = \begin{bmatrix} \theta_{a_1} \\ x_1 \end{bmatrix} \cdots \begin{bmatrix} \theta_{a_{Na}} \\ x_{Na} \end{bmatrix}^T \end{cases} \tag{2}$$

Where $N = 2(Nw + Na)$, $\boldsymbol{\theta} \in \mathbb{R}^N$ is the unknown temperatures and absolute humidities vector defined by (2), $\boldsymbol{\varphi}(\boldsymbol{\theta}, \boldsymbol{u}; \boldsymbol{\mu}) \in \mathbb{R}^N$ is a nonlinear function deduced from energy and mass balances, $\boldsymbol{u} \in \mathbb{R}^{Nu}$ contains the bong graph input variables, $\boldsymbol{\mu} \in \mathbb{R}^{N\mu}$ is a set of the bond graph parameters, $\boldsymbol{\theta_w} \in \mathbb{R}^{2Nw}$ is the vector of all walls internal θ_{wi} and external θ_{we} temperatures, and $\boldsymbol{\theta_a} \in \mathbb{R}^{2Na}$ is the vector of all air zones temperatures θ_a and absolute humidities x.

2.2 Reduction Approach

In order to build a *Reduced Order Model* (ROM), we need to construct a matrix of all possible responses of the studied system, and then extract some empirical modes from this matrix. However, such a matrix requires an infinite memory

storage size if all possible parametric and input predictions are considered.

The model reduction approach, proposed here, begins with an unsupervised *machine learning* phase to develop the *Reduced Order Model* (ROM), followed by an online phase to use the reduced model already built. During the machine learning phase, a reduced basis $\boldsymbol{V} \in \mathbb{R}^{\mathrm{N} \times \mathrm{n}}$ is constructed using an *n*-order *Truncated Singular Value Decomposition* (Truncated SVD), also called *Principal Component Analysis* (PCA), applied to a matrix of *L* different input and parameter sets simulations, randomly selected. This matrix $\boldsymbol{A} \in \mathbb{R}^{\mathrm{N} \times (L\,m)}$, where *m* is the time points number for each simulation, is defined by:

$$A_{ij} = \theta_i^{(l)}\left(t_k\right) - \theta_{ini}^{(l)} \quad \text{with } j = (l-1)m + k,\ \ 1 \le k \le m,\ \ 1 \le l \le L. \tag{3}$$

Where $\theta_i^{(l)}\left(t_k\right)$ represents the i^{th} element of the unknown vector at time t_k using the system inputs and parameters $\left(u^{(l)}; \mu^{(l)}\right)$ which are generated from a *Design Of Experiment* (DOE). We point out that subtracting the initial temperature in (3) is a trick that we propose to make the initial error null.

The reduced basis construction is then completed by a selection of state variables: using the DEIM, we obtain a list of interpolation indexes that we complete with some air zones indexes to form thereby the list $\mathcal{P}$. Our reduction approach consists of choosing the temperatures $\boldsymbol{\theta}[\wp]$ as the ROM explanatory variables. We write $\boldsymbol{\theta}_r$ these variables, which satisfy the following equations:

$$\boldsymbol{\theta} = \hat{\boldsymbol{V}}\boldsymbol{\theta}_r \tag{4}$$

$$\hat{\boldsymbol{V}}[\wp,:] = \boldsymbol{I} \tag{5}$$

$$\hat{\boldsymbol{V}}[\Re,:] = \boldsymbol{V}[\Re,:]\left(\left(\boldsymbol{V}[\wp,:]\right)^T \boldsymbol{V}[\wp,:]\right)^{-1}\left(\boldsymbol{V}[\wp,:]\right)^T \tag{6}$$

$$\Re = \{1,...,N\} \setminus \wp \tag{7}$$

Where (6) is given by the Gappy POD method [Everson 1995] which allows to reconstruct a field by measuring it only in some explanatory points that form the *Reduced Integration Domain* (RID) [Ryckelynck 2005].

In practice, this approach is non-intrusive for bond graphs since we just need to add the linear constraint $\boldsymbol{\theta}[\Re](t) = \hat{\boldsymbol{V}}[\Re,:]\boldsymbol{\theta}[\wp](t)$.

The ROM DAE system (8) is then obtained by projecting the original DAE system (1) onto the subspace $\hat{\boldsymbol{V}}[\wp,:] = \boldsymbol{I}$:

$$\begin{cases} \boldsymbol{\theta}_r\left(t=0\right) = \boldsymbol{\theta}_{ini}[\wp] \\ \dfrac{d}{dt}\left(\hat{\boldsymbol{V}}[\wp,:]\boldsymbol{\theta}_r\right) + \boldsymbol{\varphi}[\wp]\left(\hat{\boldsymbol{V}}\boldsymbol{\theta}_r, \boldsymbol{u}; \boldsymbol{\mu}\right) = \boldsymbol{0} \quad \forall t \in \left[0, t_f\right] \end{cases} \tag{8}$$

If we want to build a Reduced Bond Graph at this stage, we will need to reconstruct all walls internal temperatures, which limits the ROM speedup. In fact, these temperatures are necessary to calculate the total internal convective heat flux received by walls-adjacent air zones, and then determine their temperatures. In a perspective similar to [Ryckelynck 2015] where displacements as well as stresses fields are used to build a hyper-reduced model, we propose to perform, in addition to temperature variables reduction based on the matrix $\boldsymbol{A}$, a similar treatment on internal convective heat flux variables in order to reduce the computational time related to internal convective heat fluxes calculation.

3. APPLICATION

We apply here the reduction approach to a cabin thermal model with $Nw = 18$, $Na = 1$, n = 6, t_f = 14400 s, and by varying 8 continuous inputs and parameters: vehicle speed, ambient temperature, vehicle initial temperature, ambient humidity, solar irradiance as well as the mass flow rate, humidity and temperature of the air supplied by AC system. We note that, for this application, only internal and external walls temperatures were exported to form the matrix $\boldsymbol{A}$.

We obtain a CPU time reduction by *30 %*. Concerning the accuracy of the ROM, we generate a new DOE of 500 points, and then draw a histogram of simulations mean squared errors on air zone temperature, which is shown in Figure 2.

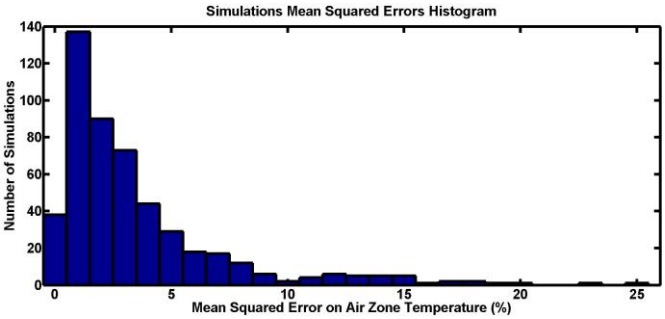

Fig. 2. Simulations mean squared errors histogram

Among the 500 simulations launched, 477 simulations are characterized by a mean squared error of less than 12.5% (equivalent to 1K), which is sufficient for air zone temperature regulation scenarios.

REFERENCES

Chaturantabut, S. and Sorensen, D.C. (2010). Nonlinear model reduction via discrete empirical interpolation. *SIAM J. Sci. Comput*., 32(5), 2737–2764.

Everson, R. and Sirovich, L. (1995). Karhunen-Loève procedure for gappy data. *Journal of the optical society of America A*, 12(8), 1657–1664.

Paytner, H.M. (1961). Analysis and design of engineering systems. The MIT press.

Ryckelynck, D. (2005). A priori hypereduction method: an adaptive approach. *International Journal of Computational Physics*, 202, 346–366.

Ryckelynck, D., Lampoh, K., and Quilici, S. (2015). Hyper-reduced predictions for lifetime assessment of elasto-plastic structures. *Meccanica*, 51(2), 309-317.

Towards enabling heterogeneous model inter-operation across abstraction levels ⋆

Marina Rantanen Modeer * **Christian Sonntag** **
Sebastian Engell ***

* *Technische Universität Dortmund, (e-mail: marina.rantanen-modeer@ tu-dortmund.de).*
** *Technische Universität Dortmund, (e-mail: christian.sonntag@ tu-dortmund.de).*
*** *Technische Universität Dortmund, (e-mail: sebastian.engell@ tu-dortmund.de).*

Keywords: Heterogeneous modelling, Model-based systems engineering, Model interaction, Abstraction

1. INTRODUCTION

Cyber Physical Systems (CPS) are inherently complex and incorporate interacting heterogeneous subsystems. Model based design of complex CPS is a multi-scope, multi-aspect challenge. In the design process of such systems, usually many different models are built. These models describe elements of the system at different levels of detail and under different assumptions, or the overall behaviour of the system in a coarse manner. Currently much effort is spent on testing and on the often costly correction of design flaws which could be reduced if an integrated model-based design approach were used. On the other hand, the required effort for building all-encompassing models of complex systems is often prohibitive, so the modeling efforts should be focused on those aspects which are crucial for the correct interaction of the elements and system function. Therefore a methodology for the integration of heterogeneous models on different levels of detail and abstraction is needed.

Based on available literature it is evident that there are currently two main approaches to this integration - co-simulation frameworks and abstractions of component models. Co-simulation frameworks enable the simulation of numerous inter-connected sub-models, but assume models on the same level of detail to enable a tight coupling. On the other hand, e.g. Sabetta et al. (2005) suggest transformations of component models into abstractions, assuming model components based on the Unified Modeling Language (UML). For a heterogeneous set of models on different levels of detail and different levels of abstraction that are formulated using different modelling concepts, another approach must be taken. The European project MULTIFORM (Hüfner et al. (2012) and Moneva et al. (2011)) introduced a design framework for the management of heterogeneous CPS models. The work presented here builds on ideas from MULTIFORM. We introduce the idea of generating abstractions of detailed models and simulations and embedding them into models that are set up in a different formalism. Useful information can thus be conveyed in a simplified manner from one model to the other.

2. COMPREHENSIVE CPS MODELING USING PARTIAL MODELS

The following hypotheses are assumed based on typical industrial development practice:

(1) Models are built to answer specific design questions and serve different purposes during the different design stages of a CPS. These models therefore cover different elements, aspects and scopes of the system being developed which gives rise to a large amount of models that are expressed in different formalisms using specialized software tools and languages. Together they constitute a partial representation of the system as a whole.
(2) Information which is properly propagated across the abstraction hierarchy can efficiently support the development of a CPS by facilitating and enabling design activities that are dependent on information generated by earlier or parallel investigations.

In typical design sequences, information is propagated from one design model to another in an ad hoc manner analysing and abstracting simulation, optimization or verification results without algorithmic support. To enable model management and information propagation using a computer based approach, model abstractions that provide a simplified representation of a detailed component model or of its behavior from one model to the other should be generated. For instance, detailed models that are developed to provide information corresponding to what is directly observable in a real system, i.e. comparable to measurements of an implementation of the system or component could be stripped to the essentials for other design activities. Such an abstraction has the potential to support model inter-operation between different levels and horizontally on the same level of abstraction. This approach also enables design tasks that would otherwise

⋆ The presented work has received funding from the European Union's Horizon 2020 Framework Programme for Research and Innovation under grant agreement no 674875.

not be possible, i.e. a design activity can embed information that has not be accessible and thereby can include simulations that were not possible earlier. This approach will first identify model dependencies, and then fit one or several models in the target modelling formalism to simulated data.

3. USE CASE: WATER LOCK DESIGN

The challenges discussed above are described through a pertinent use case that was carried out together with a large European organization that commissions, develops and maintains water locks. The organization uses an extensive model-based approach in all major design steps. Currently model interactions are heavily dependent on informal exchanges of information between model designers, and model management is mainly documentation based. In the overall water lock development process a large set of tools are used as there are specialized tools available for each specific design task.

Various design alternatives are evaluated based upon coarse, system wide models. After a concept has been decided upon, numerous Computational Fluid Dynamic (CFD) simulations are carried out with the ultimate goal to determine the filling and emptying times based on surrounding conditions and the specific canal and lock component dimensions. The simulations aim at capturing worst-case scenarios in order to formulate conservative design requirements. Subsequent activities involve mechanical, electrical and control systems design.

In the following, we discuss the interaction between a lock specific CFD model and a model that is used to synthesize supervisory controllers for water locks using hybrid automaton models of the lock operations. These are developed in the open source tools LOCKSIM and the Compositional Interchange Format (CIF) (Reniers et al. (2017)). The supervisory controller that is generated on the basis of the CIF operations model developed by Reijnen et al. (2017) is validated using a hybrid-automaton plant model that was also developed in CIF. The plant model is based on a number of assumptions about the hydrodynamic behaviour - assumptions that are based on lock design requirements. Only static information is communicated through this strategy and the model is therefore disregarding hydrodynamic conditions and events that could potentially affect the emptying and filling times that are relevant for the validation, such as an abundance or deficiency of rain water and the associated soil conditions.

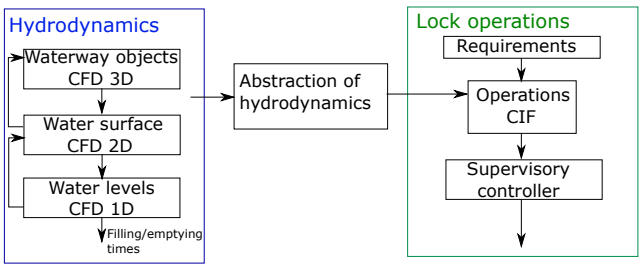

Fig. 1. Concept of supporting design activities by embedding abstracted models that result from other simulation studies.

Inside the plant model developed by Reijnen et al. (2017), the evolution of the water level is currently described by a differential equation (DE) in a separate automaton. This DE provides a coarse approximation of the evolution of the change of the water level based on sensor readings of the lock paddle positions and culvert flows. Extending the plant model with another set of automata that contain different dynamic models extracted from the CFD model, would allow the supervisory control designer to carry out more accurate validations and to update the requirements accordingly. Figure 1 illustrates the suggested generation and embedding of abstractions.

The CFD simulations clearly showed that emptying and filling times are dependent on the state of the environment. If for instance the ground is saturated with water due to rain, water flow into and out of the water lock chamber is significantly affected. To create an abstraction of the CFD model, a number of simulations are run with different inputs to cover the range of probable water conditions relevant to the lock operations model. Simulation results are then approximated by a set of models, for which the situation can be assumed to change very slowly compared to the time scale of the reaction of the supervisory controller. These different approximate models are represented as automata in the CIF plant model and are connected one by one to the overall model to generate new simulated sensor readings of the evolution of the water levels depending on given sensor inputs on lock paddle positions and culvert flows from the plant model.

4. CONCLUSION

This paper introduced the idea of generating abstractions of detailed design models to embed into models expressed in other formalisms during the development of complex CPS. The idea is described through a use case of water lock development in which detailed hydrodynamic models can be embedded into hybrid automata developed for the generation of supervisor controllers.

REFERENCES

Hüfner, M., Fischer, S., Sonntag, C., and Engell, S. (2012). Integrated model-based support for the design of complex controlled systems. In *Proc. European Symposium on Process Systems Engineering*, volume 15, 19–23.

Moneva, H., Hamberg, R., and Punter, T. (2011). A design framework for model-based development of complex systems. In *32nd IEEE Real-Time Systems Symposium 2nd Analytical Virtual Integration of Cyber-Physical Systems Workshop, Vienna*.

Reijnen, F., Goorden, M., Mortel-Fronczak, J.v.d., and Rooda, J. (2017). Supervisory control synthesis for a waterway lock. *2017 IEEE Conference on Control Technology and Applications (CCTA)*.

Reniers, M., van de Mortel-Fronczak, J., and Roelofs, K. (2017). Model-based engineering of supervisory controllers for cyber-physical systems. In *Industrial Internet of Things*, 111–136. Springer.

Sabetta, A., Petriu, D.C., Grassi, V., and Mirandola, R. (2005). Abstraction-raising transformation for generating analysis models. In *International Conference on Model Driven Engineering Languages and Systems*, 217–226. Springer.

On the Lifetime Performances of Dielectric Elastomer Transducers Under Constant Electric-Stress Loading

Yi Chen*, Lorenzo Agostini, Marco Fontana***, Rocco Vertechy***

** Department of Industrial Engineering, University of Bologna*
Bologna, Italy (e-mail: yi.chen4@unibo.it, rocco.vertechy@unibo.it)
*** PERCRO Laboratory - TeCIP Institute, Scuola Superiore Sant'Anna*
Pisa, Italy (e-mail: lorenzo.agostini@santannapisa.it)
**** Department of Industrial Engineering, University of Trento,*
Trento, Italy, (e-mail: marco.fontana-2@unitn.it)

Keywords: Dielectric elastomer generators, Fatigue, Reliability, Weibull probability distribution.

1. INTRODUCTION

Dielectric elastomer transducers (DETs) are deformable capacitors, made by highly elastic dielectric layers coated with compliant electrodes. They are electrostatic devices that make it possible to convert mechanical energy into direct current electricity and vice-versa (Carpi et al. (2008)). As such, they can be used to conceive solid-state electrostatic actuators, generators and sensors exhibiting the following properties (Carpi et al. (2008)): large energy and power densities; ease of manufacture and integration; good resistance to shocks and corrosion; silent operation; low cost.

Recently, commercial rubber membranes made of silicone elastomers, natural rubber and styrenic rubber demonstrated excellent electromechanical properties for the development of high energy density DETs. In particular, in experimental applications as generators, inflatable DETs based on silicone elastomers made it possible to consistently convert pneumatic energy into electricity at an energy density per cycle greater than 150 J/kg (see for instance Moretti et al. (2017)) and greater than 400 J/kg in case of styrenic rubber.

These experimented performances can however be sustained for a limited number of cycles only, after which the DET fails irreversibly. To date, very little information is available on the fatigue life performances of dielectric elastomer materials and of the transducers made thereof (Kornbluh et al. (2010)). Having identified electrical breakdown as the most probable mode of DET failure (Kornbluh et al. (2010)), this work reports and discusses on a set of lifetime constant electric-stress tests conducted on frame stretched circular DET specimens made of a styrenic rubber.

2. EXPERIMENTAL

An experimental test-bench (see Fig. 1) has been purposely developed for the simultaneous testing of a batch of up to 16 DET specimens by subjecting them to cyclic loading with general electric field waveforms and no controlled force or displacement. The test-bench features fully automated operation and data acquisition/saving, including automatic detection and isolation of broken DETs.

Three different batches, each made of 16 frame-stretched circular DET specimens, were prepared using a custom made styrenic rubber as elastic dielectric, carbon grease as compliant electrodes and a Delrin holed plate as a clamping frame (see Fig. 2). All specimens were identical: 25 mm in diameter ϕ, 27 μm in thickness t and with 2.6 pre-stretch.

The developed experimental test-bench was used to perform lifetime constant-stress tests on the prepared specimen batches by subjecting them to square wave electric field signals with 50% duty-cycle, 1 Hz frequency and with the following amplitudes: 127 MV/m for the first batch, 100 MV/m for the second batch and 70.3 MV/m for the third batch.

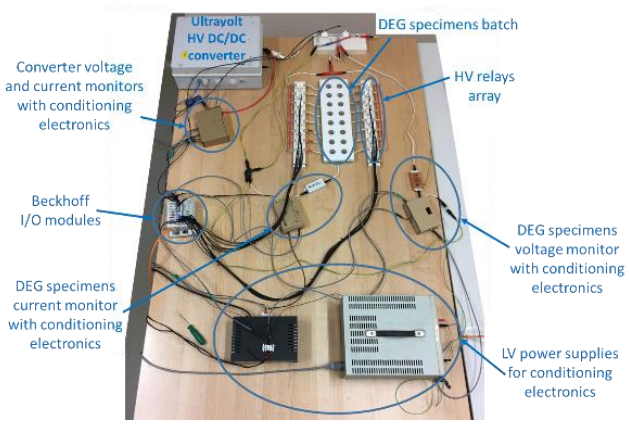

Fig. 1. Experimental set-up used for lifetime characterization.

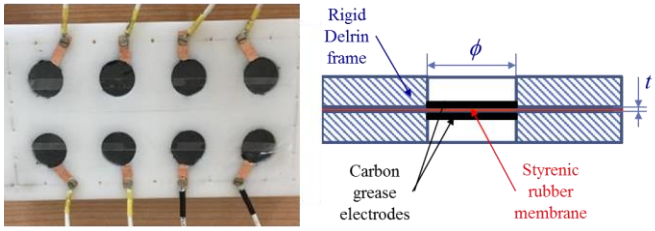

Fig. 2. Frame-stretched circular DET specimens: 1 batch of 8 specimens during test (on the left), schematic of one specimen (on the right).

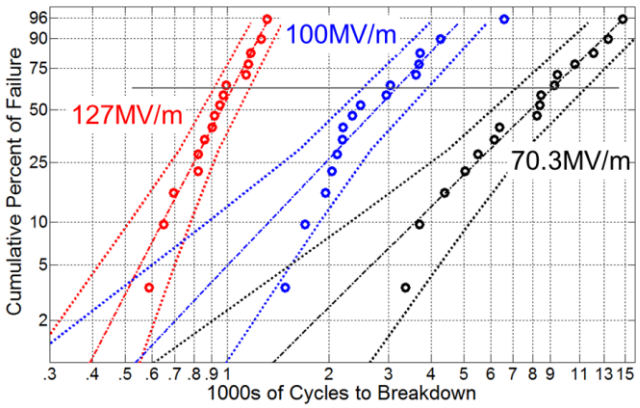

Fig. 3. Weibull plot of lifetime for specimen batches tested at different electric field levels.

Obtained results showed that identical specimens tested at the same level of applied electric field fail at different numbers of cycles, with a rather wide spread of the data. This indicated that electrical breakdown of DETs is a stochastic process.

Acquired data were then manipulated via the Ross's method (as described in the standard IEC 62539) to calculate the probability of failure associated to each broken specimen. Results are shown in Fig. 3: red circles for the batch tested at 127 MV/m, blue circles for the batch tested at 100MV/m, black circles for the batch tested at 70.3 MV/m.

3. MODEL

An analytical model was developed to correlate the number of cycles to failure to the time-law of application of electric field loads.

Following a practice existing in the power cables industry (see for instance Dissado and Fothergill (1992)), we have assumed that the time-to-breakdown dependency on applied electric field of a DET can be described by a Weibull probability distribution in the form:

$$P_F(E,t) = 1 - \exp\left\{-c\int_0^t a t^{a-1}\left[E(t)\right]^b dt\right\}$$

which, for square wave electric field signals becomes

$$P_F(E,N) = 1 - \exp\left\{\left(\frac{N}{N_c^E}\right)^a\right\},\quad N_c^E = N_c\left(\frac{E_c}{E}\right)^{\frac{b}{a}}$$

$$MCTF_E = N_c^E \cdot \Gamma\left(1 + 1/a\right)$$

where a, b, E_c and N_c are parameters to be found via numerical fitting of experimental data, while E is the amplitude of the electric field signal. N^E_c is called the characteristic life, whereas $MCTF_E$ is the mean cycle to failure.

The model was then fitted to the acquired experimental data. Results are shown in Fig. 3 with dash-dotted lines (dotted lines represent 90% confidence bounds).

4. DISCUSSION

Results highlight:

- a strong dependency of DET lifetime on the level of applied electric field; in particular, lifetime decreases as the electric field amplitude is increased;
- the proposed model is adequate to capture the correlation between level of electrical loading and failure in DETs;
- the custom made styrenic rubber shows a MCTF higher than 7000 cycles when loaded with an electric field amplitude of 70.3 MV/m; this lifetime is larger than that reported in Kornbluh et al. (2010) for DET specimens based on acrylic elastomers (VHB 4910 by 3M) and subjected to the same electric field level.

6. CONCLUSIONS

This work described the approach, experimental set-up and procedures that have been developed to characterize the lifetime of dielectric elastomer transducers (DETs) against electrical loading. In addition, it reported and discussed the results obtained from the lifetime testing of frame-stretched circular DET specimens based on a custom-made styrenic rubber. The proposed methodology and obtained experimental results can be used in a design procedure to find optimal trade-offs between DET performance and lifetime/reliability.

Future work on lifetime characterization of DETs will consider: 1) effects of electrical loading frequency; 2) effects of specimen size; 3) effect of specimen pre-stretch; 4) other materials such as silicone elastomers; 5) mixed electro-mechanical loading.

REFERENCES

Carpi F., De Rossi D., Kornbluh R. (2008). *Dielectric elastomers as electromechanical transducers: Fundamentals, materials, devices, models and applications of an emerging electroactive polymer technology*. Elsevier Science, Amsterdam.

Dissado L.A. and Fothergill J.C. (1992). *Electrical degradation and breakdown in polymers*. No. 9., IET.

Kornbluh R.,Wong-Foy A., Pelrine R., Prahlad H. and McCoy B. (2010). Long-lifetime all-polymer artificial muscle transducers. *MRS proceedings*, vol. 1271. Cambridge University Press.

Moretti G., Righi M., Vertechy R.; Fontana M (2017). Fabrication and Test of an Inflated Circular Diaphragm Dielectric Elastomer Generator Based on PDMS Rubber Composite. *Polymers*, vol. 9, n. 7, p. 283.

Magnetic Resonance Radiofrequency Pulse Design by Optimal Control ⋆

Armin Rund * **Christoph S. Aigner** ** **Karl Kunisch**[*, ***] **Rudolf Stollberger**[**, ****]

* *Institute for Mathematics and Scientific Computing, University of Graz, Heinrichstr. 36, 8010 Graz, Austria and BioTechMed-Graz, 8010 Graz, Austria (e-mail: armin.rund@ uni-graz.at).*
** *Institute of Medical Engineering, Graz University of Technology, Stremayrgasse 16/III, 8010 Graz, Austria.*
*** *Johann Radon Institute for Computational and Applied Mathematics (RICAM), Austrian Academy of Sciences, Altenbergstraße 69, 4040 Linz, Austria.*
**** *BioTechMed-Graz, 8010 Graz, Austria.*

1. INTRODUCTION

Progress in magnetic resonance imaging (MRI) often relies on optimal design of radiofrequency (RF) pulses. The aim is usually to perform a specific excitation/refocusing of the nuclear magnetization vector, whose dynamics can be predicted by the Bloch equations. However, RF pulse design is not a trivial task and different approaches were proposed, see e.g. Conolly et al. (1986), Pauly et al. (1991), Rund et al. (2017).
Here, a flexible optimal control model based on the Bloch equations is introduced. The main technical restrictions of a MR scanner hardware are modeled as inequality constraints. An optimization method based on a combined semismooth Newton/quasi-Newton method, penalty methods and trust-region globalization is built. The method is extended to time-optimal control for designing minimum-duration RF pulses. The methods are tested in realistic numerical experiments. The optimized RF pulses are validated in phantom experiments on a 3T MR scanner.

2. MODELING

Broad clinical imaging applications are based on slice-selective excitation (single-slice or recently simultaneous multislice acquisition Barth et al. (2016)), where data for one or multiple slices are collected at each acquisition. The modeling is here usually done in 1D, where a slice is defined as covering an interval in z-direction and extending along the other two directions x and y. The dynamics of the nuclear magnetization vector $\mathbf{M}$ is then modeled using the Bloch equation (without relaxation and in the rotating frame of reference)

$$\dot{\mathbf{M}}(t,z) = \gamma \mathbf{B}(t,z) \times \mathbf{M}(t,z), \qquad \mathbf{M}(0,z) = \mathbf{M}_0(z) \tag{1}$$

with spatial position $z \in (0,L)$, $L>0$, time $t \in I = (0,T)$, and $T>0$. The initial condition $\mathbf{M}_0(z)$ is typically the steady state, i.e. aligned with the strong constant external magnetic field (in z-direction) $\mathbf{M}_0(z) = M_0(z)(0,0,1)^T$ with equilibrium magnetization $M_0(z)>0$. The MR hardware allows a user-defined input of amplitudes of different magnetic fields, which are the RF pulse $(u(t),v(t))$ and the amplitude of the slice-selective gradient $w(t)$. These magnetic fields superpose to $\mathbf{B}(t,z) = (u(t),v(t),w(t)z)$.

⋆ This work is partially funded by the Austrian Science Fund (FWF) in the context of project "SFB F32-N18" (Mathematical Optimization and Applications in Biomedical Sciences). Partial support from BioTechMed-Graz is gratefully acknowledged.

3. MODELING OF THE OPTIMAL CONTROL PROBLEM

RF pulse design typically aims at designing the time-dependent amplitudes $\mathbf{u}(t) = (u(t),v(t),w(t))$ in order to optimize the competing goals of a minimum specific absorption rate (SAR), a minimum duration T, and an optimal slice profile accuracy at the terminal time T. The first two goals give rise to two objective formulations. For single transmit MRI the SAR is proportional to the power of the RF pulse, which leads to the objective

$$\min_{\mathbf{u}(t)} J_{\mathbf{e}} = \frac{1}{2}\|r\|^2_{L^2(I)} + \frac{\alpha_w}{2}\|w\|^2_{L^2(I)} \tag{2}$$

with $u = r\cos(\varphi)$, $v = r\sin(\varphi)$ and $u^2+v^2 = r^2$. Alternatively, we minimize for the duration

$$\min_{\mathbf{u}(t),T>0} J_{\mathbf{t}} = T + \frac{\alpha_r}{2}\|r\|^2_{L^2(I)} + \frac{\alpha_w}{2}\|w\|^2_{L^2(I)}. \tag{3}$$

In both cases, $\alpha_w, \alpha_r > 0$ denote regularization parameters. The third goal (best approximation of a space-dependent desired magnetization pattern in L^2 or L^∞) is posed as nonlinear state constraint

$$\mathbf{g}(\mathbf{M}(T,z)) \le 0, \qquad \forall z \in (0,L). \tag{4}$$

Technical constraints on the scanner hardware are modeled as box constraints

$$0 \le r \le r_{\max}, \qquad |w| \le w_{\max} \tag{5}$$

as well as slew rate constraints $\dot{w} \le s_{\max}$ and a power constraint for the time-optimal setting $\|r\|^2 \le P_{\max}$. Therein, $r_{\max}, w_{\max}, s_{\max}, P_{\max} > 0$.

4. METHODS

A piecewise constant discretization for the control $\mathbf{u}(t)$ is applied. Then, (1) can be solved exactly using complex

rotation matrices (Cayley-Klein formalism, see Pauly et al. (1991)). For fixed T the control constraints (5) are treated with semismooth Newton techniques using the reformulation of the first-order necessary conditions based on Robinson's normal map, see Pieper (2015). Here, we introduce a combined semismooth Newton / quasi-Newton method, were the smooth part of the second derivative is replaced by a BFGS approximation, which avoids tangent/adjoint-for-Hessian solves. The state constraints are treated with penalty methods. Adjoint based exact discrete derivatives are formed for the first derivatives. The Newton-type method is embedded into a trust-region framework using Steihaug-cg, see Steihaug (1983). The method is extended to time-optimal control by using a bilevel method, where the free terminal time is reduced in an outer loop. Here, a heuristics for global optimization is applied to exclude noncompetitive local optimizers. The methods are programmed in MATLAB, the core is parallelized in C using OpenMP.

5. NUMERICAL EXPERIMENTS

The optimization method is tested on a set of realistic examples from Grissom et al. (2016) with different number/thickness/position of the slices, and for different constraint values. A fine resolution in space and time is needed (up to 20000 points each) especially for thin slices. For measurements the temporal resolution is given by the minimum gradient raster time of the MR scanner device (10μs). The optimization runs are initialized with an existing (non-iterative) method of RF pulse design for simultaneous multislice acquisition.
In the time-fixed setting, the power of the RF pulse is reduced by approximately 50% compared to the initial pulse. In the time-optimal case, the pulse duration T can be reduced by $70-90\%$ depending on the example. Two typical time-optimal controls are depicted in Figure 1. As can be seen, both u and $\dot{g}$ are bang-bang solutions everywhere but at around the two peaks of w. Here, other inequality constraints are active that prevent a further time reduction. In examples with tighter SAR or profile constraints, the percentage of bang-bang arcs is decreased significantly. The optimized RF pulses are implemented on a $3T$ MR scanner and the measurements are compared to the simulations.

6. CONCLUSION

A tailored design of RF pulses for clinical applications is important for future directions in MRI. With the presented approach extremly short RF pulses can be generated that allow to speed up MR acquisitions significantly. In a separate work the time-optimal RF pulses were incorporated in a clinical MRI sequence resulting in a fast high-resolution full-head coverage (in 70s), see Aigner et al. (2017). The extension to parallel-transmit MRI will be investigated in the future.

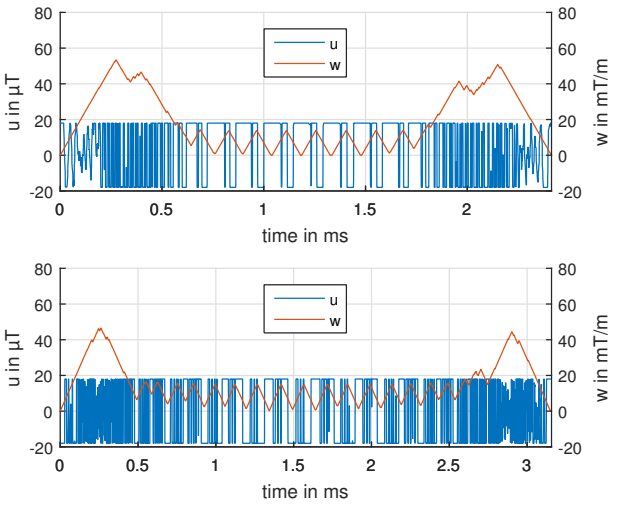

Fig. 1. Time-optimal controls (u, w) using J_t for two typical examples, a SMS refocusing pulse for a diffusion (top) and a turbo-spin echo sequence (bottom). The RF pulses are real-valued ($v = 0$) in these examples.

REFERENCES

Aigner, C.S., Rund, A., Bilgic, B., Gagoski, B., Setsompop, K., Kunisch, K., and Stollberger, R. (2017). Application of time-optimal simultaneous multi-slice refocusing to TSE/RARE. In *Proc. ISMRM 25*, 3843.

Barth, M., Breuer, F., Koopmans, P., Norris, D., and Poser, B. (2016). Simultaneous multislice (SMS) imaging techniques. *Magnetic Resonance in Medicine*, 81, 63–81.

Conolly, S., Nishimura, D., and Macovski, A. (1986). Optimal control solutions to the magnetic resonance selective excitation problem. *IEEE Transactions on Medical Imaging*, MI-5(2), 106–115.

Grissom, W.A., Setsompop, K., Hurley, S.A., Tsao, J., Velikina, J.V., and Samsonov, A.A. (2016). Advancing RF pulse design using an open-competition format: Report from the 2015 ISMRM challenge. *Magnetic Resonance in Medicine*, 1–10.

Pauly, J., Le Roux, P., Nishimura, D., and Macovski, A. (1991). Parameter relations for the Shinnar–Le Roux selective excitation pulse design algorithm. *IEEE Transactions on Medical Imaging*, 10(1), 53–65.

Pieper, K. (2015). *Finite element discretization and efficient numerical solution of elliptic and parabolic sparse control problems*. PhD Dissertation, Technische Universität München.

Rund, A., Aigner, C., Kunisch, K., and Stollberger, R. (2017). Magnetic resonance RF pulse design by optimal control with physical constraints. *IEEE Transactions on Medical Imaging*, https://doi.org/10.1109/TMI.2017.2758391.

Steihaug, T. (1983). The conjugate gradient method and trust regions in large scale optimization. *SIAM Journal on Numerical Analysis*, 20, 626–637.

Modelling and Simulation of Hybrid Systems with Neural Networks

Stefanie Winkler * **Martin Bicher** ** **Andreas Körner** *
Felix Breitenecker *

* *TU Wien, Institute for Analysis and Scientific Computing, Vienna, Austria (e-mail: {stefanie.winkler, andreas.koerner, felix.breitenecker}@tuwien.ac.at)*
** *dwh GmbH, Vienna, Austria (e-mail: martin.bicher@dwh.at)*

Keywords: Hybrid Modelling, Neural Network, Mathematical Modelling, Simulation Comparison, Data Modelling

1. INTRODUCTION

Most processes in industry as well as in nature can be rarely described with one simple model. Therefore various modelling methods established in the last years deal with implementations of complex structures. Two of this methods are topic of this contribution. Due to increasing availability of data from multiple resources research in the field of neural networks increased exponentially. Neural networks are used to imitate the human brain and enable algorithms to make their own decisions. Also in the industrial sector the importance of data increases. Therefore the research field big data is also important in current industrial research projects. Urban infrastructure is one example: Cars driving on their own, gathering information while driving to make decisions on human behalf. But it would be careless to use only data-based models for simulation of complex processes involving heavy machines. Therefore first principle models are still important and the base of modelling and simulation. In this contribution, a comparison of these controversial approaches is discussed.

2. HYBRID DYNAMIC SYSTEMS

The term hybrid is often mentioned in connection with the auto mobile industry. Apart from that there are many different areas where hybrid is used and in all these cases the wording stands for a combination of different methods or approaches respectively. In terms of mathematical modelling hybrid defines a combination of multiple modelling approaches in one model. This contribution focuses on hybrid dynamic models which consist of different discrete submodels as well as continuous structures to implement real life scenarios. Switching from one submodel to another, state variables or even underlying mathematical descriptions change at discrete points in time, called events. In order to describe such hybrid systems different formalisms were introduced over the last decade. The usage of automaton, as in Körner (2016) is very common because it gives important information about the model structure. A rough description of the submodels as well as the jump conditions for switching can be included. This formalism focuses on the mathematical modelling and the corresponding mathematical definitions. A common alternative and more simulation driven formalism would be DEVS& DESS. This formalism was first introduced by Ziegler et al. (2000) and was implemented in MATLAB by Deactu et. al (2012). This formalism started with Discrete Event System Specification (DEVS) and was later extended to include dynamic processes (DESS). Furthermore linear affine systems are a widely used method to overcome challenges of hybrid system simulation as well. Especially in the field of control this approach is used to implement hybrid system structures, as described in Potočnik et al. (2010).

3. NEURAL NETWORKS

Artificial neural networks are nowadays a commonly used method, especially in the field of computer learning. In general neural networks are based on the biological nerve structure of human brains. The artificial neural network imitates the reaction chain of a human neural network. The basic structure consists of three layers: the input, the hidden and the output layer. As the names suggest the first and the latter function as input and output nodes. The most interesting one is the hidden layer which contains a specific activation function to process the incoming signal. All three layers are connected by a pattern of edges. Each of these edges carries a certain weight which amplifies or damps the incoming signal before sending it to the next node. In general a neural network gets an input and transforms it according to the weights and activation function until the final output is generated. The remaining question is how to determine these weights and activation functions. In literature one can find different possible definitions from step and linear functions via logistic functions through to sigmoid functions as activation function. This decision depends on the application field of the artificial neural network. The weights of the edges can only be specified using training data consisting of input and corresponding output data. There are different training options for neural networks but a very common method is the back propagation. This means that the available data sets are partly used to tune the weights until the error of the neural network output to the data set output is small enough.

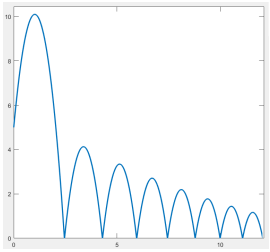

$$\begin{aligned} \ddot{h} &= -g \\ h(0) &= h_0 \\ \dot{h}(0) &= v_0 \ . \end{aligned} \qquad (1)$$

Fig. 1. The equations and graph of a bouncing ball is given.

4. CASE STUDY: BOUNCING BALL

4.1 Model Description

In the following the bouncing ball, an academic example of hybrid systems, is discussed. Considering a bouncing ball, the question might be which part of this process defines it as hybrid. As mentioned in section 2 hybrid models combine continuous and discrete processes. Regarding the bouncing ball the bounce itself represents the discrete part of the model. The bounce only occurs for a single point in time where two things happen: the ball changes its direction and additionally, to take note of the underlying physical damping process, decreases its total velocity. This process can be described mathematically with height h and velocity v. The relation of height and velocity is of course $v = \dot{h}$ and for the acceleration the relation $a = \dot{v} = \ddot{h}$ is valid. To realise the discrete event of the bounce the acceleration has to face opposite direction of gravity. Therefore the model behaviour can be given as an ODE of second order with initial conditions as shown in equation (1).

4.2 Modelling and Simulation

Equation (1) can be transformed into an ODE system applying basic transformations and therefore also be formulated as state space description. As mentioned in the model description the discrete event is defined as the moment when the ball touches the ground. If the following condition, further called jump condition, is fulfilled

$$\Big\{(h(t), \dot{h}(t)) \colon h(t) = 0 \wedge \dot{h}(t) = v(t) \leq 0\Big\}$$

the event is located and the ball's direction changes as defined in (2). The hybrid model description then consists of the state space description, the jump (2) and the jump condition.

$$J(v(t_e)) = -\lambda v(t_e), \ \lambda \in (0,1) \qquad (2)$$

In terms of neural networks hybrid is also a known term and describes a mixture of first principle models and neural networks, as seen in Psichogios et. al (1992). Due to the fact that the bounding ball can be solved analytically, as shown below, training data for the neural network can be generated. Changing the initial condition constants c_1 and c_2 varies and multiple data sets can be created.

$$\begin{pmatrix} x_1 \\ x_2 \end{pmatrix} = \begin{pmatrix} -\frac{g}{2}t^2 + c_2 t + c_1 \\ -gt + c_2 \end{pmatrix}$$

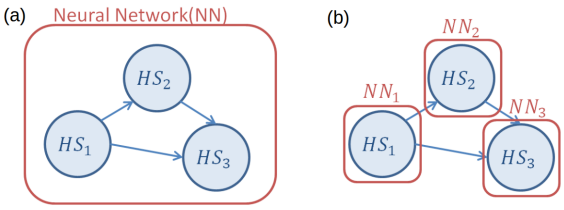

Fig. 2. Different possibilities to apply neural networks for hybrid systems.

5. DISCUSSION

Which data should be used for the input and output set? Are the initial conditions as input sufficient or is it necessary to include the time line as well. Is one hidden layer enough and which certain structure should be used. How many neural networks are necessary to simulate the bouncing ball. Is one neural network with several hidden layers sufficient, as in Fig. 2(a) or is it necessary to establish a different neural networks each simulating one flying phase of the ball, as seen in Fig. 2(b). The latter could be seen as a hybrid model using neural networks as submodels. Another possibility would be to use the mentioned approach of hybrid neural networks. The intuitive implementation takes initial values and timeline in consideration using a fully connected neural network. This of course might not be the best choice.

6. OUTLOOK

This contribution discusses the usage of neuronal networks for simulating hybrid systems in the field of engineering. The chosen case study, the bouncing ball, provides all necessary data to implement and train a neural network. Implementing the different possible structures of neural networks and compare them with common Simulink© and MATLAB© realisations determines if neural networks are useful for simulating hybrid systems. In most cases, the actual hybrid model can not be given in detail, then the gained experiences of this comparison may be applied. Another improvement of performance might be the possibility to use hybrid neural network. Therefore a more detailed analysis of these different approaches is necessary.

REFERENCES

A. Körner, S. Winkler and F. Breitenecker *Possibilities in State Event Modelling of Hybrid Systems* 9th EUROSIM Congress on Modelling and Simulation, Oulu, 2016.

B. P. Zeigler, H. Praehofer and T. G.Kim. E*Theory of Modeling and Simulation, 2nd Edition* academic Press, 2000.

B. Potočnik , G. Mušič and B. Zupančič. A New Technique for Translating Discrete Hybrid Automata into Piecewise Affine Systems *Mathematical and Computer Modelling of Dynamical Systems* pages 41-57, February 2010.

C. Deatcu and T. Pawletta. A Qualitative Comparison of Two Hybrid DEVS Approaches *SNE Simulation Notes Europe vol. 22(1)*, pages 15-24, Vienna, 2012.

D. C. Psichogios and L. H. Ungar. A Hybrid Neural Network-First Principles Approach to Process Modeling *AIChE Journal vol. 38, No. 10*, pages 1499-1511, 1992.

Reduced Basis Method for Real Time Multiple Heat Source Placement Optimization in Ablation Cancer Therapy ⋆

Zoi Tokoutsi * **Martin Grepl** ** **Karen Veroy** ***
Marco Baragona **** **Alfonso Isola** **** **Ralph Maessen** ****

* *Philips Research, High Tech Campus 4, 5656 AE, Eindhoven, NL (e-mail: tokoutsi@aices.rwth-aachen.de).*
** *IGPM, RWTH Aachen University, Templergraben 55, 52062, Aachen DE, (e-mail: grepl@igpm.rwth-aachen.de)*
*** *AICES, RWTH Aachen University, Schinkelstr. 2, 52066 Aachen DE, (e-mail: veroy@aices.rwth-aachen.de)*
**** *Philips Research, High Tech Campus 4, 5656 AE, Eindhoven, NL*

Keywords: Reduced-order models, Reduced basis method, Optimal control, Parameter optimization, Greedy optimization algorithm.

1. INTRODUCTION

Thermal ablation treatments in cancer therapy heat a target volume, enough to cause it to burn, but leave healthy tissue and neighboring sensitive structures undamaged; see Chu and Dupuy (2014). The placement of the heat source and the control of its power are essential for an effective ablation, and are affected by the size and location of the target. In the following, we propose a novel approach to the power-placement problem by dissecting it into two parts.

In the first part we determine the optimal heat source by solving a distributed elliptic optimal control problem, which is parametrized with respect to problem relevant parameters. Using the certified reduced basis method for parametrized distributed elliptic optimal control problems presented in Kärcher et al. (2017), a reliable and real-time efficient surrogate model is created.

The second part determines a reproduction of the optimal heat from the first part using heat sources produced by ablation devices. This is achieved by the optimization of the power settings and placement parameters of one or multiple heat sources. A greedy multiple heat source placement algorithm is introduced, so that multiple heat sources can be positioned in order to improve the approximation of the target function.

2. PART I: OPTIMAL HEAT DISTRIBUTION

2.1 Transfer of Heat in Living Tissue

The Pennes bioheat equation in Pennes (1948) describes the heat transfer in living tissue and approximates the cooling effect of blood circulation as an isotropic heat sink, proportional to the blood flow rate and the difference between the body core temperature and the local tissue temperature. The non–dimensional stationary *bioheat equation* is

$$\begin{aligned} -k\Delta y + cy &= u, && \text{in } \Omega \\ k\nabla_\nu y + hy &= 0 && \text{on } \Gamma \end{aligned} \tag{1}$$

where y and $u \in U = L^2(\Omega)$ are the *temperature* and *heat* functions, k is the *thermal conductivity*, c is the *blood perfusion parameter* and h is the *convection parameter*.

The corresponding weak formulation is

$$\begin{aligned} \int_\Omega k\nabla y\nabla\phi + \int_\Omega cy\phi + \int_\Gamma hy\phi &= \int_\Omega u\phi \\ &\Leftrightarrow a(y,\phi;\mu) = b(u,\phi;\mu) \end{aligned} \tag{2}$$

for all $\phi \in Y = H^1(\Omega)$, where $a(\cdot,\cdot;\mu) : Y \times Y \to \mathbb{R}$ is continuous and coercive, $b(\cdot,\cdot;\mu) : U \times Y \to \mathbb{R}$ is continuous, and $\mu \in \mathcal{D}$ represents the parameters of interest. Here, μ may include tissue parameters or geometric parameters such as the proximity of the tumor to risk structures as in Tokoutsi et al. (2017).

2.2 The Distributed Optimal Heat Problem

The optimal heat is the solution of a distributed optimal control problem, constrained by the bioheat equation (1). The computational domain is divided into *target* Ω_1, *risk* Ω_2 and *healthy* Ω_3 tissue. The target temperature is set to be 0.18 over the target Ω_1 and 0 elsewhere. Each term in the cost functional is weighted according to its significance. The optimal heat can be parametrized with respect to the problem parameters, and the weights of the summands of the corresponding cost functional.

The optimal heat u^* is determined as the solution to

$$\begin{aligned} \min_{u\in U} J(y,u) :&= \sum_{i=1}^{3} \frac{\lambda_i}{2}\|y - y_d\|^2_{L^2(\Omega_i)} + \frac{\lambda}{2}\|u\|^2_{L^2(\Omega)} \\ &= d(y - y_d, y - y_d;\mu) + \lambda\, c(u,u;\mu)/2 \\ \text{s.t. } a(y,v;\mu) &= b(u,v;\mu)\ \forall v \in Y = H^1(\Omega) \end{aligned} \tag{3}$$

⋆ This work is supported by the European Commission through the Marie Sklodowska-Curie Actions *(European Industrial Doctorate, Project Nr. 642445).*

Using the Lagrangian formulation and calculating the first order optimality conditions of the resulting optimization problem, a system of equations is obtained; see e.g. Tröltzsch (2005). Given $\mu \in \mathcal{D}$ the optimal solution $(y^*, u^*, p^*) \in Y \times U \times Y$ satisfies

$$\begin{aligned} a(y^*, \phi; \mu) &= b(u^*, \phi; \mu) && \forall \phi \in Y, \\ a(\varphi, p^*; \mu) &= d(y_d(\mu) - y^*, \varphi; \mu) && \forall \varphi \in Y, \\ \lambda c(u^*, \psi; \mu) - b(\psi, p^*; \mu) &= 0 && \forall \psi \in U. \end{aligned} \tag{4}$$

Here p^* is the adjoint function and the equations (4) correspond to the vanishing directional derivatives of the Lagrangian of (3), and are called the *state*, *adjoint* and *gradient* equations.

3. REDUCED BASIS APPROXIMATION

The efficient and reliable online solution of PART I is achieved by employing the Reduced Basis (RB) method. Using an adjusted version of the well established greedy sampling algorithm, a sample set $\mathcal{D}_N = \{\mu^1, \cdots, \mu^N\} \subset \mathcal{D}$, the associated integrated reduced basis space $Y_N = \text{span}\{y^*(\mu^n), p^*(\mu^n),\ 1 \le n \le N\}$, and the reduced basis control space $U_N = \text{span}\{u^*(\mu^n),\ 1 \le n \le N\},\ 1 \le N \le N_{\max}$, are generated. The greedy algorithm utilizes rigorous and (online-)efficient a posteriori error bounds, which are obtained by manipulating the error residual equations of the optimality system (4). It can be shown that:

Proposition 1. For any $\mu \in \mathcal{D}$ the optimal heat error in the energy heat norm $\|\cdot\|_{U(\mu)}$ satisfies

$$\Delta_N^{u,\text{ALT}}(\mu) := c_1(\mu) + \sqrt{c_1(\mu)^2 + c_2(\mu)},$$

where $c_1(\mu)$, $c_2(\mu)$ depend on the lower bound of the coercivity constant of $a(\cdot,\cdot;\mu)$, the upper bound of the continuity constant of $b(\cdot,\cdot;\mu)$, and the upper bound C_D^{UB} for the constant $C_D(\mu) := \sup_{u \in Y} |u|_{D(\mu)} / \|v\|_Y \ge 0$, and the dual norms of the residuals of the equations in system 4; for details, see Kärcher et al. (2017).

4. PART II: GREEDY MULTIPLE HEAT SOURCE PLACEMENT

4.1 Heat Source Power-Placement Optimization

The second part of our proposed method is concerned with the optimization of the power $P \in \mathbb{R}$ and placement $\chi \in \mathbb{R}^m$, $m = 5$ in 3-D, of a finite number of heat sources using the optimal heat u^* of the first part as target. We assume here that the heat sources are reproducible with state-of-the-art medical equipment. We further assume that each heat source can be described using a sufficiently smooth closed formulation, e.g.

$$Q(x, \chi, P) = P \exp\Big(- (x - \chi)^2 / (2\gamma^2) \Big), \tag{5}$$

where the variance γ^2 is fitted so that Q approximates the heat source produced by a radiofrequency ablation probe. The optimal placement $\chi^\star$ and power $P^\star$ of each heat source results from solving an optimization problem, where the target heat function $U = U(x; \mu)$ depends on $u^*(x; \mu)$

$$(\chi^\star, P^\star) = \underset{\chi,\, P}{\text{argmin}}\, I(\chi, P; \mu) := \|Q(\chi, P) - U\|^2_{L^2(\Omega)} \tag{6}$$

The power-placement optimization problem (6) is a low dimensional optimization problem which can be solved with common optimization algorithms such as quasi-Newton or trust region methods; see e.g. Nocedal and Wright (2006). Due to the non-convexity of the cost functional, there exist multiple local minima to $I(\chi, P; \mu)$.

4.2 Greedy Multiple Heat Source Placement Algorithm

The placement of multiple heat sources can be achieved iteratively until the collective heat source $Q^\star$ adequately approximates the optimal heat u^*. The proposed greedy multiple heat source placement algorithm will locate the most significant local minima of $I(\chi, P; \mu)$.

Algorithm 1. (Multiple Heat Source Placement). The algorithm is initialized with $U = u^*$ of PART I as target function. On each iteration (k), the termination criteria are checked, the target heat source is updated to $U = U - Q(\mu^{(k-1),\star})$ and $P^{(k),\star}$, $\chi^{(k),\star}$ are determined by solving (6).

The termination criteria consist of the achievement of a prescribed tolerance for the relative heat error norm or for the change in the value of the cost function. A further relevant criterion refers to exceeding a prescribed maximum number of heat sources.

5. SUMMARY

This work presents an algorithm for multiple heat source placement, motivated by thermal ablation treatments, and our steps toward real-time efficiency using the reduced basis method. Numerical results are presented to show the performance of the proposed approach.

REFERENCES

Chu, K.F. and Dupuy, D.E. (2014). Thermal ablation of tumours: biological mechanisms and advances in therapy. *Nature reviews. Cancer*, 14 3, 199–208.

Kärcher, M., Tokoutsi, Z., Grepl, M.A., and Veroy, K. (2017). Certified reduced basis methods for parametrized elliptic optimal control problems with distributed controls. *Journal of Scientific Computing*.

Nocedal, J. and Wright, S. (2006). *Numerical Optimization*. Springer Series in Operations Research and Financial Engineering. Springer New York.

Pennes, H.H. (1948). Analysis of tissue and arterial blood temperatures in the resting human forearm. *Journal of Applied Physiology*, 1(2), 93–122.

Tokoutsi, Z., Kärcher, M., Grepl, M., Veroy, K., Baragona, M., and Maessen, R. (2017). Real time optimization of thermal ablation cancer treatments. In progress.

Tröltzsch, F. (2005). *Optimale Steuerung partieller Differentialgleichungen: Theorie, Verfahren und Anwendungen*. Vieweg.

A System Based Modelling Approach for Anatomic Joints

R. Leskovar * **A. Körner** * **F. Breitenecker** *

* *Technische Universität Wien, Institute for Analysis and Scientific Computing, Vienna, Austria (e-mail: {ruth.leskovar, andreas.koerner, felix.breitenecker}@tuwien.ac.at).*

Keywords: Multibody Modelling, System Simulation, Biomechanics, Human Joints, Feedback Control.

1. INTRODUCTION AND STATE OF THE ART

This contribution deals with the development of a system based modelling approach for anatomic joints. Modelling and simulation in the field of biomechanics is a very important method to analyse the dynamic behaviour of the human body. Understanding the influence of the individual parts of the musculoskeletal system is necessary for the analysis and treatment of diseases. Furthermore, mathematical models of parts of the human body are indispensable in the development of prostheses.
The engineering progress in the last decades in the field of prostheses lead to an enormous enhancement of life quality for disabled people. Nowadays, wearing a prosthesis does not restrict daily life and normal habits so much. Modern leg prostheses adapt to the gait cycle by changing the damping of the knee as humans do it automatically. This technology reduces the risk of falling and extends activities with prostheses as doing sports and walking on uneven ground. Sensoring the knee angle and ground contact of the heel gives the possibility to control the change of the swung into the stance phase and vice versa via a microprocessor in the prosthesis. For example this technology is used in prostheses developed by OttoBock® (2011), a well known manufacturer of healthcare systems.
Among several methods exist to model a biomechanical system, two approaches to describe these systems are most common:

- Partial differential equations
- Multibody modelling.

Modelling a biomechanical system with partial differential equations is used to compute the strains and stresses in the components during small movements. Multibody models are used to describe the kinematics of the underlying system under gross movements. These two approaches describe the biomechanical system on a microscopic and macroscopic level, respectively. In order to formulate a PDE model a detailed knowledge about the system is required which is not every time available.
The main part of this contribution is the integration of a biomechanical system in a system simulation loop circuit and not the formulation of an additional biomechanical model for a human joint. This gives the opportunity to improve the technology used in prostheses and the research in the field of biomechanics of human joints.

Fig. 1. The anatomy of a human knee joint in Schabus and Bosina (2007).

2. MULTIBODY MODELS

Multibody models give the possibility to describe a biomechanical system without having all information about the interactions in the system. The possibility to build a multibody model in an acausal way does not require the mathematical formulation of the system from the first instance on. This does not only allow a fast way of modelling but an analysis of the system. Multibody models thus emphasize the most important elements in a system and their mutual interactions. Hence, multibody models are a powerful tool to model and simulate the kinematics of body parts because it focuses on the mechanical description. A mutibody model contains bodies respresenting flexible or rigid human body parts and links connecting multiple bodies with different types of movements and degrees of freedom. The equations of motion of a multibody model are derived by the Newton-Euler equations and the Lagrange formalism. The motion of rigid bodies can therefore be described by

$$M\ddot{q} + J_q^T \lambda = F. \tag{1}$$

Here M describes the mass matrix of the system, the vector q denotes the system coordinates which contain the translational and rotational movements, the matrix J_q is the Jacobian matrix of the system coordinates, λ represents the Lagrange multipliers and the vector F implies the external forces. The derivation and use of this formula is explained more detailed in Quental et al. (2012).

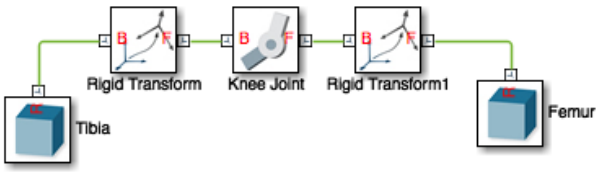

Fig. 2. Simple multibody model of a human knee joint in Simscape.

This description of the dynamics in a human body part by ordinary differential equations allows to consider the biomechanical system as a dynamic system which behaviour changes in time t depending on acting inputs u, disturbances and initial values p, where the output y can be described with an ordinary differential equation f:

$$\dot{y}(t) = f(t, u(t), y(t), p). \tag{2}$$

3. CASE STUDY - THE HUMAN KNEE JOINT

For the first case study we choose the human knee joint to implement as multibody system. The human knee joint is the most complex joint in the human body due to the complexity of the interactions of three bones and multiple ligaments and tendons. The anatomic structure of the human knee is shown in figure 1 with the three bones, the patella, the femur and the tibia as well as the main ligaments, the cruciate and the collateral ligaments.
First we implement a simplified knee model only with the two main bones connected by a revolute joint. The bones are implemented as rigid bodies. The multibody model of this system is developed in Simscape with the multibody model library which can be seen in figure 2.

4. INTEGRATION OF A JOINT MODEL IN A SYSTEM SIMULATION LOOP

As mentioned before the focus of this work is the integration of biomechanical models in a system simulation loop circuit. This closed feedback loop system will be designed in the first attempt for the multibody model but future work will include biomechanical models described by partial differential equations as well and later perhaps additional modelling approaches. This required flexibility of the loop can be seen in figure 3.
To design a closed loop it is necessary to define the input u and the output y of the model in order to create a closed feedback system. In the case of the knee the input would be an acting force on the bone, e.g. the quadriceps muscle which is activating the femur and via the knee joint the tibia as well. Alternatively, modelling a prosthesis for the whole lower limb, the leading microprocessor exerts the force. In this respect, the output y can be the angle of the knee joint in the simplest case to analyse in which phase of the gait cycle the leg is. The controller which reacts depending on the output of the biomechanical model of the knee, defines the acting force on the knee joint for the next time step. This design of a closed feedback simulation loop gives the opportunity to simulate a human gait. For the first approach it will be a walk on even ground but it is possible to design a more complex controller able to adapt not only to the ground but also to the walking speed.

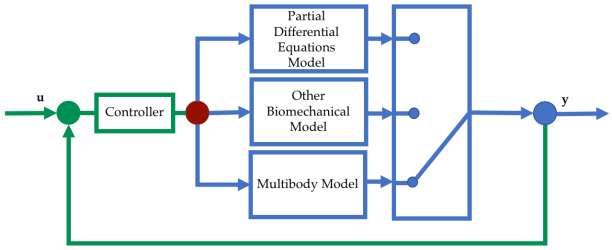

Fig. 3. Design of a feedback loop for different biomechanical models.

To ensure a stable control design specifications for the used model must be made. This will include restrictions for the in- and the output. This work will specialise on models which compute under certain forces the resulting strains in the human knee. This restriction makes sure that the designed controller works for different types of biomechanical models.
In order to design a well defined closed system simulation loop circuit, the system has to depend on time. This means the output of the biomechanical system changes their behaviour not only dependent on the input and parameters but also additionally on time.

5. OUTLOOK

Further work will focus on the specification of the biomechanical model, e.g. ligaments and muscles will be included to analyse a more complex system behaviour, related to Bersini et al. (2016). Moreover, the controller designed for the multibody model will be evaluated for different biomechanical models such as thus based on PDEs. The focus will lay on the examination of the performance and efficiency of the feedback simulation loop depending on different models and their complexity. The aim of this work is to investigate the requirements of biomechanical models for different applications which should help to validate them depending on their applications.
After evaluating the closed loop simulation circle designed for the knee joint, different joint models, as for example a shoulder joint, will be examined.
The results of the established work will be beneficial for the future design of biomechanical models and finally in the development of prosthetical products.

REFERENCES

Bersini, S., Sansone, V., and Frigo, C.A. (2016). A dynamic multibody model of the physiological knee to predict internal loads during movement in gravitational field. *Computer Methods in Biomechanics and Biomedical Engineering*, 19(5), 571–579. doi: 10.1080/10255842.2015.1051972.

OttoBock®(2011). Genium. Technical report, Otto Bock HealthCare GmbH.

Quental, C., Folgado, J., Ambrósio, J., and Monteiro, J. (2012). A multibody biomechanical model of the upper limb including the shoulder girdle. *Multibody System Dynamics*, 28(1), 83–108. doi:10.1007/s11044-011-9297-0.

Schabus, R. and Bosina, E. (2007). *Das Knie - Diagnostik, Therapie und Rehabilitation*. Springer-Verlag Wien New York.

Metabolic supply chains as Origin for Resistance Development

Mert Sezik *

* *Technische Universität Braunschweig, Institute for Computational Mathematics 38106 Germany (e-mail: m.sezik@tu-braunschweig.de).*

Keywords: mathematical modeling, supply chains, population dynamics, biological resistance

1. INTRODUCTION

The investigation of very complex dynamical systems like metabolism of an organism requires the comprehension of important subsystems. Here, we investigate metabolic resistances and in particular the link between the geometry of the metabolic network to the impact of environmental changes in the selection of resistant bio types.

2. SUPPLY CHAINS UNDER ENVIRONMENTAL INFLUENCES

We introduce a supply chain consisting of different compartments $A, B, ..$ whereas each of them can later be interpreted as gen loci in an organism. Each chain posses an inflow in form of j_{in} into the first compartment and an outflow j_{out} off the last. Between each compartment is an connection flow j. All flows are measured against a reference point. Furthermore, we introduce an outer influence $k(z)$ which connects to j and is dependent on a toxic xenophobic substance z. The factor z inhibits k, i.e an increase in z results in a decrease of $k(z)$.
In addition, we need more monotony behaviors for the system. We demand that j_{in} is monotonically decreasing in A and also j_{out} monotonically increasing in B, i.e

$$k \searrow j \searrow j_{\text{in}} \searrow A \nearrow \text{ and } k \searrow j \searrow j_{\text{out}} \searrow B \searrow .$$

Therefor, we obtain for two compartments the system

$$\begin{aligned} \dot{A} &= j_{\text{in}}(A) - j(A,B) \\ \dot{B} &= j(A,B) + j_{\text{out}}(B) \end{aligned} \tag{1}$$

with the inflow $j_{\text{in}}(A) = k_{\text{in}}(1-A)$ the outflow $j_{\text{out}}(B) = k_{\text{out}}B$ and the connecting flow $j(A,B) = k(z)(A-B)$, whereas k_{in} and k_{out} are reaction constants.
By scaling k_{out} and k_{in} to 1 we get from (1)

$$\begin{aligned} \dot{A} &= (1-A) - k(z)(A-B) \\ \dot{B} &= k(z)(A-B) + B. \end{aligned}$$

The desired biological effect is that an increase of z leads to an decrease in j and finally in an decreased j_{out}.

The faster time behavior of a metabolic chain grants us a quick adaptation and therefore in the stationary case $j_{\text{in}} = j_{\text{out}} = j$. It is important to remark that this case happens almost immediately in comparison to the heritage and growth of an organism.
By looking at the stationary case and solving it we yield

$$A^* = 1 - \frac{k(z)}{1+2k(z)} \Rightarrow \quad j^*_{\text{out}} = \frac{1}{2+k(z)^{-1}}. \tag{2}$$

Hence, an increase of the toxic substance z, i.e decrease of k, leads to an decrease of the flow between the compartments.

2.1 Different geometries

After getting insight about the basic behavior of a metabolic supply chain we take the next step by analyzing two different forms of connections between the compartments: The 'AND' and 'OR' connections.

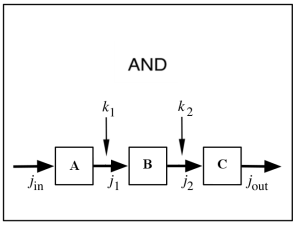

Fig. 1. Illustration of an AND connection

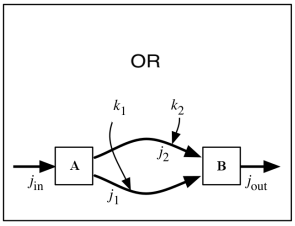

Fig. 2. Illustration of an OR connection

The AND connection is characterized by the continuous sequence of compartments and connecting flows j_i

$$\begin{aligned} \dot{A} &= j_{\text{in}}(A) - j_1(A,B) \\ \dot{B} &= j_1(A,B) + j_2(B,C) \\ \dot{C} &= j_2(B,C) - j_{\text{out}}(B) \end{aligned}$$

whereas the OR connection has two possible connection between the compartments to simulate the fallback solution of an organism in times of shortage

$$\begin{aligned} \dot{A} &= j_{\text{in}}(A) - j_1(A,B) - j_2(A,B) \\ \dot{B} &= j_1(A,B) + j_2(A,B) - j_{\text{out}}(B). \end{aligned}$$

Solving again the equations in the stationary case leads similar to (2) to the outflows

$$j^*_{\text{AND}} = \frac{1}{2+k_1^{-1}+k_2^{-1}} \quad j^*_{\text{OR}} = \frac{1}{2+(k_1+k_2)^{-1}}. \tag{3}$$

As a remark we see that the nature of (3) reminds us of electric circlets, to be more precise: resistances in sequence and parallel connection.

3. PROSPERITY OF AN ORGANISM

Next we model the prosperity of a population by the time repented variable $w(t)$. Each organism in the population

earns an amount j_{out} by the metabolism and has a basic level of consumption b. So we denote $(j_{\text{out}} - b)$ for the reproduction and growth of each organism. Under the assumption of an exponential growth with parameter γ we obtain

$$\dot{w} = \gamma(j_{\text{out}} - b)w. \tag{4}$$

The question is now which mortality s belongs to the growth (4) and this can be solved by comparison to ideal situation $\dot{w}_{\text{id}} = \gamma(j_{\text{out}} - b)w_{\text{id}} =: f(w_{\text{id}})$. Hence, this leads to

$$\dot{w} = f(w) - sw$$

and translates to

$$\gamma(j_{\text{out}} - b)w = \gamma(j_{\max} - b)w - sw \tag{5}$$

which describes ideal growth minus the mortality of a population. By solving (5) for s we obtain

$$s = \gamma(j_{\max} - j_{\text{out}})$$

which is independent of the wealth w of a population. Therefore we can interpret a lack of a metabolic product j_{out} as an increase of mortality s for the population.

4. CONNECTION OF METABOLIC OUTPUT TO RESISTANCES

In analogy with Langemann (2013) we model a population of biotypes with growth, mortality, and inheritance in a closed domain. The occurrence of the biotypes with index i in a certain domain is quantified by its population size c_i depending on the time t. Each biotype i is characterized by its growth rate $w_i > 0$, a mortality rate $s > 0$ depending of a xenophobic substance z. In general, the biotype specific resistances are unknown and so $s(z)$ were a heuristic approach to the resistance development by Langemann (2013). By using our accumulated results of metabolic chains and their geometry can know give a reason for different resistant behaviors during environmental changes.
For better understanding, we will discuss two scenarios for the population dynamic.
Case A is underlined by an AND connection between the gen loci whereas Case B has an OR connection. We denote that x_ix_i is resistant ,x_iX_i is medium resistant and X_iX_i is prone to a toxic treatment with $k_{res} = 1, k_{med} = \frac{1}{4}, k_{pr} = \frac{1}{9}$ and $i \in \{1, 2\}$. We use the same parameters for both cases and see at Table 2., im comparison to Table 1. that the combination of a resistant and a susceptible link results in agreatly decreased mortality rate for the OR connection. We interpret this effect as an alternate solution of an organism to deal with the shortage of a product. As last

Table 1. Mortality rates for an AND connection

s	X_2X_2	X_2x_2	x_2x_2
X_1X_1	0.2	0.18	0.17
X_1x_1	0.18	0.15	0.09
x_1x_1	0.17	0.09	0

Table 2. Mortality rates for an OR connection

s	X_2X_2	X_2x_2	x_2x_2
X_1X_1	0.25	0.19	0.05
X_1x_1	0.19	0.15	0.04
x_1x_1	0.05	0.04	0

we compute the behavior of the biotypes with different

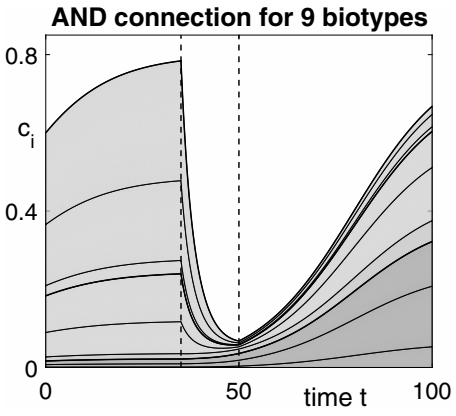

Fig. 3. Only the 3 resistant population gain an advantage after the treatment

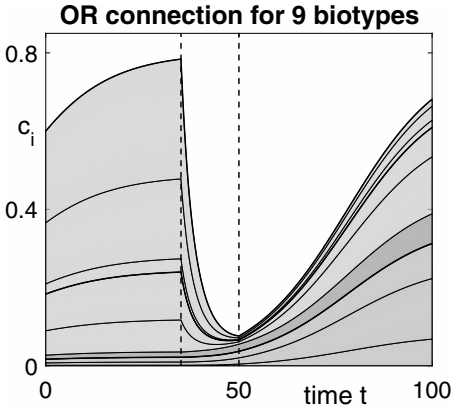

Fig. 4. Better outcome for the medium resistant biotypes after the treatment

mortality rates given by the Tables 1. and 2. As an visual indicator we color the more resistant biotypes in a stronger gray.

As result we remark that biotypes with an OR connection survive better in a changing environment which we can see at Figure 4. ,i.e the middle gray biotypes become larger after the treatment in comparison to a AND biotype with same values.

5. CONCLUSION

Through the usage of metabolic chains we were able to give a mathematical reason for different resistances of certain biotypes under environmental changes. A organism with multiple ways to circumvent a shortage of nutrition can fallback to other sources and therefore handles treatments better than organism with single connections in their metabolism.

REFERENCES

D. Langemann, O. Richter, A. Vollrath (2013) Multi-gene-loci inheritance in resistance modeling. *Mathematical Biosciences, Volume 242*

D. Langemann, M. Rehberg (2009) Unbuffered and buffered supply chains in human metabolism. *Journal of biological physics*

M.Sezik (2017) Dynamical Systems and Model Families for the Development of Resistances *unpublished*

HAPOD – Fast, Simple and Reliable Distributed POD Computation ⋆

Christian Himpe * **Tobias Leibner** ** **Stephan Rave** **

* *Max Planck Institute for Dynamics of Complex Technical Systems, Magdeburg, Germany (e-mail: himpe@mpi-magdeburg.mpg.de)*
** *Applied Mathematics, University of Münster, Germany (e-mail: {stephan.rave, tobias.leibner}@uni-muenster.de)*

Keywords: Model reduction, Proper Orthogonal Decomposition, Singular Value Decomposition

1. INTRODUCTION

Proper Orthogonal Decomposition (POD) is a widely used technique for constructing low-order approximation spaces from high-dimensional input data. Apart from numerous applications in the data sciences, POD is also a fundamental tool for the basis generation in projection-based reduced order modelling methods. In these methods, POD is used to construct low-dimensional state spaces that capture with high accuracy the relevant dynamics of a given high-dimensional discrete model. A quickly computable low-dimensional surrogate model is then obtained by projection of the governing equations of the original model onto the POD approximation space.

The POD space is obtained from a given set of 'snapshot' vectors $\mathcal{S}$ by writing the elements of $\mathcal{S}$ as a matrix of column-vectors, of which a truncated singular value decomposition (SVD) is computed. The left-singular values of this decomposition then form a basis (POD modes) of desired POD space (cf. Sirovich (1987)).

For large-scale applications with an increasing amount of input data vectors, however, computing the POD quickly becomes prohibitively expensive, in particular when the generated data is so large that the snapshot set $\mathcal{S}$ cannot be stored entirely in memory.

In this contribution we introduce a generic, easy to implement approach to compute an approximate POD based on arbitrary tree hierarchies of worker nodes, where each worker computes a POD of only a small amount of snapshot vectors $s \in \mathcal{S}$. The tree hierarchy can be freely adapted to optimally suit the available computational resources. In particular, this hierarchical approximate POD (HAPOD) allows for both, simple parallelization with low communication overhead, as well as live sequential POD computation under restricted memory capacities. We present rigorous error estimates and numerical examples which underline the performance and reliability of our approach.

⋆ Supported by the Deutsche Forschungsgemeinschaft, DFG EXC 1003 Cells in Motion – Cluster of Excellence, Münster, Germany, by the Center for Developing Mathematics in Interaction, DEMAIN, Münster, Germany, by Cells in Motion (CiM) Cluster of Excellence in flexible funds project FF-2015-07, and by the German Federal Ministry of Education and Research (BMBF) under contract number 05M13PMA.

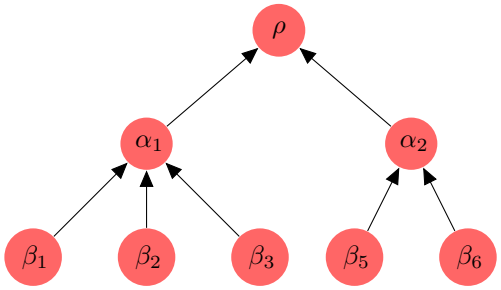

Fig. 1. Tree structure for HAPOD computation with leaf (input) nodes β_i, intermediate nodes α_i and root (output) node ρ.

2. HIERARCHICAL PROPER ORTHOGONAL DECOMPOSITION

The HAPOD algorithm is based on an abstract tree structure (cf. Fig 1) where each node of the tree corresponds to a worker node performing computations on only a small set of snapshot/POD data. The HAPOD computation consists of the following steps:

(1) Distribute snapshot vectors $s \in \mathcal{S}$ among workers at leaf nodes β_i.
(2) At each node:
  (a) compute POD of input vectors for given local error tolerance.
  (b) scale POD modes by corresponding singular values.
  (c) communicate scaled POD modes to parent node.
(3) Return the POD modes at root node ρ as output.

Note that communication is only performed upwards in the worker hierarchy from child to parent nodes. Local PODs can be computed in parallel and asynchronously as soon as all required input data is available. These properties make the HAPOD ideally suited for complex heterogeneous compute architectures and cloud computing, where frequent, synchronous communication of high-dimensional data is not an option. The HAPOD can be combined with any available algorithm for the local POD computation, possibly taking advantage of (parallelized) high-performance implementations specifically adapted to the given problem and computing environment.

2.1 Theoretical Analysis

POD is optimal in the sense that the POD space spanned by the first N modes minimizes the mean square approximation error

$$\sum_{s\in\mathcal{S}} \|s - P_{V_N} s\|, \tag{1}$$

where P_{V_N} is the orthogonal projection onto a given N-dimensional subspace V_N. In Himpe, Leibner, and Rave (2016) we show that for any given tree structure and snapshot set $\mathcal{S}$, we can define local truncation error tolerances for the mean error (1) such that for the resulting HAPOD space V_ρ the bound

$$\frac{1}{|\mathcal{S}|}\sum_{s\in\mathcal{S}} \|s - P_{V_\rho}(s)\|^2 \leq \varepsilon^{*2} \tag{2}$$

holds for any prescribed target error ε^*. Moreover, the number of resulting HAPOD modes is bounded by

$$\Big|\mathrm{HAPOD}[\mathcal{S}, \varepsilon_\mathcal{T}](\rho)\Big| \leq \Big|\mathrm{POD}(\mathcal{S}, \omega\cdot\varepsilon^*)\Big|, \tag{3}$$

where $|\,\mathrm{POD}(\mathcal{S}, \omega\cdot\varepsilon^*)|$ denotes number of modes for a POD of $\mathcal{S}$ with a target error of $\omega\cdot\varepsilon^*$ with arbitrary $\omega\in[0,1]$. At the same time, the number of HAPOD modes at the intermediate nodes α is bounded by

$$\Big|\mathrm{HAPOD}[\mathcal{S}, \varepsilon_\mathcal{T}](\alpha)\Big| \leq \Big|\mathrm{POD}(\widetilde{\mathcal{S}}_\alpha, (L-1)^{-1/2}\cdot\sqrt{1-\omega^2}\cdot\varepsilon^*)\Big|, \tag{4}$$

with L being the depth of the considered tree and $\widetilde{\mathcal{S}}_\alpha$ the set of snapshot vectors assigned to the leaves below α.

Thus, while guaranteeing a prescribed approximation error ε^*, the parameter ω allows us to control the trade off between an optimal approximation space of minimal dimension ($\omega = 1$) and reduction of computational effort, i.e. smaller intermediate PODs ($\omega = 0$).

2.2 Numerical Evaluation

In Fig 2 we show timing results for HAPOD and POD computation on 2D solution trajectories of a P_{15} moment closure/finite volume approximation of the Boltzmann equation for neutron transport, considering the checkerboard test case from Brunner and Holloway (2005). The trajectories were computed on uniform $k\times k$-grids with linearly increasing numbers of timesteps for 125 choices of scattering and absorption coefficients, yielding for $k = 200$ about 2.5 terabytes of snapshot data.

The trajectories were computed in parallel on eleven compute nodes of a distributed memory computer cluster [1] utilizing one processor core for each trajectory.

In all cases the computation time for the trajectories was negligible in comparison to the required time for the POD/HAPOD computation. Already for $k \geq 60$, the POD could no longer be computed due to memory limitations. In addition, the HAPOD was twice as fast for $k = 200$ as a standard POD for $k = 40$, even though the amount of data that needed to be processed increased by a factor of 125.

[1] Each node encloses two Intel Xeon Westmere X5650 CPUs (2×6 cores) and 48GB RAM.

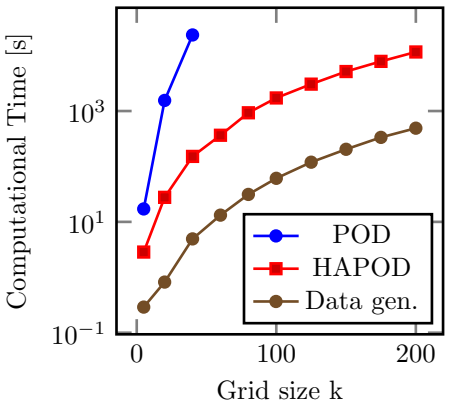

Fig. 2. Computational wall time for POD and HAPOD as well as time for snapshot generation for increasing state-space dimension and number of snapshots ($\varepsilon^* = 10^{-4}$, $\omega = 0.95$).

For full details and further numerical experiments we refer to Himpe, Leibner, and Rave (2016). A reference implementation of the HAPOD algorithm can be found under `https://git.io/hapod`.

REFERENCES

Brunner, T. and Holloway, J. (2005). Two-dimensional time dependent Riemann solvers for neutron transport. *Journal of Computational Physics*, 210(1), 386–399.

Himpe, C., Leibner, T., and Rave, S. (2016). Hierarchical Approximate Proper Orthogonal Decomposition. *submitted*. URL `https://arxiv.org/abs/1607.05210`.

Sirovich, L. (1987). Turbulence and the Dynamics of Coherent Structures Part I: Coherent Structures. *Quarterly of Applied Mathematics*, 45(3), 561–571.

MOR for the MSFEM of the Eddy Current Problem in Linear Laminated Media ★

Karl Hollaus * **Joachim Schöberl** * **Markus Schöbinger** *

* *Institute for Analysis and Scientific Computing, Technische Universität Wien, Wiedner Hauptstraße 8-10, A-1040 Vienna (e-mail: karl.hollaus@tuwien.ac.at)*

Keywords: Eddy current problem, model order reduction, multiscale finite element method.

1. INTRODUCTION

The simulation of the eddy currents in electrical devices with the finite element method (FEM) is satisfactory. However, the large systems to be solved result in high computational costs, i.e. memory requirement and computation time. Although the multiscale finite element method (MSFEM) can be exploited to simulate eddy currents in laminated iron more efficiently the complexity of the problems are still too large to solve them conveniently. The computational costs are a multiple of the costs of anisotropic models in brute force methods according to the components used in the multiscale formulation, compare with Hollaus and Schöberl (2017).

Model order reduction (MOR) has proven to be a powerful methodology to reduce the costs and is well established for linear problems. MOR with proper orthogonal decomposition (POD) has been applied to solve large scale linear problems in computational electromagnetics very successful. Strategies to select an optimal number of snapshots except those with the largest singular values can be found in Sato and Igarashi (2013) and Klis et al. (2016). Those MOR methods are interesting which exploit properties of specific problems. Splitting of the domain into a region where the solution changes strongly due to a parameter variation and the rest, MOR is applied to the rest with almost constant solution in Sato et al. (2016). For example, the speedup factor is about 1.6 for quasitatic problems in 2D by MOR with POD applied only to the linear domain in Schmidthäusler et al. (2014). MOR is frequently used to facilitate the simulation of electrical machines, see for example [Farzamfar et al. (2017)].

In the present work, the idea is to exploit the specific structure of systems coming from the MSFEM for the eddy current problem (ECP) in laminated media for MOR. For example, the entire problem region can be subdivided into air and the laminated media on the one hand and, on the other, the total solution is composed of a large scale and fine scale part. This work focuses on the second aspect which will be called structural model order reduction (SMOR), see also Klis et al. (2016).

The aim is to study the feasibility to exploit the structure of specific systems arising out of MSFEM of ECPs with laminated media for MOR. Much more accurate results are expected by MSFEM with MOR than by FEM with MOR with the same effort.

First, the basic ECP studied in the present work uses a single component current vector potential (SCCVP) T and is discussed in Sec. 2. Then, MSFEM for T is introduced. Next, MOR and structural model order reduction (SMOR) are explained briefly in Sec. 3. A comparison of numerical results obtained by MOR and SMOR are presented in Sec. 4.

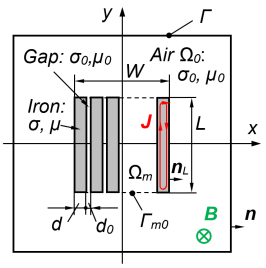

Fig. 1. Eddy current problem in 2D.

2. HIGHER ORDER MSFEM WITH THE SINGLE COMPONENT CURRENT VECTOR POTENTIAL T

2.1 Boundary value problem with T

A current vector potential $\boldsymbol{T}$ can be introduced by $\boldsymbol{J} = \operatorname{curl} \boldsymbol{T}$ fulfilling $\operatorname{div} \boldsymbol{J} = 0$ exactly. This work deals with the single component current vector potential T, e.g., pointing in z-direction $\boldsymbol{T} = T\boldsymbol{e}_z$ in the frequency domain. A simple boundary value problem (BVP) of the ECP in the frequency domain reads, see Fig. 1:

$$\operatorname{curl} \frac{1}{\sigma} \operatorname{curl} T + j\mu\omega T = 0 \text{ in } \Omega \subset \mathrm{R}^2 \tag{1}$$

$$T = T_0 \text{ on } \Gamma \tag{2}$$

2.2 Weak form with T

The weak form for the FEM in the frequency domain reads:
Find $T_h \in V_{h,T_0} := \{T_h \in \mathcal{U}_h : T_h = T_0 \text{ on } \Gamma\}$, such that

$$\int_\Omega \frac{1}{\sigma} \operatorname{curl} T_h \cdot \operatorname{curl} t_h \, d\Omega + j\omega \int_\Omega \mu T_h t_h \, d\Omega = 0 \tag{3}$$

for all $t_h \in V_{h,0}$, where $\mathcal{U}_h \subset H^1(\Omega)$.

2.3 Higher order multiscale finite element method with T

The multiscale approach up to the order 4 for the single component current vector potential

★ This work was supported by the Austrian Science Fund (FWF) under Project P 27028-N15.

$$\tilde{T}(x,y) = T_0(x,y) + \phi_2(x)T_2(x,y) + \phi_4(x)T_4(x,y) \qquad (4)$$

is considered with even micro-shape functions ϕ_2 and ϕ_4 shown in Fig. 2. Simply speaking T corresponds to the magnetic field strength $\boldsymbol{H}$ which is an even function in the lamination, therefore the micro-shape functions ϕ_2 and ϕ_4 are used in (4).

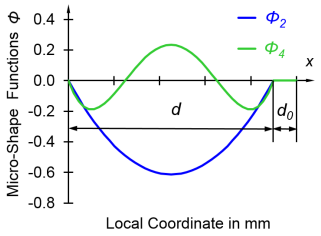

Fig. 2. Even micro-shape functions ϕ_2 and ϕ_4.

2.4 Weak form of MSFEM with T

The weak form reads as:
Find $(T_{0h}, T_{2h}, T_{4h}) \in V_{h,T_0} := \{(T_{0h}, T_{2h}, T_{4h}) : T_{0h} \in \mathcal{U}_h, T_{2h}$ and $T_{4h} \in \mathcal{V}_h, T_{0h} = T_0$ on Γ and $T_{2h} = 0$ and $T_{4h} = 0$ on $\Gamma_{m0,1} \subset \Gamma_{m0}\}$, such that

$$\int_\Omega \frac{1}{\sigma} \operatorname{curl} \tilde{T}_h \cdot \operatorname{curl} \tilde{t}_h \, d\Omega + j\omega \int_\Omega \mu \tilde{T}_h \tilde{t}_h \, d\Omega = 0 \qquad (5)$$

for all $(t_{0h}, t_{2h}, t_{4h}) \in V_{h,0}$, where $\mathcal{U}_h$ is a subspace of $H^1(\Omega)$, $\mathcal{V}_h$ of $H^1(\Omega_m)$ and ϕ_2 and $\phi_4 \in H^1_{per}(\Omega_m)$.

3. MOR AND SMOR

Assume that the MSFEM (5) results in the linear equation system

$$Ax = f. \qquad (6)$$

Furthermore, m snapshots x_i, i.e. solutions of $A_i x_i = f$ by modifying a parameter are calculated and inserted as column vectors in the snapshot matrix S with dimension $n \times m$, where usually $n \gg m$ holds. The present work uses the relative permittivity μ_r as parameter. Next, for the POD based MOR a singular value decomposition (SVD)

$$S = U\Sigma V^*, \qquad (7)$$

the star marks conjugate transpose of V, is carried out. Matrices U $(n \times n)$ and V $(m \times m)$ are Hermitian matrices. The singular values σ_i are arranged in the diagonal of Σ with $\sigma_i \geq \sigma_{i+1}$. Now, an appropriate reduced basis

$$W = [u_1\sigma_1, u_2\sigma_2, ..., u_r\sigma_r], \qquad (8)$$

matrix W represents the projection matrix, is selected considering the essential singular values σ_i, where $r \geq m$ is valid. With $x = Wy$ the reduced order model

$$W^T A W y = W^T f = Ky = g \qquad (9)$$

is obtained. Similarly, SVDs are carried out of all partitions S_i, where $S = (S_0, S_2, S_4)^T$, according to the unknowns T_0, T_2 and T_4 in the approach (4). Therefore, SMOR yields a larger reduced order model than MOR.

4. NUMERICAL RESULTS

The model shown in Fig. 1 consists of 10 laminates, $d = 1.8$mm, and air gaps in between, $d_0 = 0.2$mm. The dimensions of the domains are $|\Omega_m| = 20 \times 20$ mm^2 and $|\Omega| = 40 \times 40$ mm^2. The frequency f was chosen with 50Hz and the conductivity σ with $2 \cdot 10^6$S/m.

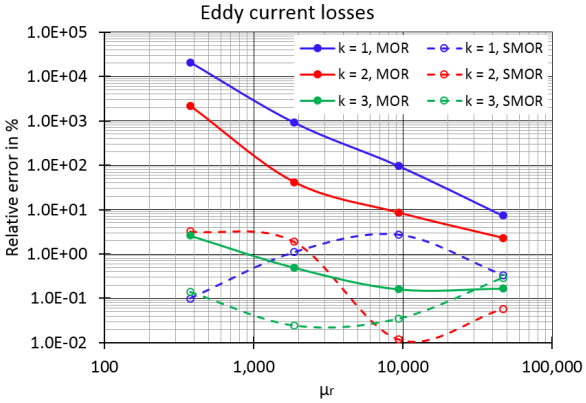

Fig. 3. Comparison of model order reduction (MOR) with structural model order reduction (SMOR).

The relative error presented in Fig. 3 is defined by comparing the eddy current losses P obtained by MOR or SMOR with those of MSFEM:

$$Relative\ error\ in\ \% = \frac{P_{(S)MOR} - P_{MSFEM}}{P_{MSFEM}} \cdot 100 \qquad (10)$$

For the snapshots, μ_r has been selected with 125, 625, 3125, 15625 and 78125. The solutions in Fig. 3 are calculated at μ_r equals 375, 1875, 9375 and 46875, i.e. $m = 5$. The number of basis vectors used in the reduced basis is denoted by k. SMOR provides already for a very small reduced basis reasonable results. The error of MOR decreases for increasing μ_r clearly. MOR and SMOR reduce the MSFEM system by factor of about 100.

5. CONCLUSION

SMOR seams to be working properly already with very few basis vectors, i.e. low dimension of the reduced basis. An extension of SMOR to large and nonlinear problems in 3D will be studied in the future.

REFERENCES

Farzamfar, M., Belahcen, A., Rasilo, P., Clenet, S., and Pierquin, A. (2017). Model order reduction of electrical machines with multiple inputs. *IEEE Trans. Ind. Appl.*, 53(4), 3355–3360.

Hollaus, K. and Schöberl, J. (2017). Some two-dimensional multiscale finite element formulations for the eddy current problem in iron laminates. *IEEE Trans. Magn., (under revision).*

Klis, D., Burgard, S., Farle, O., and Dyczij-Edlinger, R. (2016). A self-adaptive model-order reduction algorithm for nonlinear eddy-current problems based on quadratic-bilinear modeling. *IEEE Trans. Magn.*, 52(3), 1–4.

Sato, Y., Clemens, M., and Igarashi, H. (2016). Adaptive subdomain model order reduction with discrete empirical interpolation method for nonlinear magneto-quasi-static problems. *IEEE Trans. Magn.*, 52(3), 1–4.

Sato, Y. and Igarashi, H. (2013). Model reduction of three-dimensional eddy current problems based on the method of snapshots. *IEEE Trans. Magn.*, 49(5), 1697–1700.

Schmidthäusler, D., Schöps, S., and Clemens, M. (2014). Linear subspace reduction for quasistatic field simulations to accelerate repeated computations. *IEEE Trans. Magn.*, 50(2), 421–424.

MSFEM for the Linear 2D1D-Problem of Eddy Currents in Thin Iron Sheets ⋆

Markus Schöbinger * **Joachim Schöberl** * **Karl Hollaus** *

* *Institute for Analysis and Scientific Computing, Technische Universität Wien, Vienna, Austria (e-mail: markus.schoebinger@tuwien.ac.at).*

Keywords: eddy current, multiscale finite element method, numerical model

1. INTRODUCTION

In rotating electrical machines, it is reasonable to assume that each iron sheet is exposed to the same field, thus it suffices to simulate only one sheet. In the case of the thickness of the sheet being small compared to the other dimensions, the three dimensional problem may be further reduced to a two dimensional one, coupled with a separate one dimensional problem in the direction of the thickness, which will be assumed to be the z axis throughout this contribution. Examples of such an approach have been presented in Bottauscio and Chiampi (2002) and J. Pippuri and Arkkio (2010), where the coupling is realized via a nested iteration, and F. Henrotte and Geuzaine (2015), where this principle was used in the context of homogenization.

This contribution presents a novel approach to this idea utilizing a multiscale finite element method (MSFEM, Hollaus and Schöberl (to be published)). The main principle is to express the behavior of the solution along the z axis via a polynomial ansatz which directly couples into the two dimensional problem, thereby eliminating the need to repeatedly solve two dependent problems. Such a method will be developed and tested for both the A formulation and the T formulation. All models assume a linear, time-harmonic setting.

2. **A** FORMULATION

In three dimensions, the weak form of the eddy current problem is given as: Find the magnetic vector potential $\mathbf{A} \in H(\mathrm{curl})$, satisfying suitable boundary conditions, so that

$$\int_\Omega \mu^{-1}\mathrm{curl}\,\mathbf{A}\cdot\mathrm{curl}\,v + i\omega\sigma\mathbf{A}\cdot\mathbf{v}\,d\Omega = 0 \tag{1}$$

for all test functions $\mathbf{v} \in H(\mathrm{curl})$. In (1) μ denotes the magnetic permeability, i the imaginary unit, ω the angular frequency and σ the electric conductivity.

For the 2D1D model the ansatz

$$\mathbf{A} = \begin{pmatrix} A_{1,1}(x,y)\phi_1(z) \\ A_{1,2}(x,y)\phi_1(z) \\ 0 \end{pmatrix} \tag{2}$$

is chosen. Here the dependency on the coordinate z, aligned with the sheet thickness, is modeled by the linear polynomial function ϕ_1, which is normalized to vary between 1 and -1 along the thickness of the sheet. $A_{1,1}$ and $A_{1,2}$ stand for the two components of one two dimension unknown $\mathbf{A_1} := (A_{1,1}, A_{1,2})^T \in H(\mathrm{curl})$. Here and in the following the space $H(\mathrm{curl})$ in two dimensions is defined via the two dimensional curl operator, which is given as

$$\mathrm{curl}\,\mathbf{A_1} := \frac{\partial A_{1,2}}{\partial x} - \frac{\partial A_{1,1}}{\partial y}. \tag{3}$$

To derive the 2D problem, the ansatz (2) is used in the three dimensional relation (1) for the trial function and the test function, which leads to

$$\begin{aligned}\int_\Omega \mu^{-1}\begin{pmatrix} -\phi_1' A_{1,2} \\ \phi_1' A_{1,1} \\ \mathrm{curl}\,\mathbf{A_1}\end{pmatrix}\cdot\begin{pmatrix} -\phi_1' v_{1,2} \\ \phi_1' v_{1,1} \\ \mathrm{curl}\,\mathbf{v_1}\end{pmatrix} + \\ i\omega\sigma\begin{pmatrix} A_{1,1}\phi_1 \\ A_{1,2}\phi_1 \\ 0\end{pmatrix}\cdot\begin{pmatrix} v_{1,1}\phi_1 \\ v_{1,2}\phi_1 \\ 0\end{pmatrix} d\Omega = 0.\end{aligned} \tag{4}$$

Decomposing the iron sheet Ω in the form $\Omega = \Omega_{2D} \times [-\frac{d}{2}, \frac{d}{2}]$ with the sheet thickness d, in (4) the integration over the z coordinate can be carried out, using basic analysis for the integrals involving the known function ϕ_1. This results in the two dimensional problem: Find $\mathbf{A_1} \in H(\mathrm{curl})$ so that

$$\begin{aligned}\int_{\Omega_{2D}} \mu^{-1}\left(\frac{4}{d}\mathbf{A_1}\cdot\mathbf{v_1} + \frac{d}{3}\mathrm{curl}\,\mathbf{A_1}\mathrm{curl}\,\mathbf{v_1}\right) + \\ i\omega\sigma\frac{d}{3}\mathbf{A_1}\cdot\mathbf{v_1}\,d\Omega_{2D} = 0\end{aligned} \tag{5}$$

for all $\mathbf{v_1} \in H(\mathrm{curl})$.

Because it is not straightforward to use physically meaningful boundary conditions in this setting, the problem is driven by first solving a corresponding magnetostatic problem, which is then used as a right hand side for (5).

3. **T** FORMULATION

For the T formulation the three dimensional problem is given as: Find the current vector potential $\mathbf{T} \in H(\mathrm{curl})$ so that

$$\int_\Omega \rho\mathrm{curl}\,\mathbf{T}\cdot\mathrm{curl}\,\mathbf{v} + i\omega\mu\mathbf{T}\cdot\mathbf{v}\,d\Omega = 0 \tag{6}$$

⋆ This work was supported by the Austrian Science Fund (FWF) under Project P 27028-N15.

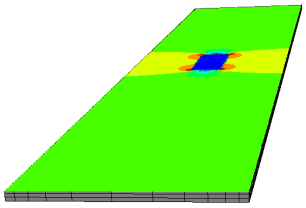

Fig. 1. The iron sheet in the numerical example. Its dimensions are a width of $6mm$, a length of $30mm$ and a thickness of $0.5mm$. At the center of the sheet there is a hole of dimension $1.2mm$ times $3mm$. The material parameters are given as $\mu = 1000\mu_0$ and $\sigma = 2.08 \times 10^6 S/m$.

for all test functions $\mathbf{v} \in H(\mathrm{curl})$, with given Dirichlet boundary conditions for $\mathbf{T}$. Here $\rho = \sigma^{-1}$ denotes the electric resistivity.

For the 2D1D model, a similar ansatz as in the case of the A formulation is chosen:

$$\mathbf{T} = \begin{pmatrix} T_{2,1}(x,y)\phi_2(z) \\ T_{2,2}(x,y)\phi_2(z) \\ 0 \end{pmatrix} \tag{7}$$

Here the behavior in the direction of the thickness is modeled using the even function ϕ_2, which is a quadratic polynomial in z.

Analogous to the process for the A formulation, the ansatz (7) is plugged into (6) and the integration over the z direction is carried out analytically, leading to the problem: Find $\mathbf{T_2} \in H(\mathrm{curl})$ so that

$$\int_{\Omega_{2D}} \mu^{-1} \left(\frac{16}{3d} \mathbf{T_2} \cdot \mathbf{v_2} + \frac{8d}{15} \mathrm{curl}\, \mathbf{T_2} \mathrm{curl}\, \mathbf{v_2} \right) + i\omega\sigma \frac{8d}{15} \mathbf{T_2} \cdot \mathbf{v_2}\, d\Omega_{2D} = 0. \tag{8}$$

for all $\mathbf{v_2} \in H(\mathrm{curl})$. The problem is again driven using the solution of an auxiliary problem for the right hand side.

4. A NUMERICAL EXAMPLE

In order to test the models developed in sections 2 and 3, a simple numerical example is carried out. The dimensions of the problem and the used material parameters can be taken from figure 1.

Figure 2 shows the relative error in the calculated losses. The reference solution was calculated by solving the original problems, (1) and (6), on a three dimensional mesh, respectively. It can be seen that the error increases with higher frequencies, as expected. Out of the given 2D1D models, the one for the T formulation performs better, because it is able to simulate the boundary effects, as can be seen in figures 3 and 4.

5. CONCLUSION

The presented method allow for a reasonably precise calculation of the eddy current losses for low frequencies. An extension into a higher frequency range is possible by including additional ansatz functions. Future work will include testing the applicability of these models in the nonlinear setting. An additional extension will be the development of a modification for the A formulation, which is able to resolve the boundary effects.

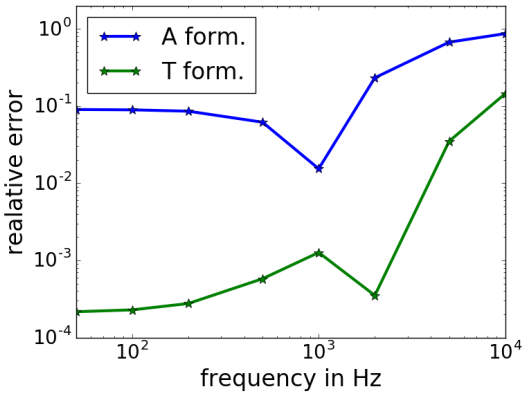

Fig. 2. The relative error in the calculated losses for both formulations.

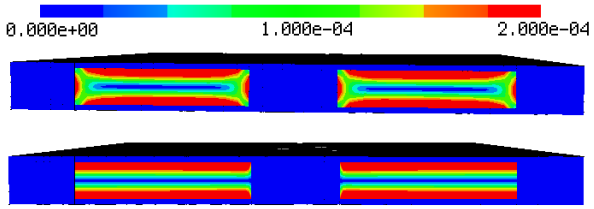

Fig. 3. Absolute value of the magnetic vector potential A in a cross section of the sheet for the reference solution (top) and the 2D1D model (bottom) at 100Hz.

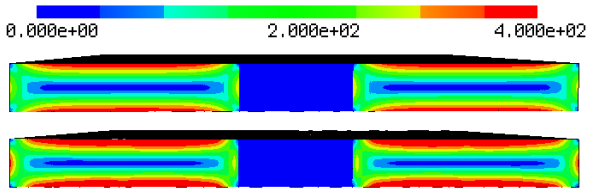

Fig. 4. Absolute value of $\mathrm{curl}\, T$ in a cross section of the sheet for the reference solution (top) and the 2D1D model (bottom) at 100Hz.

REFERENCES

Bottauscio, O. and Chiampi, M. (2002). Analysis of laminated cores through a directly coupled 2-d/1-d electromagnetic field formulation. *IEEE Trans. Magn.*, 38, 2358–2360.

F. Henrotte, S. Steentjes, K.H. and Geuzaine, C. (2015). Pragmatic two-step homogenisation technique for ferromagnetic laminated cores. *IET Sci. Meas. Technol.*, 9, 152–159.

Hollaus, K. and Schöberl, J. (to be published). Some two-dimensional multiscale finite element formulations for the eddy current problem in iron laminates. *IEEE Trans. Magn.*, to be published.

J. Pippuri, A. Belahcen, E.D. and Arkkio, A. (2010). Inclusions of eddy currents in laminations in two-dimensional finite element analysis. *IEEE Trans. Magn.*, 46, 2915–2918.

CO-SIMULATION – AN EMPIRICAL SURVEY: APPLICATIONS, RECENT DEVELOPMENTS AND FUTURE CHALLENGES

Gerald Schweiger*, Georg Engel, Josef-Peter Schöggl*****
Irene Hafner****, Thierry Nouidui*******, Claudio Gomes********

** AEE INTEC Institute for Sustainable Technologies, Gleisdorf, Austria*
(email: g.schweiger@aee.at)
*** AEE INTEC Institute for Sustainable Technologies, Gleisdorf, Austria*
(email: g.engel@aee.at)
**** Institute for Systems Sciences, Innovation & Sustainability Research, University of Graz, Austria*
(email: josef.schoeggl@uni-graz.at)
***** dwh GmbH - Simulation Services und Technical Solutions, Vienna, Austria*
(email: irene.hafner@dwh.at)
****** Lawrence Berkeley National Laboratory, Berkeley, USA*
(email: tsnouidui@lbl.gov)
******* University of Antwerp, Antwerp, Belgium*
(email: Claudio.GoncalvesGomes@uantwerpen.be)

Keywords: Co-Simulation; Computer Modelling; Numerical Simulation; Expert Interviews

1. INTRODUCTION

In recent decades, simulation-driven development has increasingly become established as a central method in industry and academia. This is leveraged by computational advances, like the recent emergence of equation-based modelling languages, which offers new possibilities compared to block diagram modelling using imperative programming languages. Classically, systems are modelled in a single tool, which is referred to as monolithic approaches. With the increased complexity of systems and the need for linking several domains in one model, monolithic approaches have restrictions: Sometimes it is not possible to simulate a complex system in a single tool, but even if it is possible, very often there are more suitable tools available for different subsystems. Ideally, every subsystem is modelled in a tool that meets the particular requirements for the domain and the structure of the model. Thus, the need for coupling different tools is a pragmatic one. Co-simulation is an approach to enable a simulation of complex single or multi-domain systems that consists at least two subsystems (modelled in different tools) which solve coupled (algebraic) differential systems of equations (Gomes et al. 2017).

An overview of co-simulation approaches and tools, research challenges, and research opportunities are presented, e.g. in the references (Trcka 2008; Atam 2017; Mathias et al. 2015; Gomes et al. 2017). The proposed empirical survey aims to merge different views of heterogeneous communities which are working in the field of co-simulation, on the state of the art, research gaps and future challenges.

2. METHOD

As a methodological foundation of the empirical survey, the Delphi method will be adopted. The Delphi method is a forecasting technique that bases on the collection and compilation of expert knowledge from a panel of experts in a multi-stage process (Dalkey & Helmer 1963; Hsu & Sandford 2007). It fosters group communication which is intended to deal with complex problems, particularly for the case where there is insufficient knowledge, lack of historical data, or lack of agreement found within the studied field (Okoli & Pawlowski 2004). The Delphi method is also conceived to be useful particularly for solving interdisciplinary research problems in a heterogeneous environment (Stern et al. 2012). Moreover, it enables determining probable future scenarios.

We aim at integrating 15-30 experts in our Delphi study, because despite the lack of a mandatory minimum requirement, for instance (Clayton 1997) states that 15-30 participants are adequate for studies involving experts with a homogenous expertise background. For selecting the sample of participants, a Knowledge Resource Nomination Worksheet (KRNW) will be used as a guideline (Delbecq et al. 1986; Okoli & Pawlowski 2004).

The Delphi study will form two rounds. The first round will comprise a mix of open-ended and closed-ended questions. The second round will only include closed-ended questions that will be formulated based on the results of the first round. In addition to these standard questions, an additional quantitative analysis of the strengths, weaknesses,

opportunities and threats (SWOT) of co-simulation utilizing the Analytic Hierarchy Process (AHP) will be conducted.

The SWOT-AHP method was introduced by (Kurttila et al. 2000) to increase the effectiveness of a primary SWOT analysis as a decision-making tool (Reinsberger et al. 2015). In this study, the SWOT-AHP method is utilized to enrich the results of the Delphi study by providing an additional and new perspective on the current state of co-simulation.

3. EXPERT INTERVIEWS

The questionnaire for the first round of the Delphi study consisted of four parts: (i) the roots of co-simulation. This includes questions about different origins for co-simulation, concepts, wording and scientific and industrial communities. (ii) Theoretical questions. Included are questions regarding the state-of-the-art, research gaps and open issues within continuous, discrete and hybrid co-simulation. (iii) Functional Mock-Up Interface (FMI). Since FMI is already widely used and it is a promising candidate to become the standard for industry and academia, a section with specific FMI related questions was designed. (iv) Questions related to an overall SWOT-AHP analysis of co-simulation.

At this stage of the survey, the first round of interviews and the expert selection for the second round have both been completed; more than 40 experts have already committed to participate in the second round.

4. PRELIMINARY RESULTS

In the first round of interviews, experts had to select three factors for the categories “Strengths”, “Weaknesses”, “Opportunities” and “Threats”. In the following, we present the results for the pre-selection of SWOT factors in hierarchical order.

Strengths: (i) Every sub-system can be implemented in a tool that meets the particular requirements for the domain, the structure of the model and the simulation algorithm; (ii) cross-company cooperation is supported (e.g., suppliers and system integrators can exchange virtual "trial components" before signing contracts); (iii) every sub-system can be implemented in a tool that meets the particular requirements for the domain, the structure of the model and the simulation algorithm.

Weaknesses: (i) Computational performance of co-simulation compared to monolithic simulation; (ii) robustness of co-simulation compared to Monolithic simulation; (iii) licenses for all programs are required to couple different simulation programs.

Opportunities: (i) Growing co-simulation community / growing industrial adoption; (ii) better communication between theoretical/numerical part, implementation and application/industry; (iii) user-friendly tools (pre-defined master algorithms, integrated error estimation, sophisticated analysis to determine best parameterization of solvers and master algorithm).

Threats: (i) Insufficient knowledge/information of users in co-simulation may lead to improper use (e.g. wrong or missing error estimation, stability issues etc.); (ii) lack of exchange/cooperation between theoretical/numerical part, implementation and application/industry; (iii) incompatibility of different standards and co-simulation approaches.

REFERENCES

Atam, E., 2017. Current software barriers to advanced model-based control design for energy efficient buildings. *Renewable and Sustainable Energy Reviews*.

Clayton, M.J., 1997. Delphi: a technique to harness expert opinion for critical decision-making tasks in education. *Educational Psychology*.

Dalkey, N. & Helmer, O., 1963. An Experimental Application of the Delphi Method to the Use of Experts. *Management Science*.

Delbecq, A.L., Van de Ven, A.H. & Gustafson, D.H., 1986. Group Techniques for Program Planning: A Guide to Nominal Groups and Delphi Process.

Gomes, C. et al., 2017. Co-simulation: State of the art. *Report*

Hsu, C. & Sandford, B., 2007. The delphi technique: making sense of consensus. *Practical Assessment, Research & Evaluation*.

Kurttila, M. et al., 2000. Utilizing the analytic hierarchy process (AHP) in SWOT analysis — a hybrid method and its application to a forest-certification case. *Forest Policy and Economics*.

Mathias, O., Gerrit, W. & Leon, U., 2015. No TitleLife Cycle Simulation for a Process Plant based on a Two-Dimensional Co-Simulation Approach. *Computer Aided Chemical Engineering*.

Okoli, C. & Pawlowski, S.D., 2004. The Delphi method as a research tool : an example , design considerations and applications. *Information & Management*.

Reinsberger, K., Brudermann, T. & Posch, A., 2015. The role of photovoltaics in energy transition - Assessing the prospects for a regime shift. *Gaia*.

Stern, T. et al., 2012. Identifying innovation barriers using a Delphi method approach: the case of technical lignin in the wood-based panel industry. *International Wood Products Journal*.

Trcka, M., 2008. Co-simulation for Performance Prediction of Innovative Integrated Mechanical Energy Systems. PhD thesis .

Potential field based optimization of a prey-predator multi-agent system

Valentin Baillard * **Alexandre Goy** * **Nicolas Vasselin** *
Cristina Stoica Maniu **

* *CentraleSupélec, LMI department, Gif-sur-Yvette, France (e-mail: {valentin.baillard; alexandre.goy; nicolas.vasselin}@student.ecp.fr).*
** *Laboratoire des Signaux et Systèmes, CentraleSupélec-CNRS-Univ. Paris-Sud, Université Paris Saclay, Gif-sur-Yvette, France (e-mail: cristina.maniu@centralesupelec.fr)*

Keywords: Multi-agent systems, potential field, numerical simulation, optimization.

1. INTRODUCTION

The field of multi-agents systems (MAS) is marked out by various methods and approaches (Ren and Cao (2011)). For formation control, graph theory (Mesbahi and Egerstedt (2010)) is a natural paradigm for systems with imperfect information coupled to agents' dynamics, while set-theoretic methods (Blanchini and Miani (2007)) are suitable for addressing uncertainty and implementing constrained control for MAS (Nguyen (2016)). Intelligent control, including Artificial Intelligence (AI) and game theory (Vrancx et al. (2007)) capabilities, is a way to investigate individual behavior effects on collective processes. Potential fields (Leonard and Fiorelli (2001)) are used for *formation tracking* (Ren and Cao (2011)), but scarcely used to the best of the authors' knowledge for *formation producing*.

In this context, this work is part of an educational project on multi-agent systems for the analysis of the dynamics of a swarm of mobile agents. This paper proposes a framework for the optimization of adversarial potential-based prey-predator-like problems. The adversarial potentials are decomposed onto a basis set with different weights. Each weight is individually optimized in a Particle Swarm Optimization-like manner using a Covariance Matrix Adaptation Evolution Strategy (CMA-ES). The first contribution of this paper is related to the partitioning of the potentials followed by a global cost function optimization step, allowing for a topology-based, parameter-based or constraint-based behavioral analysis of a MAS, in a problem with multiple variables. The second contribution is a proof of concept on a "Cops & Robbers" case study, relying both on optimization and environmental variables.

The paper is organized as follows. Section 2 introduces the mathematical tools and methods. Section 3 presents the considered scenario and assumptions, as well as an analysis of the simulation results. Concluding results and current work are drawn in Section 4.

Notation. Let $x, y \in \mathbb{R}^n$. Their euclidean distance is denoted by $d(x, y)$ and the i-th component of x by $x^{(i)}$.

[1] The authors acknowledge the support of the Research Professions stream (Filière Métiers de la Recherche) of CentraleSupélec.

2. THEORETICAL BACKGROUND

The general framework of this paper considers interactions between two adversarial teams of agents (team $\mathcal{A}$ and team $\mathcal{B}$) evolving in an environment $\mathcal{E} \subseteq \mathbb{R}^n$, at speed $v_\mathcal{A}$ and $v_\mathcal{B}$ resp., along with a set of objectives $\mathcal{O}$. With respect to a given objective function F, team $\mathcal{A}$ minimizes F and team $\mathcal{B}$ minimizes the opposite objective function $-F$. The behavior of both teams is achieved by optimizing a potential field decomposed according to its sources.

2.1 Potential fields

A potential is a differentiable function $U : \mathcal{E} \to \mathbb{R}$. Let $c \in \mathcal{A} \cup \mathcal{B}$ be an agent. It generates a potential $U_c^\mathcal{A}$ towards team $\mathcal{A}$ and a potential $U_c^\mathcal{B}$ towards team $\mathcal{B}$. For any objective $o \in \mathcal{O}$ there are similar potentials $U_o^\mathcal{A}, U_o^\mathcal{B}$. Moreover, the borders of the ambient environment generate additional potentials $U_\mathcal{E}^\mathcal{A}$ and $U_\mathcal{E}^\mathcal{B}$. By the principle of superposition, any agent $c \in \mathcal{C}$ (where $\mathcal{C}$ is either $\mathcal{A}$ or $\mathcal{B}$) is thus subject to a potential of the form

$$U_c = \sum_{a \in \mathcal{A}} U_a^\mathcal{C} + \sum_{b \in \mathcal{B}} U_b^\mathcal{C} + \sum_{o \in \mathcal{O}} U_o^\mathcal{C} + U_\mathcal{E}^\mathcal{C} \tag{1}$$

In order to restrict the dimensionality of the problem, only potentials of the following shape are allowed

$$U : x \mapsto \sum_{k \in \mathbb{Z}} u_k \cdot d(x, y)^k, \text{ with } y \in \mathcal{E} \tag{2}$$

where $(u_k)_{k \in \mathbb{Z}}$ is a finitely supported real sequence of optimization parameters. The environment potential takes into account the distance from x to the borders of the environment (considered as a hyperrectangle parallel to the x, y axes). In this setting, the environment potential is a finite sum of terms of the shape

$$U : x \mapsto \sum_{k \in \mathbb{Z}} u_k^{(i)} |x^{(i)} - \alpha|^k \tag{3}$$

for $i \in [\![1, n]\!]$ and some $\alpha \in \mathbb{R}$. The system starts from arbitrary initial positions for the teams $\mathcal{A}$ and $\mathcal{B}$ and evolves in a discrete time. At time $t + 1$, each agent $c \in \mathcal{C}$ (with $\mathcal{C}$ either $\mathcal{A}$ or $\mathcal{B}$) is moving in the opposite direction of the gradient $-\nabla U_c$ at speed $v_\mathcal{C}$, with U_c computed at time t. After a specified number of steps, or when it meets a stopping criterion, the value of F is returned.

2.2 Parameters optimization

For the proposed model, all the behavioral information is contained into the parameters u_k defined in (2) and $u_k^{(i)}$ defined in (3). A CMA-ES algorithm (Hansen (2007)) is used to optimize the parameters regarding the objective function F. CMA-ES is a stochastic optimization strategy best applied to real functions of which only evaluations are known (e.g. simulation results).

3. CASE STUDY

This section presents numerical simulations in a specific case based on a true story (Williams (2015)). This case study (Fig. 1) considers $n_{\mathcal{A}}$ policemen drones (light blue dots) and $n_{\mathcal{B}}$ yakuzas drones (green dots), moving with equal speeds in a rectangle defined by the 2 dark blue dots. The yakuzas have 2 physical objectives (yellow dots): one supply objective s (center) and 4 delivery objectives d (sides). A delivery is a completion from s to d. Initially, each yakuza seeks out objectives d. If it reaches a d, the new objective becomes s. If it reaches s, it seeks objectives d again. A yakuza is removed from the simulation if it encounters a policeman. Any drone colliding with a rectangle border is also removed. The objective function F is the total number of deliveries made by the yakuzas during the simulation.

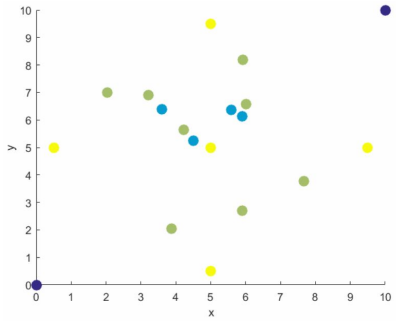

Fig. 1. Extract of a Matlab simulation ($n_{\mathcal{A}} = 4$, $n_{\mathcal{B}} = 8$)

Policemen have no information about the yakuzas' objectives. The potentials are decomposed on the basis described in (1) and (3) restricted to the powers $k \in \{-2, -1\}$ for computational reasons. This leads to 14 parameters entering the CMA-ES algorithm, which are then optimized regarding a single team's objective function. A video illustration of the simulation results is provided at www.youtube.com/watch?v=GscU1e3sc04.

Repulsive interaction corresponds to $u_k > 0$, while $u_k < 0$ yields an attractive interaction. The potential coefficients corresponding to $k = -1$ are associated to a long-range interaction. The long-range attractive potential of the objectives is observed to be larger than the other long-range potentials. The $k = -2$ coefficients (corresponding to a short-range action) are displayed in Fig 2, for a number of policemen $n_{\mathcal{A}} = 4$. Each plot represents the u_k parameter of a component of the potential $U_{\mathcal{B}}$, according to (1)-(3). Three phases are identified. After a highly non-beneficial situation for a single yakuza, the behavior becomes strongly objective-oriented for $n_{\mathcal{B}} \geqslant 2$ (i.e. u_{-2} of the objectives goes to the normalized value -1 in Fig. 2). A drastic behavior change can be seen from $n_{\mathcal{B}} \approx 6$: for more yakuzas, the winning strategy goes from full to mitigated inter-yakuza and yakuza-policemen repulsion (the blue and orange curves scale down towards 0 in Fig. 2). This can be understood as a trade-off between safety at low $n_{\mathcal{B}}$ and high-pay risk from collective action inducing easier workaround at higher $n_{\mathcal{B}}$. The borders intuitively remain strongly repulsive all along.

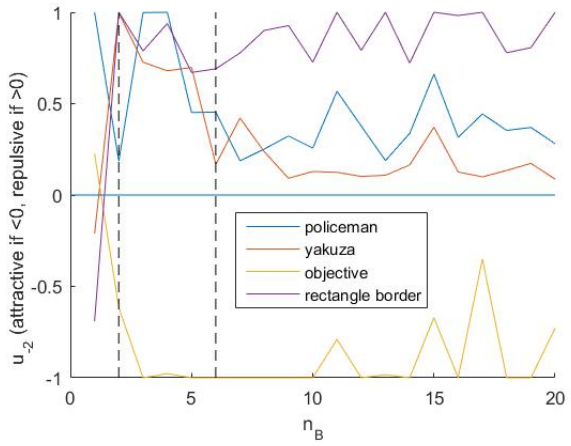

Fig. 2. Team $\mathcal{B}$ potential coefficients u_k w.r.t. $n_{\mathcal{B}}$ yakuzas

4. CONCLUSION AND FUTURE WORK

This paper proposed a potential-based framework using a decomposition basis for the optimization of the behaviors in a prey-predator-like problem. The simulation results highlighted a change of strategy for different numbers of agents in a "Cops & Robbers" scenario.

Future investigations on the $F(n_{\mathcal{A}}, n_{\mathcal{B}})$ map will define the advantage regions for each team. Analyzing the optimized behaviors from a refined model could unveil new strategies and confirm existing ones: by allowing new environment topologies (e.g. objectives numbers and locations, obstacles), by allowing lower k-values or by implementing adversarial optimization.

REFERENCES

Blanchini, F. and Miani, S. (2007). *Set-theoretic methods in control*. Birkhäuser.

Hansen, N. (2007). The CMA evolution strategy: a comparing review. *Towards a new evolutionary computation. Studies in fuzziness and soft computing*, 192.

Leonard, N.E. and Fiorelli, E. (2001). Virtual leaders, artificial potentials and coordinated control of groups. *Proc. of the 40th IEEE CDC*.

Mesbahi, M. and Egerstedt, M. (2010). *Graph theoretic methods in Multiagent networks*. Princeton Univ. Press.

Nguyen, M.T. (2016). *Safe predictive control for multi-agent dynamical systems*. Ph.D. thesis, CentraleSupélec.

Ren, W. and Cao, Y. (2011). *Distributed coordination of Multi-Agent networks*. Springer.

Vrancx, P., Verbeek, K., and Nowé, A. (2007). Decentralized learning in Markov games. *IEEE Transactions on Systems, Man, and Cybernetics*.

Williams, R. (2015). Tokyo police are using drones with nets to catch other drones. *The Telegraph*.

SNE SIMULATION NOTES EUROPE

Simulation Notes Europe (SNE) provides an international, high-quality forum for presentation of new ideas and approaches in simulation - from modelling to experiment analysis, from implementation to verification, from validation to identification, from numerics to visualisation - in context of the simulation process.

SNE seeks to serve scientists, researchers, developers and users of the simulation process across a variety of theoretical and applied fields in pursuit of novel ideas in simulation and to enable the exchange of experience and knowledge through descriptions of specific applications. SNE puts special emphasis on the overall view in simulation, and on comparative investigations, as benchmarks and comparisons in methodology and application. Additionally, SNE welcomes also contributions in education in / for / with simulation.

SNE, primarily an electronic journal, follows an open access strategy, with free download in basic layout. SNE ist the official membership journal of EUROSIM, the federation of European simulation societies and simulation groups. Members of EUROSIM societies are entitled to download SNE in an elaborate and extended layout, and to access additional sources of benchmark publications, model sources, etc. Print SNE is available for specific groups of EUROSIM societies, and starting with Volume 27 (2017) as print-on-demand from TU Verlag, TU Wien.

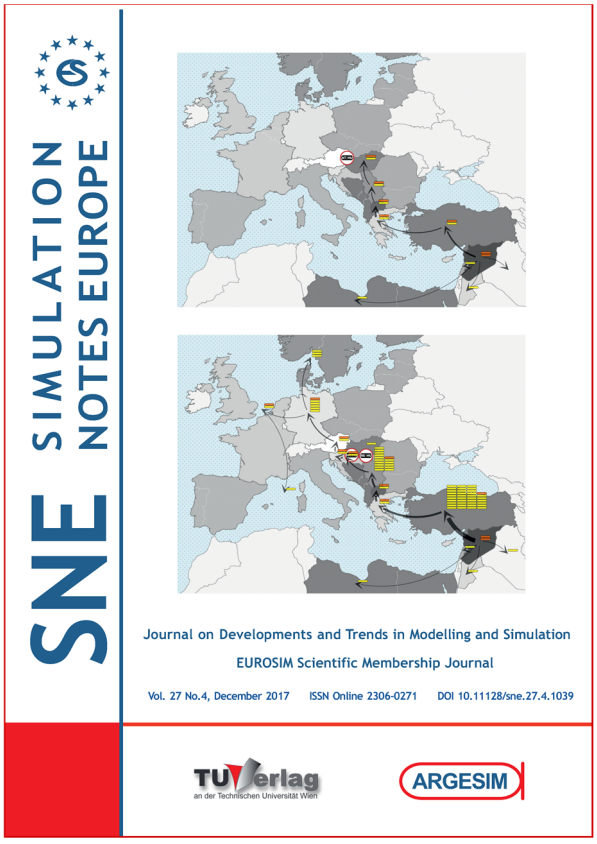

www.sne-journal.org

ARGESIM Publisher, Vienna, www.argesim.org
ARGESIM Report no. 55, ISBN: 978-3-901608-91-9 (ebook)
DOI: 10.11128/arep.55